Growth, structural and electro-optical properties of GaP/Si and GaAsPN/ GaP single junctions for lattice-matched tandem solar cells on silicon

Samy Almosni

Thèse

THESE INSA Rennes
sous le sceau de l'Université européenne de Bretagne
pour obtenir le titre de
DOCTEUR DE L'INSA DE RENNES
Spécialité : Physique - Optoélectronique

présentée par
Samy ALMOSNI
ECOLE DOCTORALE : *SDLM*
LABORATOIRE : *FOTON*

Growth, structural and electrooptical properties of GaP/Si and GaAsPN/GaP single junctions for lattice-matched tandem solar cells on silicon.

Thèse soutenue le 23/02/2015
devant le jury composé de :

Mustapha Lemiti
Professeur (INL, INSA LYON) / Président du jury / Examinateur
Daniel Lincot
Directeur de recherche (IRDEP-CNRS) / Rapporteur
Thomas Hannappel
Professor Doctor (Technische Universität Ilmenau) / Rapporteur
Arnaud Etcheberry
Directeur de recherche (ILV, UVSQ) / Examinateur
Olivier Durand
Professeur (FOTON, INSA RENNES) / Directeur de thèse
Charles Cornet
Maitre de conférence HDR (FOTON, INSA RENNES) / Co-encadrant de thèse
Christophe Levallois
Maitre de conférence (FOTON, INSA RENNES) / Co-encadrant de thèse

Growth, structural and electrooptical properties of GaP/Si and GaAsPN/GaP single junctions for lattice-matched tandem solar cells on silicon.

Samy Almosni

ACKNOWLEDGEMENTS

Firstly, I want to deeply acknowledge my research advisor, Professor Olivier Durand (FOTON), for giving me the possibility of doing my PhD thesis on such a hot topic. His great skills in material science, his availability and the confidence that he has had for me during those last three years, was very important to me. As well, I would like to thank the members of my reading committee: Daniel Lincot (IRDEP), Thomas Hannappel (TU-Ilmenau), for their recommendations and comments. It helped me a lot to have a better understanding of my research and to improve this manuscript. It also was great pleasure to be able to interact with great researcher such has Mohamed Henini (University of Nottingham), Yara Gobato (UFSCar) Robert Kudrawiec (Wroclaw-UT), Jean François Guillemoles (IRDEP), Mustapha Lemiti (INL), Filip Tuomisto (Aalto), Anne Ponchet (CEMES) and Mircea Modreanu (Tyndall). Also I want to thanks Pr James S. Harris (Stanford) and Dr. Homan Yuen (Solar Junction) for giving me the opportunity to meet them and for their priceless advices on the growth of dilute nitride materials. I had the pleasure of working with many great coworkers in the FOTON lab such as Alain Le Corre, Nicolas Bertru and Slimane Loualiche. They're prodigious sources of knowledge and their know-how in molecular beam epitaxy and photonic devices has been extremely helpful in lab. I'm very thankful to Charles Cornet for all the patience he had when he was teaching me everything there was to know about molecular beam epitaxy of III-V compound and for all the attention that he has paid to my work during those past three years. I'm grateful to Karine Tavernier and Christophe Levallois, who have spent a lot of time working with me in cleanroom. It really was a pleasure to work with them because of their good mood so communicative. I'm appreciative to Antoine Létoublon, Yoann Leger, Nicolas Chevalier, Jean Philippe Burin, Thomas Batte, Matthieu Perrin, and Hervé Folliot, all of your help and advice in the areas of materials characterization / processing was priceless. I want thanks Jacky Even, Alain Rolland, Laurent Pedesseau and Jean-Marc Jancu for their help in devices modeling, all the discussion that we had were very stimulating. I'm thankful to all the

students that I met during this thesis and especially to Cedric Robert who gave me a lot of advice on the photoluminescence measurements, Tra Thanh Nguyen who helped me a lot with X-Ray diffraction measurements, Pierre Rale (IRDEP) and Thomas Quincy for all the good moments that we have spent during those three years. I want thanks Julien Lapeyre, Mickaël Coqueux, Yu Zhao, Kamil Klaime, Julie Le Pouliquen, Tony Rohel, Maud Guezo, Cathy Queffelec and Ghislaine Riaux, who have already helped me from one way or another. Finally I thanks all my family and all my friends who have supported me during this great adventure.

TABLE OF CONTENT

INTRODUCTION

Background, motivations and objectives

According to numerous reports, made by governmental organization such as the United Nations (U.N.) and non-governmental ones such as Greenpeace, our civilization is facing major issues such as global warming, the rarefaction of fossil energy resources, and a worldwide energy consumption growth.[1] These three problems are all linked to our energy production and consumption balance which is not in equilibrium with the earth capabilities, considering the available technologies. One part of the way to solve this problem could pass by a massive development of renewable energies, and more specifically of the photovoltaic (PV) energy. Indeed the solar energy is the largest renewable energy supply available and has the potential to cover a significant share of the energy needs of humanity.[2]

The main motivation for the development of low-cost high efficiency solar cells is: to reduce the use of non-renewable energy such as fossil fuels, that has been incriminating to be the cause of global warming; and to provide a competitive alternative for the electricity mass production to nuclear power plants. In this regard, research efforts are focused towards significant price reductions, to reach the grid parity worldwide without any form of subsidies, and to compete economically with other non-renewable energies.

This would allow a quick and sustainable development of the solar energy, which might have a huge impact on our society. Indeed from a societal perspective, the photovoltaic industry has the potential to create more than 2,000,000 jobs worldwide.[3] Also, as a decentralized energy, PV could ease the access to energy in rural areas, thus enabling improved healthcare, education and providing economic opportunities in emerging countries.

From the economic point of view, it is expected that PV will reach competitiveness with worldwide peak power prices before 2020.[4] The coming decade is considered decisive in terms of which countries or global regions will dominate the

future PV industrial sector. Therefore the research effort in this sector is important considering its rapid growth and the economic opportunities that it can bring.

One possible way to reach the grid parity is the elaboration of high-efficiency Concentrated PhotoVoltaics (CPV) solar cells on low-cost substrate. This is the main target of this thesis that has been done in the framework of the ANR project MENHIRS. Indeed, increasing cell efficiency while lowering cell costs are great levers to decrease the overall CPV system cost.[5,6]

In this context, MENHIRS project puts together six French partners, and an associated European partner: FOTON (growth of III-V materials, coordination), INL (Si-based PV technology), CEMES-CNRS (structural characterizations), IRDEP-CNRS (research in PV development), EDF R&D (a European leader in the Energy sector), HELIOTROP (French manufacturer of high concentration photovoltaic modules (HCPV)) and AALTO (a Finnish associated academic partner specialized in point defect characterization). The project approach aims to combine the advantages of high efficiency III-V multi-junctions solar cells (MJSC) and the low-cost silicon substrate.

Dissertation overview

This PhD work focuses on the growth optimization and device development with dilute nitrides materials lattice matched with GaP (001) and GaP/Si (001) pseudo-substrate. The main purpose aims to combine the advantages of high efficiency III-V multi-junctions solar cells (MJSC) and the low-cost silicon substrate in order to promote a large scale development of the photovoltaic energy.

In chapter 1, a state-of-the-art of III-V multijunction solar cells is proposed. Material growth and design challenges related to the fabrication of MJSC are underlined. Finally we present the motivation for choosing the pseudomorphic approach to monolithically integrate III-V absorbers on silicon, in parallel with issues to be overcome.

Chapter 2 briefly introduces the experimental techniques used in this work. They include a growth cluster, which is composed of a Si UHV/CVD chamber connected under UHV to a III-N-V MBE chamber, a rapid thermal furnace, structural characterizations by X-ray diffraction (XRD) techniques; surface morphology characterizations by Atomic Force Microscopy (AFM), optical measurement by

continuous wave photoluminescence cw-PL from 20 to 300K and electrical measurements of contact resistance, doping concentrations and solar cells efficiency respectively by circular transmission line method, C-V measurements and I-V measurements under AM1.5G illumination.

Chapter 3 presents the study of the GaP/Si interface growth optimization. This study focuses on growth parameter impacts on GaP prenucleation, nucleation and regrowth layer, and presents a strategy to limit the generation of structural defects at the GaP/Si interface.

Chapter 4 summarizes results obtained on the growth optimization of the GaAsPN dilute nitride compound grown lattice-matched on GaP (001) substrate by studying the effect of N and As contents, V/III beam equivalent pressure (BEP) ratio, growth temperature and thickness on the optical and structural properties. A comparison with the growth issues encountered during the GaInAsN(Sb) system optimization (which has led to the highly rewarded 1 eV subcell), and reported in the literature, is proposed.

Chapter 5 presents results obtained on the growth and design improvement of the 1.7 eV GaAsPN-based dilute-nitride solar cells grown on GaP (100), by studying the effects of the growth temperature, the absorber doping and the p-i-n structure on the optical and electrical properties. Clear correlations are established between optical and electrical measurements, giving a simple way to optimize the growth of dilute nitride compound by studying their PL properties. Lastly, as the main aim of this thesis, is to grow a high efficiency solar cell on Si, results on the tunnel junction simulation are presented, revealing strategic information on the tunnel junction polarity.

CHAPTER 1. III-V MULTIJUNCTION SOLAR CELLS FOR CPV

In this chapter, we first briefly describe the main processes that allow the generation of electricity from the sunlight, underlining main effects that limit solar cells efficiencies and possible ways to overcome those limitations. A state-of-the-art of multijunction solar cells, starting from the history of the first commercially viable multijunction design to the very last ones is drawn. We discuss the challenges, results and limitations of the various III-V-made multijunction approaches that have paved the way for the monolithic integration of III-V PV on Si substrate. Finally, we present with more details the advantages and the challenges of III-V PV on Si, and motivate the use of the pseudomorphic approach adopted by the MENHIRS consortium.

1.1 Electricity generation from the sunlight

A lot of different classes of thin-films materials are used to elaborate photovoltaics such as amorphous silicon, hybrid perovskites, chalcogenides, kesterites, or organic materials.[7,8,9,10] But up to now, most of commercially available solar cells are made of thick Si semiconductor materials either mono-crystalline or poly-crystalline. However, the crystalline silicon PV technology is now very mature, as testified by the small difference of efficiency between best laboratory cells (25%) and best industrial modules (>22%). Moreover, the efficiency of record cells did not progress much in the past 15 years since this technology is already close to the theoretical efficiency limit. The generation of current in a semiconductor based solar cell depends on two key processes. The first one is the absorption of incident photons coming from the sun to create electron-hole pairs in the semiconductor material. The second process is the extraction of these carriers using an electric field usually generated by a p-n junction. As energy harvesting devices, solar cells are subject to several thermodynamic / electronic processes which limit their efficiency. They are well described by the so-called detailed-balance model and explained in the following.[11,12] Figure 1-1 presents

standard incident solar spectrum measured for space applications (without atmospheric filtering effects: AM0), flat plate modules (with atmospheric filtering effects: AM1.5G) and solar concentrators (with atmospheric filtering effects and without diffused light: AM1.5D).

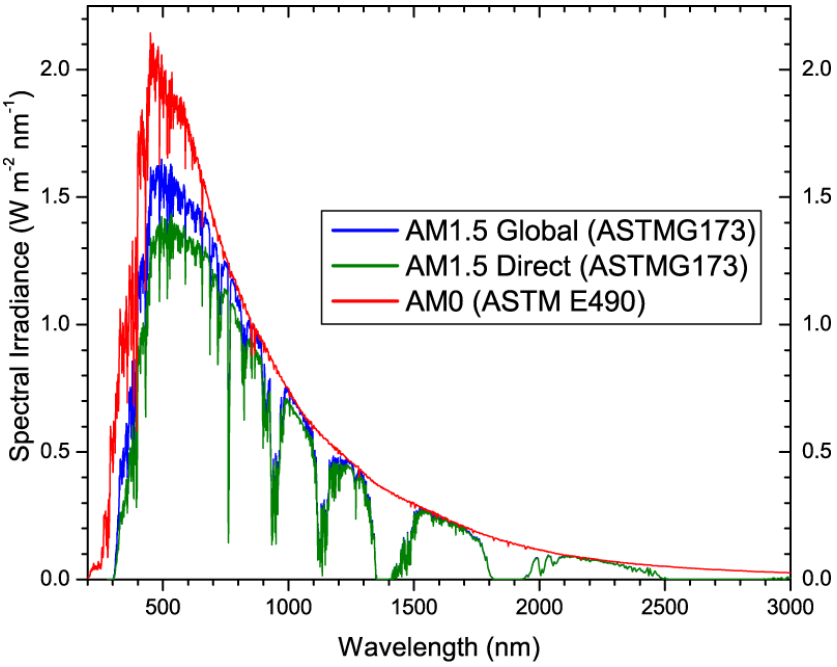

Figure 1-1 : Incident solar spectrum for different applications: space, flat plate modules and concentrator.

As one can notice the sun is emitting polychromatic light with different photons energies. In conventional semiconductors, photons with energy below the semiconductors bandgap energy will not be converted in electron-holes pair. Therefore, the first cause of the efficiency limitation comes from the energy bandgap (E_g) of the semiconductor absorber. E_g gives threshold beyond which the material begins to absorb light. This limit gives rise to losses by transparency. Second, the absorption of photons with energy above the bandgap energy generates "hot carriers" that will thermalize to the energy band edges, through a very fast phonon-mediated process, leading to a loss in the cell bias and an increase of the lattice temperature. Figure 1-2 displays the evolution of theoretical short circuit current density J_{sc} (top) and open circuit voltage V_{oc} (bottom) for a semiconductor single junction as a function of the material energy bandgap for different incident solar spectra.[13] The J_{sc} decrease with the increase of the bandgap is

due to the material transparence while the V_{oc} increase with the increase of the bandgap is due to the higher splitting of the Fermi level inducing a lower thermalization of absorbed carriers. Therefore, considering the material bandgap as the most important parameter, there is a balance between both transparency and thermalization effects.

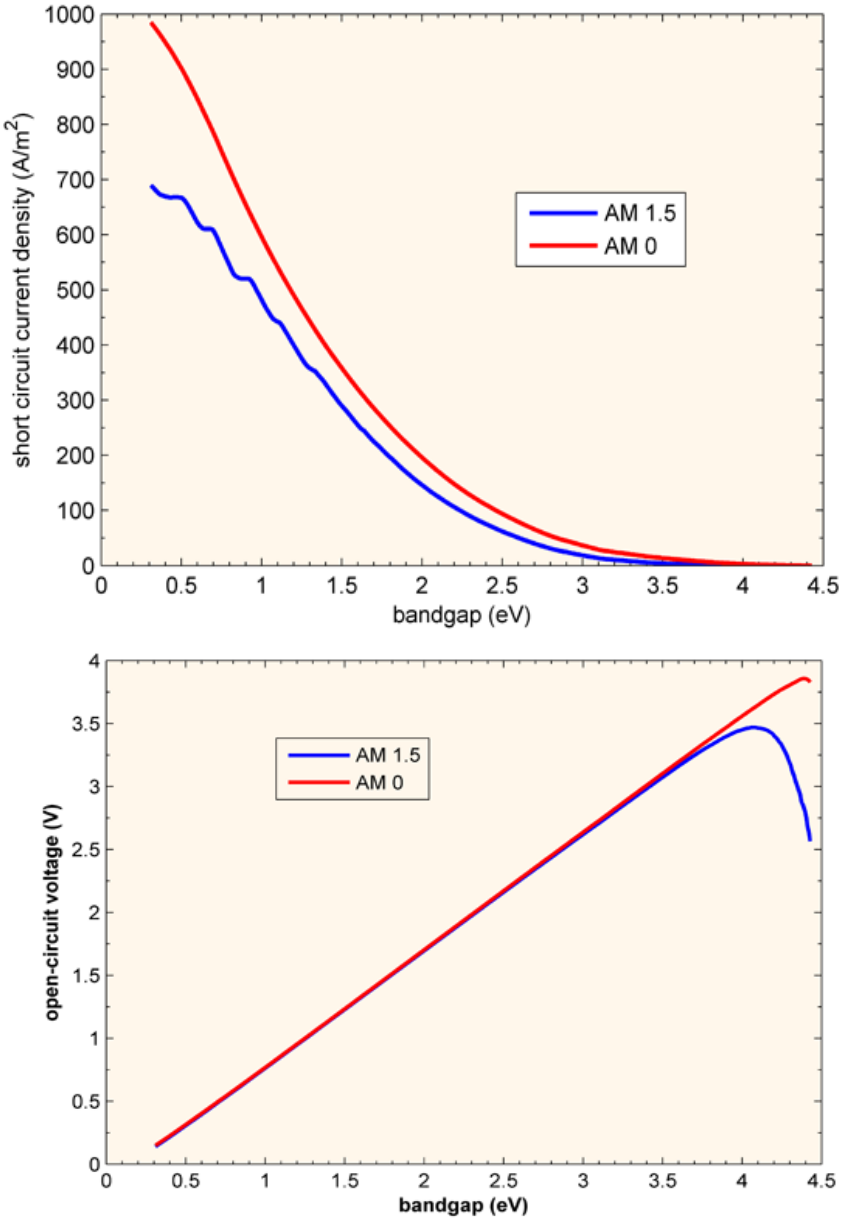

Figure 1-2 : Evolution of (top) theoretical short circuit current density J_{sc} and (bottom) open circuit voltage V_{oc} as a function of the material energy bandgap for different incident solar spectra.[13]

This trade-off has led to the well-known detailed balance limit of efficiency, expressed first by Shockley and Queisser and refined by Würfel through a

thermodynamic approach.[11,14] Indeed, according to the Shockley Queisser detailed-balance model, the efficiency limit under non-concentrated sunlight condition is 31% (for a bandgap of 1.4 eV considering the AM 0 spectrum), and this efficiency limit under fully concentrated sunlight condition reaches 41% (for a bandgap of 1.1 eV). The SQ limit of a single junction is presented as a function of the bandgap in Figure 1-3

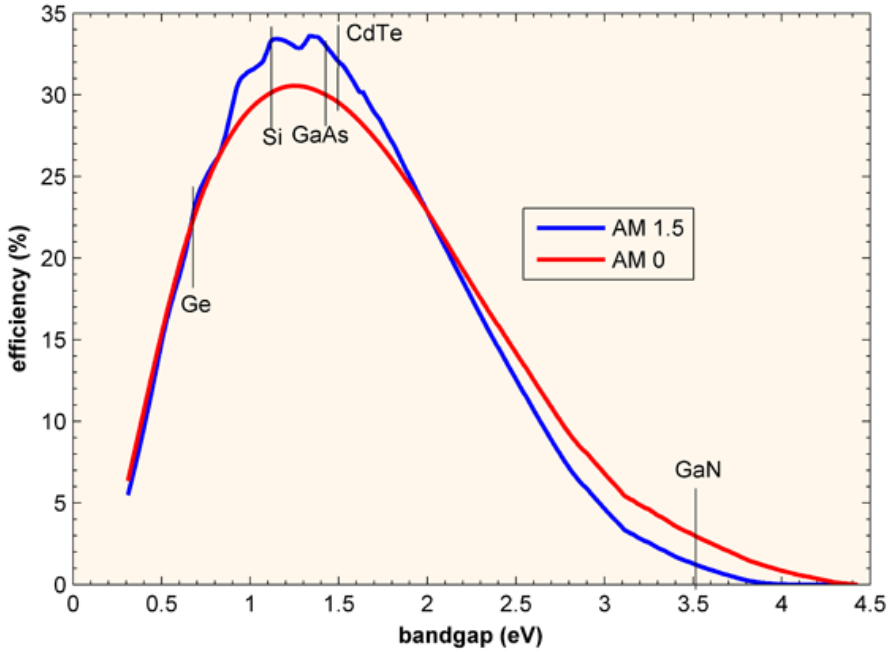

Figure 1-3 : Solar cell efficiency limit as a function of bandgap calculated using the Shockley-Queisser approach.[13]

As shown in Figure 1-4, in the SQ approach the solar cell can be modeled ideally using an electrical equivalent scheme composed by a continuous photo-generator in parallel with a diode (representing the pn junction). The continuous photo-generator electrical properties (J_{sc},V_{oc}) are strongly correlated with the material bandgap energy. Independently of the SQ intrinsic limitation of solar cells, others sources of losses reduce their efficiency in realistic operating conditions. Those losses can have different origins such as reflections, Joule effect in metallic contact or the presence of structural defects in the semiconducting material. They can be modeled by adding series and shunt resistances (R_s, R_p) to the equivalent electrical scheme, which has a strong impact on the Fill Factor. Figure 1-4 displays the corresponding simplified solar cell electric scheme. In order to minimize those losses, different cells architecture can be used.[15] Most of them use highly doped materials with wider bandgap than the absorber as back and front

surface field (BSF and FSF) to improve the efficiency by reducing series resistance and increasing shunt resistance. Also anti-reflective coatings are used to maximize the cell absorption of the solar spectrum. Moreover, a window layer can also be used to reduce the losses by carrier surface recombination. As an example Al is added to GaInP forming Al(Ga)InP in the emitter region. It helps to reduce the surface recombination velocity of carriers, that reduces the blue response of the cell, and hence its current. Also due to its large conduction band offset with GaInP, this material helps the electron collection in the cell. Al(Ga)InP is used in the BSF (Back Surface Field) region, as well, due to its large valence band-offset with GaInP which help the hole collection in the cell.

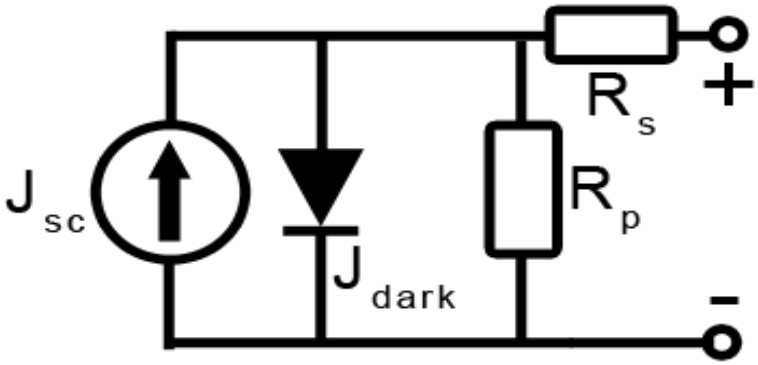

Figure 1-4 : Simplified solar cell electric scheme, including parasitic series and shunt resistances.

The lab efficiency records for single GaAs and Si solar cells, respectively 25,6 and 28%, are now close to the SQ limit considering each bandgap, making difficult and expensive any improvement of the efficiency of those single junction cells due to the SQ limit and almost unavoidable other losses, such as Joule losses in the metallic contacts.[16] Those technologies can thus be considered as mature (i.e. with a very limited potential of improvement). To exceed this limit and reach higher efficiencies, advanced concepts have to be used.

1.2 High efficiency multijunction solar cells

To reduce the thermodynamic losses in solar cells, several concepts have been proposed such as intermediate band and hot carrier solar cells.[17,18,19] The multijunction

solar cells (MJSC) is the most mature of those concepts. Indeed, the highest efficiencies ever registered for photovoltaic devices has been obtained using MJSC.[20] It is a direct way of overcoming the fundamental limitations by using several absorbers with different band gaps, each one dedicated to harvest a part of the solar spectrum so that the losses due transparency and thermalization are both reduced.[21] It is done by stacking the cells so that the top cell has the highest band gap, and harvests the highest energy photons, while the bottom cell has the smallest band gap, collecting the lowest energy photons. Among the different ways to connect electrically the cells, the most commonly used is the two-terminal stacking. In this case, each cell is series-connected by a tunnel junction, which should have a higher band gap than the cell below, be highly doped, and thin (few nanometers) to minimize its photons absorption and to allow an efficient carrier tunneling of the photogenerated carriers.[22] Figure 1-5 shows a typical band diagram scheme of a single junction and a two-junction ("tandem") solar cell.

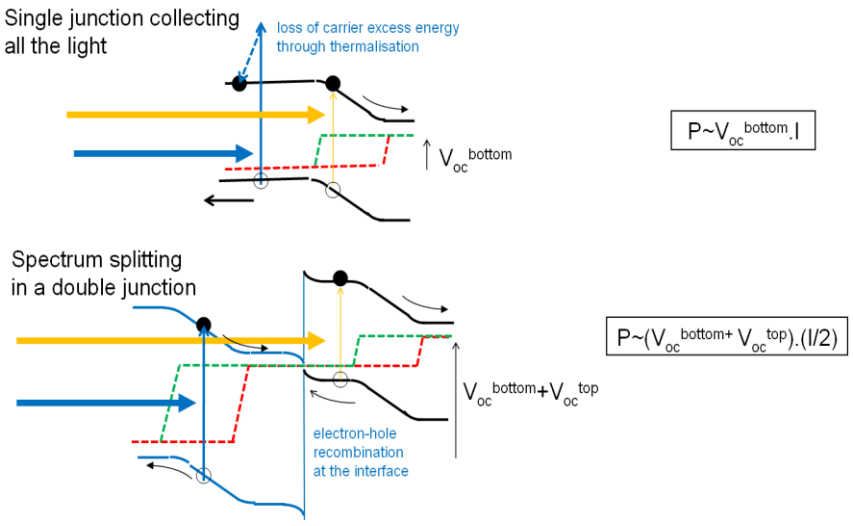

Figure 1-5: Band diagram scheme of a single (up) and a tandem (down) solar cell.

In this configuration, cells are series-connected through the tunnel junction, thus the cell displaying the lowest current will limit the electric current through the overall MJSC. Therefore, to improve the efficiency, the bandgap of each cell has to be adjusted carefully to obtain a current matching between all the subcells. Figure 1-6 shows the maximum efficiency for a tandem solar cell under the AM1.5G spectrum as a function of its subcells bandgaps. In practice, such structure is realized by monolithical epitaxial growth of the different layers constituting the MJSC stack, using either metal-organic

vapor phase epitaxy (MOVPE) or molecular beam epitaxy (MBE), or/and using non-epitaxial methods such as wafer bonding, or epitaxial lift-off (ELO).[23,24]

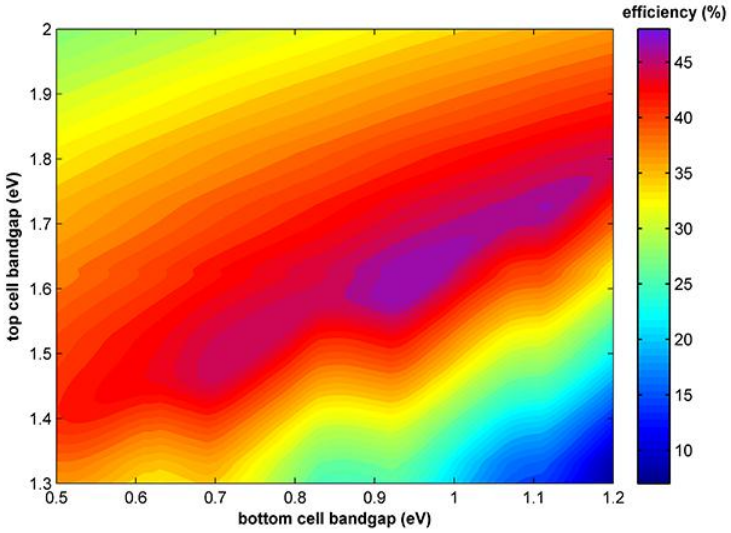

Figure 1-6: Evolution of the overall efficiency of a tandem solar cell, as a function of top and bottom subcell bandgaps. The maximum efficiency for a tandem solar cell under the AM1.5G spectrum without concentration is 47 %. Using a 1.1 eV Si bottom cell, the maximum efficiency is obtained for a top cell with a 1.7 eV bandgap.[13]

Most of the research progresses on MJSC have been realized on III-V material systems lattice matched with Ge, GaAs and InP substrates. This is due to their well-known excellent optical and electrical properties and their strong absorption due to their direct bandgap.[25,26,27] Figure 1-7 displays the energy bandgap versus the lattice constant of the III-V and especially of dilute nitride compounds.[13] The availability of ternary compounds such as GaInP lattice-matched to GaAs and quasi-lattice-matched with Ge, with adapted direct bandgap (see Figure 1-7), explains why this material system have been firstly studied for PV applications. The interest of lattice matched structure is to limit, or avoid, the misfit dislocations formation in epitaxial layer, that can reduce the solar cells performance. Different approaches such as wafer bonding, metamorphic and the use of dilute nitride materials, have managed to lower the overall cost by optimizing the bandgap combination and thus increase the efficiency through a better current matching. However, maintaining the GaAs, or Ge substrates to build the high efficiency III-V MJSC, undoubtedly incurs a substantial cost associated with such substrates.[20] Nevertheless, a III-V/Si tandem solar cell on Si substrate promises high efficiency at

relatively low cost: a 1.7 eV junction on a 1.1 eV Si junction has the theoretical potential to achieve nearly the optimal efficiency for a tandem solar cell on silicon (cf Figure 1-6). Therefore a great research effort is now put on the integration of III-V PV on Si.

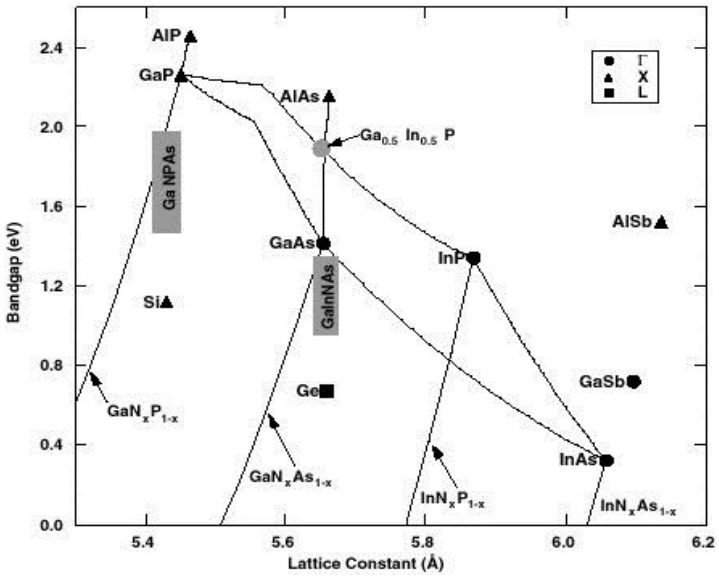

Figure 1-7: Energy bandgap as a function of the lattice constant of some of the group IV and group III-V semiconductors. [28]

However, the use of Si substrates for high efficiency III-V MJSC has been impeded due to the large mismatch of both the lattice constants and the thermal expansion coefficients, between the substrate and the conventional cell alloys. These mismatches result in high densities of dislocations, leading to both low efficiencies and limited lifetime. The approach followed during my PhD work is based on the progresses made on the growth of GaP/Si and diluted nitride materials. Those progresses have given the hope of growing optically-active lattice-matched III-V materials on silicon using a GaPN based material.[28,29,30] Indeed, by adding a small amount of arsenic and nitrogen in the GaP compound, a 1.7 eV pseudo-direct bandgap GaAsPN alloy, lattice-matched to Si can be grown. Considering the 1.12 eV energy bandgap of Si, this could open the route for a high efficiency lattice-matched solar cell on silicon. To understand the challenges and the interest of growing a lattice matched III-N-V/ Si tandem solar cell compared to the other approaches, a state of the art of the III-V MJSC for CPV is reported in the following.

1.3 Very high efficiency MJSC for terrestrial CPV and space applications

1.3.1 Lattice matched approach development

(a) History and first breakthrough

In the early eighties, numerous teams have focused their research effort on designing tandem cells devices with direct bandgap III-V compounds. To gain advantage of the low-cost Si substrate, most of those cells were first based on mechanical stacks of a high-bandgap top cell on a Si bottom cell or monolithic combinations of AlGaAs, GaAs, GaInAs or GaAsP on Si, without success, though those structures could theoretically reach efficiencies around 36–40%.[5] In particular, in GaAs on GaInAs or GaAsP-based monolithic structures on Si, the interface defects due to the lattice mismatch between the III-V compounds with Si substrates were detrimental for the PV performances. Moreover, in the lattice-matched AlGaAs/GaAs system which could display a 36% theoretical efficiency, the strong effect of oxygen on AlGaAs even at low levels hampered its development at a commercial scale.[31]

In 1984, researchers at the National Renewable Energy Laboratory (NREL) proposed to work on the GaInP/GaAs system lattice-matched with a GaAs substrate, which has become the first commercially viable MJSC.[32] It was made of a $Ga_xIn_{1-x}P$ top cell (compound with a bandgap typically ranging from 1.8 to 1.9 eV) monolithically grown on a lattice-matched interconnecting tunnel junction and a 1.44 eV GaAs bottom cell. The Al-free and lattice-matched GaInP/GaAs approach proposed by NREL solves the issues previously encountered for a theoretical efficiency of 34%. Since 1990, efficiencies higher than 27% under AM1.5G have been obtained by modifying the top cell thickness to achieve current matching, for terrestrial application (under AM1.5G solar spectrum) as well as for space application (under AM0 solar spectrum and taking into account the particles irradiation).[33,34,35,36,37,38] Then, the aerospace sector was rapidly attracted by these properties. Production of GaInP/GaAs solar cells (on Ge substrates) started in 1996, and the first GaInP/GaAs-powered satellite was launched in 1997. The record in efficiency, for terrestrial applications, is equal to 34.1% (under concentration of 467 suns, NREL).[39]

(b) III-V triple-junction solar cells development

Following the development of the mature GaInP/GaAs tandem cell, in 1997, researchers have proposed to add a third junction. Germanium was chosen as it was the perfect candidate due to its 0.67 eV narrow band gap and quasi-lattice-matching with GaAs. Introducing these third junction as the bottom one, the lattice matched (LM) GaInP/Ga(In)As/Ge stack displays [1.86eV/1.39eV/0.67eV] bandgaps combination, while highly current-mismatched due to an excess of photon absorption in the Ge bottom cell, this MJSC can theoretically reach a 38.6% efficiency without concentration.[40] The small In amount (around 3%) in the GaAs was set for better lattice- and current-matching. However, even though Ga(In)As is closely lattice-matched with the Ge substrate, a high quality Ga(In)As/Ge heterointerface has been historically difficult to obtain, due to the mismatches in both the crystal structures and local chemistries. The polar (GaAs epilayer)/non-polar (Ge substrate) growth have first impeded the successful III-V/Ge monolithic integration, resulting in interface-related structural defects such as anti-phase domains (APD) and stacking faults (SF). While various "recipes" for the growth of GaAs on Ge(100) with good structural quality have been proposed, many present contradictory results.[41,42,43,44,45,46] The cause of those different behaviors is not fully understood. It might be a consequence of differences in reactor design or material purity. It could also be connected to the quality of the Ge substrates preparation. Other research let think that it is related to the prenucleation conditions or the structure of the (100) Ge surface prior to the GaAs nucleation step. Nevertheless a few guidelines have been given to reduce the APD formation such as the cleanliness of the Ge substrate and its orientation (6° off along the [110] direction), to obtain bi-atomic step at the Ge surface, a full Ga monolayer coverage and the use of low-temperature migration enhanced epitaxy to promote a 2D growth.

Once the control of the heterointerface structural quality was achieved, the main problem was the control of group V or group III dopant diffusion into the Ge substrate. Due to the high temperatures (500-800°C) often needed for the heteroepitaxy, diffusion of both Group III and Group V atoms into the Ge substrate cannot be suppressed. Thus the challenge is to control this diffusion process while obtaining a defect-free GaAs heteroepitaxial layer with a suitable doping type and level.[47,48] A full presentation of the best process is beyond the scope of this chapter, but here are

summarized the conclusions drawn in the literature (which we have been used in the framework of this thesis):[40-45]

(1)- Because of the thermal activation of the diffusion process, junctions are more stable at lower growth temperatures.

(2)- In the three-junction GaInP/Ga(In)As/Ge solar cells, the most important parameter of the Ge-cell is its output voltage, as the Ge cell is not the current-limiting junction. The Ge cell bias depends strongly on both the quality of the III–V/Ge interface and the Ge structural quality itself.

(3)- Due to its lower diffusion coefficient, P element is a better group V dopant for Ge than As.

Using such lattice-matched triple junction on Ge substrate, the last efficiency record using this approach was set by Spectrolab in 2010 at 41.6 % under 364 suns, close from its theoretical maximum (48% under 500 suns).[49,50] Then, an improvement has been proposed using more optimal bandgap combinations than the [1.86eV/1.39eV/0.67eV] combination of the lattice-matched and current-mismatched GaInP/Ga(In)As/Ge structure. Nowadays, Lattice-Matched (LM) GaInP/Ga(In)As/Ge multijunction solar cells are standards for both space and terrestrial concentrator applications, with a lot of companies able to grow these cells such as *Spectrolab and Azurspace*. The fabrication of these multijunctions is achieved by metal-organic chemical vapor deposition (MOCVD) or molecular beam epitaxy (MBE).[27,49,50]

1.3.2 Metamorphic and non-epitaxial approaches

(a) Lattice-mismatched approach

The route to achieve higher efficiency is to approach the [1.75eV/1.18eV/0.70 eV] optimal bandgaps combination, for which the current-matching is achieved, by lowering the bandgaps of both the top and middle cells through an increasing of their indium content. However, this is obtained by paying the price of increasing the lattice-mismatch, and thus increasing the density of defects. The obtained structures are called LMM (Lattice-MisMatched). However, an efficiency of 41.1% at 454 suns has been obtained in 2009 for a quasi-current-matched and lattice mismatched $Ga_{0.35}In_{0.65}P/Ga_{0.83}In_{0.17}As$/Ge cell with bandgaps combination of [1.67eV/1.17eV/ 0.67 eV].[51] With this bandgap combination, the top and middle cells display a 1.2% lattice

mismatch with the Ge substrate, meaning that they have been grown metamorphically. An essential part for this metamorphic solar cell structure is the use of an optimized step-graded buffer structure made from a $Ga_{1-y}In_yAs$ buffer layer between the Ge subcell and the middle subcell. The step-graded buffer consisted of seven 200 nm thick GaInAs layers with stepwise increased indium content from 1% to 17%. The misfit dislocations generated in the buffer during the relaxation of the lattice stress were then well confined at the interfaces between the layers with different In content. Moreover, the bandgaps of the different layers inside the buffer layer are large so that the overall buffer is transparent to photons that have to be absorbed by the junction below. However, considering such a defects-containing structure, an important uncertainty remains about the evolution of the dislocations location with time, under solar cell operation. The tunnel diode consist of an intrinsically C-doped p-AlGaInAs layer and a Te-doped n-GaInP layer, and avoids the generation of dislocations by good lattice-matching with the surrounding layers. With this approach, obtaining the perfect current matching, to reach the theoretical efficiency, by decreasing the top two junction band gaps has been found to be very difficult because the cell performance is very sensitive to dislocations in the top GaInP junction.

(b) **Inverted metamorphic solar cells**

Thus a new concept has been proposed by the NREL to obtain a better current matching while minimizing the propagation of strain-induced defects through the device structure by growing the junctions in increasing order of lattice mismatch to the substrate in an inverted lattice-mismatched structure (IMM).[24] The GaInP junction (1.86 eV) is grown first on a GaAs substrate, leading to a strained GaInP subcell while displaying a defect-free surface suitable for the growth of the slightly mismatched $Ga_{0.96}In_{0.04}As$ middle junction (1.34 eV). Then, a highly mismatched $Ga_{0.63}In_{0.37}As$ junction (0.93 eV) is grown on top of the structure. Thus its strain-induced defects have limited effects on the other junctions. Since the growth of the subcells have implied an inversion in the bandgap order, this structure implies to remove the substrate to allow the light enter through the highest-bandgap subcell first. Therefore, prior to the GaAs substrate removal, the structure is first bonded to a low-cost host substrate (either Si or Glass, or a flexible substrate) for mechanical support. Again, step-graded buffer layers

are used between the mismatched junctions to relieve strain and confine dislocations away from the active regions of the junctions. The success of this approach is due to the tolerance of GaInAs to threading dislocations and to advances in the understanding of the growth of mismatched structures.[52] This approach has led to a record of efficiency (April 2013) set by sharp with 44.4% efficiency under 302 suns.[53] Nevertheless the effect of lattice mismatch on the reliability of those solar cells still needs to be evaluated.

(c) Wafer bonded quadruple junction

The theoretical optimum for a four-junction solar cell under AM1.5d spectral conditions is reached for a set of declining bandgap energies with 1.9, 1.4, 1.0, and 0.5 eV. In 2010, promising results were reported for inverted metamorphic devices reaching AM0 (space solar spectrum) one-sun efficiencies up to 33.6%.[54] In this configuration, two lattice-mismatched GaInAs bottom junctions are combined with a GaInP/GaAs top tandem by using buffer layers to relax the crystal lattice. Dislocations cannot be completely avoided in this configuration, and this leads to constraints in device performance. Wafer bonding is another technology to combine lattice-mismatched materials without creating dislocations. Two crystal structures are brought closely together forming atomic bonds at the interface.[55–57] This technology requires two epitaxial structures (and thus the use of two wafers) with low surface roughness and a specific surface preparation but offers the advantage of combining the best defect-free semiconductors in a multi-junction solar cell device. Wafer bonding has been used by several authors in the past.[58–61] In 2014, for the first time, results of a four-junction device, have reach the level of the best triple-junction solar cells setting the efficiency world record with a peak efficiency of 44.7% at 297 suns concentration. This is achieved by a $Ga_{0.51}In_{0.49}P$/GaAs top tandem bonded to a $Ga_{0.16}In_{0.84}As_{0.31}P_{0.69}$/$Ga_{0.47}In_{0.53}As$ bottom tandem solar cell (Figure 1). This combination is close to the ideal bandgap combination for a four-junction device and allows one to reach excellent material quality for all junctions. Though important improvement have been made in term of wafer recycling. All bonding methods require two substrates, one for epitaxy and one for the layer transfer. This makes bonding

technics expensive, even if the LM substrate can be re-used multiple times, giving the need of a monolithical integration.

1.3.3 Dilute nitrides multi-junctions lattice-matched cells

In the case of the lattice matched $Ga_{0.49}In_{0.51}P/Ga_{0.99}In_{0.01}As/Ge$ material combination, the Ge bottom junction is known to generate a large excess current, which limits the device performance. To reach higher efficiency and maintain a lattice-matched architecture and avoid reliability issues, Solar Junction has resolved the long standing problem associated to dilute nitride III-V compounds and is now manufacturing a lattice-matched multijunction solar cell employing an 1 eV GaInNAsSb bottom subcell. This dilute nitride material system was first explored in 1994 in the active zone of laser diodes.[62,63] Researchers were interested because it was observed that adding small amounts of nitrogen in III-V material such as GaAs leads to a decrease of the lattice constant along with a large decrease of the bandgap (called "giant bandgap bowing effect").[64] This specific behavior of the III-V dilute nitrides has been successfully described using the Band AntiCrossing model (BAC) and tight binding calculations (TBC).[65,66,67,68] Electronegative N Atoms in GaAs and others III-V material tend to localize electrons with energy levels lying near the GaAs conduction band. The interaction between the N localized states and the GaAs Γ-extended states lead to the splitting of the conduction band into two subbands, thus lowering the bandgap of the material. By controlling the N and In compositions in GaAs, the GaInNAs alloy can be lattice-matched to GaAs or Ge, while having a bandgap ranging from 0.8 eV to 1.4 eV.[69]

Huge effort was made by many groups to grow GaInNAs single and multijunction solar cells. First, despite all these efforts, intrinsic defects or defects associated with N-induced localizes energy states, or H or C impurity species resulted in short minority carrier diffusion lengths, and therefore low quantum efficiency which resulted in low photocurrents and made it unsuitable as a third junction under the GaAs/InGaP subcells.[70,71] Its development has been slowed by problems related to the MOCVD growth which is the standard technique used in industry to fabricate III-V solar cells. Nevertheless, dilute nitrides have been intensively studied using MBE,

which is the technology usually adopted for research of novel materials. Indeed, MBE has clear advantages over MOCVD for the dilute nitrides growth, as it reduces C-doping and hydrogen related complexes.[69,72,73] Moreover, MBE allows a higher level of control of growth conditions as it enables relatively low growth temperatures which avoid phase separation and clustering effects, while the V/III ratio and the N amount available for nucleation can be controlled more precisely.

Nevertheless the growth window is narrow due to the large difference (more than 20%) between GaAs and GaN lattice constants and due to the huge difference between As and N atomic orbital energies, thus the growth of high structural quality GaNAs (and other dilute nitrides) is much more difficult than all classical III–V alloys [74–76,77,78] Moreover, it has been shown that dilute nitride materials are metastable; they have a propensity for separating rather than forming a homogeneous alloy. To incorporate enough nitrogen into the material, the growth has to be done at much lower temperature (in far-from-equilibrium conditions) than the growth of N-free alloys. This reduces the growth window for dilute nitrides with sufficient N concentration. This window becomes even narrower with increased indium content, due to a tendency to three dimensional (3D) growth with higher indium content. More recently, it was shown that the introduction of Sb into GaInNAs, expands the growth window towards two dimensional (2D) epitaxy while enabling the incorporation of higher In and N compositions. Under the optimum growth conditions, antimony is incorporated into the alloy at levels of 5–8%, well above the incorporation level of nitrogen, which is characteristic of reactive surfactants.[79] One more central discovery was that the atomic N incorporation coefficient is constant. It means that the growth rate controls the N concentration when other growth parameters are constant.[80,81] This gives to dilute nitride alloys major advantage in terms of yield and reproducibility as compared to any equivalent mixed column V, III–V alloy semiconductor system.[82] Note that influence of other growth parameters on the N incorporation was also observed but the control of N concentration, and therefore the energy gap of GaInNAsSb, via group III rate seems to be the most reasonable from the practical/technological point of view.[80,83,84]

Non-radiative recombinations originating from point defects are known to be one of the biggest challenge for the dilute nitrides. They are mainly due to the low MBE growth temperature and the use of plasma source to produce reactive atomic nitrogen. In

general, the nature of N-related defects is not well understood.[71,73,85–90] A portion of these defects can usually be removed by post growth annealing.[91–96] Though, to realize high quality dilute nitrides the number of N-related defects in as-grown materials should be reduced, which can be done through a purposely designed N plasma source and optimal operation.[97–101] For instance, low radiofrequency (RF) power and high flow produce the fewest ions impinging the surface, which minimize the point-defects generation, but also the N incorporation. Also it has been shown that using smaller, fewer holes in the aperture at the end of the plasma source decreased plasma damage and improved the stability of the plasma. [102] To eliminate the ions from the molecular beam, electrically biased metal plates can be mounted at the exit aperture of the nitrogen cell,[77] which significantly improves the optical quality of GaInNAsSb. This finding has been one of the keys to the successful realization of high quality GaInNAsSb based solar cells. Indeed, this approach has led to an important record of efficiency in 2012, by Solar Junction, with 44 % efficiency under 967 suns using a GaInP/GaAs/GaInAsN(Sb) triple junction with the following bandgap combination: 1.89 / 1.41 / 1 eV.[103] Another method has been developed to minimize the ion impact on the growth of dilute nitride materials such as the use of an ADDON valved rf plasma source that will be described more in details in the following chapter.

All these approaches to build high efficiency III-V MJSC are performed on expensive GaAs, or Ge, substrates. However, a III-V/Si tandem solar cell on Si substrate promises high efficiency at relatively low cost. Indeed, the PV market is still strongly dominated by Si single junction solar cells due to their lower production cost and the maturity of the Si industry. Thus in order to increase the market throughput of III-V MJSC researchers have proposed to use Si substrate instead of the III-V or Ge substrate which would allow a drastic cost reduction.

1.4 III-V Tandem solar cells on Si substrate

1.4.1 Motivation for the integration on Si

The use of Si as an alternative substrate material for III–V epitaxial solar cells in place of the common MJSC substrate materials (GaAs and Ge) would significantly reduce the cost of the PV energy. Indeed Si is at least 10 times cheaper than the

conventional MJSC substrate materials (1-3$ per square inch for Si wafers). Moreover, Si is also available in larger wafer sizes (300mm diameter in 2009 and 450 mm today) than typical 100–150 mm diameter of Ge or GaAs wafers. Since epitaxy and wafer-processing costs do not significantly change with wafer size, moving to a large area substrate (Si) would also decrease the solar cell fabrication cost. Another significant advantage of Si is that by shifting the III–V solar cell technology toward a Si platform, the mature Si technology can be accessed, enabling fast production ramp-up, high volume, and high market throughput. With expected solar conversion efficiencies of 30-40%, III-V MJSC on Si hold great promise to enable a large PV energy production, with significantly faster ramp-up and reduced capital investment than what could be expected for a technology requiring niche manufacturing, helping for a rapid and cheap energetic transition. Given the potential for cost reduction through both materials and manufacturing and the promise of III–V solar cell efficiencies nearing 40%, the case of III–V/Si is quite different from every other PV technology, already mature or being developed. Indeed, even for low-cost, lower-efficiency thin films technologies, or for Si and III–V cells produced in a niche environment, such rapid scaling is very difficult as significant market penetration requires both high efficiency and high throughput. Some silicon physical properties also present distinctive advantages over the conventional GaAs or Ge substrates for terrestrial CPV, space-based and photo-electro-catalysis PV systems. For water splitting system tandem structures might provide both adequate potential and efficient utilization of the solar spectrum. Compared to the more classical InP based system which needs bias to work, tandem structure could operate without any power input apart from the sun. Moreover due to the strong resistance of GaP to corrosion the Si/GaPN tandem structure could fulfill the requirement in term of stability needed for such application.[104,105] For space-based PV systems, cell weight is a very important parameter due to launch payload weight and stowage limitations. Silicon has a mass density less than half that of the GaAs and Ge, meaning comparably sized solar cells on Si would weigh less than half of those based on the more conventional substrate materials. Furthermore, Si is also mechanically stronger, with fracture toughness twice that of GaAs and 50% greater than Ge, allowing for the use of thinner Si substrates and thus even greater reduction in system mass. Therefore, high-performance III–V/Si solar cells with conversion efficiencies equal to or greater than that achievable by state-of-

the-art III–V/Ge cells would yield an increase in specific power (W/kg) of at least 2×, but potentially upward of 4× (roughly 300 W/kg for GaInP / GaAs /Ge triple junction).[106]

For terrestrial applications, these particular properties are not very important, although reduced cell mass and increased mechanical strength are certainly beneficial, especially for use in such applications as large-area roof-top systems. However Si substrates possess a thermal conductivity approximately 2× higher than GaAs and Ge, in the case of terrestrial concentrator systems, where the mitigation of excess heat is paramount to high-performance operation, providing a more efficient transfer of heat out of the PV cell is another advantage.

As might be expected, given the numerous substantial advantages of III–V/Si hetero-integration for solar cells, several researches have been undertaken in pursuit of this goal. In the next sections we will discuss of the challenges and the results on III-V tandem solar cells grown Si.

1.4.2 **Non-Epitaxial methods**

The first methods for integration use non-epitaxial steps to transfer III–V materials to Si substrates such as wafer bonding.[107,108,109] However for solar cells, where relatively large area is required, wafer bonding approaches suffer from mismatch issues due to difference in the coefficient of thermal expansion (CTE) between III–V compounds and Si, giving rise to cracking. Recently, III-V/Si integration has been achieved using the Smart Cut™ technology. In this technology, layers are removed from their epitaxial host substrate via a hydrogen ion implantation process that physically weakens a thin region of material beneath the epitaxial layer to accomplish layer separation by exfoliation. This technique yielded to crack-free GaInP/GaAs dual-junction solar cell structures bonded to Si, with promising preliminary results.[110] Even if bonding processes are attractive for a variety of reasons, they generate a different set of potential limitations as compared with the monolithical heteroepitaxial integration. As for the case of the wafer bonded quadruple junction, bonding technics are expensive due to the use of two substrates.

1.4.3 **Metamorphic approaches**

(a) Si/SiGe virtual substrate

Knowing the numerous difficulties (i e materials mismatches) involved with III–V PV materials grown directly on Si substrates introduced earlier and explained in detail in the following section, a considerable amount of research has concentrated on splitting the problem into less complicated ones. This explains why another group-IV material, Ge, has received much attention. Indeed while the issues of the heterovalent interface still exist for GaAs grown on Ge (discussed in the next section), the problematic lattice constant mismatch and thermal expansion mismatch are almost suppressed. This makes the III–V/IV growth easier. Also, much attention has been paid on the Ge/Si system, where problems linked to the heterovalent interface are totally removed. In this system, only lattice constant and thermal expansion mismatches remain.[111,112] In fact, Ge/Si (and the SiGe alloys) is the classical system in which much of the basic science regarding lattice mismatched heteroepitaxy of Face-Centered Cubic (FCC) materials has been studied.[47] Two main methods for the Ge/Si integration exist: direct Ge growth on Si substrates, with adapted strategies for dislocation density reduction, and compositionally graded SiGe buffers.

To our knowledge, the only approach with PV commercial outlet uses compositionally graded SiGe alloy buffers. As discussed previously for the case of III–V metamorphic cells, the objective of these methods is to relief the misfit in a controlled and efficient way. Until now, step grades have found more success. After the important work of the early 1990s on the realization of relaxed $Si_{1-x}Ge_x$ layers on Si substrates rapid progress were made in the development of a step-graded SiGe buffer technology to yield low defect density Ge virtual substrates.[47,113] This original buffer design spreads the lattice mismatch strain over a thickness of about 10 μm and uses a midgrowth ($Si_{0.5}Ge_{0.5}$) chemical–mechanical polishing to reduce the deep crosshatch-induced surface roughness (a result of dislocation glide at misfit interfaces). Moreover it takes into account the difference in thermal expansion between the various alloy compositions and final Ge layer, and yields to a final Threading Dislocation Density (TDD) of 1×10^6 cm^{-2}, a value allowing the realization of efficient solar cells. Numerous researchers have since further refined the SiGe buffer process, reporting final Ge layer TDDs in the

10^5 cm^{-2} range reinforcing SiGe as the current state-of-the-art path for highly mismatched III–V compound integration on Si substrates.[114]

(b) GaInP/GaAs dual junction on Si substrate

With all the improvement recently made in the growth of SiGe/Si virtual substrate, efforts for growing a GaInP/ GaAs dual junction are increasing but are currently at an early stage. Nevertheless already interesting performances have been reported. It was demonstrated that p/n GaAs solar cells integrated on Si can reach very similar performances to homoepitaxial p/n GaAs solar cells.[115] The main effect of the low concentration of residual dislocations on minority carrier transport in GaAs/Si solar cells is the large disparity of electrons and holes mobility which affects the choice of the device polarity. As in the case of the single-junction cells, the transmission electron microscopy (TEM) reveals very high-quality material through the whole structure, and includes not only GaAs and GaInP cells, but a thin GaAs p+/n+ tunnel junction that provides a low-resistance connection between the series-connected sub-cells.[116] With this architecture, a V_{oc} value of 2.21 V under AM0 illumination is reported. Assuming that the GaAs sub-cell provides V_{oc}~0.98 V from the single-junction experiments, the GaInP is providing V_{oc} ~1.23 V. Note that this is an underestimated value of V_{oc} for the GaInP cell since the spectrum incident on GaAs is now at a much lower incident flux due to the presence of the GaInP top cell, which in reality will slightly reduce the GaAs V_{oc} value. The overall high value for the V_{oc} of the dual-junction cell indicates that very good material quality has been maintained throughout the dual-junction structure. This was confirmed by the reasonable match with the V_{oc} value obtained for identical dual junctions grown on GaAs and processed side-by-side, which produced 2.34 V under AM0 conditions. The overall efficiency of the dual-junction cell on Si was 16.8% under AM1.5G illumination. The performance is limited by several external factors that reduce the current output by several $mA.cm^{-2}$, including a large 10% grid shading, the use of a GaAs tunnel junction as opposed to a wider bandgap tunnel junction, and a relatively poor antireflection coating. Correcting such issues, this very promising technology should realize 1-sun efficiencies well in excess of 20% on Si for only two active junctions. Future works can lead to the addition of a third Ge sub-cell using the

top layer of the SiGe graded buffer, following the example of GaInP/GaAs/Ge triple junctions that are state-of-the-art but are grown on high-cost Ge substrates.

(c) GaAsP/SiGe tandem solar cells on Si substrate

Another very interesting approach has been proposed by 4Power.[117,118] They have demonstrated a monolithically integrated solar panel on Si that allows scaling of cell output voltage on the wafer level, with a GaAsP/SiGe dual junction solar cell on Si. This provides ideal bandgaps to reach the highest efficiency for solar spectra between AM0 and AM1.5. Combined with CMOS-based active power management the solar panel on wafer (SPOW) design enables maximum output power and ideally managed power profiles under non-ideal, and time-varying illumination conditions. This results in improved reliability, lower system cost, and higher specific power over conventional III-V PV array technology. The structure is grown in a IV/III-V MOCVD growth cluster. The threading dislocation density of the SiGe buffer layer is very low (in the range of 8.10^5 cm^{-2}). The III-V layer is free from APD. The Ge diffusion in the III-V layer is low in the range of 10^{16} cm^{-3}. The structure is grown at high growth rate enabling the solar cell production in less than an hour. The last reported efficiency of these cells was around 20% but large improvements are expected as the tunnel junction was not optimized. From 4Power point of view, reaching a 30% efficiency is a realistic objective for this cell configuration. Tough those performances would be fantastic and would totally change the energy market, due to the lack of experience on the reliability of metamorphic solar cells, industrials are still afraid of investing in this solution which gives room for research on a lattice matched approach that would combine: high efficiency, low cost and high reliability.

1.4.4 The Pseudomorphic approach and its challenges

The lattice matched approach using dilute nitride material, which is the main research topic of this thesis, may offer several advantages. Though a number of material issues, explained in detail below remain to be solved, this architecture would combine: high efficiency, low cost and high reliability, making it potentially very interesting for a large scale development of the PV energy. In pursuit of this goal, researchers at NREL have proposed in 2002 to work on the GaPN dilute nitride material system, as this

material can be lattice matched with Si and have a strong absorption around 1.9 - 2 eV making it suitable as the top junction absorber.[28] Moreover by adding Al, As, In or Sb, and controlling the N content in the layer one can theoretically form lattice-matched alloys having bandgap around 1.7 eV which could allow a better current matching with the Si cell. Using this approach they have demonstrated a tandem solar cell with a 5.2 % efficiency, using a MOCVD-grown 1.7 - 1.8 eV direct bandgap GaAsPN dilute-nitride (p-i-n top junction lattice-matched with the Si), deposited on a 1.1 eV diffused Si bottom cell.[119] However, though the dilute III-V nitride addresses the lattice mismatch issue, the efficiency achieved was low due to the low-structural-quality of the III-V/Si interface, GaAsPN top junction and the poor quality of the tunnel junction and contacts.[119] In the following I present in detail the main challenges related to the pseudomorphic approach to understand the interest of this thesis work.

(a) GaP/Si virtual substrate

As was discussed previously, there are a number of important materials incompatibilities between group-III–V and group-IV semiconductors. Strategies necessary for the successful integration of GaP materials on Si substrate were pull out from the research done on GaAs/Ge, including necessary substrate orientation and preparation, and the proper control of GaP nucleation on the Si surface.[45,120–125] Unfortunately due to the strength of the Si-N bonds and amorphization of the III-V/Si interface, GaPN can't be grown directly on Si and a thin GaP layer has to be grown.[119] In the following I present in detail the main challenges related to the growth of III-V compound on Si substrate, and the analogies and differences between GaAs/Ge and GaP/Si integration to understand the strategies that have paved the way for the successful integration of III-V semiconductors on group-IV substrate.

i. Materials challenges for III-V/Si monolithic integration

The unifying goal of all monolithic approaches is the control of defects related to the multiple materials properties incompatibilities, which can be detrimental to solar cell performance. In the following section we will discuss about the material incompatibilities and the challenge of the metamorphic and the pseudomorphic approaches

Most of the problems were materials-related issues of the III–V/Si heteroepitaxial interface, due to several materials properties differences such as: lattice constant, thermal expansion and heterovalent interface. Indeed GaP is polar material with a zinc blend crystalline structure having a 5.450 Å lattice constant while Si is non-polar with a diamond-like crystalline structure having a 5.431 Å. A number of crystalline defects may result, due to the mismatch of crystal symmetries between the two types of materials. [118,119,120,124,125–128,129,130,131,134,135] These defects can be divided into two classes. On one hand, extended planar defects such as: stacking faults and microtwins (MTs) are due to nonoptimal III–V nucleation morphology and growth of polar material on non-polar one.

On the other hand anti-phase domains (APDs) and anti-phase boundaries (APBs) are due to the heterovalent interface, (growth of polar III-V materials on nonpolar Si substrates). Both types of interface defects are electrically active, potentially detrimental to any integrated devices. They are especially problematic for minority carrier devices, such as solar cells, as they can serve as highly efficient recombination centers, as well as current shunt paths.[136,137]

Given the many difficulties and potential sources of detrimental defects in the monolithic integration of high-performance III–V materials on Si substrates, it is not surprising that it is still a highly active area of research, even after over 30 years of constant attention, but not yet a mainstream technology. However, much progresses have been made over the years, bringing the goal ever closer to the full realization of optoelectronic device on Si. In the last decade, the development of a methodology for epitaxial integration of GaAs on Ge(100) substrates has paved the way for a III–V on Si technology through the use of SiGe graded buffers. And recent works have even helped break through the barriers that had been preventing a realization of direct III–V/Si integration, demonstrating high-quality devices, and defect-mitigated epitaxy of GaP on Si(100).[138,139,140]

We discuss in the next sections of this chapter some of the approaches undertaken to monolithically integrate III–V semiconductors on Si substrate to produce high-performance PV materials.

ii. Analogies between GaP/Si and GaAs/Ge system

A key issue to the GaP/Si(100) growth is the presence on Si substrate of mono-atomic surface steps together with an incomplete monolayer coverage of the silicon surface by group III-V atoms, which lead to the formation of APDs by shifting the crystal structure by one-half unit cell, i.e the atoms are configured in the opposite order to those in the perfect lattice system. The boundary, composed of Ga-Ga or P-P bonds is therefore a crystallographic defect. This can be avoided when having biatomic steps at the silicon surface and a full monolayer coverage at the beginning of the growth. Thus using a bi-stepped approach on vicinal silicon substrates, GaP/Si heteroepitaxial films almost free of large-scale APD can be grown in some specific conditions, demonstrating the importance of proper substrate orientation and bi-stepped surface. [125,134]

It has also been shown that the cleanliness of the group-IV substrate is very important to achieve high-quality III–V/IV heteroepitaxy. Many results have underlined the negative effect of carbon contamination and the importance of Si and Ge surface preparation for III–V/IV.[121,141–143] In order to avoid the problems caused by C impurities at the surface, homoepitaxial layers of Si or Ge can be grown before the III–V nucleation, efficiently burying surface impurities and providing a surface free of contaminant. This step is necessary to reach the highest-quality GaAs/Ge and GaP/Si heterointegration.[121,142,144]

Another important step for the GaP/Si integration is the control of the III–V nucleation morphology to promote a 2D growth avoiding the generation of planar defects (SF and MTs) commonly found in such films.[145] It has been shown that use of low-temperature migration enhanced epitaxy (MEE) strongly reduces the generation of these defects that occur during the GaP nucleation process.[146] Moreover, this step can be used to avoid the generation of APDs at the interface and limits interdiffusion across the interface due to the low temperature of this step, preventing cross-doping issues.[121,147]

iii. Differences between GaP/Si and GaAs/Ge

Even if a lot of analogies can be made between the GaP/Si and GaAs/Ge heteroepitaxial systems, they do have key differences. One of importance resides in their surface reactivity with group-V elements. Indeed phosphorous has been shown to roughen the surface through the displacement of Si atoms unlike arsenic on the Ge surface.[148] Thus for the GaP/Si growth, the exposure of the silicon surface during the

MEE III–V nucleation should be controlled with care to yield high-quality, APD-free epilayers. [121,147] One should notice that there are several apparent ambiguities in the literature on the effect of Ga, As and P pre-layers, which may result from various nucleation conditions (substrate preparation, nucleation temperature, growth method (MBE versus CVD), and group-V species (As_4 versus As_2, PH_3 versus P_2, etc).

Also, as previously mentioned, there exists a difference in coefficient of thermal expansion ratios between GaP/Si. GaP and Si differ by more than 50%, unlike Ge and GaAs, which means that the misfit strain state at the heterointerface is not constant with respect to temperature, and must be taken into account in growth designs to prevent detrimental issues regarding relaxation and epilayer cracking.

Taking account of all these methods, a GaP/Si pseudo-substrate with TDD below 10^6 cm^{-2} can be grown enabling the fabrication of a lattice matched MJSC on Si using a dilute nitride absorber.[135]

(b) The tunnel junction

As was discussed previously, the tunnel junction has a tremendous importance in the MJSC as it electrically connects the top and the bottom cell. Strategies necessary for the successful tunnel junction realization were pull out from the research done on GaInP/GaAs tandem solar cells, including necessary high doping and thin tunnel junction thickness. In the following I present an overview of TJ properties, then I discuss the main challenge involved in the realization of the TJ, finally I present the different TJ that has been considered for the pseudomorphic approach.

i. Tunnel junction overview

The role of the tunnel-junction (TJ) in a multijunction cell is to offer a low-resistance connection between the BSF of a cell and the emitter (FSF) of the lower gap cell beneath it. Without the TJ, a pn junction would be created between the BSF and the emitter with a polarity in opposition to that of the top or bottom cells and, when illuminated, would produce a photovoltage that could roughly reduce the photovoltage generated by the top cell. A tunnel junction is a p ++ / n ++ junction where p ++ and n ++ are degenerately doped materials. The space-charge region for a p ++ / n ++ junction should be very thin, typically ≈ 10 nm. For reverse bias and small forward biases, the TJ behaves like a resistor, due to tunneling through the space-charge region. In forward

bias, for current densities over a critical value called the peak tunneling current Jp, this resistor-like behavior disappears and the voltage drops across the TJ because of thermo-ionic emission, causing a decrease of the overall multijunction voltage. The peak tunneling current expression is dominated by the following term:

$$J_p \propto e^{-\frac{E_g^{3/2}}{\sqrt{N^*}}}$$

Where Eg is the bandgap and $N^* = N_A N_D/(N_A + N_D)$ is the effective doping concentration.[149] The value of Jp must be larger than the photocurrent of the tandem cell. For a concentrator tandem cell, with bandgap of 1.1 and 1.7 eV for the bottom and the top cell respectively, operating at 1000 suns, Jsc ≈ 17 A.cm^{-2}. Figure 1-8 displays a theoretical plot of the current versus voltage for a tunnel diode. It has an initial peak in its I-V characteristics where the tunneling current (J_p) can be determined, followed by a region of negative resistance, and finally a region of high conductivity.

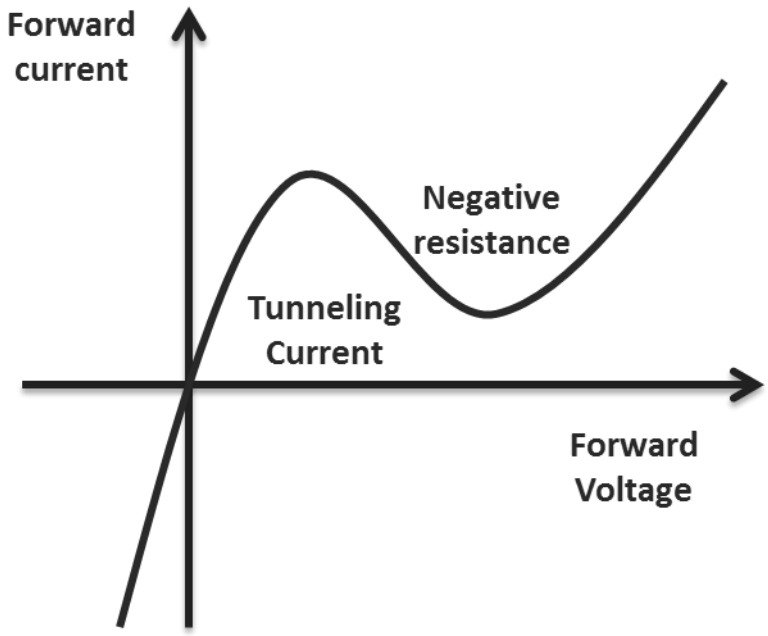

Figure 1-8: Theoretical plot of the current versus voltage for a tunnel diode.[150]

ii. Challenges related to the tunnel junction

In order to ensure an efficient carrier tunneling between the top and the bottom cell the doping concentration must be heavy. The heavy doping results in a degenerate bandgap, where conduction band electron states on the n-side are aligned with valence band hole states on the p-side. The first high-efficiency GaInP/GaAs dual-junction solar

cells were fabricated using an optically thin GaAs TJ. The best tunnel junctions were doped with C and Se. Because of the low diffusion coefficient of this dopant, the tunnel junctions were reasonably stable under the thermal conditions required to grow the top cell, and were capable of operating at more than 1000 suns, i.e. Jp >17 $A.cm^{-2}$. They were also less than 30 nm-thick and obscured less than 3% of the light destined for the lower cell. Despite of the higher bandgap and its associated drawback, the p ++-AlGaAs/n ++-GaInP hetero-TJ proposed by Jung and coworkers is the preferred TJ for one-sun operation and may be suitable for concentration.[151] It takes advantage of good incorporation of C and Se in AlGaAs and GaInP respectively. It allows high values of the effective doping concentration, which explains why peak tunneling currents as high as 80 $A.cm^{-2}$ have been reported. This TJ is also thermally stable; Jp is reduced to about 70 $A.cm^{-2}$ when annealed for 30-min at 650 ◦C and to about 30 $A.cm^{-2}$ for a 30-min annealing at 750 ◦C. Finally, this TJ is more optically transparent than a thin GaAs TJ due to its higher bandgap and yields a higher tandem cell photocurrent. In conclusion, in order to maximize the tunneling current, and minimize the voltage drop and absorption losses, the TJ should be highly doped and optically thin.

iii. Tunnel junction considered for the pseudomorphic approach

Lattice matched tunnel junctions with Si have not been studied extensively but have tremendous importance to realize a high efficiency tandem solar. In the attempt of Geisz et *al.* to make a tandem cell, they have use a III-V (GaPN (Se) / GaP(Zn)) tunnel junction.[119] This was motivated by the difficulties to have a high "p" doping in the GaPN samples but also to the significant diffusion of P atoms in Si that was creating a homojunction in the Si cell. Recently a Si tunnel homojunction has been proposed to overcome this issue. Using a rapid thermal diffusion process they have obtained peak current density over 5.6 $A.cm^{-2}$ which allows for operation under at least 250-sun illumination for Si-based double-junction solar cells (ideally with 1.68-eV bandgap for the top cell, generating a maximum short-circuit current of ~ 21 $mA.cm^{-2}$ at 1 sun AM1.5G) or 400-sun illumination for triple-junction cells (ideally with 1.45- and 1.94-eV top cells and a short-circuit current of roughly 14 mA/cm^2 at 1 sun AM1.5G. Thus using a "p" substrate, the phosphorus diffusion process could help to form the tunnel junction.

(c) GaPN based top cell

The growth of GaPN based single solar cells on GaP has not been studied by many groups unlike the GaInAsN(Sb) system on GaAs.[119,152,153] None of those groups has managed to grow GaPN alloys, with minority carrier diffusion length over 1 µm, until now. The best results using this approach have been obtained at the NREL using a p-i-n structure.[119,154] Efficiency of roughly 4% were measured, these cells exhibit a low current in the top junction which has been attributed mainly to the expected low minority carrier diffusion length in the dilute nitride absorber and problems related to the electric properties of gallium phosphide (surface recombination velocity, deep centers).[119,154–158] In the following, I present the challenge related to the growth of the dilute nitride top cell.

i. Lattice matching control

The successful implementation of the GaInP cell on the GaAs cell to make a lattice-matched tandem solar cell explains why one of the goal of this thesis is to grow lattice matched dilute nitride compounds on Si. As shown in Figure 1-7, for $x \approx 0.5$, $Ga_xIn_{1-x}P$ has the same lattice constant than GaAs with a bandgap energy between 1.8 and 1.9 eV just like lattice matched $GaPN_{0.02}$ on Si. Lattice matching is the ideal situation to reach the perfect defect-free heteroepitaxy, as it avoids dislocations formations, which are known to be centers for non-radiative recombination in III-V semiconductors. It also reduces the overall lifetime and efficiency of solar cells. A strong relation exists between the lattice mismatch, the critical thickness of a layer and the current that can be delivered by the cell, as it has been demonstrated with GaInP/GaAs tandem solar cells.[159] The lattice mismatch is the difference between the lattice constant of an epi-layer and its substrate divided by the substrate lattice parameter. The critical thickness is the thickness from which the epi-layer begins to release its elastic energy (caused by the lattice mismatch) by creating dislocations that reduce the current. Figure 1-9 displays a simplified cross-sectional scheme showing the elastic and plastic stages of misfit strain accommodation for a compressive semiconductor film on a thick substrate.

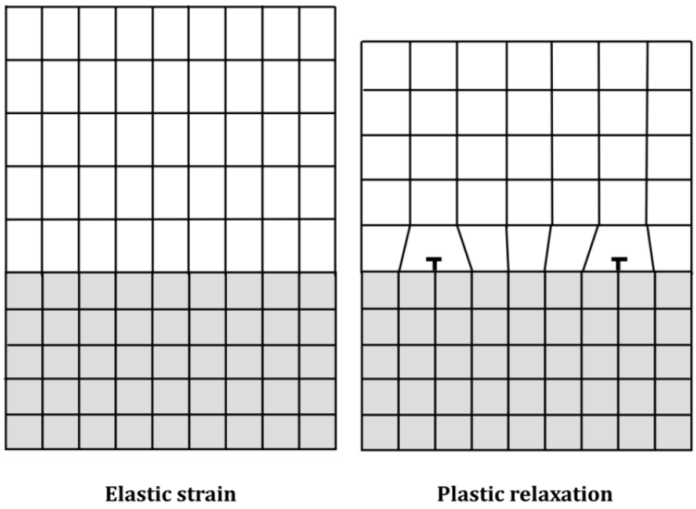

Figure 1-9: Simplified cross-section showing the elastic and plastic stages of misfit strain accommodation for a compressive semiconductor film on a thick substrate.

The mostly used approach to calculate the critical thickness was proposed by Matthews and Blakeslee (M&B) using the following equation.

$$h_c \cong \left(\frac{b}{f}\right)\left(\frac{1}{8\pi(1+\nu)}\right)\left(\ln\left(\frac{h_c}{b}\right)+1\right)$$

Where f is the lattice mismatch, b the intensity of the burgers vector, ν is the Poisson ratio of the thin layer and h_c is the Critical Thickness (CT). Figure 1-10 displays the critical thickness as a function of the lattice mismatch for the GaPN alloy according to M&B, Fisher and People and Bean models, the triangles are experimental value.[160–165] As one can see in Figure 1-10 the value calculated using the M&B approach underestimate the experimental CT value. This can be explained by the fact that this model considers the formation of dislocation at the thermodynamic equilibrium, while the dislocation formation is also driven by kinetic phenomenon as shown by Dodson *et al.*[166]

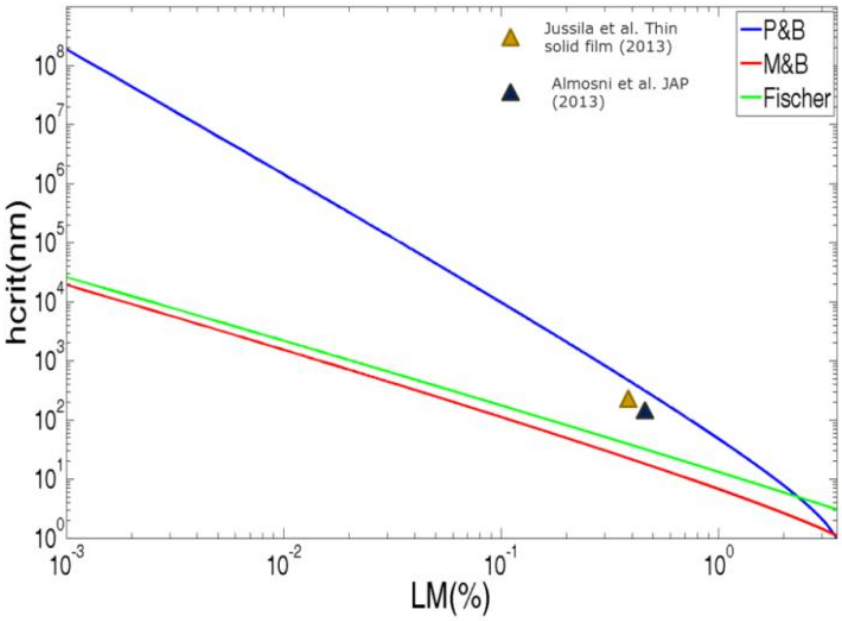

Figure 1-10 : Critical thickness as a function of the lattice mismatch according the M&B, Fisher and People and Bean model, and experimental values for GaPN alloys grown on GaP

Considering the absorption coefficient of III-V and dilute nitride material having direct bandgap such as GaInP or GaPN based material, to match the current of the other cells in the stack, the absorber region of the top cell should be about 1 µm thick. Using the Matthews and Blakeslee approach this would mean that the lattice mismatch should be less than 2.10^{-2} %. One should notice that due to different thermal expansion coefficient, two different materials cannot be lattice matched at room and at the growth temperature. To minimize dislocations formation and thus maximize the cell's current, the layers should be lattice matched with the substrate at the growth temperature due to kinetic reasons.[166,167] Indeed, the creation of dislocation is easier at higher temperature. Also, it usually requires a higher energy to generate dislocations in a compressively strained material as compared with a material under tension. Therefore the epi-layer should be grown slightly compressively strained on the substrate in order to minimize the dislocation formation and maximize the current deliver by the cell. Using AlGaInP as BSF and FSF layers in the cell structure and by controlling carefully the GaInP growth condition, efficiencies over 16% have been reached on GaInP single junction firstly by MOCVD and more recently by MBE.[168,169]

ii. Dilute nitride growth optimization

As for GaInAsN(Sb) the metastability of the GaPN alloy, makes difficult the growth of GaPN alloy with high minority carrier diffusion length, especially when using MOCVD growth technique.[170] Indeed the MOCVD growth technique is known to lead to layer with higher C, H and O impurities densities (than MBE), which are known to decrease the minority carrier diffusion length in dilute nitride materials. The study of the electric properties of GaPN-based alloys is thus of primary importance but very few paper have been published on this subject.[171–173-174] This can be attributed to the difficulty of electrical measurements on high bandgap material with low conductivity. It can also be explained by the difficulty to dope dilute nitride materials.[175,176] Therefore, developing GaPN-based alloys for PV applications requires a careful study of its structural defect, in order to optimize the growth parameters.

Several structural defects exist in dilute nitride materials such as point defects, alloys fluctuations and phase separation.[177–181] Those defects are believed to be the cause of the poor electrical properties of GaPN-based alloys. The origins of these defects are still not completely understood but are usually attributed to N composition, N clusters, P_{Ga} antisite, Ga_i interstitial, Ga_v lacuna and to C and O impurities.[67,70,154] The generation of these defects is strongly dependent of the growth parameters such as growth temperature, V/III ratio, but also to the N content, plasma operation, layer thickness and post growth annealing process.[69] For instance, on one hand the generation of point defect has been reported to be lowered at high growth temperature (580°C), while phase separation has been shown to appear for thick layers grown at high temperature. On the other hand, the phase separation can be suppressed at lower growth temperature (450°C).[177] Thus a compromise on the growth temperature has to be found to minimize the generation of point defects while suppressing the phase separation, knowing that an annealing step can help to heal defects until a certain point.[69,179,181–183] Another interesting structural property of GaPN is its higher resistance to dislocation formation due to the hardening effect of N, as compared to the GaP, which increases its critical thickness.[164] Experimentally, while phase separation or dislocation can be easily observed using classical structural characterizations such as X-Ray Diffraction (XRD) looking at the layer pic splitting or its integral breath increase, point defects and alloy fluctuations are very difficult to analyze using structural characterization methods.

Hopefully the addition of nitrogen in a dilute regime has huge effects on electronic and optical properties of the GaPN alloy. One of the major effect is the giant bandgap bowing effect of nitrogen in dilute regime, which is due to the interaction of N states with the GaP matrix.[29,30,68] This phenomenon has already been described using the band anti crossing (BAC) model and tight binding calculation (TBC), and can be observed by the red-shift of the photoluminescence (PL) peak of GaPN samples when increasing the N content. Another important effect of N is the change in the nature of the energy bandgap transition going from an indirect transition to a pseudo-direct one.[184,185–187,188,189] All these effect are related to the incorporation of nitrogen in group V lattice site. But the N content and point defects have also a strong influence on the time-resolved PL spectra. Therefore due to its strong relation with the structural properties and thus the electrical properties, the study of the optical properties has been used in this thesis to optimize the physical properties of GaPN-based alloys.

iii. Defects and ohmic contact on gallium phosphide

In order to study the growth of GaPN-based alloys, it can be interesting to work on GaP substrates to separate issues coming from the III-V/Si interface to those related to the dilute nitride absorber.[154] Nevertheless it can bring other issues linked to the GaP substrate. It has been shown that GaP substrates contain very detrimental impurities, for the PV properties (especially for the current deliver by the cell), such as isoelectronic nearest-neighbor Zn-O pair, which act as recombination centers limiting the GaP solar cells efficiency below 4%.[158,190,191,192–194] Also it has been shown that even epitaxial layers grown in a solid source MBE chamber can contains O impurities if the temperature of the phosphorus cracker is higher than 800°C.[195] Moreover due to its high surface recombination velocity it cannot be used as a window layer or it needs to be passivated.[190,196]

Another issue with the use of a GaP substrate was to developed ohmic contact on GaP. Indeed a solar cell should be connected to a device or a grid with no adverse change to its current-voltage characteristics and no additional voltage drop. It can only be done through low-resistance ohmic contact on the semiconductor. An ideal ohmic contact, when combined with the semiconductor, displays no barriers to the carrier flow whatever the sign of the bias. Ideally, this occurs when the work functions of the

semiconductor and the metal are about the same, and there are no appreciable interface states which tend to pin the Fermi Level. In order to provide some understanding on ohmic contacts, basic physics of metal-semiconductor contact is briefly discussed in this section. When a metal and a semiconductor with different workfunctions are brought into contact at thermal equilibrium, their Fermi levels align.[149] Thus the electrical characteristic of the contact can be ohmic or Schottky depending on the work function of the metal (ϕ_m) and the work function of the semiconductor (ϕ_s). Figure 1-11 displays the n-SC/metal band diagram before (a) and after (b) being put in contact for both cases rectifying (top) and ohmic contact. (bottom)

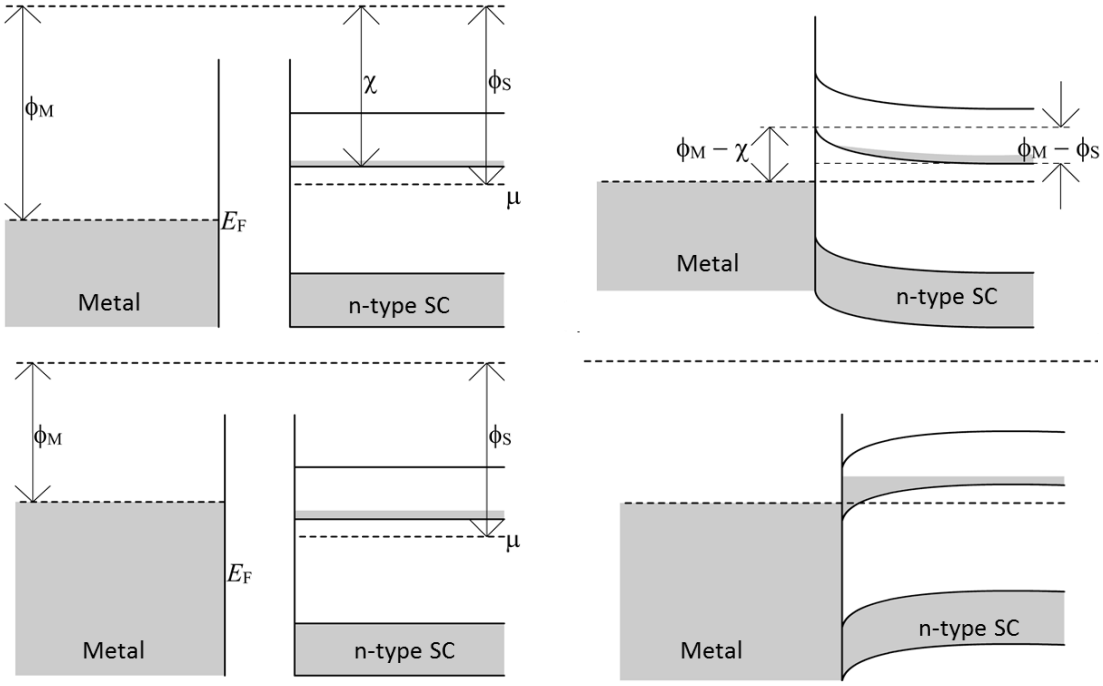

Figure 1-11: band diagram at a n-SC/metal interface before (left) and after (right) being put in contact for both case rectifying (top) and ohmic contact (bottom).[197]

Considering the energy band diagram for n-type semiconductors, the contact is ohmic if $\phi_m < \phi_s$ and Schottky if $\phi_m > \phi_s$. However several other interfacial phenomena also affect the contact resistance including semiconductor surface states, causing the barrier height to be less sensitive to the metal work function (ϕ_m).[149]

In the case of wide bandgap semiconductors such as p-GaP, there is an additional difficulty since no metal presents a large enough workfunction. Hence, it is not an easy task to achieve a good ohmic contact between p-GaP and metal. Figure 1-12 presents typical ohmic (left) and rectifying (Shottky) (right) I-V curve.

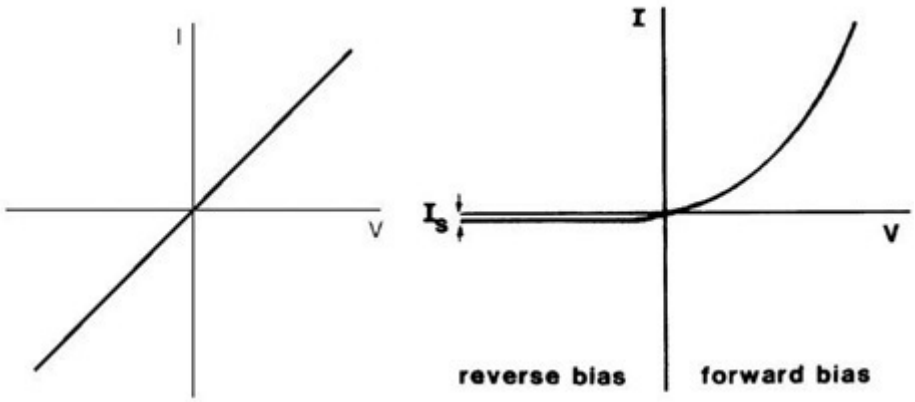

Figure 1-12: Typical ohmic (left) and rectifying/Shottky (right) I-V curve.[197]

However as the work function of the semiconductor varies with doping concentration, a common way to form ohmic contact in solar cells is to highly dope the semiconductor at the interface with the metal. This can be realized during the growth or through diffusion of dopant with a plasma or thermal process.

(d) Conclusions

In the general context of the development of pseudomorphic tandem solar cells on silicon, the work presented here aims to contribute to the improvement of the growth and design of a Ga(As)PN/Si tandem solar cell. My work during this thesis has mainly focused on the optimization of the growth, design and characterization of materials and devices for the tandem solar cell development. This was performed through (1) advanced structural, optical characterization and annealing of Ga(As)PN-based alloys grown on GaP substrates, (2) improvement of the structural quality of the GaP/Si interface and (3) realization of PV devices with performant ohmic contacts, good electrical properties, and tunnel junctions simulation. These three topics are presented in the following (chapter 3, 4, 5).

CHAPTER 2. SOLAR CELLS FABRICATION, SIMULATION AND CHARACTERIZATION TECHNICS

During this thesis, my main goal was to optimize the diluted nitride solar cells development. I have thus worked on: dilute nitride growth / annealing optimization using structural, optical and electrical characterization; and on solar cells processing (ohmic contact on GaP, GaP etching…) using electrical characterization. In order to improve the solar cells structure, I have also worked on the solar cells simulation using the software SILVACO.

2.1 Solar cells fabrication at FOTON

2.1.1 UHVCVD-MBE growth

(a) Growth cluster for III-V integration on Si

In order to avoid any cross-contamination between both the Si and the III-V material, it is mandatory not to mix both in the same growth reactor. Indeed, each one is a dopant for the other one. Therefore, the first approach to the pseudomorphic integration of III-V on silicon using a growth cluster has been proposed by the Toyohashi University of Technology, Japan, through the development of a UHV growth cluster composed of two MBE systems.[144] Silicon is provided by electron beam evaporator in a dedicated MBE. The transfer is performed under ultra-high vacuum. Furukawa et al. demonstrated with this setup that the co-doping (particularly doping of the silicon by the phosphorus) is dramatically reduced when the sample is grown in the two-MBE chambers growth cluster, as compared to a process using a single chamber growing both III-V and Si species.

The second approach has been proposed by the Philipps University Marburg, Germany. In this case the 300 mm AIXTRON cluster is composed of a silicon MOVPE chamber and a III/V MOVPE chamber separated by a transfer chamber also under controlled atmosphere.[123,198]

Finally, the Harris group at the Stanford University has also developed a cluster composed of two Varian Mod Gen II MBE chambers. In this case the two chambers, one dedicated to III-V growth and the other for group IV growth, are also connected together by a transfer tunnel under UHV.

A full discussion of the growth parameters influence on the properties of the dilute nitrides will be proposed in chapter 4. Even if I did not have personally performed the sample growth during this thesis (the samples have been grown by T. Rohel at FOTON-OHM/INSA lab), I have been strongly involved in the optimization of the dilute nitride materials and the GaP/Si interface, through the elaboration of the growth strategies and the annealing optimization (performed by myself). In the following, I describe the RIBER UHVCVD-MBE growth cluster developed at FOTON laboratory for the photonics on silicon research program. The scheme of this cluster is shown in Figure 2-1.

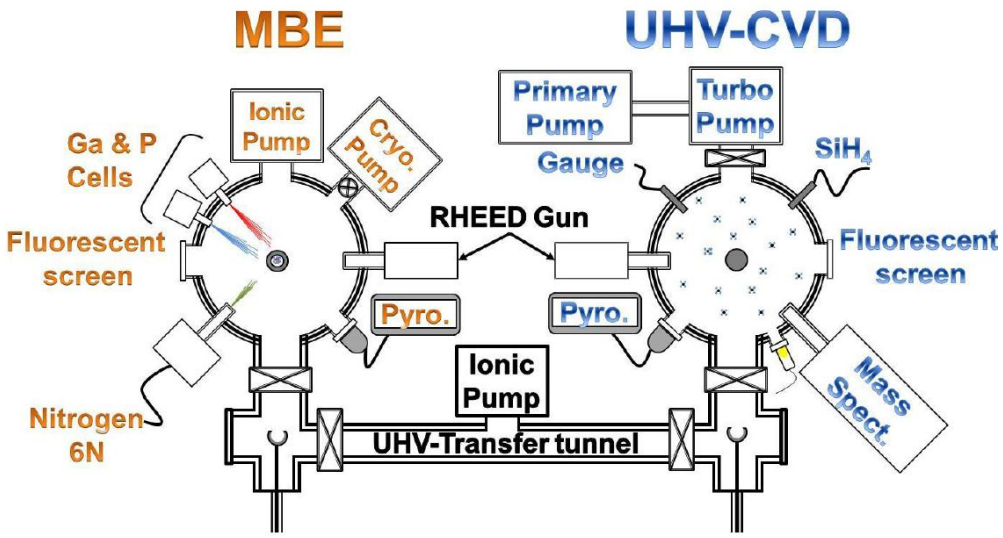

Figure 2-1: UHVCVD-MBE growth cluster developed at FOTON laboratory.[125]

(b) UHVCD chamber

The UHV-CVD reactor is connected to pumping systems allowing a residual pressure as low as 10^{-10} Torr as well as a high pressure of 10^{-1} Torr. The pressure is probed by a filament-based extractor gauge which works in the range of 10^{-10} – 10^{-5} Torr. During the growth at high pressure, this extractor gauge has to be turned off to protect the filament. The growth pressure is then monitored by a capacitive CTR gauge which works in the range of 10^{-5} – 10^{-1} Torr. 2 inches diameter silicon wafer are cleaned

ex-situ and then loaded to the reactor onto a molybdenum holder. The substrate holder is heated in the back side by a pyrolytic boron nitride (PBN) coated graphite resistance heater. The feeding power for this heater is controlled by a Eurotherm 900 power supply. Substrate's temperature can be measured by an Eurotherm thermal couple and a fibre infrared pyrometer which works in the range of 575°C – 1000°C. A mass spectrometer is plugged in the reactor to monitor the different species during the substrate degassing. Silane (SiH_4) and hydrogen (H_2) are injected through a mass flow/Baratron flux/pressure controller where their flux/pressure can be set between 0.001 to 10 Torr before sending to the reactor.

The choice of a CVD-like technique has been motivated by different reasons. First, as compared to other techniques, CVD depositions allow to grow thick layers, with well-controlled doping levels. This may be important in the context of photonics integration on silicon, especially for Si solar subcell development if needed. Moreover, the mobility of species at the growth front is increased by the presence of hydrogen-terminated surfaces, induced by the use of hydrogenated molecules (SiH_4, GeH_4, AsH_4, B_2H_6 …).[199] Finally, the control of the atomic steps organization at the growth surface is easier as compared to the H_2-free MBE growth.[135,200–202] Indeed, having a monodomain (bi-stepped) silicon surface is crucial for subsequent APD-free GaP overgrowth.

(c) MBE chamber

On the contrary, for the III-V compounds growth, a MBE chamber is used. The group III elements (Ga, In, Al) are provided through conventional Knudsen effusion cells containing pure metal solid sources while the group V elements (P, As, Sb) are supplied via valved-cracker cells where solid sources of these elements are heated. Upon heating, phosphorus and arsenic are released in the form of tetramers (P_4, As_4). They are then cracked to form P_2 and As_2 molecules which have higher sticking coefficients.[203,204] The valves at the exit of the cells allows a good control of the beam flux. The growth pressure is usually in the range of 10^{-7} – 10^{-5} Torr while the residual pressure is as low as 10^{-11} Torr. The growth rate of the III-V compounds is controlled by the group III flux.

The choice of the MBE growth mode for the III-V compounds has been made because it allows a fine control of thicknesses, interfaces and compositions which are of

primary importance to produce high quality single crystal material. Moreover due to its high non-equilibrium operating conditions, this growth mode is well suited for the growth of metastable materials such as dilute nitrides, as compared to MOCVD.[69,73] MBE operates in an ultra-high vacuum (UHV) environment, where fluxes of atoms or molecules are directed towards a single crystal substrate. These atomic and molecular species adsorb onto the surface and either bond into the growing crystal or desorb if a bonding site is not available or the temperature is too high. The fluxes are supplied by very high purity solid sources, either through evaporation or sublimation which reduces residual doping. In MBE operating conditions when the pressure can reach $\approx 10^{-5}$ Torr, the mean free path is still on the order of a meter. The distance between the sources and the substrate is 30-50 cm, well below the mean free path even considering growth pressures. The source flux can be considered as a beam since the atoms and molecules do not have any collisions with other species during their travel from the source to the substrate. Growth rates are low (typically <1 µm/h) as compared to other epitaxial growth techniques. Mechanical shutters block the molecular beam when the source is not needed during the layer growth. This method is sufficient to obtain atomically abrupt interfaces, which is of primary importance to realize high tunneling peak current using Esaki diodes (tunnel junctions) or to control precisely the nanostructures thicknesses and compositions, since the shuttering time is much shorter than the monolayer formation time due to the slow growth rate.

Another important feature in the FOTON MBE chamber is the presence of an ADDON rf plasma source which allows to grow dilute nitride alloys (such as GaPN, GaInAsN, GaAsPN, etc.). High purity nitrogen gas (6N) is injected to the cell through a 2 sccm mass flow controller connected to a getter, which allows a precise control of the gas flux at 0.1 sccm. A plasma is generated by a copper antenna which gives radio frequency electromagnetic radiation (f = 13.7 MHz). Different species could be generated inside the cell: electron, metastable ions N_2^+, atomic nitrogen.[97–102] To reduce the impact of the high energy charged species, which are known to damage epilayers, a mobile valve is installed at the exit of the plasma cavity. Such set-up allows avoiding the impinging of these high energy charged species on the sample surface (known to produce numerous point defects, for instance). Figure 2-2 display a scheme of the ADDON rf plasma cell.

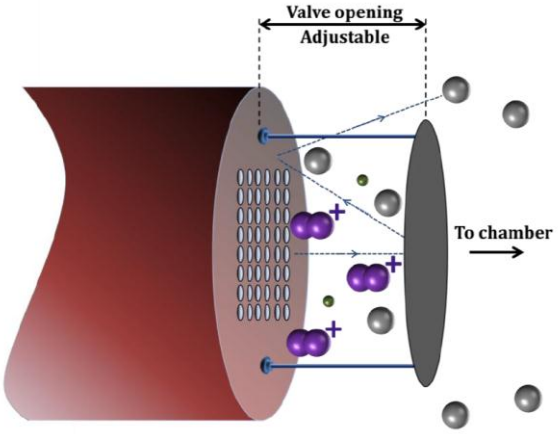

Figure 2-2: Scheme of the ADDON rf plasma cell.

The opening distance of the valve can be adjusted to produce more or less amount of atomic nitrogen sent to the growth chamber. The plasma cell parameters involved in the control of nitrogen incorporation are: RF power, nitrogen flux and the valve opening. By varying these parameters, two working modes can be observed:

- Low brilliance mode under a medium working power (< 350 W) and high nitrogen flux (> 1.5 sccm). The low brilliance mode produces a low amount of atomic N.

- High brilliance mode under a high working power (> 350 W) and low nitrogen flux (< 0.7 sccm). This mode is preferred for nitrogen incorporation because the production of atomic N is very efficient. Both operating modes can be easily distinguished by eyes. However, a rigorous analysis of the optical emission spectra of the nitrogen plasma has allowed us to optimize the working parameters.[205]

2.1.2 Rapid thermal annealing

In-situ or post-growth thermal annealing has been extensively investigated as a mandatory method to improve the optical and electrical quality of dilute nitride alloys. This annealing process allows migration of atoms and eliminates some of the various defects which appear in the material during the growth.[69,90,95,96,181,206,207] For instance, intrinsic point defects have been identified in GaIn(N)As and GaPN as As_{Ga} antisites, N interstitials, and Ga vacancies.[70,87,174,178,208] In most cases, annealing of dilute nitride samples lead to a strong enhancement of the emission intensity, a higher quenching temperature and a narrowing in the FWHM. It also leads to a blueshift of the PL

spectrum, which can be explained by a defect-assisted interdiffusion process such as nitrogen migration from interstitial to substitutional site, enabling an electronic bandstructure modification.[209] The magnitude of these effects depends largely on annealing parameters (time, temperature and atmosphere), they also seem to be related to the growth conditions. A full discussion on how annealing affects the characteristics of dilute nitrides optical emission will be proposed in chapter 4. However, previous studies on GaInNAs(Sb)/GaAs QW samples, show that annealing can reduce the S-shape emission behavior of the PL intensity with respect to the measurement temperature.[210] The S-shape is an non-monotonous variation of the PL peak energy. It is a characteristic feature of dilute nitride, caused by nitrogen localized states that are introduced in the III-V bandgap. Its reduction implies that the annealing step limits the impact of localized states.[211] It is believed that the reduction of the S-shape behavior is due to the decrease of alloy fluctuations induced by a reorganization of nitrogen inside the layer, improving the N uniformity.[212] Indeed, they found that carriers localization is strongly affected by both growth and annealing temperatures. By optimizing them, nitrogen localized states can be dramatically reduced leading to a vanishing of the S-shape behavior. Removal of the S-shape feature in dilute nitrides has been reported also by other means, for example adding GaInNAs barriers in the GaAs/GaAsN MQWs structure or adding antimony into the material.[213–217] Even if annealing of GaPN material grown by MBE at low temperature (480°C) has not been studied extensively, several papers tend to show that rapid thermal annealing can have the same impact on this dilute nitride alloy than the one observed on GaAsN.[181,183,206] All the annealing experiments in this study has been performed under a forming gas atmosphere using a JIPELEC JetFirst rapid thermal annealer (RTA) which allows temperature ramp up to 300°C/s from room temperature to 1200°C.

Figure 2-3: JIPELEC JetFirst rapid thermal annealer.

This RTA have been ordered and delivered during my thesis, I have participated to its setting up, mainly by creating recipes from 500°C up to 1000°C. As described in the following, I have optimized the annealing process to improve the GaPN-based compound structural and optical qualities. Figure 2-3 displays an image of the JIPELEC furnace.

2.2 Solar cell parameters modeling

SILVACO was used to model and optimize the design of the solar cells. This software numerically solves Poisson's equation coupled with continuity equations for both electrons and holes under steady state or transient conditions over a 2D mesh. The optimization was accomplished by altering the thicknesses and doping concentrations of the different layers, but also by creating and modifying the material properties of the GaAsPN absorber layer. Even though I didn't wrote the script used to simulate our solar cells, which has been made by Alain Rolland from FOTON-OHM/INSA lab, I have been involved in the solar cells simulation by suggesting inputs and producing experimental values of electrical and optical parameter such as residual doping concentration and complex refractive index. SILVACO has been chosen because it allows for thousands of combinations to be investigated without the costly fabrication of the actual solar cells and also because, as far as I know, it is the only software that is able to model tandem or MJSC solar cells and especially the electrical properties of the tunnel junction.[218]

2.2.1 Virtual solar cells and light sources

A command file called the deck build is needed for the solar cells simulation. This command file permits to build a computer-generated solar cell. The illumination is then modeled using a power file that can simulate, for instance, an AM1.5G solar spectrum.

Within this simulation the origin of the beam for 2D optical sources can be defined. In the present work, a 90-degree angle of incidence has been chosen indicating that the beam is perpendicular to the surface of the solar cell. The incident beam can reflect back into the cell from the bottom contact of the solar cell. A power file is defined containing irradiance levels as a function of wavelength. The wavelengths in these files are given in microns and the irradiance levels are provided in watts per square centimeter per micron ($W/cm^2/\mu m$). The final portion of the beam statement indicates the starting and ending wavelengths and the corresponding wavelength resolution.

The software produces output files that can be plotted using programs such as TonyPlot or Matlab for visualization.

2.2.2 Simulation source code

This section will present the structure of the SILVACO program files. All SILVACO files are divided into the following main sections: (Mesh, X-Mesh, Y-Mesh, Regions, Electrodes, Doping, Material properties, Models, Light beams, Solving)

First the cell's mesh is defined. It consists of many triangles, the density of which determines the accuracy of the simulation. The accuracy will determine the amount of time required for an iteration of the program. The mesh density is varied to provide a more accurate simulation where the majority of the electrons-holes are produced. If the mesh is too large the simulation results can be false and if the mesh is too fine the amount of time required to run the simulation can overpass the computation capabilities.

The cell is then separated into regions made of different materials, the electric contacts (electrodes) are defined and the doping level for each region is assigned. Then, the material properties have to be defined. While a large library of common materials is provided by SILVACO, new materials such as dilute nitrides must be defined by the user. A model for generation and recombination of carriers is also used to evaluate the electrical properties of the structure. SILVACO provides a large choice of

recombination processes with more than 70 different models available. The model used to evaluate the simulated cell in this thesis was the Shockley-Read-Hall (SRH) process since it is known to be one of the dominant process recombination in our materials, with the radiative process. Indeed the carrier lifetimes in the SRH model were determined to provide the closest results to the experimental cell.[218]

Finally, the solve instruction is used to evaluate the structure at each triangle intersection and generate output files, that are compared to experimental files.

2.3 Characterization of materials and devices

2.3.1 Structural characterization

(a) Atomic Force Microscopy

The atomic force microscopy (AFM) is a local probing method which gives information on a sample surface topography. This fast and non-destructive method allows extracting quantitative and qualitative information on the surface morphology. We have used a 2007 Veeco diInnova AFM experimental setup, allowing 100x100 µm² images with a Z scale maximum amplitude of ~6 µm (Figure 2-4). The AFM microscopy works as follow: a tip (typically made of Si_3N_4 or Si) is fixed on a deformable cantilever which scans the studied surface using a piezoelectric tube. The tip/surface interaction allows extracting the sample topography. The tip/surface interaction can be of various types: Van Der Waals force, capillarity, electrostatic, thermic or magnetic etc…, depending on the sample.

Figure 2-4: 2007 Veeco diInnova AFM setup in FOTON laboratory.

The deviation of the cantilever Z due to those interactions is proportional to the tip/samples interaction force F:

$$F = kZ$$

In this thesis I have used the AFM in contact mode. In this mode, the tip contacts the surface, and the deviation of the cantilever from a reference position is measured when the tip sweeps along the surface.

The deflection of the cantilever is measured via the reflection of a laser. The tip is mounted on a reflective cantilever and laser beam is reflected on it to a four quadrant photodiode Figure 2-5.

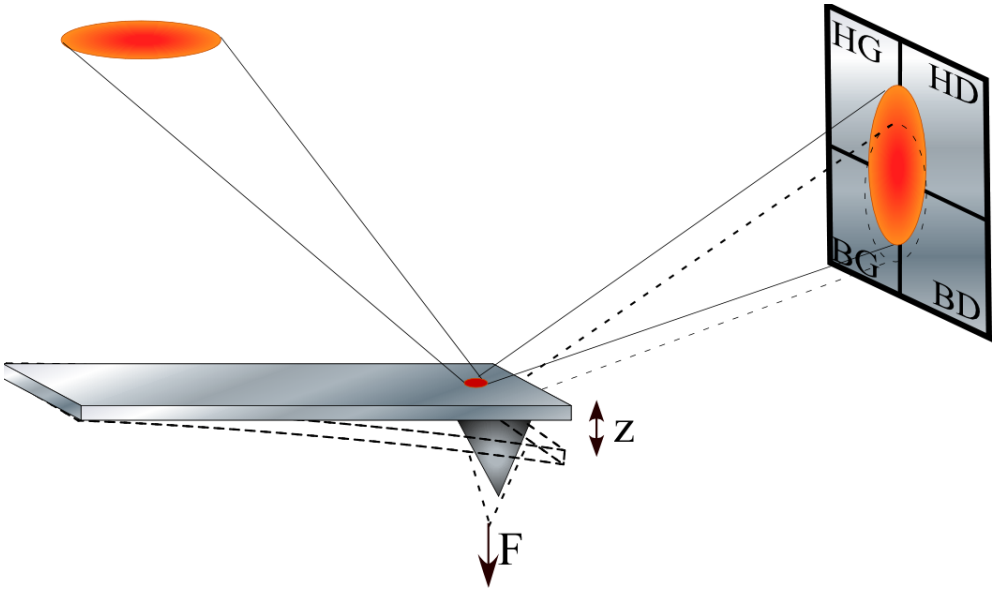

Figure 2-5: Scheme of the deflection detection using a reflected laser on four quadrant photodiode.

The sample support is made of a piezoelectric ceramic, which is controlled by an electric feed-back loop. When the tip moves along the surface, the spot's relative position with respect to the reference is recorded and sent to feedback loop. At the same time, the ceramic changes the sample position according to the signal from feed-back loop so that the spot can go back to the reference position. The signal from the loop is used to plot the surface topography.

(b) X-Ray Diffraction

We have used thorough X-ray scattering techniques for qualitative and quantitative evaluation of the studied thin films. Since the peak positions in an X-ray diffraction pattern are directly related to the atomic distances, one may obtain information such as strain, film thickness, relaxation, and phase segregation and it can provides an estimation of samples composition rather quickly and nondestructively. It is also useful for obtaining values such as layer thickness and composition by examining the features

within the diffraction pattern. Readers may refer to many books for a complete understanding of x-ray diffraction (XRD) principle and techniques.[219,220] In this document, I only present the techniques that I have used which are typical ω/2θ scans and reciprocal space mapping.

i. X-Ray diffraction lab setups

XRD are performed using a Philips diffractometer. A conventional setup of this system is schematically shown in Figure 2-16. The X-ray tube uses a copper anode to produce X-ray radiations. The feeding power is typically set at 35 kV and 40 mA. A 4-bounces Ge (022) symmetric monochromator is used to select the $K_{\alpha 1}$ rays with a wavelength of 1.54056 Å and to obtain a low incident beam angular divergence of 12 arcsec. The goniometer is a 4-circles which allows basic translation in the Descartes space (X, Y, Z) and 4 rotation axis: omega, 2-theta (detector), phi and chi (see Figure 2-6). ω is the incident beam angle with respect to the sample surface and 2θ is the angle between the incident beam direction and the detection position. An anti-diffusion slit of 1 mm is installed at the entrance of the detector. There is no optics after the sample so that we have performed XRD rocking-curves using this apparatus.

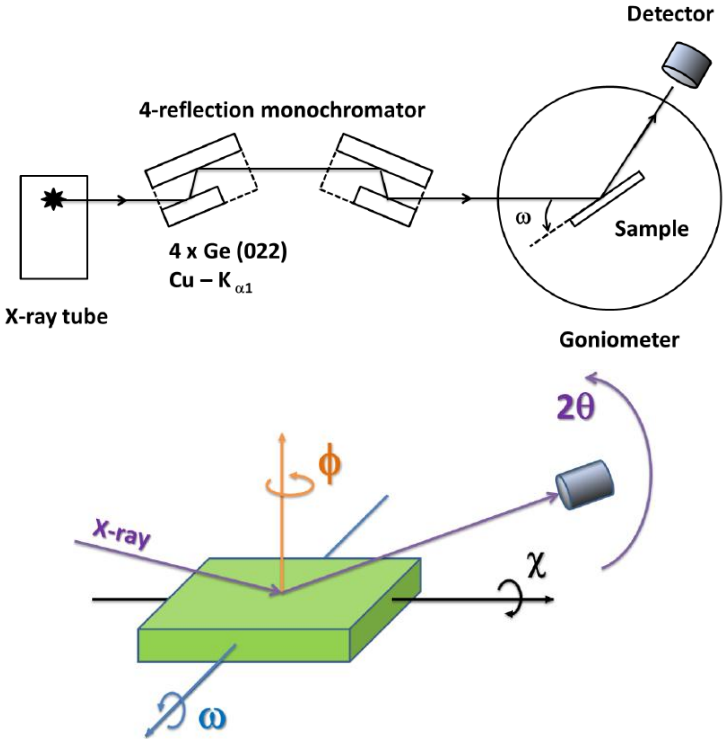

Figure 2-6: Schematic representation of a double crystal HRXRD setup (top). Sketch of the 4 rotation axis of the Philips goniometer (bottom).

We have also done reciprocal space mappings (RSM) using a Bruker D8 diffractometer equipped with a copper anode, a 4-bounces Ge (022) asymmetric (for more signal) monochromator is used to select the Kα1 rays with a wavelength of 1.54056 Å and to obtain a low incident beam angular divergence of 18 arcsec. The goniometer is a 4-circles which allows basic translation in the Descartes space (X, Y, Z) and 4 rotation axis: omega, 2-theta (detector), phi and chi (see Figure 2-6). ω is the incident beam angle with respect to the sample surface and 2θ is the angle between the incident beam direction and the detection position. An anti-diffusion slit of 3 mm is installed at the entrance of the detector. The feeding power is 40 kV and 40 mA and equipped with a 1D position-sensitive detector with 2.7° opening (which can be seen as back optics between the sample and the detector). With this apparatus, we have performed transverse-scans (ω-scans with a low acceptance angle of the detector), ω/2θ and RSM.

ii. ω/2θ coupled scan

The most common scan performed on HRXRD for epitaxially grown semiconductors is the ω=2θ scan of the (004) planes. Here, the diffraction vector is perfectly perpendicular to the surface and thus only measures components out-of-plane. Constructive interference of X-ray radiation occurs at certain angles of diffraction depending on the lattice spacing as given by Bragg's Law:

$$2d_{hkl}\,sin(\theta) = n\,\lambda$$

where n is the order of the diffraction and can be any positive integer, λ is the wavelength of the incident X-rays, ω is the scattering angle, and d_{hkl} is the spacing between the (hkl) planes. For cubic crystals, d_{hkl} is related to the lattice spacing a by the following relationship:

$$\frac{1}{d_{hkl}} = \frac{(h^2 + k^2 + l^2)}{a^2}$$

When measuring fully relaxed, unstrained films, Bragg's Law is sufficient for most analysis since the film relaxes to its equilibrium lattice parameter. For example, the (004) ω=2θ scan of a fully relaxed GaPN film gives information on composition based on the lattice spacing d_{hkl}. For fully coherent films, a more complex analysis is needed. Strained GaPN films grown on GaP are tetragonally distorted such that the (004) plane

spacings are different from its relaxed value. A typical ω–2θ XRD profile of a GaPN/GaP epilayer is shown in Figure 2-7. The nitrogen content (corresponding to the 2θ value) can be extracted considering the peak layer position using the following approximations:

In a cubic crystal, the free of strain lattice parameter, a_{FOS} can be calculated from the measured (004) lattice parameter a_{004} using the relationship:

$$a_{FOS} = \frac{(\frac{C_{12}}{C_{11}} a_{GaP} + a_{004})}{(1+\frac{2C_{12}}{C_{11}})}$$

The constant a_{GaP} is the lattice parameter for GaP. Parameters C_{11} and C_{12} are the stiffness coefficients for the film where the ratio $2C_{12}=C_{11}$ is approximately 0.9 for most III–V materials.[221] So for GaPN, using the unstrained lattice parameter, the N concentration can be calculated using Vegard's Law, which is valid in the dilute regime.[78]

$$x = \frac{a_{FOS} - a_{sub}}{a_{GaN} - a_{sub}}$$

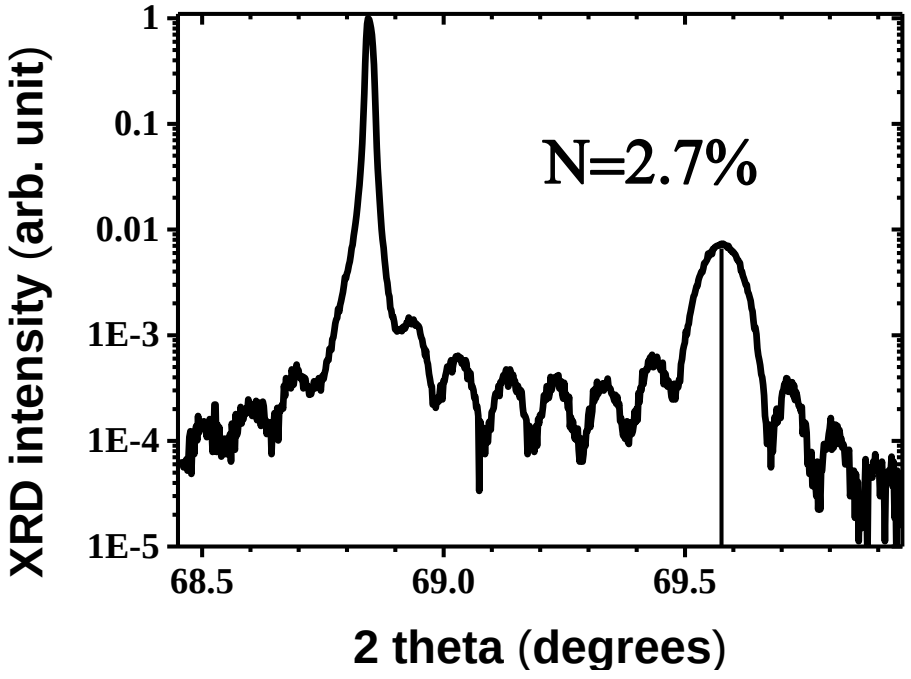

Figure 2-7: XRD pattern around the (004) Bragg peak position, of a 100 nm $GaPN_{0.027}$ layer, grown on a GaP substrate.

However, the strain and compositional values obtained using the described method has to be taken with care. Indeed, obtaining absolute N concentrations via X-ray diffraction simulation can only lead to erroneous results. Indeed, the above calculations assumed all atoms were located in substitutional sites. It has been reported that a significant amount of N is found on interstitial sites.[208]

Since N is a small atom and the rf plasma itself can create highly energetic N species, it is not surprising that N is found on both interstitial and substitutional sites. The N found in the interstitial sites does not contribute to the strain as they would on substitutional sites. Since very little strain is added to the system from these atoms, their contribution to XRD diffraction is neglected here. Other methods such as Rutherford backscattering spectrometry (RBS) and secondary ion mass spectrometry (SIMS) are required to make a more accurate determination of N content. Another problem is the ambiguity in determining compositions of alloys with four or more elements. In a ternary compound, it is simple to analyze the change in lattice parameter, and thus strain, due to the addition of one element in the III–V semiconductor. However, once two elements are added, the source of the strain becomes more complex. For example in GaAsPN, there are an infinite number of combinations of As and N compositions which will give the same lattice parameter. One can obtain an estimation of the concentrations by crossing tight binging calculations of the energy bandgap with XRD and photoluminescence results to give a range of As or N compositions, as it will be explain with more details in the next section.

The observed thickness fringes (or Pendellösung oscillations) in Figure 2-7 indicate that the correlation length of the diffraction planes is perfectly uniform from one interface to the other. From the fringes positions and integral breadth of the epilayer diffraction peak, we can measure the thickness of the epilayer by two methods. The first one is to use the Scherrer equation:

$$t = \frac{\lambda}{\Delta(2\theta).cos(\theta_B)}$$

where $\Delta(2\theta)$ is the integral breadth of the epilayer diffraction peak, θ_B the Bragg angle. In Figure 2-7 $\Delta(2\theta)$=0.0017 rad and θ_B =34.785°. Using the Scherrer law the thickness, found for this epi-layer is 118 nm.

The other, and more accurate, method is to use the Pendellösung fringes, through a plot of the ω-2θ curves in the reciprocal coordinates Figure 2-8, and then plot the fringes order as a function of their positions, the slope of this plot (line) gives us the thickness of the epilayer. Practically we use the **S** vector coordinates which is a reduced form of the scattering vector **Q:**

$$S = \frac{Q}{2\pi} = \frac{2sin(\theta_B)}{\lambda}$$

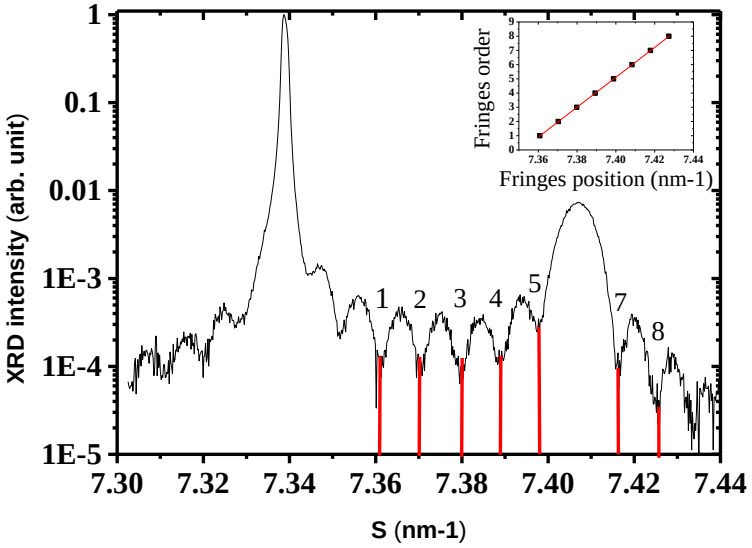

Figure 2-8: XRD pattern around the (004) Bragg peak position, of a 100 nm $GaPN_{0.027}$ layer, grown on a GaP substrate.

Using the second approach the thickness found for this layer is 105 nm. This value is in agreement with the one given using Scherrer law.

iii. Reciprocal space mapping (RSM)

Using conventional ω-2θ curves, in order to obtain an accurate unstrained lattice parameter value, one has to assume there was no relaxation. If any relaxation has occurred, this would shift and possibly broaden the peak leading to false results. One method to measure the degree of relaxation is to use a reciprocal space mapping (RSM). A RSM is a series of 2θ scans holding ω constant. The ω value is then increased incrementally such that a plot is obtained showing contours of diffracted intensity in reciprocal space. RSMs are usually plotted with the out-of-plane (00l) direction as the z-axis (S_z direction in the reciprocal space) and the in-plane (hk0) direction as the x-axis

(S_x direction in the reciprocal space). Complementary to the (00l) direction which gives information on the growth direction, the other most common diffraction direction for RSMs is the (224) set of planes which gives also information along the sample surface. If all layers are grown coherently on the substrate, the RSM will display a Bragg peak from the layer, elongated along the growth direction due to the low layer thickness (also called "truncation rod), located at the same Sx position than the substrate Bragg peak Sx position, due to the same in-plane lattice parameter value. However, any relaxation effect will induce diffraction intensities which will be found with different in-plane values than the substrate, depending on the degree of relaxation which can be partial or complete. Figure 2-9 presents a RSM of a partially relaxed 100 nm thick GaPN layer grown on GaP (001) performed on the GaP (224) reflection.

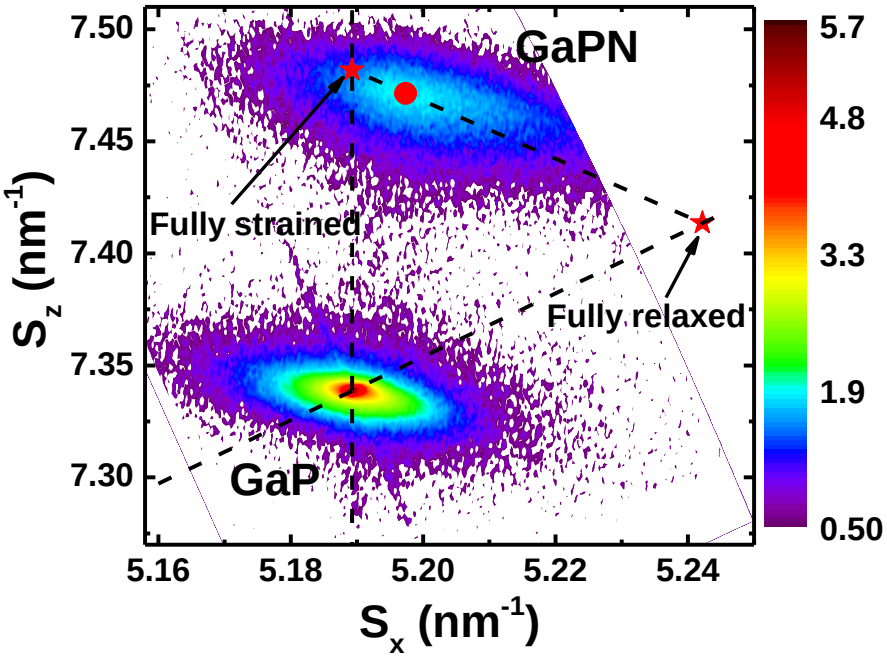

Figure 2-9: RSM of a partially relaxed 100 nm thick GaPN layer grown on GaP (001) performed on the GaP (224) reflection.

As shown in Figure 2-9 the relaxation may be neither complete nor uniform so a smear of diffraction intensities could develop originating from the unrelaxed reciprocal lattice point to the fully relaxed one, which can give information on how the crystal relaxes.

2.3.2 Optical characterization

(a) Photoluminescence

Photoluminescence (PL) is a powerful technique for assessing material quality through its optical properties. It is one of the most useful technique when developing a new (optically active) material system. It is non-destructive and requires virtually no sample preparation or complex device architectures. Moreover, variation of different parameters (e.g. temperature or pump power) can be used to obtain band offsets, identify various transitions, and even explore the structural quality of the material.[85,216,222,223] The time-dependent evolution of the PL signal can be used to accurately determine carriers dynamics such as carrier lifetimes.[224,27,72] Indeed, in order to optimized the GaInAsN(Sb) alloy for PV applications, PL has been widely used because of the strong effect of the nitrogen incorporation on GaInAs optical properties and due to the strong relationship occuring between electrical and optical properties in this dilute nitride compound.[95] The PL experimental setup at FOTON-OHM/INSA consists in a 15 mW/cm² incident pump beam at a 405 nm wavelength (3 eV), optics to focus and collect the light, a spectrometer to measure the emission spectrum of the sample and filters to attenuate the contribution of the pump beam to the signal. In order to study the evolution of the PL parameters with respect to the temperature, I have used a Helium bath closed cycle cryostat to study the PL properties from 20K to 300 K. The emission is averaged for many clock cycles to obtain sufficient signal-to-noise ratio. Data collection and analysis are performed by computer. Figure 2-10 displays FOTON experimental setup at room and low temperature.

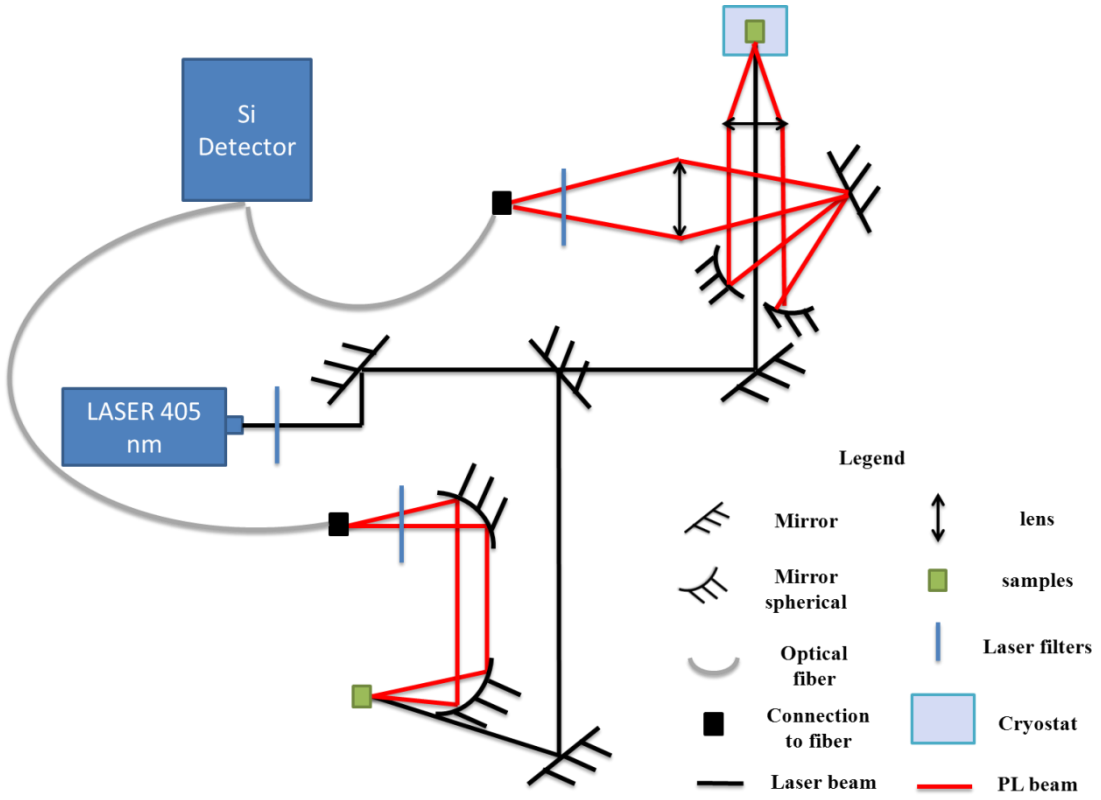

Figure 2-10: FOTON experimental setup at room and low temperature.

2.3.3 Electrical characterization

(a) Circular Transmission Line Method

The basic of the circular transmission line model (CTLM), that I have used to measure the specific contact resistance ρ_c, are introduced. For a contact between two dissimilar materials, such as metal and semiconductor, there exists a contact resistance, *Rc*, which is a metal- and geometry-dependent parameter as its magnitude is determined by the sheet resistance of the conducting semiconductor, the contact area. Consequently, contact resistance is not a useful parameter to characterize contacts. Another parameter that is independent on the measurement and geometry of the contact, known as the specific contact resistance, ρ_c, is often used to characterize the contact quality. The specific contact resistance is defined as the resistance of a unit area of the thin interfacial layer between the bulk metal and semiconductor sample.[225] Physically, ρ_c is the finite resistance seen by the infinitesimal current crossing the metal-semiconductor interface that has an infinitesimally small potential difference. As the specific contact resistance ρ_c cannot be measured directly but must be inferred from a measurement on a

real contact, hence several approaches have been used to model the current-voltage behavior of the contact and to extract ρ_c. One of them is the circular transmission line method (CTLM).[226,227] In this approach circular test pattern are used to determine the specific contact resistance of ohmic contact systems in semiconductor devices that avoid the fabrication of a mesa structure needed when using a rectangular test pattern. As a result, circular pattern has been chosen in this work. Using a constant electrical current (i_o) through the inner circular and outer contact pads there will be a voltage drop, ΔV, across the separation (d) between two points (see Figure 2-11). This voltage drop across the separation d, is related to the total resistance R_T through the relation $R_T = \Delta V/i_0$

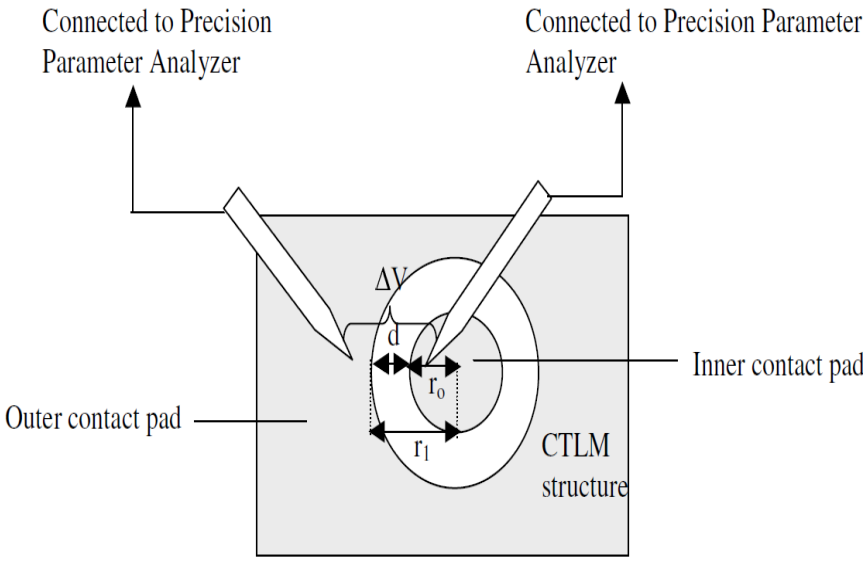

Figure 2-11: CTLM test pattern scheme.

Thus using different values of d, the $R_T(d)$ dependence is plotted. From this plot one can extract the transfer length L_T and the semiconductor sheet resistance R_{sh} to deduce the specific contact resistance ρ_c ($\rho_c \approx L_T * R_{sh}$).[225] As shown in **Figure 2-12** the transfer length can be extracted from the intercept value (when d equals 0) while the sheet resistance can be extract from the slope and the radius value of the circular pattern r_1

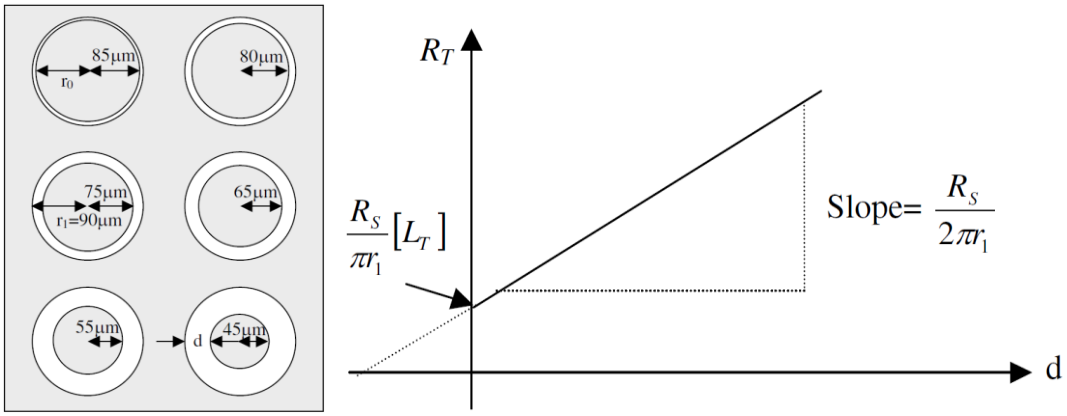

Figure 2-12: (left) Test pattern with different values of d used in this work. (right) R_T(d) curve that allows determining the sheet resistivity and the specific contact resistance from the voltage drop.

(b) Hall effect

Hall effect is a very powerful technics to determinate the semiconductor resistivity (ρ), mobility (µ) and carrier concentration (n). When an electric current flows through a conductor in a magnetic field, the magnetic field exerts a transverse force on the moving charge carriers which tends to push them to one side of the conductor.[228,229] A buildup of charges at the sides of the conductor will balance this magnetic influence, producing a measurable voltage between both sides of the conductor. This measurable transverse voltage is called the Hall voltage. From the hall voltage measurements and the resistivity of samples one can extract the carrier concentration and mobility from the following two equations:

$$V_H = \frac{BI_s}{ned}$$

$$\rho = \frac{1}{ne\mu}$$

Where n is the charge carrier density in cm^{-3}, B the magnetic field in Tesla, I_s the current in A (A=Wd), d the sample thickness in m, ρ the resistivity in Ω.cm, and µ the mobility in cm^2/Vs.

Figure 2-13 presents the Hall measurement principle scheme.

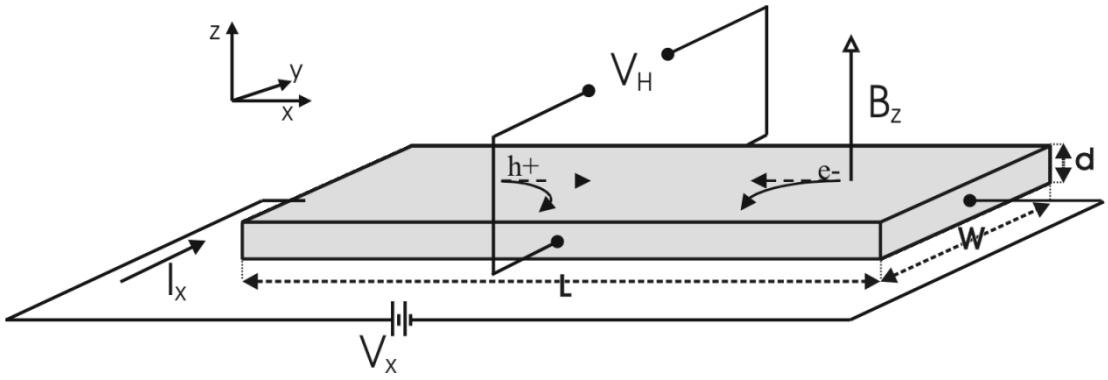

Figure 2-13: Hall measurement principle scheme.[230]

Hall effect experiments have been conducted during my thesis, to measure the mobility of GaP layers and to measure the carriers mobility in the dilute nitride alloys. The main issue with these measurements is to ensure ohmic contacts especially when working on wide band gap semiconductors.

(c) C-V

The C-V method is an electric, non-destructive measurement of the barrier capacitance of semiconductor junctions, like p-n junctions, metal- semiconductor junctions and even metal-oxide-semiconductor (MOS) structures. Its non-destructive character and large applicability gave the method a widespread, almost universal usage in the semiconductor industry. In order to obtain the doping profile, the C-V (capacitance versus voltage) measurement is done using a Shottky contact with the front layer, and using a circular test pattern and a mesa-etch step. The circular pattern radius size depends on the capacitance measurements capabilities.[231] In direct polarization the space charge region length is given by the relation:

$$W(V) = \sqrt{\frac{2\varepsilon_s(V_d - V)}{eN_d}}$$

Where ε_s is the semiconductor permittivity, N_d the carrier density and V_d the diffusion bias of the diode.

The differential capacity is given by:

$$C(V) = \left|\frac{dQ}{dV}\right| = S\sqrt{\frac{\varepsilon_s eN_d}{2(V_d - V)}} = \frac{\varepsilon_s S}{W}$$

Thus the doping concentration is given by:

$$N_d = \frac{-2}{\varepsilon_s e S^2} \frac{1}{d\frac{1}{C^2}\Big/dV}$$

I have used C-V measurements to calibrate the doping concentration of GaP layers and to measure the residual doping of dilute nitride alloys.

(d) I-V under illumination

As explained previously in chapter I, the I-V characteristics of p-n junctions allow the determination of the efficiency yield (η) of solar cells, defined as the maximum output power on the incident power ratio. This measurement also allows the determination of the following main parameters: the short circuit current density (Jsc) the open circuit bias (Voc) and the fill factor (FF).

Such that

$$\eta = \frac{P_{max}}{P_{inc}} = \frac{FF.V_{oc}.J_{sc}}{P_{inc}}$$

Where $P_{inc} \approx 1000$ W/m² (for AM1.5G, known as the "standard test conditions").

In a solar cell the diode equation can be written as follow (Figure 2-14):

$$J = J_0(e^{\frac{q(V-r_sJ)}{nkT}} - 1) - J_{ph} + \frac{V - Jr_s}{R_{sh}}$$

Where r_s and R_{sh} are respectively the series and the shunt resistance in Ω.cm², and n the ideality factor of the diode.[232] n ranges from 1 (for an ideal diode) to 2 (diode dominated by SRH recombinations). Thus when J → 0 the J-V slope allows extracting the series resistance and when V→ 0 the J-V slope gives access to the shunt resistance. As explained in chapter one, an ideal solar cell would have an infinite shunt resistance and a series resistance equal to zero. In classical high quality solar cells such as GaAs single junction the shunt and series resistance are typically over 10000 Ω.cm² and below 0.1 Ω.cm² respectively.[233] An example of a GaAsPN/GaP solar cell J-V curve is shown in Figure 2-14

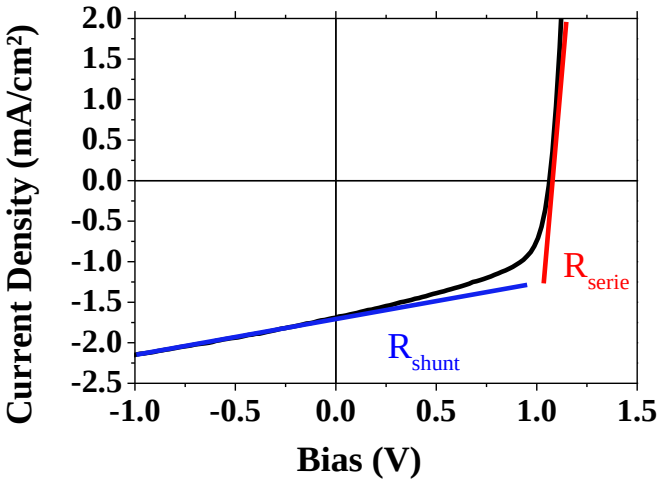

Figure 2-14: Typical GaAsPN/GaP solar cell J-V curve.

All the I-V curves displayed in this thesis have been performed at the institute of research and development of photovoltaic energy (IRDEP, partner of the MENHIRS project) using class AAA solar simulator.

(e) Quantum efficiency

The spectral response is conceptually similar to the quantum efficiency. The quantum efficiency gives the number of electrons generated by the solar cell as compared to the number of incident photons on the device, while the spectral response is the ratio of the current generated by the solar cell to the incident power on the solar cell.[5,234] Typical GaAsPN/GaP solar cell quantum efficiency curves are shown in Figure 2-15

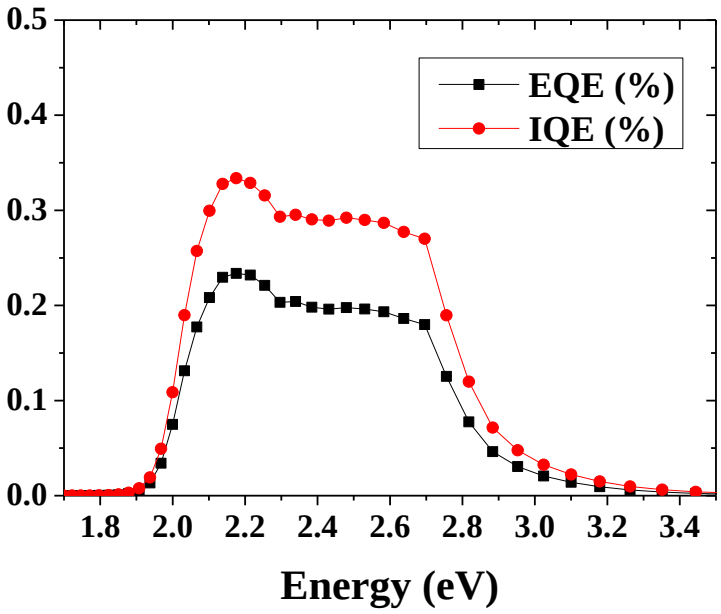

Figure 2-15: Typical GaAsPN/GaP solar cell external (black) and internal (red) quantum efficiency curves, as a function of the incident beam energy.

The quantum efficiency is limited at low energy by the inability of the semiconductor to absorb photons with energies below the band gap (transparency losses). For photons with energy higher than the bandgap, the EQE is limited by reflection losses but also because materials issues such as surface recombination and low minority carrier diffusion length. In order to study the issues related to the absorbing material and solar cell structure, the internal quantum efficiency (IQE) is usually studied. The IQE is the number of collected carrier on absorbed photon (α) ratio:

$$IQE = \frac{EQE}{\alpha}$$

IQE measurements allow identifying where issues are coming from in the solar cell structure. As an example it is known that front surface passivation affects carriers generated near the surface, blue light is absorbed very close to the surface, thus high front surface recombination will affect the "blue" portion of the quantum efficiency. Similarly, green light is absorbed in the bulk of a solar cell and a low diffusion length will affect the collection probability from the solar cell bulk and reduce the quantum efficiency in the green portion of the spectrum. All the IQE curves shown in this thesis have been obtained at the institute of research and development of photovoltaic energy

(IRDEP). The measurement has been performed using an Oriel IQE-200. This apparatus uses a 250 W quartz tungsten halogen (QTH) lamp, monochromator, an optical chopper, a lock-in amplifier, and a calibrated silicon photodetector. For thick samples where the transmission of photon having energy higher than the bandgap of the absorber is near zero, setup is designed to provide a simultaneous, real-time readout of EQE and IQE in a single measurement, as it allows the measure of the sample reflectivity.

In the following, I present the main results obtained during my Ph.D. thesis on GaP/Si interface and Ga(As)PN growth optimization. Finally results on the realization of GaAsPN/GaP solar cells are presented.

CHAPTER 3. STUDY OF THE GAP/SI INTERFACE

The first issue to be overcame for the development of III-V/Si tandem solar cell is the control and suppression of the crystalline defects that arise mainly at the III-V/Si interface due to mismatch of local chemistry. Indeed, a very high level of structural quality is required so that the efficiency could reach at least 80% of the theoretical value. During this thesis I have participated to the GaP/Si interface optimization by participating to the growth optimization giving suggestions for studies and by doing AFM measurements on GaP layers grown onto Si. This work has been conducted in close collaboration with Olivier Durand, Charles Cornet, Christophe Levallois, Antoine Létoublon, Thomas Quinci, Thanh Tra Nguyen, Yanping Wang, Tony Rohel and K.Tavernier. In this chapter, I describe briefly the main structural defects (microtwins/stacking fault and antiphase domains) encountered in GaP layers coherently grown on Si, and routes to characterize them. Then I show the results obtained on the optimization of the nucleation and regrowth parameter on the GaP/Si interface. Finally I present some results on the influence of the pre-nucleation layer and its impact on the APD formation/annihilation.

3.1 GaP/Si structural defect

3.1.1 Stacking fault and microtwins

(a) MT and SF description

Microtwins originate from a rotation of the crystal by 180° around a <111> direction. A model of microtwin in GaP structure is schematically represented in **Figure 3-1**, as given by Skibitzki *et al* [235]

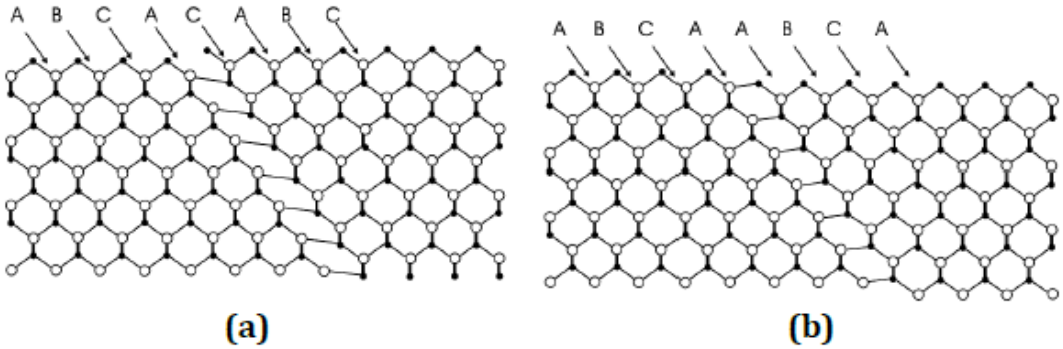

Figure 3-1: Planar defects of the zinc-blende crystal : (a) intrinsic stacking fault, (b) extrinsic stacking fault.[235]

A stacking fault is bound by two partial dislocations formed by the dissociation of a perfect dislocation. As shown in Figure 3-2 a perfect dislocation in a III–V compound is dissociated into two Shockley partial dislocations (with burgers vectors equal to $a_0/6[2\text{-}1\text{-}1]$ and $a_0/6[11\text{-}2]$) according to Mader and Blakeslee as it is energetically favorable.[236,237,238]

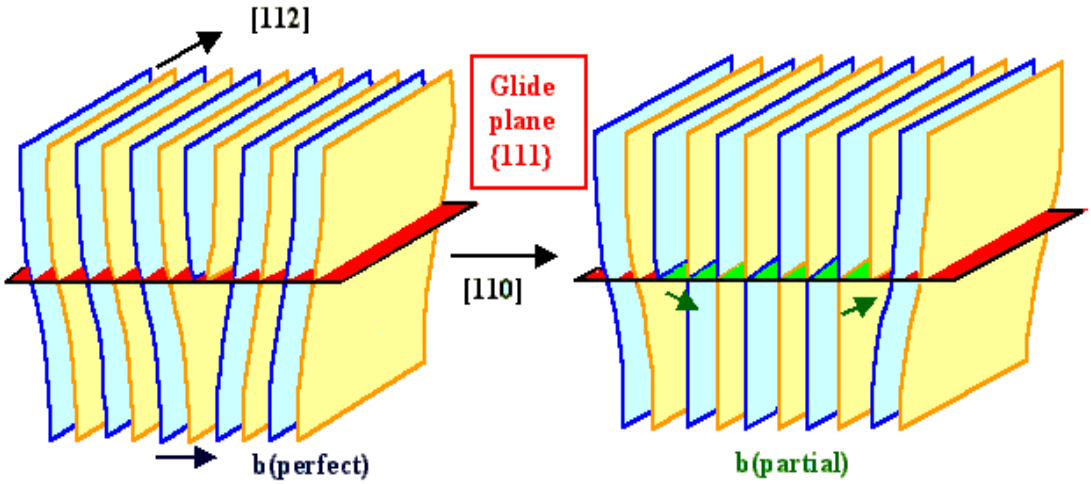

Figure 3-2: Perfect dislocation in a III–V compound (left) dissociated into two Shockley partial dislocations with burgers vectors equal to $a_0/6[2\text{-}1\text{-}1]$ and $a_0/6[11\text{-}2]$ (right) according to Mader and Blakeslee.[232]

According to reports, stacking faults and microtwins are generally formed at the early growth stage of GaP/Si.[146] Three dimensional growth and the coalescence of the 3D nucleation sites were attributed to be the reason for their formation. Nevertheless, the particular role of the polar on non-polar GaP nucleation on Si step edges cannot be neglected.

(b) MT detection

MT can be analyzed using XRD pole figures. MT are small domains of rotated crystal inside a main crystalline phase which induce additional reciprocal lattice points (Figure 3-3). Indeed, MT formation inside a GaP (001) matrix create additional MT {111} planes that are inclined by 39° from the original GaP {111}. They are therefore inclined by 16° from the (001) planes. GaP {111} MT reflections can be found with an inclination in χ of 16° from the surface normal, whereas GaP {111} from the main phase can be found with a χ inclination at about 55° from the surface normal.[239,240] As a direct consequence of the 4-fold symmetry of the cubic structure, 4 variants of MT can

be obtained, lying on {111} planes. After alignment of 2θ (detector position) and ω (sample rocking) to the Bragg position corresponding to GaP (111) planes, we fix the ω and 2θ angles and perform a XRD pole figure, corresponding to circular ϕ scans (0° - 360°) for each χ angle position ranging typically from 0° (diffraction vector along the surface normal direction) to 60°.

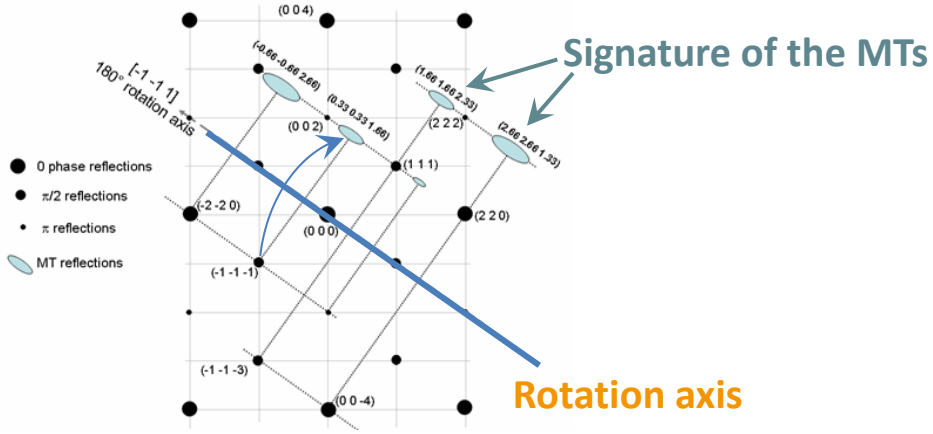

Figure 3-3: Reciprocal lattice points of GaP. The black, circles represent strong, medium and weak reflections as a function of their size. The blue ellipsoid shapes indicate the diffraction spots of MT. This schema presents 1 out of the 4 MT variants

Figure 3-4 presents a pole figure performed on a GaP/Si thin layer sample at the GaP (111) Bragg angle. The silicon (001) substrate presents a miscut of 6° toward the [110] direction in order to lower the antiphase domains density (this will be explained in part 3.1.2). Due to the fourfold symmetry, 4 symmetric GaP {111} Bragg peaks at χ≈55° are measured. Note that the 4 GaP {111} spots are overlapped by the four corresponding Si {111} spots because of the large opening of the detector (their Bragg peak position are close one to each other). The four lower intensity peaks at χ≈16° correspond to the MT reflections. The 4 MT variants (A, B, C, D) are indicated in the figure.[235] Note that the MT-A and MT-C are shifted in χ by ±6° due to the substrate miscut. The inset describes the sample alignment at an initial position corresponding to ϕ=0°. The direction movement of the ϕ angle is also indicated.

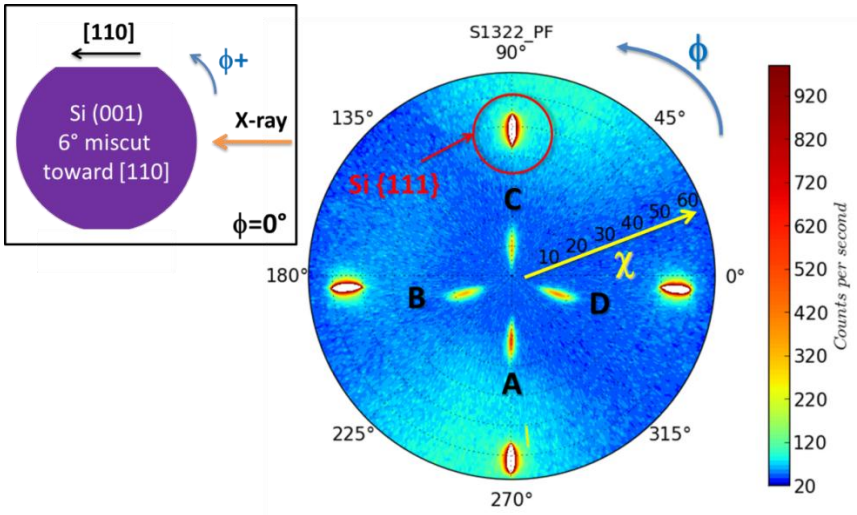

Figure 3-4: Pole figure measured on a GaP/Si sample (6° off Si substrate). The 4 larger and brighter peaks at χ≈55° correspond to GaP {111} reflections (which are overlapped by Si {111} reflections because of their vicinity and wide opening detector), the 4 weaker peaks at χ≈16° correspond to MT reflections. The four MT variants are named by ABCD convention as indicated on the figure. Intensity in counts per second is represented in log scale. Inset depicts sample alignment at initial position corresponding to ϕ=0° and the positive direction movement of ϕ motor is also indicated.

The characterization of micro-twin using pole figure performed on classical XRD lab setup is very interesting as it allows a fast and non-destructive characterization of GaP/Si sample without using TEM or synchrotron. Detailed study of microtwins limitation in the GaP/Si system will be reported the following.

3.1.2 Anti-phase domains

(a) APD description

As described in chapter 1, one of the main challenge in developing a Ga(As)PN/Si tandem solar cell is to obtain a GaP/Si platform with a low defects density at the interface, which implies not only to lower the MTs density but also to reduce the density of antiphase domains (APDs).[122,123,241–245] The APDs are characteristic of the growth of a polar material on a non-polar one. Figure 3-5 shows how the antiphase defects form and may annihilate, following Lin *et al.*[122] Antiphase boundaries (APBs) may occur if there is sublattice occupation disorder at the interface where adjacent regions are initiated with either Ga-Si or P-Si bonds. The APB defects may also occur in the absence of sublattice occupation disorder due to the single atomic steps at the Si surface. The condition to avoid, or lower, the APD formation is to obtain an uniform

monolayer of either Ga or P nucleated on the Si surface and a Si surface consisting of double atomic steps. This scenario can be achieved through proper Si surface preparation and appropriate nucleation conditions for the initial deposition of GaP on Si. Any remaining Antiphase boundaries must then be annihilated in order to achieve high-quality GaP films, by appropriate growth conditions. Indeed APBs act as recombination centers, cause strain fields in the crystal, and can lead to lower optical properties.[246–248]

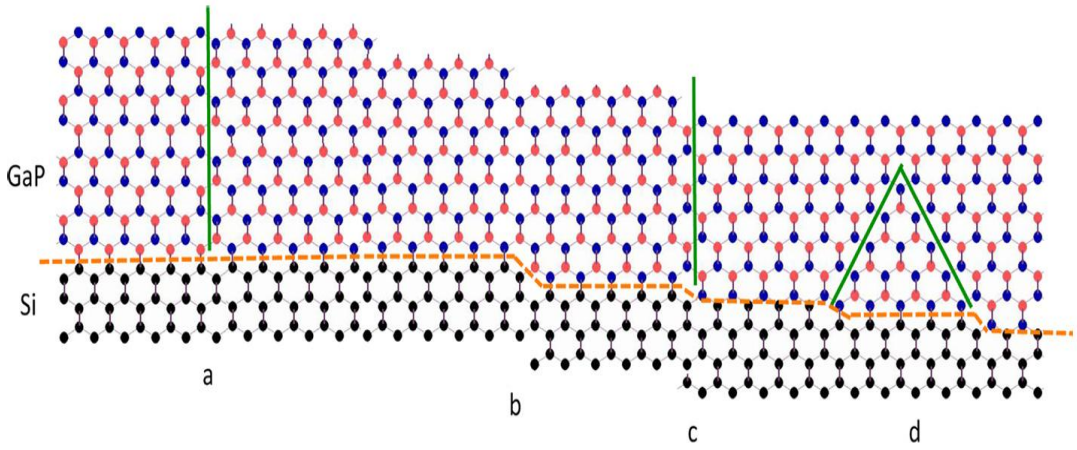

Figure 3-5: A schematic of the (110) cross-section of GaP on Si showing how APBs may form and propagate through the GaP film. (a) Sublattice occupation disorder at the GaP/Si interface produces an APB, where Ga and P atoms in the region to the left of the APB are different sublattices from the region to the right of the APB. (b) Defect-free GaP on Si is achievable only when there is an energetic preference to produce a uniform monolayer of either all Ga or all P atoms on the Si surface and any steps on the Si surface are a multiple of two atomic steps (or no steps). (c) An APB can still form when there is no site occupation disorder at the interface but when there is a single atomic step on the Si surface. This particular APB is propagating along the (011) plane. (d) APBs can propagate along other planes such as (111). In this scenario, it is possible for two adjacent APBs to self-annihilate.[122]

APBs cannot be created or destroyed with post-growth treatment such as RTA. Thus, APBs must either be prevented at the first stages of the growth.[122] The next section describes some approaches or considerations that need to be taken into account to minimize antiphase defects in polar-on-nonpolar films.

(b) APD detection

There are several methods that can be used for the detection of APBs and domains and for assessing their distribution in a film.[249] Anisotropic etching of the surface may yield information on APDs bounded by{111}B planes, if the APDs are large enough. However, these method cannot detect small APDs and are destructive. In X-ray scattering, one can exploit the intensity of weak reflection such as the (002) and (006) in

the case of a zinc-blende crystal to derive information on the APDs. Indeed, the weak Bragg reflections are sensitive to the APDs while the strong reflections such as the (004) are not sensitive to the APDs. Using a Williamson-Hall like method one can extract information on the APD lateral size.[241] However XRD gives statistical information on APDs. To obtain a local information on these defects, we have used TEM and STM measurements which are a spatially-resolved analysis method, complementary to the XRD.[241] Transmission electron microscopy (TEM) images have been obtained using dark field (DF) imaging, which allow obtaining reversed contrast from regions with different crystal polarities. Indeed, it has been shown from dynamical beam intensity calculations, that the (11-1) and (-11-1) image pair in <110> projections allows to image small (<10nm) antiphase regions and determine their geometry, using a low sample tilt to adjust proper excitation conditions.[250] TEM measurements have been done in collaboration with A. Ponchet and J. Stodolna at the CEMES group in Toulouse. The micrographs have been recorded using a Philips CM20 FEG TEM/STEM apparatus in high resolution and conventional modes, with an acceleration voltage of 200 kV. The zone axis [1-10] has been selected for imaging. Thin plates have been prepared by mechanical polishing and ion thinning.

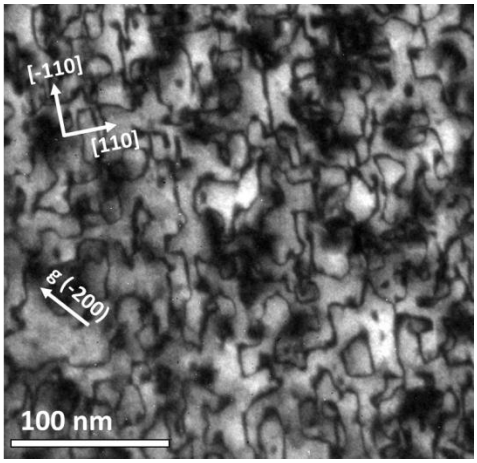

Figure 3-6: Plan view TEM micrograph selecting the (-200) reflection (sample: 20 nm GaP/Si, MEE 350°C). In this view mode, the dark lines indicate anti-phase boundaries. Anisotropy of the boundaries can be observed on this image.

Figure 3-6 shows a TEM micrograph in plan-view mode, with the projection closed to the [001] direction. In dark field imaging mode, the dark lines visible on this image indicate the APBs. Crystallographic directions are also indicated in the figure. As one

can observe in this figure, a preferential orientation of these dark lines can be noticed along [110] and [-110] directions. We can also notice shorter APB distances along [110] than along [-110].

3.2 Work on nucleation and regrowth parameter

As explained in chapter 1, the defect density lowering at the GaP/Si interface implies a two-step growth with a low temperature migration enhanced epitaxy (MEE) growth step prior to a conventional MBE growth step at higher temperature. This study focuses on the GaP nucleation layer, and then on the MBE regrowth sequence optimization.

3.2.1 GaP nucleation layer

As suggested by Grassman *et al* a careful study of the MEE growth sequence is required.[121] The MEE growth technique consists of alternative substrate exposure of Ga and P. The MEE step is performed at low temperature around 350°C. The growth have been performed on carefully prepared Si substrate using a recipe developed at FOTON in the frame Thanh Tra Nguyen thesis , and heated to 800°C during 10 minutes before GaP growth.[251] The total Ga coverage per MEE cycle has been carefully adjusted because it is found to strongly affect the epilayer's smoothness and defects density.[121] Ga cell temperature is calibrated to a growth rate of 0.1 ML/s, and a ML of Ga is first sent to the sample. After a growth interruption, the surface is exposed to phosphorus overpressure and the cycle is repeated up to obtain a 20 ML thin GaP film (which corresponds to 5 nm). In order to optimize the growth sequence I have proposed to performe AFM measurements to find the optimal Ga coverage per MEE cycle to promote a 2D growth. Thus I have searched for the growth conditions that minimize samples roughness. Figure 3-7 shows AFM images of 20 ML thin GaP/Si samples with different amount of Ga coverage per MEE cycle. The minimum of surface roughness is assumed to correspond to the expected 1 complete Ga atomic layer coverage.

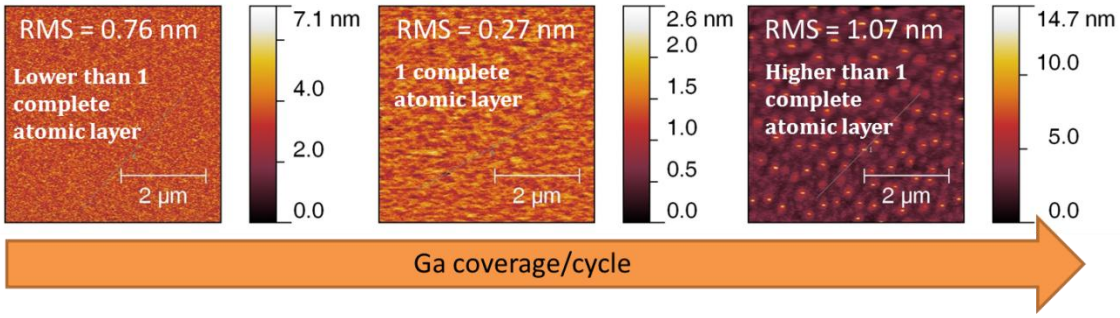

Figure 3-7: AFM images of 20 ML thin GaP/Si samples with different amount of Ga per MEE cycle.

The optimal Ga coverage have then been used to grow 40 ML of GaP by MEE and this provides a similar result as compared to the 20 ML-thick samples, with a RMS roughness as low as 0.3 nm, which can be considered as atomically flat. This very low roughness is compatible with the subsequent growth of smooth MBE-grown GaP layers and heterostructures for the top cell development. Moreover, an XRD pole figure, developed at FOTON in the frame Thanh Tra Nguyen thesis, performed on this sample reveals very low MT density, as presented in Figure 3-8. The fractional volume density estimated from this pole figure measurement is 1.04 %.

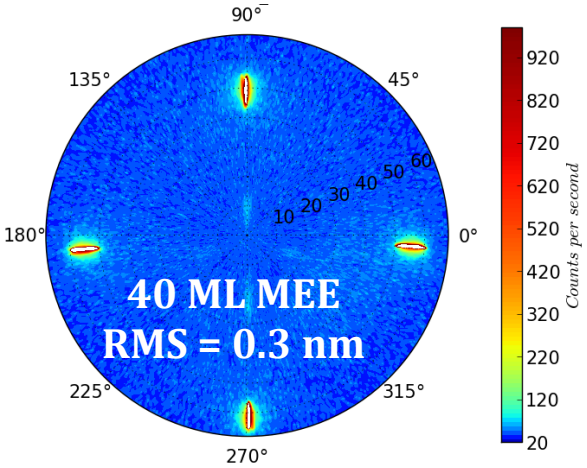

Figure 3-8: Pole figure measurement on 40 ML MEE GaP/Si using the optimal MEE procedure. Microtwins fractional volume density is evaluated to 1.04 %.

Using this optimized recipe for the GaP nucleation layer growth, we have then work on the regrowth sequence that allow a more conventional MBE growth needed for a subsequent GaAsPN growth. This growth mode allows a higher growth rate that will help to grow the p-i-n solar cell.

3.2.2 Second growth step: GaP regrowth by MBE

The optimized 40 ML (10 nm-thick) MEE GaP nucleation layer is then followed by a MBE growth of a 35 nm GaP thin film, leading to an overall 45 nm-thick GaP layer (well below the critical thickness). The influences of both the growth temperature and the V/III BEP ratio have been studied, leading to the conclusion that the surface roughness depends strongly on the III-V growth conditions. After optimization of the growth conditions, we have obtained a GaP/Si platform, with a typical RMS roughness as low as 0.3 nm. In this optimized recipe the regrowth temperature is 500°C and the V/III BEP ratio is near unity. Figure 3-9 shows the AFM image measured on this sample. Moreover, in order to study the structural defects, pole figure measurement has been performed on the same sample. As presented in Figure 3-9, the residual MT level is significantly reduced, and even not detectable with a lab XRD setup

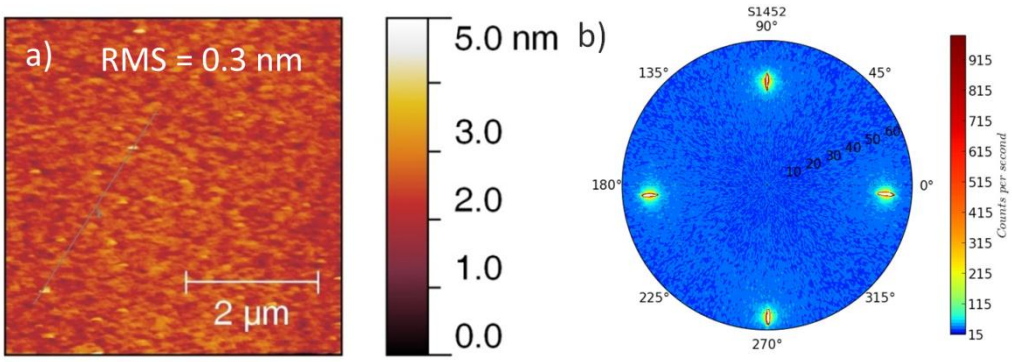

Figure 3-9: (a) 5x5 µm² AFM image performed on the optimal sample shows flat surface with a RMS roughness of 0.3 nm; (b) Pole figure measurement on this sample shows no MT.

However, as evidenced by Figure 3-10 (a) and (b), TEM and scanning tunneling microscopy ballistic electron emission microscopy (STM-BEEM) studies performed in collaboration with CEMES and IPR (Institut de Physique de Rennes) have shown the presence of APD in our optimized GaP/Si platforms grown with the optimized two-step growth sequence and with the MEE step only. The TEM micrograph shows that APB are formed at the early stage of the GaP growth during the nucleation process, at the GaP/Si interface.

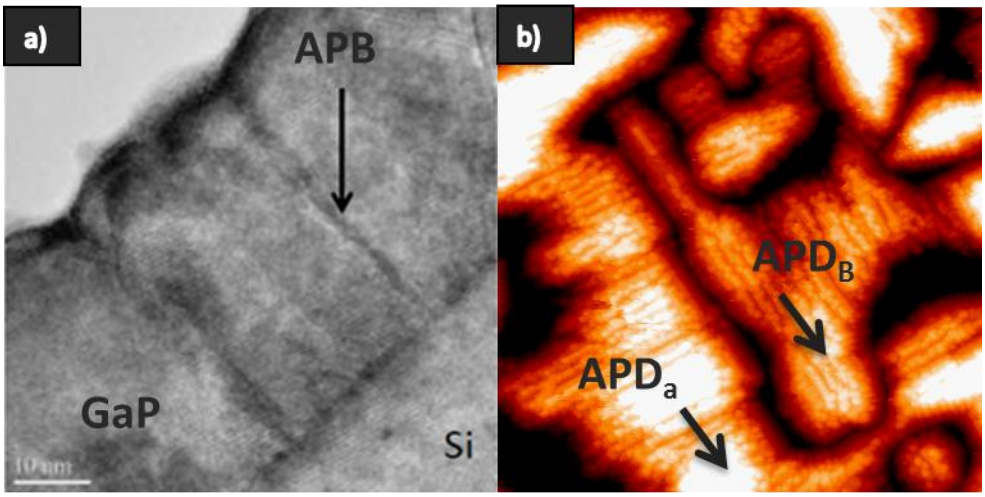

Figure 3-10: (a) cross-sectional TEM micrograph of 45 nm GaP layer grown on Si using an optimized MEE/MBE recipe and (b) plan-view STM image of 10 nm GaP layer grown on Si using an optimized MEE recipe evidencing the presence of APD.

The STM image shows that the sample roughness originates from the creation of APBs, as already reported by Jussila et al.[124] Thus in order to grow a high quality "defect-free" GaP/Si platform, further improvement of the growth procedure still needs to be performed. We have then studied the influence of a pre-nucleation layer at the very beginning of the nucleation process.

3.3 Al influence on APDs annihilation

A recent study, initially designed to study the influence of the growth temperature on the structural defects generation has given us important information to improve the GaP/Si platform quality. In this study, the 40 ML MEE GaP nucleation layer optimal growth is followed by 4 MBE 35 nm-thick GaP layers each grown at different temperature. The GaP layers are separated from one to each other by separated 2 nm-thick AlGaP markers. The sample has been purposely growth for a TEM study in cross section, as shown in Figure 3-11. One can observed that a strong APD annihilation occurs after the first AlGaP marker, at only 10 nm of the interface.

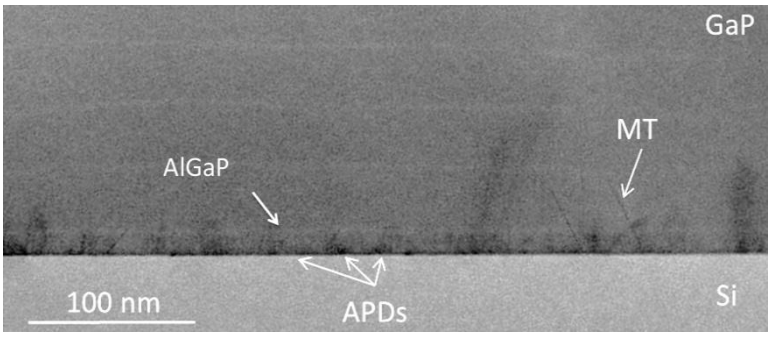

Figure 3-11: TEM micrograph showing the eraly APD annihilation on the first AlGaP marker located at 10 nm of the interface.

The influence of the AlGaP layer on the APD annihilation was already observed in the A.C.Lin thesis at Stanford University.[122,252] In this work, it was proposed to attribute such behavior to the different surfaces mobilities of Al and Ga atoms, which favors the anisotropic migration of atoms, and allows the main phase atoms to bury the antiphase atoms, and form a single phase surrounding layer. Starting with an AlGaP nucleation layer on Si would also provide number of advantages.

First, Al atoms have a lower mobility than Ga atoms on the Si surface due to the stronger Al-Si bonding than the Ga-Si one, with binding energies of 3.6 eV and 2.9 eV, respectively.[253,254] This compensates the tendency of the Ga atoms to cluster and form a non-uniform layer of GaP on Si.

Second, the solid solubility of Ga in Si is 4 orders of magnitude larger than the Al in Si one. At 500◦C, the maximum concentrations are 0.3% for Ga atoms and 0.0002 % for Al atoms in Si. At 700◦C, the concentrations are 2 % for Ga atoms and 0.0012 % for Al atoms in Si.[255,256] The low solid solubility of Al in Si indicates that an Al-Si phase is much less likely to form compared to Ga-Si. Considering the growth of III-V on Si, it is preferable that the group III atoms react with phosphorus rather than the Si substrate. Therefore, abrupt interface between the III-V film and Si will be obtained when some of the Ga is replaced by Al (in $Al_{0.5}Ga_{0.5}P$) as compared to the growth of pure GaP where any Ga-Si interaction would make the interface less abrupt.

Finally, Al is highly reactive and getters residual oxygen on the Si surface that would otherwise prevent epitaxial nucleation of III-V on Si in the presence of an oxide. The impurity trapping of carbon and oxygen in AlGaAs/GaAs superlattices has been shown to smoothen surfaces.[257] Different solid solubilities of impurities in AlGaP and the gettering effect of Al may allow impurities (carbon, oxygen) to ride on the surface

and not get incorporated into the nucleated interface where it can cause defects at the interface. Thus we are now studying the influence of AlGaP prenucleation layer it should increase the quality of the GaP/Si platform and get even an APDs-free GaP/Si platform.

3.4 Summary

In summary, a MT defect-free GaP/Si platform, displaying a smooth surface, has been obtained through an optimized two-step growth procedure, which begins with a low temperature MEE growth of a 10 nm-thin GaP layer followed by a 35 nm-thick MBE grown GaP layer, at higher temperature. The growth conditions optimization implied the study of the influence of the Ga coverage, the III-V ratio and the growth temperature. Indeed, we have developed a GaP/Si platform growth recipe by achieving flat surface and very low MT density. It was shown that using AlGaP epilayers promote the annihilation of APDs at early stage of the growth. Finally, the use of an AlGaP prenucleation layer will be tried in a forthcoming study to grow APD-free GaP/Si interfaces.

CHAPTER 4. STUDY OF THE GAASPN ABSORBER

Nitrogen induced defect are detrimental for both the electronic and optical properties of the devices and, therefore, have to be avoided or eliminated. In the present chapter, I describe the main growth parameters influencing the nitrogen incorporation in the GaPN-based alloys and present the overall PL properties of our dilute nitrides. A model of low temperature PL is presented. Using tight-binding calculations developed at FOTON, XRD and PL measurements, a method is proposed to determine the composition of the GaAsPN quaternary alloy.[184,258] *Then, I present results on the Ga(As)PN growth and annealing optimization using structural and optical characterizations. Finally I discuss the similarities between GaAsPN and InGaAsN materials systems. I have myself participated to the dilute nitride growth through recipe elaboration and performed the annealing optimization. For this, I have performed XRD, AFM and PL measurements on the Ga(As)PN layers grown on GaP(001) substrates. This work has been done in close collaboration with Olivier Durand, Charles Cornet, Christophe Levallois, Jacky Even, Jean-Marc Jancu, Mathieu Perrin, Jitesh Kuyyalil, Tony Rohel, Thanh Tra Nguyen and Cedric Robert.*

4.1 N content control in GaPN

One has to keep in mind that for PV application the N content in the Ga(As)PN layer should be above 2%, depending on the As content, in order to ensure the lattice-matching condition with the substrate (the perfect lattice matching is obtained with a 2% nitrogen content in the GaPN case). Moreover, reaching a bandgap energy down to 1.8 eV (the GaP compound has an indirect bandgap of 2.26 eV at 300 K) implies to add enough As atoms in the GaPN lattice, while increasing the nitrogen content to keep the lattice matching conditions. Indeed, a 1.8 eV top junction absorber is required to fulfill the current matching condition with the Si bottom cell. In a first step, we have studied the structural properties, to find the optimal growth and annealing conditions of this ternary compound, prior to the GaAsPN quaternary compound study. First, the influence of MBE growth conditions on the nitrogen incorporation has to be clarified. For instance, Harris et al. state that the sticking coefficient of N is nearly one during GaAsN growth, while Harmand et al. measured a modification of the N incorporation with group V partial pressure which suggests that N is in competition with the other

group V elements.[69,80] Therefore, in order to clarify the growth parameters influence on the N incorporation in GaPN, we have evaluated the N incorporation for different V/III (Beam Equivalent Pressure) BEP ratio, growth rate and temperature.

4.1.1 Effect of temperature and V/III BEP ratio

Figure 4-1, displays the N content in a 100-nm nominally thick GaPN layer grown on GaP (001) as measured by the GaPN(004) Bragg peak position in θ/2θ XRD experiments. One has to remind that the N amount measured in this case corresponds to the substitutional N. The N content is plotted for different V/III BEP ratio at different substrate temperatures. The plasma cell parameters are kept constant (400 W, 0.5 sccm, 100% valve opening) according to the optimized values found by Thanh Tra Nguyen during his PhD.[205,251] The growth rate and the Ga BEP have been fixed respectively at 0.2 ML/s and $2.7\pm1\times10^{-7}$ Torr.

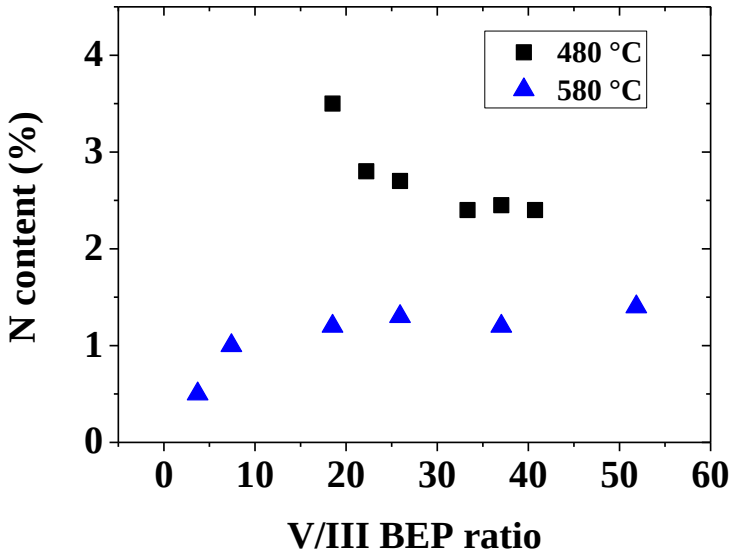

Figure 4-1: Evolution of the N incorporation as a function of V/III BEP ratio in GaPN compounds for different growth temperatures: 480°C (black squares), and 580°C (blue triangles).

These results clearly indicate that temperature and phosphorus BEP play a decisive role in the N incorporation. It can be seen from the figure that for a same P flux, the N content decreases with increasing temperature. This can be explained as follows: at low temperature, the desorption of N_2 is limited since the mobility of nitrogen adatoms is

reduced. The incorporation of nitrogen is thus enhanced at low temperature allowing N incorporation over 2% which is suitable for PV applications. At higher temperature, the N content decreases due to increased N_2 desorption, while the mobility of adatoms increases. This is a classical behavior of diluted nitrides alloys and widely reported in the literature.[259,260] Moreover, as shown in Figure 4-1, the 480°C black curve clearly shows that there is a prominent effect of the phosphorus BEP on the nitrogen incorporation in GaPN. At a V/III BEP ratio of ≈ 20 and 480°C, the nitrogen composition is approximately ≈ 3.5 %. One has to mention that samples grown at lower V/III BEP ratio, and at this growth rate, are relaxed which leads to a small variation of their N composition.[205] At 480°C, and above V/III BEP ratio of 20, the N incorporation decreases monotonically with respect to the V/III BEP ratio and reaches a steady value of about ≈ 2.3%, interpreted as a consequence of the good P_2 coverage of the surface, limiting the N adatoms mobility.

At a higher substrate temperature of 580°C, a random statistical distribution of N incorporation is observed for low phosphorus BEP with low nitrogen content characteristic of the uncontrollability and un-predictability of the N incorporation in GaPN at high temperature. This is likely due to monoatomic and diatomic nitrogen desorption. At higher V/III BEP ratio, the nitrogen content seems to be constant around 1.3%, also due to the good P_2 coverage of the surface, limiting the N adatoms mobility. This value is however too low to reach the lattice-matching condition to the silicon, for a 1.8 eV GaAsPN compound.

4.1.2 Influence of the growth rate

Then, in order to control the nitrogen content more accurately, the growth rate influence on the nitrogen incorporation has been studied. Figure 4-2 displays two typical ω/2θ XRD diagrams for two 100-nm nominally thick GaPN samples grown at 0.2 and 0.5 ML/s respectively, while keeping the other growth parameters constant (phosphorus BEP = 7 10^{-6} torr, 480°C):

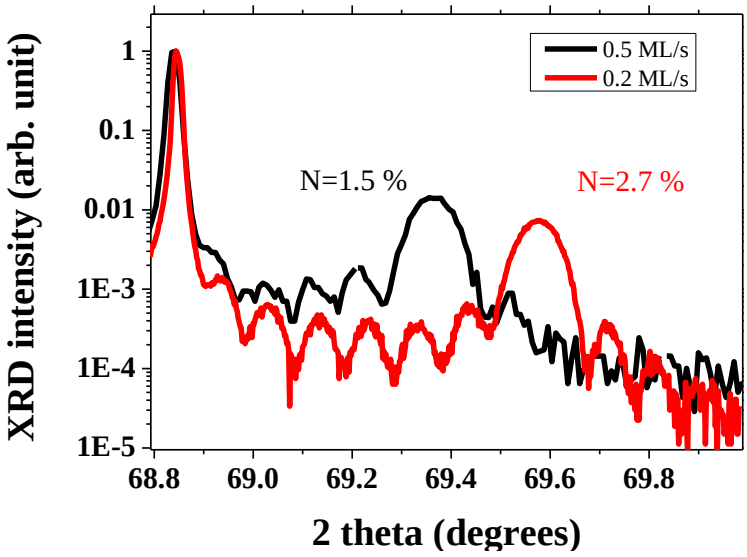

Figure 4-2: ω/2θ XRD diagrams of two GaPN samples grown at 0.2 (red line) and 0.5 (black line) ML/s revealing different N incorporation.

It can be clearly seen from the figure that, at the temperatures studied, the N content decreases with the growth rate. This is a classical behavior observed in III-N-V alloys, such as GaAsN.[69] This results shows that a control of the N incorporation can be made through the growth rate, all the other growth parameters being fixed, as already shown in the InGaAsN(Sb) system.[80,81] This gives to the GaPN dilute nitride alloy a major advantage in terms of yield and reproducibility as compared to any equivalent III–V compound containing several column V elements, such as GaAsP or GaInP for instance.[82] Finally, the actual thickness of the GaPN layers has been inferred using the thickness fringes positions in the XRD diagrams, through n versus fringes position in the diffraction vector space, n being the order of the thickness fringe. Using this method the thickness of both layer has been calculated to be (105 ± 5) nm.

4.1.3 GaPN relaxation with N content

Figure 4-3 shows XRD profiles from five GaPN samples with various nitrogen content values, in substitutional positions, as estimated by the GaPN (004) Bragg peak positions.

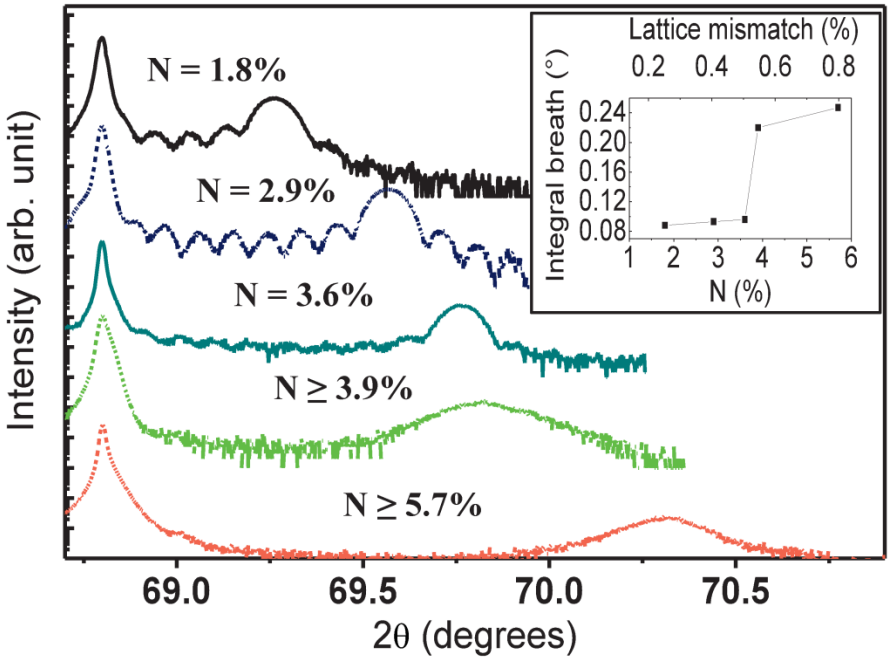

Figure 4-3: XRD ω/2θ scans of 100 nm-thick GaPN samples with different nitrogen content, around the (004) Bragg peak. The peaks in the left corresponds to the GaP(004) Bragg diffraction from the substrate. Inset gives the integrated width as a function of N content and lattice mismatch.

In the following, the samples are composed of 100-nm thick GaPN layers on GaP(001) substrates. Again, the thicknesses have been experimentally verified through the thickness fringes spacing (in the first 3 XRD profiles which display thickness fringes), and found equal to 105 ±5 nm in the first 3 samples. Profiles corresponding to samples with nitrogen content under 3.6 % show well-defined thickness fringes (with a very good contrast), characteristic of a high degree of lattice plane correlation along the growth direction, from one interface to the other one, i.e through the whole layer thickness. This indicates a well-defined thickness with low surface and interface roughnesses. For the GaPN sample with a 3.6% nitrogen content, even if the fringes contrast is lower, the well-defined set of thickness fringes in the ω/2θ scans still demonstrates a good GaPN layer structural quality. The slight lowering of fringes contrast in this scan may be an indication of a weak plastic relaxation process. The evolution of the GaPN(004) Bragg peak integral breadth has also been plotted since it can been relied to the diffraction planes correlation length, also called crystallite size (through the Scherrer law, for instance).[261] If the diffraction planes are correlated from

one interface to the other one, then this correlation length should give the sample thickness. Otherwise, some relaxation effects may lower this correlation length by introducing some structural disorder, likely at the layer-substrate interface. The evolution of the integral breadth (IB) of the GaPN peak, as a function of N content and of the calculated lattice mismatch (from the Bragg peak position) is given in Fig 3 inset. The IB increases from 0.096° to 0.22° in the [3.6 - 3.9 %] nitrogen composition range. This increase may be due to variation of both thickness and lattice parameter. Considering that the layer thicknesses do not vary from one sample to the other one (as verified from the 3 first samples), this suggest that a structural disorder has taken place, lowering the diffraction planes correlation length, suggesting a relaxation process. Therefore, we have concluded that a relaxation process starts to occur when the lattice mismatch is over a value in the [0.51 - 0.55%] range for a 100 nm thick GaPN layer. According to our calculations performed using the relationship provided by Matthews and Blakeslee (p31), the relaxation process should occur when the lattice mismatch is above 0.36% in a 100 nm thick layer. This confirms that the Matthews and Blakeslee model underestimates the value of the critical thickness (CT).

4.1.4 Summary

To grow GaPN layers with controlled N content over 2% (necessary for PV application) the growth should be made at low temperature (<480°C) with high V/III BEP ratio. For instance, a nitrogen incorporation around 3.5 % has been reached with a V/III BEP ratio of 20. Moreover, a steady-state value of nitrogen content (2.5% at a 480°C growth temperature) has been obtained at higher V/III BEP ratio, which will allow highly reproducible growth of GaPN layers.

Our results also pointed out the importance of the kinetics mechanism in the N incorporation. Indeed, from the thermodynamic point of view, the GaN bond is stronger than the bond strength of GaP, the incorporation of nitrogen should thus be increased at higher temperature, which is not the case.[170,262,263] Moreover, while the solubility limit of nitrogen in GaP at thermodynamic equilibrium is only 10^{16} atoms/cm^3 at 900K, the results obtained here clearly exceed this value. Indeed, 2% of nitrogen in GaP is equivalent to $5x10^{20}$ atoms/cm^3.[170] Therefore, the thermodynamic equilibrium of solid-

vapor cannot describe the nitrogen incorporation in this case. A possible solution can be reached into the use of kinetics models, as proposed by P. Kratzer and coworkers for homoepitaxial GaAs.[264]

Finally, results on 100 nm GaPN layers grown on GaP(001) substrates confirm the hardening effect (resistance to dislocation formation) of nitrogen as confirmed by GaPN layers grown well above their critical thickness.

4.2 Dilute nitride optical optimization

As explained in chapter 2, PL has been widely used to study the strong effect of the nitrogen incorporation on the III-V optical properties and due to the relationship between electrical and optical properties in dilute nitride materials.[95]

4.2.1 General properties of GaPN photoluminescence

The nitrogen main effect on optical properties of III-V alloys, in a diluted regime, arises from a strong bandgap bowing. Its origin is widely debated.[29,30,189,265–267] This effect is huge in the case of the GaPN alloys and the incorporation of nitrogen in GaP also turn its bandgap from an indirect to a pseudo-direct one, which strongly enhance the optical properties of this compound, as revealed by its PL intensity improvement. One has to pay attention that the N effect on optical properties (enhanced PL intensity) can be counterbalanced by the formation of non-radiative defects (N_i interstitials, Ga_v vacancies, Ga_i interstitials, and P_{Ga} antisites) which reduce the PL intensity, in non-optimized dilute-nitride compounds.[268–270] The influence of these non-radiative defects can be studied by measuring the PL quenching with temperature, from 10 to 300K ($I_{10K/300K}$). Indeed $I_{10K/300K}$ has been related to the non-radiative (NR) trap density in the dilute nitride alloys, using Monte-Carlo simulations.[268] Rubel et al. have shown that at temperatures above 150 K, the PL quenching approaches its asymptotic value $I_{10K/300K} = [1+N_{nr}\nu_0\tau_0/(N_{nr}+N_t)]^{-1}$ where τ_0 is the exciton lifetime, ν_0 is the attempt-to-escape frequency, N_{nr} and N_t the non-radiative center and trap concentration respectively.

Another important feature in dilute nitride materials is the carrier localization due to N incorporation, leading to localized electronic levels inside the bandgap. This effect can be evidenced through temperature dependant PL measurements (see Figure 4-4 and

Figure 4-5), by the so-called "S-shape" variation of their energy bandgap with temperature and by their low energy exponential bandtail at low temperature.[271–275] This particular behavior can be separated into three ranges. At very low temperatures the peak energy slowly decreases due to the excitons of higher energy localized states being gradually redistributed into low energy localized states. As the temperature increases, the peak energy increases rapidly in the second range, as the excitons gain more thermal energy and start to be activated into delocalized states. In the third range, excitons are completely delocalized and the PL peak energy decreases as expected from band gap shrinkage with temperature.[276] The S-shape behavior has been successfully explained and simulated by thermal activated hopping processes assuming an exponential density of localized states originating from nitrogen aggregates that create cluster state (CS).[277,278] The influence of CS can be studied by measuring the energy scale of short range fluctuations/disorder E_{short} and the Stokes shift. Figure 4-4 displays the variation of the PL peak energy (taken at its maximum in intensity) of a 100 nm $GaPN_{0.02}$ layer grown on a GaP substrate (green dots). For comparison, the red dots show a typical bandgap variation of a 2.1 eV energy bandgap III-V alloy following the well-known Varshni law. E_{short} has been determined by measuring the temperature T_{short} for which the PL emission energy begins to increase and using the following formula: [269]

$$\frac{T_{short}k_B}{0.775} \approx E_{short}$$

The theoretical Stokes shift can also be estimated from this figure using the PL peak emission energy difference between an alloy following a Varshni law and the dilute nitride. Here at 20 K the Stokes shift is approximately 100 meV.

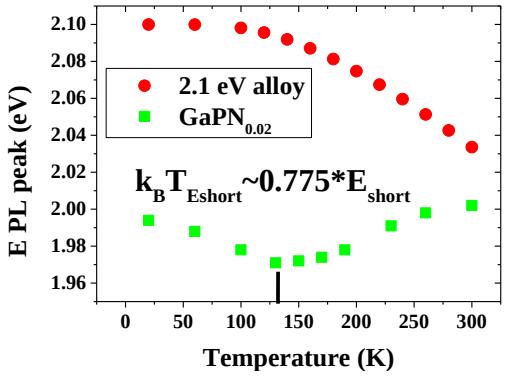

Figure 4-4: Variation of the PL peak energy from a typical 100 nm $GaPN_{0.02}$ layer grown on GaP.

The low energy bandtail is related to the energy difference between the perturbed host states (PHS) created and the lowest cluster states. It can be studied by measuring the energy scale of long range fluctuations/disorder E_{long}. E_{long} is usually determined by roughly extracting the slope of the PL spectrum exponential bandtail at low energy, measured at low temperature. In order to accurately extract the energy scale of the compositional fluctuation at long range, I've proposed to develop a PL model following the approach proposed by Bosa et al.[279]

4.2.2 Photoluminescence model at low temperature

The emission model that we have developed to extract E_{long} is based on the approach proposed by Bosa et al.[279] In this model all the localized nitrogen states have the same special extent (corresponding to the exciton size) and dipolar moment. The only difference is their energy. The energy of the cluster I is modeled by a random value (r.v.) Xi where all the r.v. are considered independent and identically distributed (i.e.d.) in energy, following the probability law $p_x(E)$. Clusters are then grouped in region of size N which corresponds to a capture surface where carriers relax in the lowest energy cluster. If j index the capture surface, the carrier emission energy in the surface j will be

$$Y_j = min(X_j, X_{j+1}, \dots, X_{j+N-1}).$$

All the emission energy Y0, Y1 etc… are also r.v. and considered as i.e.d., thus they all follow the same probability law $p_Y(E)$. Therefore, using the derived partition function $Z_Y(E)$, one can find:

$$Z_Y(E) = P[Y \leq E] = \int_{-\infty}^{E} p_Y(E')dE'$$

The event Y≤E is wrong only if every Xi > E. Thus

$$Z_Y(E) = 1 - P[(X_1, \dots, X_N) \in]E, +\infty[^N]$$

$$Z_Y(E) = 1 - (P[X_1 \in]E, +\infty[])^N$$

$$Z_Y(E) = 1 - (1 - Z_X(E))^N$$

Thus

$$p_Y(E) = N p_X(E)(1 - Z_X(E))^{N-1}$$

In this model the PL spectra has the same shape than the p_Y function. Compared to the model developed by Bosa et al. which take a Gaussian law for the probability $p_X(E)$ our model uses an exponential law such that :

$$p_X(E) = \begin{cases} \dfrac{e^{\frac{E-E_0}{E_{long}}}}{E_{long}} \; if \; E \leq E_0 \\ 0 \; if \; E > E_0 \end{cases}$$

Where E_{long} is the mean value of the energy difference between the perturbed host state (E_0) and the clusters states.

Thus for $E \leq E_0$

$$Z_X(E) = e^{\frac{E-E_0}{E_{long}}}$$

$$p_Y(E) = N \frac{e^{\frac{E-E_0}{E_{long}}}}{E_{long}} [1 - e^{(\frac{E-E_0}{E_{long}})}]^{N-1}$$

And $P_Y(E) = 0$ when $E > E_0$. This function has its maximum for $E_{max}=E_0-E_{long}.\ln N$, thus we can use the following equivalent formula:

$$p_Y(E) = \frac{e^{\frac{E-E_{max}}{E_{long}}}}{E_{long}} [1 - \frac{1}{N} e^{(\frac{E-E_{max}}{E_{long}})}]^{N-1}$$

For N value over 100 (which is the case in common PL experiment also called macro-PL) this last expression does not depend anymore on the N parameter and become, for large N values:

$$p_Y(E) = \frac{e^{\frac{E-E_{max}}{E_{long}}}}{E_{long}} e^{-e^{\left(\frac{E-E_{max}}{E_{long}}\right)}}$$

In practice to fit experimental PL spectra we have use the following expression.

$$I_T(E) = I_{noise} + I_T \frac{exp^{\frac{E-E_{max}}{E_{long}}}}{E_{long}} exp^{-exp^{\left(\frac{E-E_{max}}{E_{long}}\right)}}$$

Where I_{noise} is the intensity of the noise during PL measurements and I_T is the PL integrated intensity at the temperature T.

Figure 4-5 displays an experimental PL spectrum at 15K of a GaPN layer, with a fit using the present model and compared with the model developed by Bosa et al.

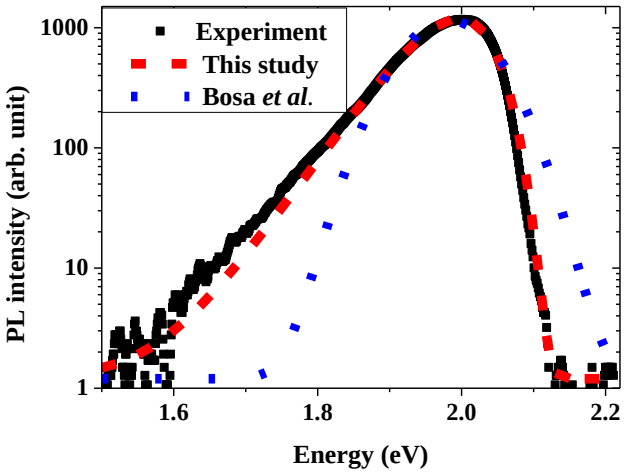

Figure 4-5: Experimental PL spectra at 15K of a $GaPN_{0.02}$ layer (black line), with a fit using the formula found with our model (red dash) and with the model developed by Bosa et al. (blue dot).

The good agreement between the experimental PL spectra and our model is believed to be due to the use of an exponential law Considering its low number of free parameters and the low parameter interdependency as compared to the model developed by Bosa et al. are advantages of the developed model to study the PL of dilute nitride layers. Up to now, twenty-five Ga(As)PN samples have been tested using this model. Adjusted Chi-square values over 0.990 have been found on all these samples, with an average of 0.996.

Considering the alloy fluctuations and NR traps density detrimental effect on the dilute nitrides PV optical properties, and in order to optimize the growth of the GaPN alloy, we have therefore search the growth and annealing conditions that minimize the following parameters: the Stokes-shift, the S-shape, E_{short}, E_{long}, $I_{10K/300K}$.

4.3 Study of GaPN growth

In order to get information of the growth parameters influence on the GaPN structural and optical properties, 100 nm GaPN layers have been grown on GaP(001) substrates with varying growth temperature and V/III BEP ratio.

4.3.1 Growth temperature influence at high V/III ratio

(a) Impact on structural properties

Figure 4-6 displays a XRD diagram from two 100 nm thick GaPN samples grown at two different growth temperatures (resp. 450°C and 480°C), and at a growth rate equal to 0.2 ML/s and a V/III BEP ratio equal to 21. These growth parameters have been carefully chosen since they are known to lead reproducible GaPN layers with N content around 2.5%, as shown in the previous part. Both XRD profiles reveal a small difference in the N incorporation. Assuming a Vegard's law and a fully coherent growth, the N content can be estimated as 2.7% for the sample grown at 480°C and 2.8% for the one grown at 450°C. The sample grown at 480°C shows well-defined thickness fringes. This indicates a well-defined thickness layer (i.e. low surface and interface roughness) but also a high degree of lattice plane correlation through the whole layer. This is consistent with a biaxially fully strained GaPN epilayer onto GaP (with low plastic relaxation). On the contrary thickness fringes are almost not visible for the sample grown at 450°C and the diffraction peak is larger meaning that the diffraction planes correlation length is lower. This clearly indicates a lower crystalline quality. Given the similar nitrogen composition measured in both samples, this lower crystalline quality should not be due to the lattice mismatch with the substrate. Indeed, we think that the lower crystalline quality is due to some N related defects enhanced by the low growth temperature. This is supported by the strong difference of surface roughness between both samples which can be seen on the AFM image presented in Figure 4-6 inset. Indeed, the sample grown at 450°C have a higher r.m.s. roughness (12.4 nm) compared to the one grown at 480°C (2.2 nm) due to a larger amount of hole at its surface. The nature of these holes at the samples surface hasn't been determined yet but we think that they might be related to N related defect.[259]

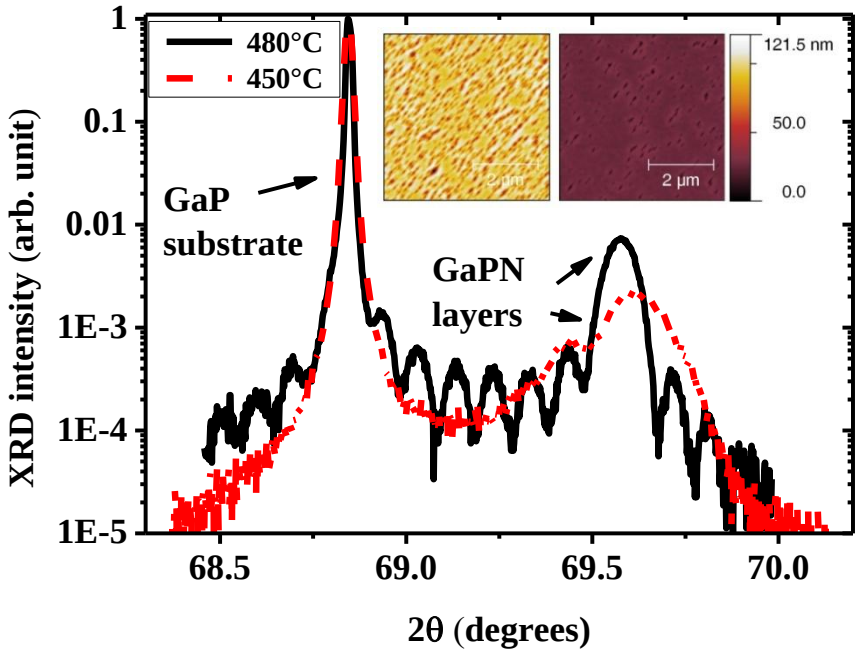

Figure 4-6: ω/2θ XRD diagram performed around the (004) Bragg reflection of 100 nm thick GaPN layers grown at 450°C (red dash) and 480°C (black line) on GaP(001) substrates. Inset: AFM images of the 100 nm thick GaPN layers grown at 450 (left) and 480°C (right).

No particular change has been noticed on the XRD diagram or surface morphology after annealing process, which implies that these structural defects, revealed through the XRD and AFM experiments, can't be healed with an annealing process. This might be due to a very high density of Ga_i defect which are known to be enhanced in dilute nitride material grown at low temperature and that cannot be healed.[280]

(b) Annealing effect on optical properties on GaPN layers grown with a high V/III ratio

As already described in part 2.1.2, an ex-situ annealing process is known to dramatically enhance the optical properties of the dilute-nitrides compounds, so that it is considered as a mandatory step to obtain optimal optical and PV properties.[69,90,95,96,181,206,207] This is confirmed in the case of the GaPN samples. Indeed, the PL of both samples is strongly affected by an annealing process, which implies that the atomic arrangement is modified by the annealing conditions. Both samples have a similar behavior upon annealing as one can see in Figure 4-7

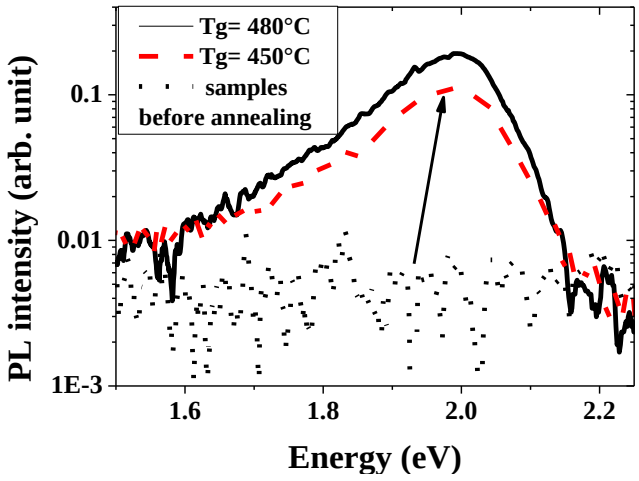

Figure 4-7: room temperature PL spectra of 100 nm thick GaPN layers grown at 450 (red dash) and 480°C (black line) on GaP substrate annealed at 800°C during 5 min and non-annealed (black dot).

Before annealing, the GaPN layers show no luminescence at 300K while after the annealing process (800°C during 5 min) they both exhibit room temperature PL. Moreover we have observed a strong reduction of the PL quenching (10 times lower) after the annealing process. This can be attributed to a decrease of Ga vacancies (Ga_v) N-As complex and P_{Ga} antisite during the RTA process.[281–283] A strong blueshift (80meV) of the PL peak energy has also been observed after annealing. This blueshift has been attributed to reduction of the N cluster density.

Figure 4-8 displays the room temperature PL peak intensity and integral breath of GaPN samples before annealing and after annealing at 800°C during 1, 5 and 10 min. All samples show a strong increase in their PL intensity and a significant reduction of their PL integral breath (IB). This indicates an improvement of the dilute nitrides optical properties. Nevertheless samples grown at 450°C has a much lower PL intensity (approximately a factor 50 after annealing at 800°C during 10 min) and a much larger IB than those grown at 480°C. This might be due to a higher Ga_i density in the sample grown at low temperature as expected by structural measurements.

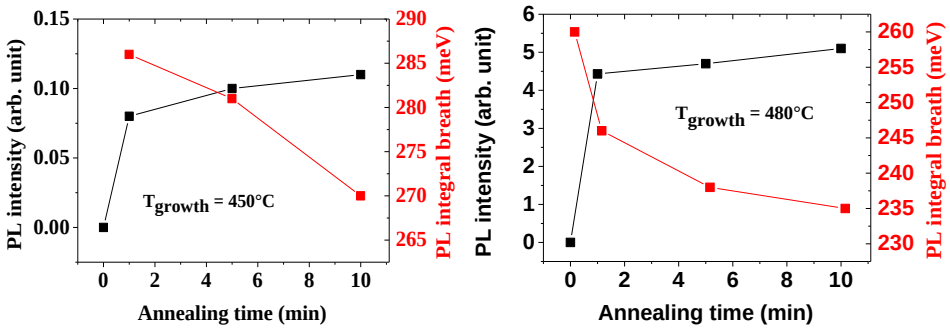

Figure 4-8: PL peak intensity and PL peak integral breath at room temperature from GaPN epilayers grown at 450°C (top) and 480°C (bottom) and annealed for 0, 1, 5, and 10 min at 800°C

This indicates that the annealing step might not be able to heal some of the defects generated at a low growth temperature as in the GaAsN case.[280]

(c) Growth temperature effect on optical properties of annealed GaPN layers grown with a high V/III ratio

In the following, all the results have been obtained after annealing at 800°C during 5 min as this recipe allow a fast and strong improvement (PL intensity increase, PL linewidth decrease) of the GaPN optical properties.

Tg (°C)	E_{long} (meV)	T_{short} (K)	E_{short} (meV)	$I_{10K/300K}$
450	49	190	21	5900
480	41	160	18	1500

Table 1: PL properties of 100 nm thick GaPN layers grown at 450 and 480°C on GaP(001) substrates and annealed at 800°C during 5 min

Temperature-dependent PL analyses reveal also different behaviors of these samples, as presented in Table 1. As already described in part 2.1.2, an ex-situ annealing process is known to dramatically enhance the optical properties of the dilute-nitrides compounds, so that it is considered as a mandatory step to obtain optimal optical and PV properties.[69,90,95,96,181,206,207] The sample grown at 450°C shows higher compositional fluctuation energy scale at long (+8 meV) and short range (+4 meV), and a PL quenching almost 4 times stronger than the sample grown at 480°C. These results show that the sample grown at 450°C has higher non radiative (NR) center density and alloy fluctuation than the sample grown at 480°C. One can notice that this trend is in agreement with the XRD and room temperature PL measurements, while no structural difference after and before the annealing step has been highlight with the XRD

experiments. This is certainly due to the fact that XRD is sensitive to long range crystalline order. Therefore, it is likely that the annealing step acts mainly on point defects, which are difficult to be detected by XRD.

From XRD, AFM and PL measurements, one would expect better optical and electrical properties for the samples grown at higher temperature considering their higher crystalline quality, lower PL quenching, and compositional fluctuation energy scales at short and long range. Nevertheless the presence of holes on the sample surface grown at 480°C surface indicate that defects still remain in this GaPN layer, which needs further structural optimization

4.3.2 V/III ratio influence on GaPN

(a) Influence on structural properties

In order to understand the V/III ratio influence on the GaPN layers optical properties, we have studied two GaPN layers with the same N content but with different V/III ratio. This can be done by reducing the V/III ratio through an increase of the growth speed and a decrease of the phosphorus flux.

Figure 4-9 displays a XRD diagram from two 100 nm GaPN layers grown on GaP (100) using the same growth parameter (T_{growth} = 480°C), with a V/III BEP ratio of 5 (growth rate = 0.8 ML/s ; phosphorus pressure = 5 µtorr) and 21 (growth rate = 0.2 ML/s ; phosphorus pressure = 7 µtorr), respectively. Both samples show well-defined thickness fringes, indicating a coherent growth along the overall 100 nm thickness. The XRD profiles reveal no strong difference in their N incorporation. Considering the Vegard's law and assuming a fully coherent growth, the N compositions are 2.4% and 2.7% in the samples grown respectively with V/III BEP ratio of 5 and 21.

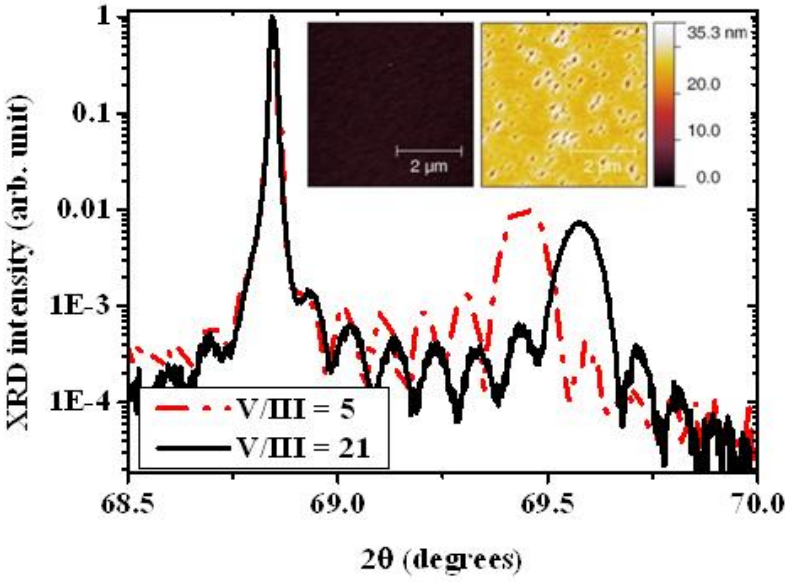

Figure 4-9: ω/2θ XRD diagram performed on the (004) reflection of 100 nm thick GaPN layers grown with V/III BEP ratio of 5 (red dash-dot) and 21 (black line) on GaP substrate, and AFM images of 100 nm thick GaPN layers grown with V/III BEP ratio of 5 (left) and 21 (right) on GaP substrate.

Nevertheless, as shown in the AFM image presented in the inset of Figure 4-9, the sample grown with a V/III BEP ratio equal to 21 has a higher roughness (2.2 nm) compared to the one grown with a V/III BEP ratio equal to 5 (0.4 nm) due to a larger amount of hole at its surface. This result proves that the presence of holes on the GaPN layers surfaces is not only related to the growth temperature but also to the V/III ratio. Thus the crystalline quality of sample grown at lower temperature (450°C) might be improved by a careful control of the V/III ratio. No particular change has been noticed on XRD diagram or surface morphology after annealing process.

(b) Annealing effect on optical properties of GaPN layers grown at low V/III ratio

Another interesting result is that the sample grown with a low V/III BEP ratio has a different behavior upon annealing than the one grown with a high V/III BEP ratio see Figure 4-10. Even if after annealing it also exhibits a reduction of E_{long} (- 40 meV) accompanied by a strong blue-shift of the PL peak emission (+ 230 meV), its behavior concerning its PL intensity variation is different. The PL intensity of the sample grown with a low V/III BEP ratio decrease after the annealing process contrary to samples grown at high V/III BEP ratio (Figure 4-7). Moreover, after annealing an increase of the

PL quenching (4 times higher from 87 to 350) has been observed on this sample. The blueshift has been attributed to reduction of the N cluster density. The increase of the PL quenching after annealing has been attributed to lower carrier localization. Indeed a lower carrier localization could allow more carriers to travel to the sample surface, increasing surface recombination that would reduce the PL intensity.[70]

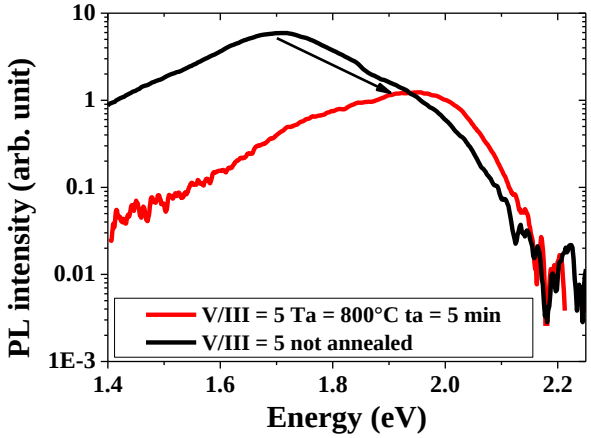

Figure 4-10: room temperature PL spectra of 100 nm thick GaPN layers grown on GaP with V/III BEP ratio of 5 and not annealed (red dash). Black line: same measurement after annealed at 800°C during 5 min.

(c) V/III ratio effect on optical properties of annealed GaPN layers

Huge differences due to the modification of the V/III ratio are also evidenced by the PL properties of the annealed samples presented in Table 2 The sample grown with a V/III BEP ratio equal to 5 shows higher compositional fluctuation energy scale at long (+11 meV) and short range (+5 meV). However its PL quenching is almost 5 times lower than the sample grown with V/III BEP ratio equal to 21.

V/III	E_{long} (meV)	T_{short} (K)	E_{short} (meV)	$I_{10K/300K}$
5	52	200	22	350
21	41	160	18	1500

Table 2: PL properties of 100 nm thick GaPN layers grown with V/III BEP ratio of 5 and 21 on GaP(001) substrate annealed at 800°C during 5 min

According to our PL modelling, these results indicate that the sample grown with a smaller V/III BEP ratio has higher alloy fluctuations but a lower NR center density than the sample grown with a larger V/III BEP ratio. This result is remarkable as it shows that the PL quenching and thus the NR center density in the GaPN layers is not only

related to the growth temperature but also to the V/III ratio, like in the GaAsN alloy where the reduction of the V/III BEP ratio has been proven to reduce the Ga vacancies density.[282]

Those last results indicate that it might be possible to grow samples with low PL quenching at low temperature (<480°C) by playing on the V/III ratio. Many works have shown that a low growth temperature decreases alloy fluctuation in dilute nitrides, showing the need of growing more samples to fully optimize the GaPN growth. Nevertheless in order to study the incorporation of As, we have chosen to follow the growth approach developed for the dilute nitride system GaInAsN. We have thus set the following growth recipe to start study the GaAsPN:

- Growth temperature = 480°C
- V/III BEP ratio = 10
- Growth rate = 0.5 ML/s

This recipe only allows an incorporation of 1.5% of nitrogen in GaPN which won't be enough to work on Si substrate and ensure the lattice-matching. Nevertheless the interest of this recipe is to prevent from any dislocation that could happen in GaPN, due to the lattice mismatch with the GaP substrate. Thus this recipe allows comparing the optical properties of the lattice matched GaAsPN alloy with non-relaxed GaPN samples.

4.4 Study of the GaAsPN quaternary alloy

4.4.1 Choice of the lattice matched alloy

Once an optimal recipe was found for the GaPN growth, we have worked on the growth of a lattice-matched compound on the GaP(001) substrate. One has to mention that a further optimization will be necessary when growing on the GaP/Si(001) platform since the GaAsPN lattice parameter will be slightly different than on a pure GaP substrate. With the MBE growth chamber used at FOTON lab a large variety of lattice matched dilute nitride such as (Al)GaAsPN, (Al)InGaPN, (Al)GaPNSb, could have been grown. However, an optimization of the growth parameter to reach the lattice matching for all these material was not feasible. In order to choose which material will be studied in priority we have performed tight-binding and critical thickness calculations on GaAsPN and InGaPN compounds to determine which alloy has the

closest energy bandgap to the required 1.8 eV, keeping the lattice-matching condition with a Si substrate, while having a 1 µm critical thickness.

(a) Bandgaps of GaAsPN and InGaPN

The GaAsPN and InGaPN bandgaps are obtained using an extended basis $sp3d5s^*s_N$ tight-binding calculations adapted for the description of nitrogen incorporation in dilute regimes.[66,184] This model already shown its ability to fit the experimental data with a good accuracy.[184] In Figure 4-11, black lines (solid and dashed) represent the nitrogen amount to get the lattice-matched quaternary alloys with a (001)-oriented silicon substrate, as a function of As or In content. Red lines (solid and dashed) give the modeled bandgap of the corresponding alloy. As an example, the GaAsPN (InGaPN) alloy with an As (In) content equal to 18% would need 6% (10%) of N to be lattice-matched with Si, giving an alloy with an energy bandgap of 1.58 (1.32) eV. From these calculations, to guarantee a 1.7 eV bandgap energy, the optimized composition of lattice-matched $GaAs_xP_yN_{(1-x-y)}$ and $In_xGa_{1-x}P_{1-y}N_y$ are $GaAs_{0.122}P_{0.83}N_{0.048}$ and $In_{0.07}Ga_{0.83}P_{0.95}N_{0.05}$, respectively, as illustrated in the figure with thick black arrows for the specific case of GaAsPN (the first one allows to get the As composition, and the second one allows to extract the corresponding N composition). .

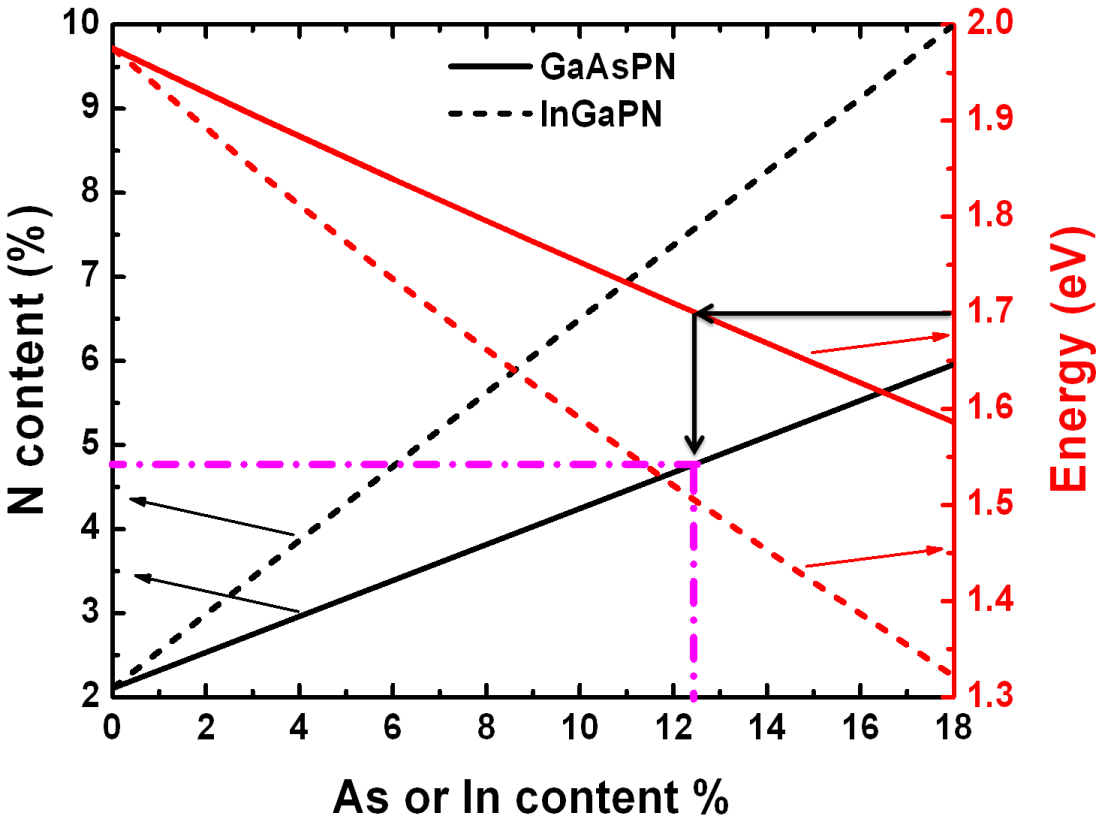

Figure 4-11: Bandgap and composition of GaAsPN and InGaPN alloys lattice matched with Si. Black lines represent the evolution of nitrogen content in GaAsPN (solid line) or InGaPN (dashed line) alloys as a function of As or In content to get the exact lattice matching. Red lines give the bandgap energy for the corresponding GaAsPN (solid line) or InGaPN (dashed line) alloys, as determined with sp3d5s*sN tight binding calculations.

However, dilute-nitride layers with high N content are known to present poor structural quality due to the low solubility of N in GaP, while structural optimization has been demonstrated through annealing processes.[182,170] The main issue is thus to keep the grown layers under the critical thickness to achieve a pseudomorphic growth, while adding enough As or In to reach the expected 1.7 eV bandgap, and keeping a reasonable amount of nitrogen incorporated.

(b) Critical thickness of GaAsPN and InGaPN

Considering that the typical thicknesses of deposited III-V layers on silicon in tandem solar cells are around 1 µm, this value will be considered in the following as a lower limit for the critical thickness. The critical thickness of those materials can be determined using the relationship given by J. W. Matthews and A. E. Blakeslee.[284]

Where f is the lattice mismatch, b the intensity of the burgers vector, n is the Poisson ratio of the thin layer and h_c is the critical thickness. As described in chapter 1, this model is known to be in good agreement with the experimental data, while underestimating the critical thickness. The validity of the Vegard's law is assumed for the lattice parameter of these alloys. The iso-contour plots of the CT for GaAsPN and InGaPN between 100 nm and 1 µm are represented in Figure 4-12, as a function of nitrogen content and As and In content respectively.

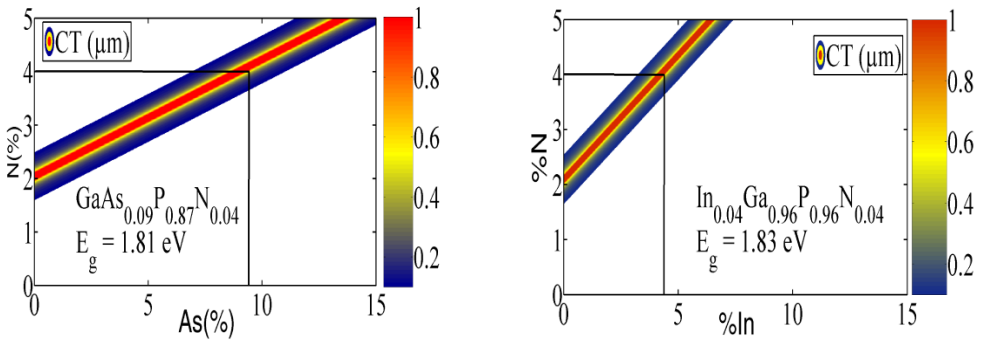

Figure 4-12: iso-contour plot of the critical thickness (CT) for GaAsPN (left) and InGaPN (rigth) alloy between 100 and 1000 nm.

The value found using the M&B approach for the GaP/Si CT (absence of N and As) is equal to 40 nm. This value is coherent with the experimental observations (50-90 nm), knowing that the M&B approach underestimate the CT due to kinetic processes.[285,286] In the case of the GaAsPN alloy, assuming a 1 µm threshold on CT, and a maximum of 4 % nitrogen (allowing to keep reasonable crystalline quality), the As content is equal to 9 %. According to tight-binding calculations, this would give a 1.81 eV bandgap for the $GaAs_{0.09}P_{0.87}N_{0.04}$ alloy (at 300K), which is not far from the expected 1.7 eV room temperature energy bandgap. In the InGaPN case (see Figure 4-12), considering the same threshold and the same limit for the nitrogen composition (4 %), the indium content is equal to about 4 %. The tight-binding calculations for this $In_{0.06}Ga_{0.94}P_{0.96}N_{0.04}$ alloy, gives a 1.83 eV bandgap energy. The GaAsPN alloy allows reaching slightly lower bandgap than the InGaPN alloy. Moreover, InN bonds are also difficult to deal with from the growth point of view.[287] In conclusion, the GaAsPN alloy seems to be a more appropriate choice for low cost tandem cell architecture.

4.4.2 GaAsPN composition determination

Since GaAsPN is a quaternary alloy with three group-V atoms, therefore its composition determination is challenging. Figure 4-13 displays a GaAsPN energy bandgap map of the relaxed bulk alloy as a function of its composition in the dilute regime (N<6%) as determined by sp3d5s*sN tight binding simulation. Black lines represent the possible GaAsPN compositions for 3 different lattice mismatch with the substrate (0;-0.36;+0.36%) that correspond to 3 different lattice parameters. The composition for these quaternary compound is derived by crossing the results from XRD, PL and tight binding calculations.[184] Indeed as explained in chapter 2 the nitrogen composition in GaPN was estimated using Vegard's law. Although the nitrogen and arsenic composition in GaAsPN could not be clearly determined from these measurements, the compositions were then estimated based on: the measured lattice parameter which allow us to draw a line of possible composition on the GaAsPN bandgap map; and on the PL peak emission which allow us to draw another line of possible composition on the GaAsPN bandgap map that will cross the line from XRD measurements, giving the composition. For instance, a lattice matched alloy with GaP ($\Delta a/a=0\%$) with a 1.65 eV PL peak emission would have the following composition $GaAs_{0.16}P_{0.8}N_{0.04}$. However, this approach can be erroneous since many error sources may occur due to the non-perfect coherent growth, the point defect effects in the dilute nitride alloys, and the difficulty to identify the nature of the PL main peak of such alloys.

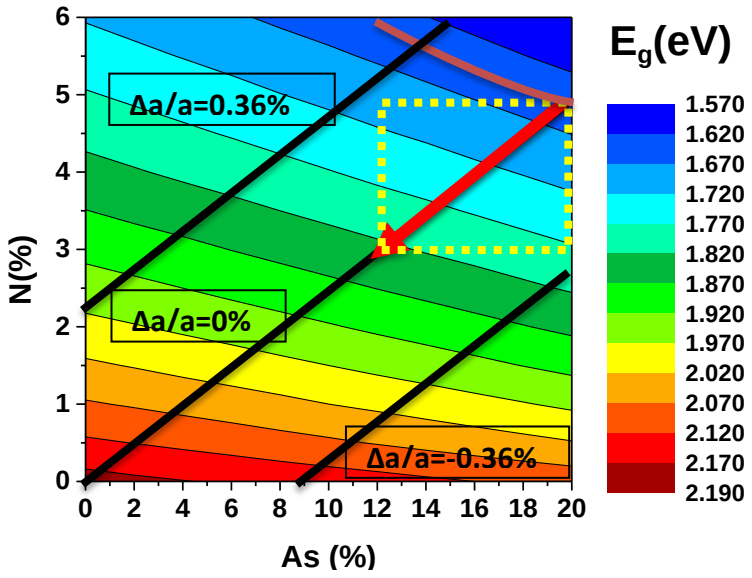

Figure 4-13: GaAsPN energy bandgap at 300K as a function of nitrogen and arsenide content as given by the $sp^3d^5s^*$ tight binding model for a relaxed bulk alloy.

In order to take into account those error sources and to give an estimation of this technique accuracy, we assume that all error sources affect the Stokes shift and the overall material fluctuations can be estimated from this last parameter. Considering an arbitrary maximum Stokes shift of 0.2 eV (red arrow), and a fully coherent growth, the method accuracy (dotted yellow square) is the following: ±1% for the nitrogen content and ±4% for the arsenide content.

4.4.3 As content control

Controlling the composition of the GaAsPN still remains challenging because of the three V elements composing the alloy.[288,289,290,291] Arsenic content is set by varying the As flux in the growth chamber, with all other growth conditions similar to the one used to produce a 1.5% nitrogen content in the GaPN (Growth temperature = 480 °C ; growth rate = 0.5 ML/s ; P = 400W). Only the V/III BEP ratio varied from one sample to the other, due to the As flow change. Figure 4-14 shows XRD ω/2θ profiles from GaAsPN samples with different As compositions.

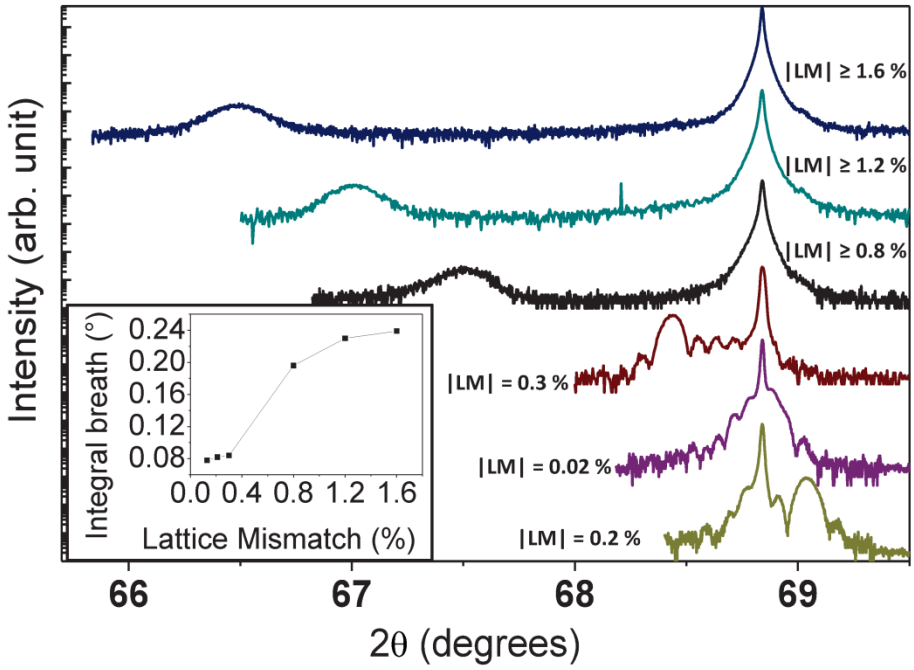

Figure 4-14: XRD ω/2θ scans of 100 nm-thick GaAsPN samples around the (004) Bragg reflection. Inset gives the integrated GaAsPN Bragg peak width as a function of the lattice mismatch.

The samples with a lattice mismatch above 0.8 % are relaxed, similarly to what has been observed for the relaxed GaPN samples. The lattice parameter in this case is underestimated because of compressive strain. The profiles corresponding to the samples with lattice mismatch under 0.3 % show well-defined thickness fringes. This indicates a high degree of diffraction plane correlation through the layer thickness. The inset in Figure 4-14 shows the IB of the GaAsPN peak, with respect to the lattice mismatch. The IB increases from 0.08° to 0.19° in the [0.3 – 0.8%] lattice mismatch range, due to a lowering of the diffraction planes correlation length (crystallite size) which is attributed to the relaxation process. Within the uncertainty on the experimental determination of the critical thickness, the value found for the GaAsPN alloy is coherent with the calculated value (0.36% for 100 nm) on the GaP substrate. As presented in Figure 4-14, a Δa/a GaP mismatch as low as 0.02% is measured on one of the samples, determined with the "strain-free" lattice parameter of the corresponding GaAsPN alloy. The GaAsPN peak and the GaP substrate peak are very close which indicates a quasi lattice-matched layer. For this sample the composition has been estimated to be

$GaAs_{0.1}P_{0.88}N_{0.02}$ using low temperature PL, XRD measurements of the lattice parameter and tight binding calculation. According to our calculations, a 100 nm thickness is far below the calculated critical thickness (800 nm) with this 0.02% lattice mismatch; thus no relaxation due to stress accumulation is expected in this layer. This is further confirmed by AFM measurements which give a 0.3 nm root mean square roughness on a 10*10 µm² image. Any plastic relaxation of the layer would have been detected so far by pits formation visible in AFM.[292] This observation is therefore coherent with the XRD measurements and demonstrate that we are able to grow lattice matched GaAsPN.

4.4.4 Influence of As on N incorporation

In order to determine the impact of As on the N incorporation in GaAsPN, we have studied the evolution of GaAsPN composition in the 4 samples with LM in the range of [0.02-1.2]% coming from the set presented in the last section. As some of these samples didn't displayed any PL signal (even at low temperature), absorption and photoreflectance (PR) measurements have been performed to measure accurately their bandgap energies.[275,293] These measurements have been realized on our samples in the frame of a collaboration that I did initiate with the team of R. Kudrawiec at Wroclaw University in Poland. This has allowed us to determine their composition, by crossing those results with tight binding calculations and XRD measurements. Figure 4-15 displays the PR and absorption measurements, performed on the sample set.

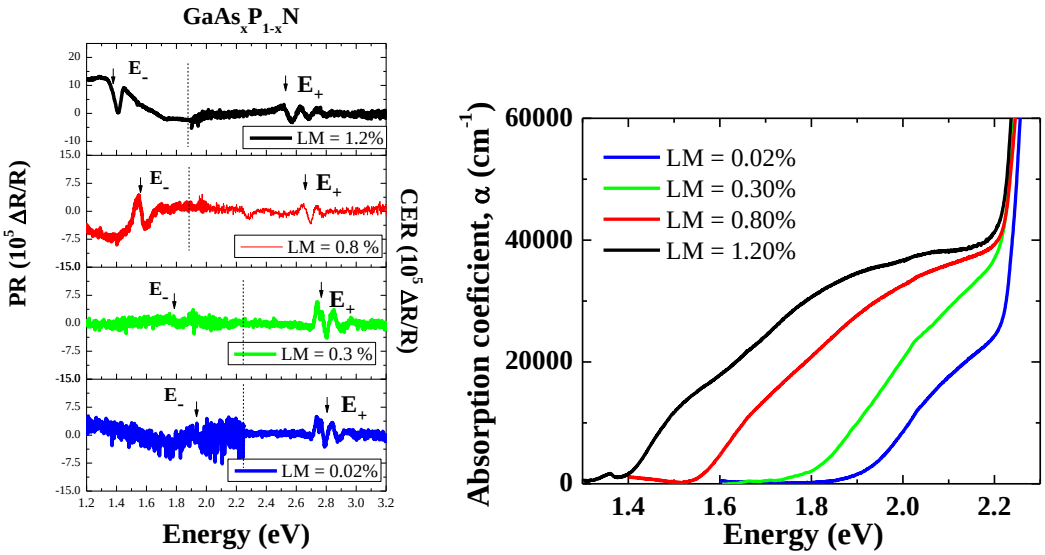

Figure 4-15: PR (left) and absorption (rigth) measurements performed on samples with different LM 0.02% (blue line) 0.3% (green line) 0.8% (red line) and 1.2% (black line). The only difference between sample is the As flux used in their growth recipe

The sample with a LM of 0.02 % has an energy bandgap (E_-) of 1.9 eV consistent with PL measurements performed on this sample. According to TB calculation this sample has the following composition $GaAs_{0.05}P_{0.93}N_{0.02}$. The sample with a LM of 0.3 % has an energy gap (E_-) of 1.8 eV consistent with PL measurements performed on this sample. According to TB calculation this sample has the following composition $GaAs_{0.20}P_{0.77}N_{0.03}$. The sample with a LM of 0.8 % has an energy gap (E_-) of 1.55 eV. According to TB calculation this sample has the following composition $GaAs_{0.35}P_{0.61}N_{0.04}$. The sample with a LM of 1.2 % has an energy gap (E_-) of 1.4 eV. According to TB calculation this sample has the following composition $GaAs_{0.50}P_{0.45}N_{0.05}$.

Sample	Lattice mismatch (%)	Bandgap energy (eV)	Composition
1	0.02	1.92	$GaAs_{0.05}P_{0.93}N_{0.02}$
2	0.3	1.78	$GaAs_{0.20}P_{0.77}N_{0.03}$
3	0.8	1.55	$GaAs_{0.35}P_{0.61}N_{0.04}$
4	1.2	1.37	$GaAs_{0.50}P_{0.45}N_{0.05}$

Table 3: Lattice mismatch, energy bandgap measured by XRD and PR and samples compositions deduced by tight binding calculations.

Note that these results should be taken with care, as the increasing strain relaxation in samples containing more As, result in a lowering of the bandgap not taken into account in TB calculations. This would lead to overestimate the real nitrogen

composition. But still, these results seem to indicate that N incorporation is enhanced by As incorporation. This effect could be explained by the non-neglectable influence of strain on N incorporation, as the increase of the N content allows a strain decrease in samples with high As content. Also the N incorporation could be enhanced by the higher surface roughness of sample with high As content.[292]

4.4.5 Effect of As incorporation on GaPN optical properties

For this study two 100 nm Ga(As)PN samples grown on GaP(001) substrates, at 480°C with a V/III BEP ratio equal to 10 and a growth rate of 0.5 ML/s are considered. One sample has be grown quasi-lattice matched with the GaP substrate using an As flux of 0.35 µtorr. The other sample has been grown without As exposure. XRD measurements presented earlier (see Figure 4-2 and Figure 4-14) performed on both samples show well-defined thickness fringes, indicating a coherent growth. Considering this assumption and assuming Vegard's law the N content is 1.5% for the GaPN sample. For the GaAsPN sample the composition has been estimated to be $GaAs_{0.10}P_{0.88}N_{0.02}$ using low temperature PL, XRD measurements of the lattice parameter and tight binding calculation.

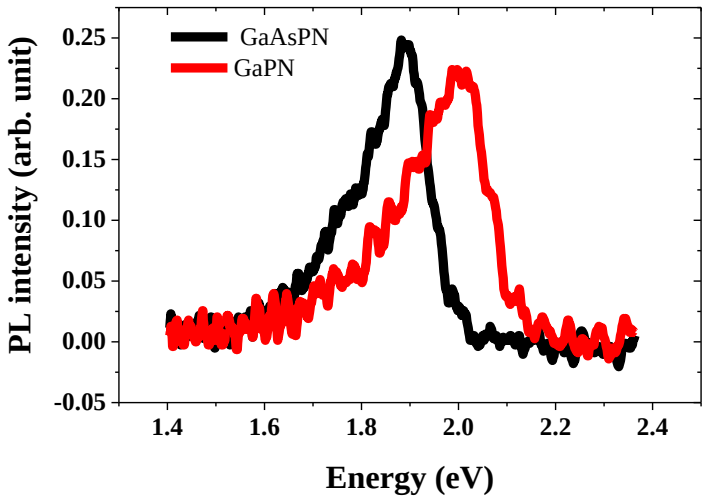

Figure 4-16: room temperature PL spectra of 100 nm thick GaPN layers annealed at 800°C during 5 min grown without (red dot) and with As (black line) on GaP substrate.

The GaAsPN layer is quasi-lattice matched (Δa/a=0.07%) with the substrate and is thus quasi strain-free as compared to the GaPN one (Δa/a=0.2%). No strong differences can be seen between both samples surface, they both have a 0.3 nm r.m.s roughness.

Both samples have a similar behavior upon annealing as samples grown with a high V/III BEP ratio. Indeed, they exhibit a PL intensity enhancement and a reduction of the PL linewidth together with a strong blue-shift of the PL peak emission.

Nevertheless even if both XRD diagram and behavior upon annealing are similar, PL properties presented in Table 4 show some differences between both samples. The GaAsPN sample shows a PL quenching almost 4 times lower than the GaPN sample. Consequently, the sample grown with As has a lower NR center density than the As-free GaPN sample. One possible explanation could be related to the fact that NR traps generation is dependent of strain effects on N incorporation. This is supported by the fact that Ga_i originate from local strain due to the N incorporation, that could be reduced by adding As in GaPN.[280] Also as one can see in Figure 4-16 the PL peak emission is closer to the targeted 1.8 eV for the GaAsPN sample which confirms the fact that with As can be used to effectively reduce the energy bandgap of the GaAsPN alloy while keeping the lattice matching with the substrate.

As	E_{long} (meV)	T_{short} (K)	E_{short} (meV)	$I_{10K/300K}$
0%	45	160	18	1500
10%	45	160	18	400

Table 4: PL properties of 100 nm thick Ga(As)PN layers grown with and without As on GaP substrate annealed at 800°C during 5 min

From these results one should expect better electrical properties for the samples grown with As, quasi lattice-matched with the GaP substrate, considering its lower PL quenching and its bandgap closer to 1.8 eV.

4.4.6 Influence of the layer thickness

We have grown thick GaAsPN layers on GaP(100) substrates to study the influence of the layer thickness on GaAsPN structural and optical properties. Figure 4-17 displays a XRD diagram from a 1 µm-thick GaAsPN sample grown using the same growth parameter as in the previous part (Tgrowth = 480°C, V/III BEP ratio = 10) but with the thickness increased from 0.1 to 1 µm. The observed XRD peak splitting, which was not visible in thinner layers, indicates that phase separation has occurred in this thick layer. This might be due to a too high growth temperature, as high growth temperature has been shown to enhance phase separation in the GaAsN alloy. Even if the origin and the

effect of phase separation are still unclear (e.g. spinodal decomposition of the metastable alloy is sometimes considered as responsible for this), many groups have shown that high efficiency dilute nitride solar cells do not present phase separation.[69,72] This peak splitting corresponds to a difference of 0.0012 nm of lattice parameter or a 0.13% difference in the nitrogen incorporation assuming that the composition variation is only due to a inhomogeneous repartition of the nitrogen content in the layer. One can notice that, a difference of 1% in the nitrogen incorporation on thick GaPN layers has already been reported in the literature in the case of relatively high growth temperature.[294] The reciprocal space mapping around the (224) reflection (Figure 4-17) shows no evidence of any stress relaxation. This is clearly indicated by the GaAsPN peaks alignment with the GaP substrate peak. Moreover, no difference in surface morphology has been noticed between the 1 µm and the 100 nm layer.

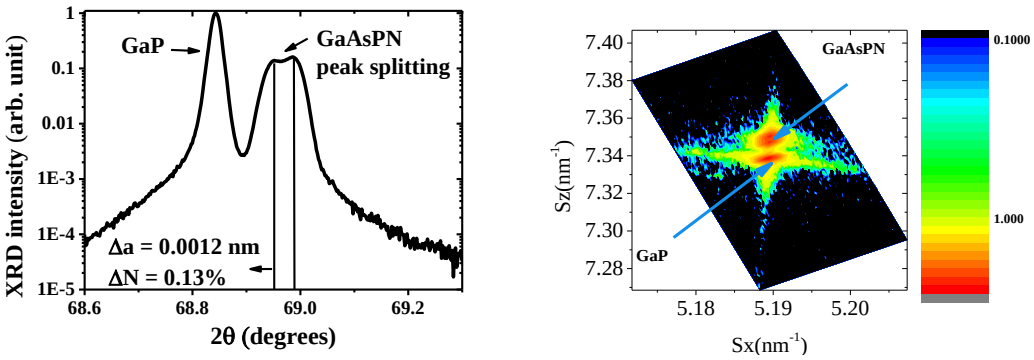

Figure 4-17: XRD diagram (left) and RSM (top) performed on the (004) and (224) GaP reflection respectively, of a 1 µm thick GaAsPN layer grown quasi lattice matched with the substrate.

Even if the 1 µm-thick sample has a similar behavior upon annealing than the 100 nm GaAsPN sample, some small differences have been evidenced in their PL properties. The 1 µm thick sample has the same compositional disorder energy scale at long and short range than the 100 nm thick sample. However, it has a quenching of the PL intensity more than 5 times larger as compared with the 100 nm sample. This probably means that the 1 µm sample has a larger NR center density than the 100 nm sample. This result reinforces the argument that the NR center density might be strain-related. From these results one should expect better electrical properties for the 100 nm sample, considering its lower PL quenching, and compositional fluctuation energy scales at long range. It is also clear that growth parameters should be optimized to get

rid of the phase separation separation phase to improve the electrical properties of the dilute nitride alloys.[69,72]

Absorption measurements performed at IRDEP on the 1 µm-thick GaAsPN sample, in the frame of Pierre Rale PhD Thesis, have allowed us to extract its absorption coefficient. Figure 4-18 displays the absorption spectrum of a GaAsPN layer (red line), GaAs (black line) and GaP (blue line). The steep slope of the GaAsPN alloy absorption spectra, lower than the one of the GaAs direct bandgap material, and higher than the GaP one evidences the pseudo-direct nature of the GaAsPN alloy.

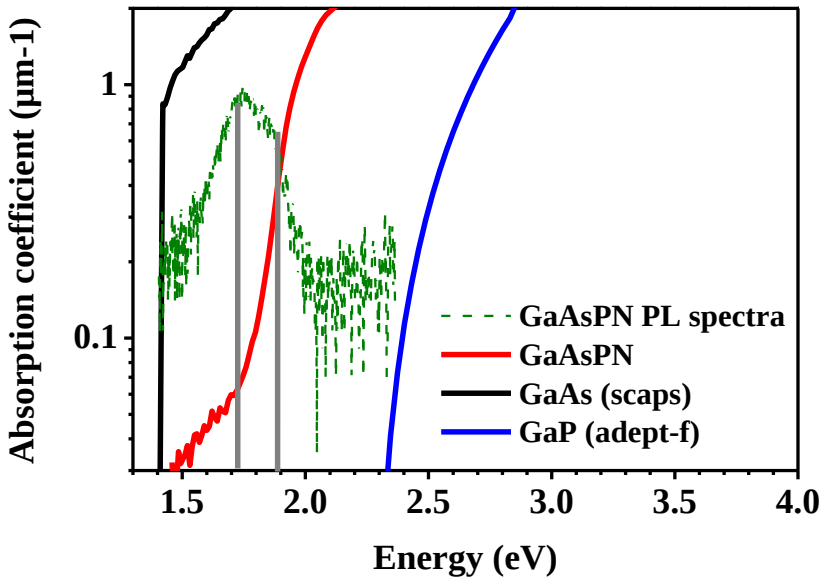

Figure 4-18: Measured absorption coefficient of a GaAsPN layer (red line), of GaAs extracted from the software SCAPS (black line) and of GaP (blue line) extracted from the software ADEPT-F.

Also from PL measurements performed on the GaAsPN sample at 300 K (green dashed line) two emission peak are visible at 1.73 and 1.84 eV. Those two peaks seems to correlate with two region of absorption the first located roughly between 1.5 and 1.7 eV and the other over 1.7 eV, which could be a consequence of the phase separation. From PL measurements at room temperature performed before and after annealing of the GaAsPN sample presented in Figure 4-19 it appears that the RTA process favor the optical efficiency of the higher energy transition. But after annealing, two peaks are still visible. An interesting fact is the difference of behavior upon annealing of the two PL peaks. Indeed no blue shift of the PL peak energy located at 1.73 eV is observed after RTA. These results indicate that radiative centers responsible for the PL peak at 1.73 eV

cannot be modified by the RTA process. On the contrary a strong blue shift (100 meV) of the PL peak energy located at 1.84 eV is observed. This indicates that radiative centers responsible for the PL peak at 1.84 eV can be modified by the RTA process. This difference of behavior can be due to the presence of different N clusters.

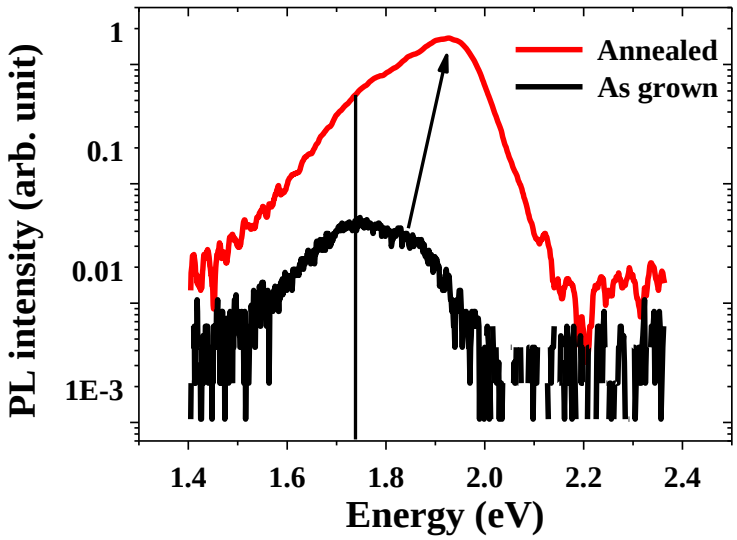

Figure 4-19: PL measurements at room temperature performed before (black line) and after (red line) annealing of 1µm thick the GaAsPN sample.

4.4.7 Growth parameter impact

In order to understand the impact of growth temperature and growth rate on the GaAsPN material grown with V/III ratio of 10, nine samples have been grown at 3 temperature (420 – 450 - 480°C) and 3 growth rates (0.2 - 0.8 - 1.1 ML/s). As we were modifying the growth conditions (growth rate and growth temperature), we were not sure to be perfectly lattice matched with the GaP (100) substrate. Hence in order to avoid any dislocation formation due to possible lattice mismatch, the GaAsPN absorber layer thickness has been set at 300 nm. In this study the sample were all annealed at 800°C for 5 min, the As flux has been carefully decreased while the growth rate was increased from 1.6 to 4.3 10^{-7} torr, in order to keep the lattice matching with the substrate. According to XRD measurements performed on all the samples, the lattice mismatch has been kept under 0.1% for all the samples, with no evidence of plastic relaxation (GaAsPN pic broadening). From this study two main trends have been

observed between the growth rate and the energies scale of compositional fluctuation and between the growth temperature and the PL quenching.

(a) Growth rate impact on N incorporation in GaAsPN

Figure 4-20 displays the PL peak energy dependence for 4 samples grown at 1.1 ML/s at 420°C (blue squares) and 480°C (black squares) and at 0.2 ML/s at 420°C (greens squares) and 480°C (red circles). As expected the growth rate has a strong impact on the energy bandgap of samples at low temperature as it can been seen on Figure 4-20. Samples grown at 0.2 ML/s have their PL peak emission located at 1.9 eV while samples grown at 1.1 ML/s are closer to 2 eV. This shows that between 420°C and 480°C, when the V/III ratio is fixed around 10, the N incorporation in the strained GaAsPN alloy is not much affected by the growth temperature, but is mainly controlled by the growth rate. As mentioned previously while studying the GaPN alloy, this behavior was also noticed for the GaInAsN alloy.[287]

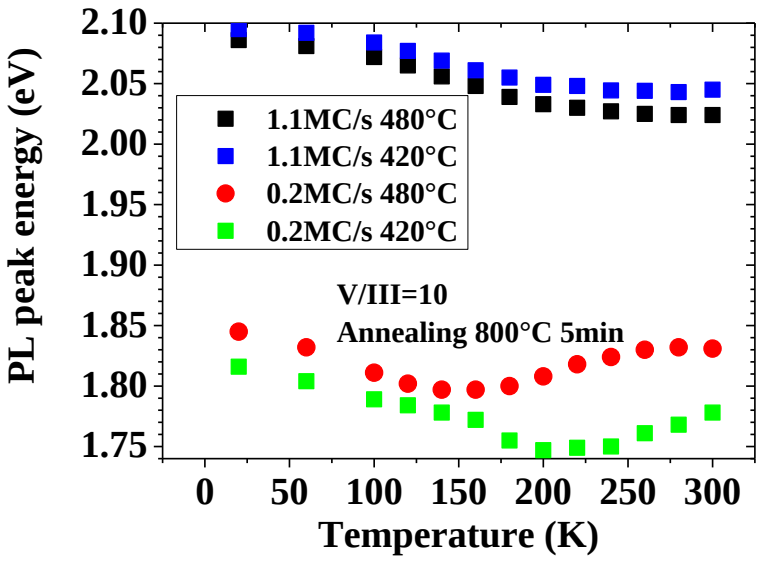

Figure 4-20: PL peak energy dependence for 4 different samples grown at 1.1ML/s at 420°C (blue squares) and 480°C (black squares) and at 0.2ML/s at 420°C (greens squares) and 480°C (red circles).

(b) Compositional fluctuations at long and short range

Figure 4-21 displays the evolution of the energy scale of the compositional fluctuation at long range (E_{long}) as a function of the growth rate for all the samples. Samples grown at 0.2 ML/s have E_{long} in the range of [46-54] meV. Those values are

much larger than the ones found for samples grown at 0.8 and 1.1 ML/s which have E_{long} in the range of [43-47] meV and [41-43] meV respectively.

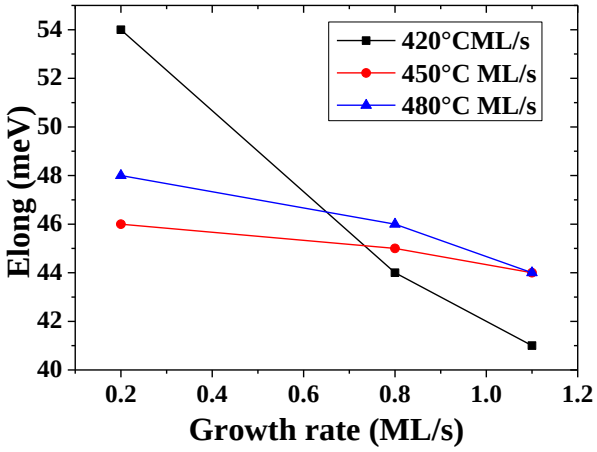

Figure 4-21: Evolution of the energy scale of the compositional fluctuation (E_{long}) at long range as a function of the growth rate.

From this figure, one can conclude that when the growth rate increases, E_{long} decreases. Another interesting feature in this figure is the growth temperature effect on E_{long}. The sample grown at low temperature (420°C) have E_{long} in the [41-54] meV range while sample grown at 450°C and 480°C have E_{long} in the [44-46] meV and [44-48] meV range respectively, from this information we conclude that E_{long} is more sensitive to the growth rate at low temperature (420°C).

The growth rate has also a strong influence on the energy scale of the compositional fluctuation at short range E_{short}. Figure 4-22 presents the PL spectra from 20 to 300K of the two samples grown at 480°C at 0.2 ML/s (left) and 1.1 ML/s (right).

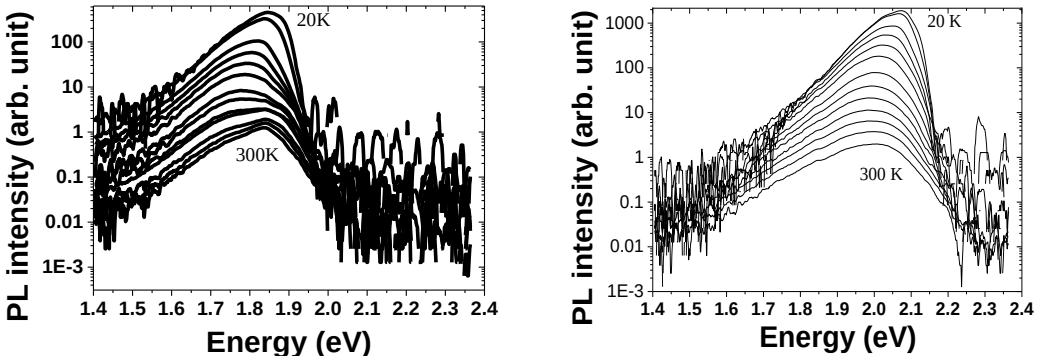

Figure 4-22: PL spectra from 20 to 300K of the two samples grown at 480°C at 0.2 ML/s (left) and 1.1ML/s (right).

The impact of the growth rate on E_{short} is evidenced by the quasi suppression of the S-shape character seen when the growth rate is increased between 0.2 and 0.8 ML/s.

This result is also supported by the samples behavior upon annealing. Figure 4-23 displays the PL spectra from two samples grown at 480°C at 0.2 ML/s (black spectra) and 1.1 ML/s (red spectra) before (dotted) and after (line) annealing at 800°C during 5 min. As one can see, the sample grown at 1.1 ML/s does not show any blueshift after annealing. One the contrary, the sample grown at 0.2 ML/s presents a strong blueshift (100 meV) after annealing (the post-annealing blue-shift being attributed to the presence of N clusters in dilute nitride alloy).[209] These results tend to indicate that the sample grown at 1.1 ML/s has a lower N localized states density, as compared to the one grown at 0.2 ML/s.

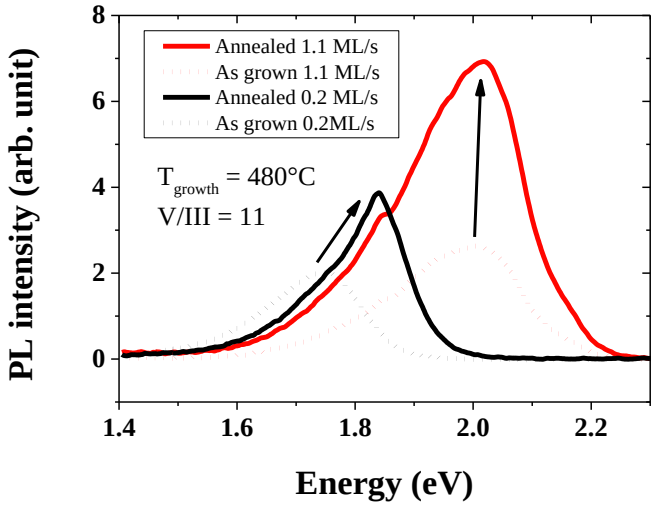

Figure 4-23: PL spectra from two samples grown at 480°C at 0.2 (black spectra) and 1.1 ML/s (red spectra) before (dotted) and after (line) annealing at 800°C during 5 min.

The growth temperature has also a strong impact on the energy scale of the compositional fluctuation at short range E_{short}. Figure 4-24 presents the PL spectra from 20 to 300K of the two samples grown at 420°C at 0.2 ML/s (left) and 1.1 ML/s (right).

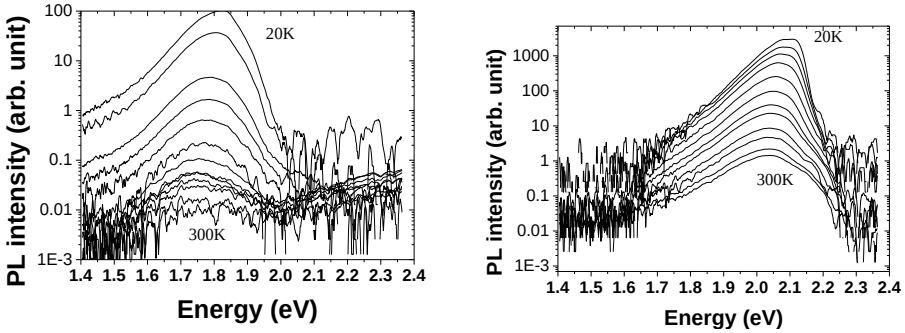

Figure 4-24: PL spectra from 20 to 300K of the two samples grown at 420°C at 0.2 (left) and 1.1ML/s (right).

The impact of the growth temperature on E_{short} is evidenced by the quasi suppression of the s-shape character even for the sample grown at 0.2 ML/s, when the growth temperature is decrease between 480 and 420°C.

In summary, increasing the growth rate and decreasing the growth temperature decreases E_{long} and E_{short}, because it decreases the density of localized N-states. This can be explain as follow: on one hand, the decrease of temperature reduces the mobility of N atoms at the surface avoiding them to form clusters. On the other hand the increase in growth speed reduces the available time for N atoms to form clusters before being buried.

Unfortunately increasing the growth rate decreases the N content, which by itself increases compositional fluctuation when N is under 2%, as it has been shown theoretically and recently experimentally.[269,277] A solution to keep a high N content while having high growth rate could be to re-optimize the plasma parameters or the V/III BEP ratio.

(c) PL quenching

Figure 4-25 displays the PL quenching ($I_{10K/300K}$) as a function of the growth rate for all the samples. Samples grown at 0.2 ML/s have $I_{10K/300K}$ in the [300-60000] range while samples grown at 0.8 ML/s and 1.1 ML/s have $I_{10K/300K}$ in the range of [500-14000] and [850-1400] respectively.

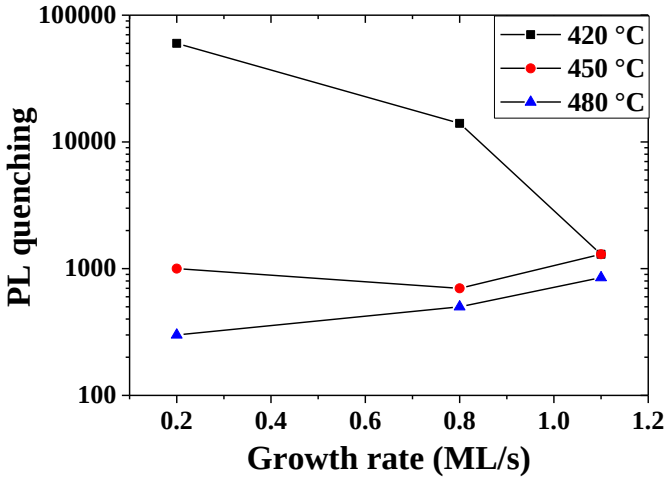

Figure 4-25: PL quenching evolution as a function of the growth rate

From this figure, one can conclude that when the growth rate increases, $I_{10K/300K}$ become less sensitive to growth temperature. Another interesting feature in this figure is the two different trends observed for samples grown at 420°C and those grown at higher temperature. For samples grown at 420°C a clear decrease of the PL quenching is observed with increasing growth rate. This can be explained by the higher homogeneity in those samples due to the higher growth speed as shown in the last section. On the contrary, for the samples grown at 450°C and 480°C, an increase of the PL quenching is observed with increasing growth rate. This can be explained by the reduction of N content in these layers not compensated by the homogeneity increase. Indeed it has been previously shown that the N content has a strong impact on E_{long} and E_{short} and should be in the 2-4 % range to minimize the effects of compositional fluctuations.[270,295,67]

(d) Summary

From the results presented above, to minimize the PL quenching and energy scales of compositional fluctuations at short and long range, one should:

- Have N content in the 3-4% range
- Use V/III BEP ratio in the 8-12 range
- Grow at low temperature (<500°C) at high rate >1 ML/s

4.5 Similarities between GaInAsN and GaAsPN growth

The MBE growth of GaPN-based dilute nitrides has numerous similarities with its arsenide counterpart GaAsN. As it has been shown in previous section and also in other articles, the incorporation of nitrogen is very sensitive to growth temperature and V/III ratio, in both alloys.[294,296–298] Moreover, their behaviors upon annealing are similar. Indeed, a post-growth annealing seems to reduce the alloy fluctuations as indicated by the PL linewidth decrease. Even though an exhaustive study of growth parameter hasn't been realized and still needs to be done, these first-stage results are encouraging. Further growth studies have to be performed to suppress the alloy fluctuations and the NR centers in the GaPN-based compounds, with the strategy already developed for the GaInAsN(Sb) alloy. Indeed, this strategy should allow to greatly enhance the GaAsPN minority carrier diffusion length. For instance, complementary to the two-step growth approach, the next growth recipes should allow obtaining nitrogen content in the [2-4] % range, should use a growth temperature between 420 and 480 °C and a V/III BEP ratio in the [8-12] range. Also as the optimized annealing parameters depend on N content and growth conditions the annealing conditions should be slightly reoptimized around the value found in this thesis (800°C 5 min).[285,294,296,297–304] Indeed, a temperature around 450°C is a prerequisite in order to incorporate a nitrogen amount over 2%. Moreover, the V/III ratio has to be carefully adjusted in order to decrease the alloy fluctuations and the NR center density.

4.6 Summary

We have studied the nitrogen incorporation in the GaPN-based alloys as a function of different key parameters of the growth. The influence of growth conditions on N incorporation has been clarified. Especially, the N content evolution with V/III BEP ratio for different growth temperatures clearly demonstrates prominent dependence of the former on the latter. We thus demonstrate that there is a competition between N and P at the growth front, implying that N incorporation coefficient depends on GaPN growth conditions. Moreover, we have shown that the growth rate controls the N concentration when other growth parameters are constant, as already shown in the GaInAsN(Sb) system.

Then we have developed a specific modelling of the photoluminescence properties and demonstrated that the quantitative determination of the E_{long}, E_{short} and $I_{0k/300K}$ can be used to qualify the material overall quality. We then present results from temperature dependent PL measurements to optimize the GaPN-based growth and the annealing process. In order to grow high-quality high N-incorporation dilute nitride materials, it is found that the growth temperature should stay in the [300-500°C] range, with a V/III BEP ratio between 8 and 12, like in the growth of the GaInAsN compounds, to minimize the PL quenching and the energy scale of the compositional fluctuation at long and short range. An annealing step at 800°C during 1-10 min is found to improve the dilute nitride material quality as it strongly reduces the PL linewidth.

Then, we have worked on the bulk GaAsPN dilute nitride material. We have shown a good control of the As incorporation in GaP, which allows to grow quasi lattice matched GaAsPN layers on GaP(001) substrate. A comparison between a GaPN and a lattice matched GaAsPN sample grown in similar growth conditions shows an improvement of the optical properties attributed to the lattice mismatch decrease as no strong difference in their N incorporation has been evidenced, and also to the addition of As, which reinforces the direct bandgap character. A study performed on 300 nm thick strained GaAsPN samples has shown that increasing the growth rate and decreasing the growth temperature decreases E_{long} and E_{short}, because it decreases the density of localized N-states caused by compositional fluctuations. Finally, a comparison between the GaInAsN and GaAsPN compounds has been drawn, in particular on the growth parameters influence. This comparison indicates clear similarities between both material systems, which pave the way to the growth of high quality GaAsPN alloys, continuing following the approach which has allowed the successful development of the GaInAsN-based 1 eV junction.

CHAPTER 5. GAASPN SINGLE JUNCTION SOLAR CELLS

In chapter 4 we have presented results on the growth and annealing optimization of the dilute nitride GaAsPN materials. I will present here the realization of first-stage Ga(As)PN solar cells on GaP(001) substrates, which will be used as the top junction of the future III-V/Si tandem cells. This work has been led in close collaboration with Olivier Durand, Charles Cornet, Christophe Levallois, Pierre Rale (IRDEP), Alain Rolland, Karine Tavernier, and Tony Rohel. I have myself participated to the solar cell optimization through solar cell design and process elaboration. For this, I have designed masks for the front contact also I have performed CTLM, C-V and Hall measurements to study GaP doping and contacts on GaP. In this chapter, I present a studies performed on GaAsPN top cell. Then, the correlation between PL and I-V properties is discussed. Finally, I present the preliminary results which have been obtained on the simulationof a GaP/Si an Si/Si tunnel junctions.

5.1 Preliminary studies

Before studying GaAsPN based solar cells I have worked on the modelling of the top cell, GaP doping and on the development of the ohmic contacts. My main objectives were to model the optimal cell thicknesses and to achieve low resistance ohmic contacts on GaP.

5.1.1 GaAsPN solar cell modelling

The minority carriers diffusion length in diluted-nitrides materials are known to be low due to point defects and spatial localization of carriers caused by nitrogen fluctuating composition, nitrogen localized states or unintentional incorporation of impurities. That's why, a p-i-n PV structure for the top cell has been selected in this study.[300,301,295] The p-i-n junction consists of three differently doped regions. For such a structure, there is an intrinsic or non-intentionally-doped (nid) layer sandwiched between a p- and an n-doped regions. Typically this kind of structure is used in amorphous silicon and dilute nitride solar cells, to improve the intrinsic layer minority carrier diffusion length through a field-aided carrier collection in the overall intrinsic layer.[27,296,298,302,303]

The design of the top GaP/GaAsPN/GaP p-i-n junction has been theoretically studied using SILVACO-ATLAS as a function of the GaAsPN absorber thickness. The carriers mobilities and lifetimes values (respectively 1000 $cm^2.V^{-1}.s^{-1}$ and 0.1 ns) used as input parameters in the simulation, were extracted from the literature.[304,28,305] Those value are also supported by calculus of the GaAsPN theoretical mobility. This mobility can be calculated using the following formula:

$$\mu = \frac{q\tau}{m^*}$$

Where m^* is the carrier effective mass (that can be calculate by TB), τ is the carrier scattering time (that can be linearly interpolated from GaP, GaAs and GaN value).[306,307,305] For instance in the $GaAs_{0.30}P_{0.67}N_{0.03}$ alloy, τ_e = 0.4 ps, m* = 0.25 m_0 where m_0 is the electron rest mass, which give a mobility around 3000 $cm^2/(V.s)$. As expected due to the N incorporation, those values are lower than for classical III-V materials having direct bandgap such as GaAs (respectively 8000 $cm^2.V^{-1}.s^{-1}$ and 3 µs). On the other hand, the absorption coefficient (see Figure 4-18) and the optical constants (n,k) of GaAsPN have been extracted respectively from experiments performed at IRDEP and from ellipsometry measurements performed at Institut de Physique de Rennes (IPR). Figure 5-1 displays the n,k value of the GaAsPN alloy as extracted from ellipsometry measurements.

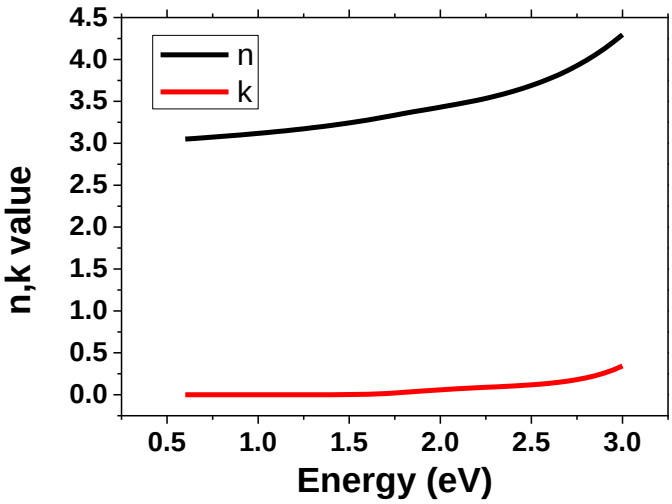

Figure 5-1: n,k value of the GaAsPN alloy as extracted from ellipsometry measurements.

Due to issues when modelling a thick substrate, the following virtual structure has been modeled: GaP (30 nm) n = 1e18 cm^{-3} / GaAsPN / GaP (250 nm) p = 1e18 cm^{-3}.

Also has no measurement of the electronic affinity on the GaAsPN has been realized for the moment we have assume that the bandgap reduction was due to an increase of electronic affinity caused by the nitrogen atoms that only affect the alloy conduction band. Figure 5-2 (top) shows the energy band diagram of the modelled solar cells. According to this modelling there is a good holes collection but it exists a barrier for the electrons collection. This barrier width could be reduce by highly doping the GaP(n) layer or using AlGaP which has an higher electronic affinity (3.98 eV) than GaP (3.8 eV).

Using these parameters, the evolution of the I-V curve as a function of the absorber thickness has been calculated with SILVACO (see Figure 5-2 bottom). From these calculations an optimal top cell efficiency has been found equal to 9.42 % for a 1 µm thickness.[304]

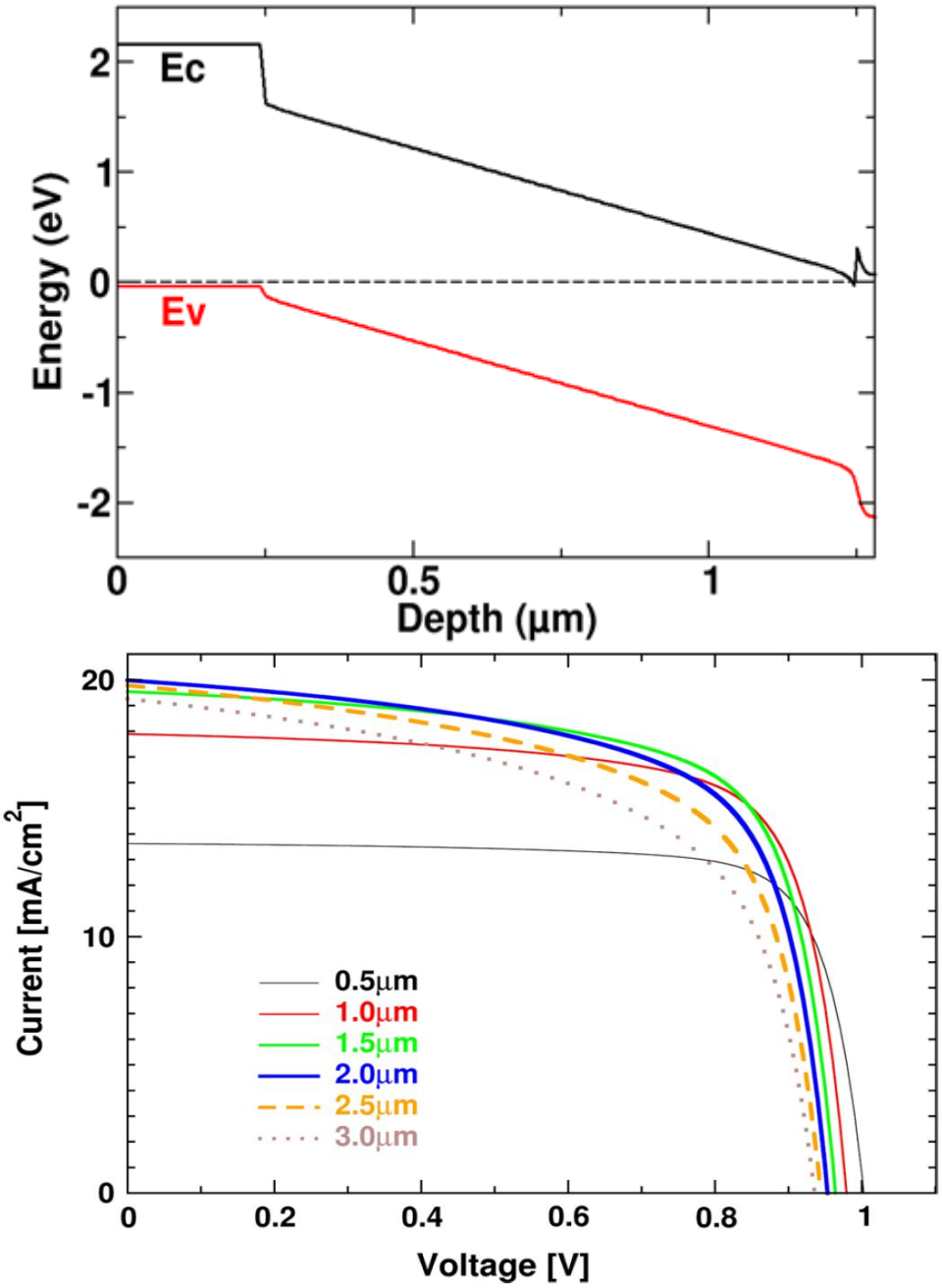

Figure 5-2: GaAsPN solar cells energy band diagram (top). Evolution of I-V curves under AM1.5G illumination as a function of the absorber thickness as calculated with SILVACO (bottom).

This is an encouraging result since the carrier mobility and carrier lifetime that have been used in the modelling are low, and considering that improvement of the structural quality of the GaP-based dilute-nitride materials is on the way to reduce the influence of the remaining defects.

5.1.2 Tunnel junction modeling

As explained in chapter 1, the main approach to connect electrically two cells in a MJSC, is to use a two-terminal structure with a tunnel junctions (TJ), or Esaki diodes, placed between the two cells, offering a low resistance due to its high doping (≈1.10^{19} cm-3) and good optical transparency due to its low thickness (≈ 50 nm).[308] To obtain optimal performances, leading to a good voltage addition from the stacked subcells, abrupt dopants profile should be obtained and thus diffusion of dopants in the TJ should be minimized. Also the TJ structure has to be compatible with the overall growth conditions. In particular, using modelling, two different tunnel junctions have been investigated and found suitable for the 1.7 eV / 1.1 eV targeted tandem cell structure: a hybrid GaP(n+)/Si(p+) TJ and a Si(n+)/Si(p+) one, considering a n-type Si absorber in the bottom junction. Considering uniform doping of 5.10^{19} cm^{-3} on both junction sides (reachable experimentally according to Hall measurements on doped GaP and Si layers), theoretical current densities as large as 4.4 10^5 mA/cm² in the GaP(n+)/Si(p+) TJ case and $5.5.10^2$ mA/cm² for the Si(n+)/Si(p+) one has been calculated, suitable for the tandem cell application.[304] Obviously, the final choice between both will be depending on the actual experimental structural properties reached for each TJ, in particular the maximum doping level, the material structural quality and the dopant diffusion properties between both III-V and Si materials.

5.1.3 GaP doping

By definition, the p-i-n solar cell has, on each side of the absorber zone, p and n doped layers. Beryllium and silicon are used respectively as p and n dopant due to their high solubility in GaP and their low ionization energy. The dopants are evaporated during the growth using classical Knudsen cells.

The dopant concentration is modulated by varying the dopant cell temperature or the growth rate and is expressed by the simple relation:

$$C = \frac{F(T)}{Gr}$$

Where Gr is the growth rate and F the dopant beam proportional to the partial pressure of which the temperature dependence is given by the well-known Clapeyron law:

$$ln(P) = -\frac{\Delta H_{sub}}{RT} + K$$

Where ΔH_{sub} is the sublimation enthalpy of dopant, and K a constant. Therefore, the evolution of the dopant concentration as function of the cell temperature can be represented by an arrhénius plot.

The slope of this curve is given by the sublimation enthalpy, characteristic of the evaporated material. It doesn't depend on the cell geometry, neither on the host material as long as the doping concentration is below the dopant solubility limit. In order to get the actual value of this doping, Hall effect and C-V measurements were performed on several samples grown with different dopant cell temperature. The experimental results obtained by C-V measurements for p and n doping are plotted in Figure 5-3. These results have been confirmed through Hall and SIMS measurements.

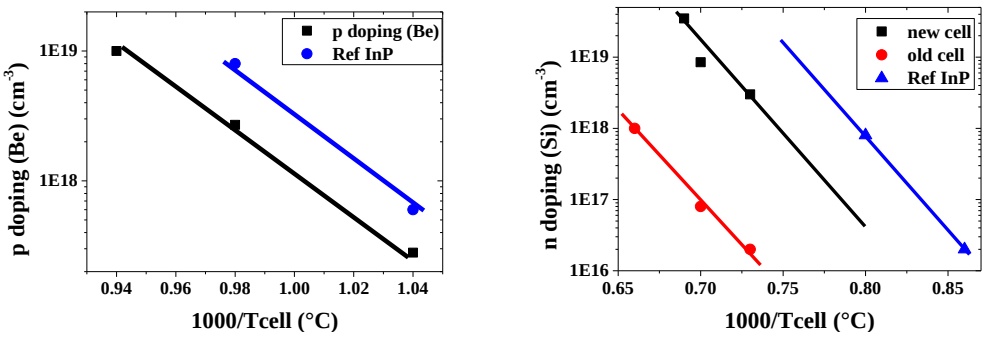

Figure 5-3: Doping concentration as a function of the dopant Be (left) and Si (right) cell temperature in GaP and InP as obtained by C-V measurements.

From these figures we can clearly see that the slope depends on the dopant material. In order to increase the n doping in our samples, a new Si cell has been installed in the MBE system during this thesis. As expected, the slope doesn't depend on the geometry of the cell neither on the host material. We are now able to grow highly doped ($1^{e19}cm^{-3}$), n-doped as well as p-doped, GaP layers suitable for the growth of p-i-n solar cells on GaP, in particular concerning the high-doping level mandatory for the tunnel junction elaboration.

5.1.4 Ohmic contacts on GaP

Since electrical carriers should be collected efficiently, ohmic contacts constitute an important part of the PV device. Low resistance ohmic contacts are required to lower as much as possible any additional detrimental effect on the device. As explained in section 2.3.3.a, obtaining a low resistance ohmic contact requires the use of an appropriate contact alloy which can be difficult for a p-type large bandgap material such as GaP, for instance. The main properties required for ohmic contacts are linear, symmetrical I-V characteristic and high reliability and reproducibility, which impose an annealing technological procedure. As explained in section 2.3.3.a, an ohmic contact with a high bandgap material such as GaP requires a high doping level at the semiconductor/metal interface. This high doping level can be ensured using dopant diffusion from the metallic contact to the semiconductor through RTA annealing at around 550°C.

Thus in order to have ohmic contact on GaP I have tried many alloy combinations such as: Au/Sn and Au/Si on n-GaP substrate and Au/Ge and Au/Zn on p-GaP substrate. Gold has been chosen to insure a high conductivity and stability over oxidation to the alloy. Sn, Si, Ge and Zn were used as dopant sources. In these tests the 30 nm dopant layers were first deposited followed by a 200 nm Au layer. Unfortunately, all the dopants (Sn, Si, Ge, Zn) that we have used were not alloyed with GaP after the annealing process, when they were directly deposit on it. This has been attributed to a lack of wettability of these dopants on GaP.

Indeed It was found that the use of a wetting/diffusion layer was fundamental in order to alloy and diffuse the dopant sources in the GaP and ohmic contact. Figure 5-4 displays microscopy image of Au/Ge based contact with (right) and without (left) Ni wetting/diffusion layer. From this photo it is clear that the use of a Ni wetting layer leads to a better alloy between the metallic contact and GaP.

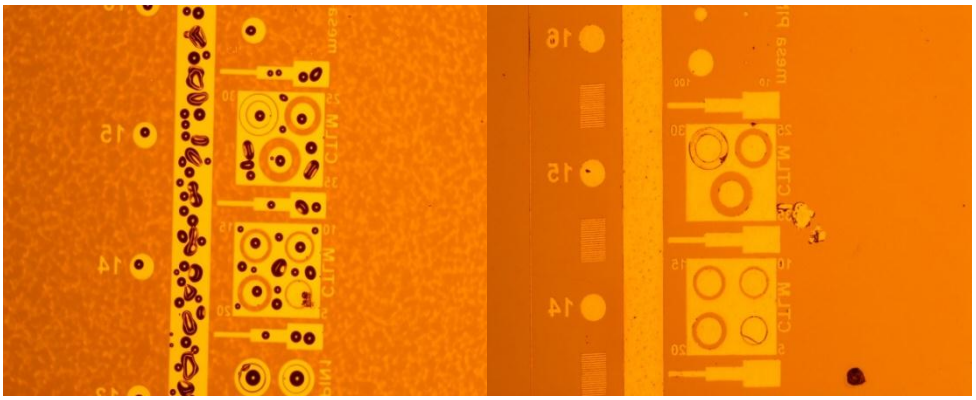

Figure 5-4: Photography of Au/Ge-based contacts with (right) and without (left) Ni wetting/diffusion layer.

By using thin wetting/diffusion layers such as Ni or Pd and an annealing step at 540°C during 3 min, we have managed the realization of ohmic contacts on n- and p-GaP substrate.

For n-type GaP substrate, I've proposed to use a metallic contact based on (Ni/Au/Ge), with an optimized annealing temperature at 530°C. With such a deposition sequence and as described by Peternai et al.[309], ohmic contact with a symmetrical I-V behavior is obtained with a very good reproducibility of the mechanical stability. During this thesis a low contact resistivity of 10^{-5} Ω.cm² has been reached on n-GaP substrate (n=1.10^{18} cm^{-3}), which validates the n-type electrical contact reaching state of art values.

For the p-type GaP , I've proposed to relie on the work reported by Baojun *et al* and Zhang *et al*, where a Pd//Au/Zn stacking has been employed, with an annealing temperature at 550°C [310,311] As in the n-type doping case, ohmic contact with a low contact resistivity of 10^{-5} Ω.cm² has been reached on p-GaP substrate (p=1.10^{18} cm^{-3}), which validates the p-type electrical contact reaching state of art values.

Figure 5-5 presents the CTLM measurements for the two types of contact. From these measurements, the specific contact resistances of Ni/Au/Ge and Pd/Au/Zn have been extracted, and a low contact resistivity of 10^{-5} Ω.cm² has been found for both.

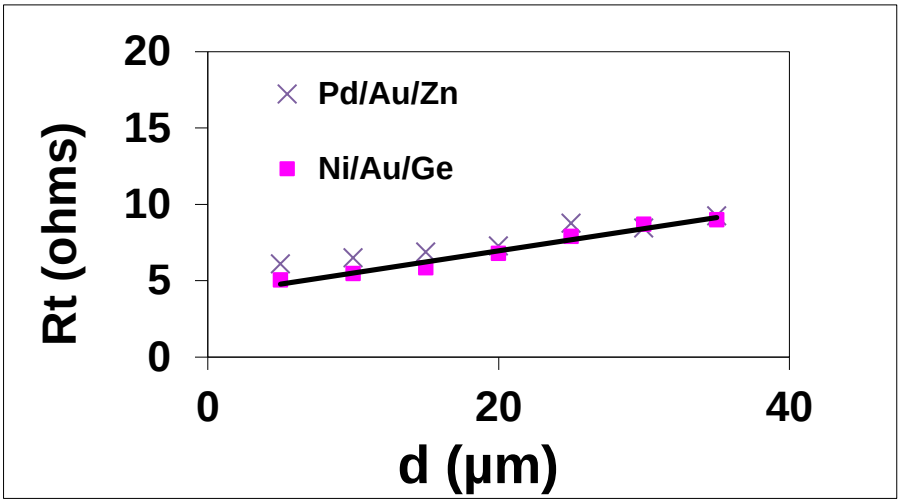

Figure 5-5: Total resistance as function of spacing d for Pd/Au/Zn and Ni/Au/Ge based contact on GaP.

5.1.5 Solar cells processing

Single GaAPN/GaP solar cell devices were fully developed at FOTON laboratory. Figure 5-6 resumes the main step that has been used to make the solar cells.

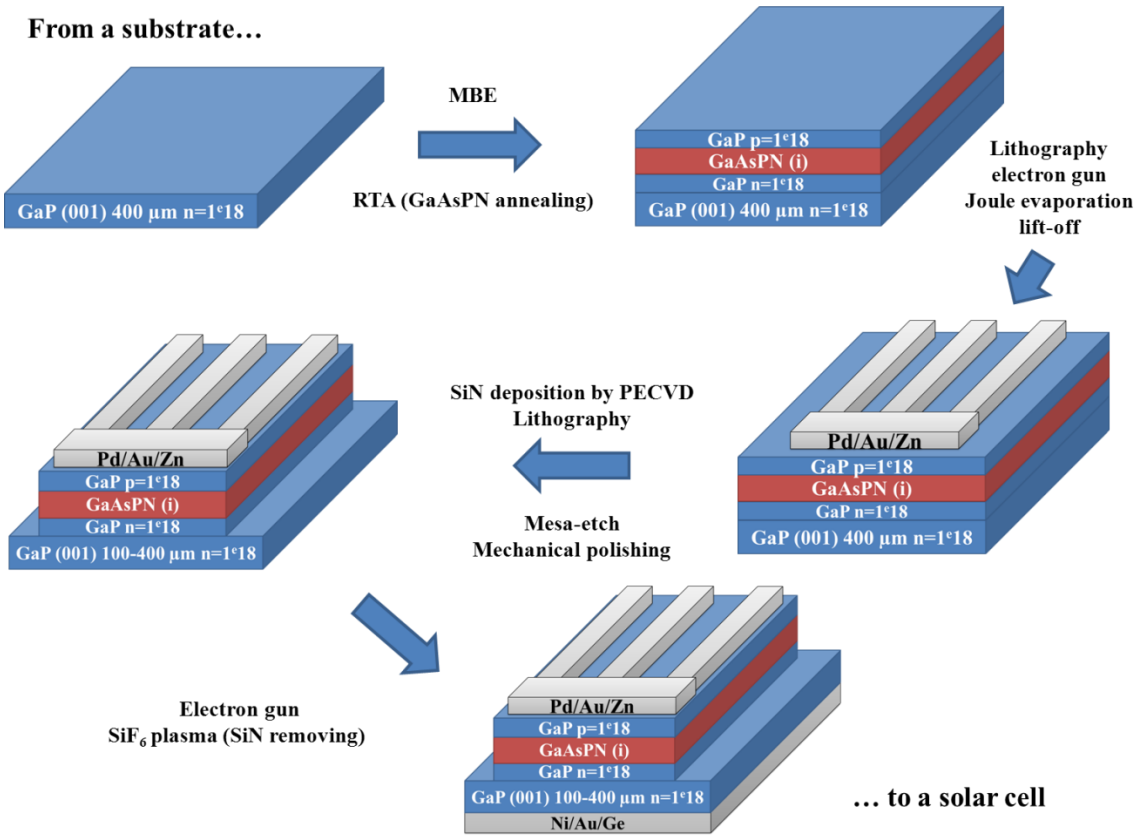

Figure 5-6: main steps used to process the solar cells.

After the MBE growth solar cells are annealed at 800°C during 5 min in order to improve the GaAsPN optical properties. A front-fingered contact is first deposited through a lift-off procedure, after an oxide removal from the surface which was done in a 5% HF solution during 30s. The fingers size is 2.5 mm * 5 µm, the fingers are spaced from each other of 300 µm. The busbar size is 2.5 mm * 0.5 mm A combination of electron gun and Joule evaporator is then used to deposit the Pd/Au/Zn-based front contact. The use of two different evaporators can be explained by the fact that Zn could induce pollution in the deposition chamber, leading afterwards to deposition of n-contact with a strong "p" residual doping caused by Zn. Another important feature which has been noticed on the Zn evaporation, while working on its deposition, is its tendency to violently evaporate from the solid phase instead of smoothly evaporates like gold, making homogenous and reproducible deposition difficult. Two important parameters have been noticed during these tests to avoid any Zn violent evaporation and to ensure a homogenous deposition. The first one is the residual pressure before evaporation which should be as low as possible (under 10^{-6} torr). The second one relies on the electric current used to heat the Zn which should also be as low as possible.

For the photolithography step, I have used a Karl Suss MJB4 Mask Aligner to define the solar cells front contact grids and their area. The MJB4 is designed to offer the flexibility required in a R&D laboratory environment. Line space resolution up to 0.8 micron can be achieved under optimum conditions in the vacuum mode. In this work, all the photolithography steps have been performed in soft contact allowing line space resolution of 5 µm.

After the lift-off process, the front sample surface is protected using photoresist and the substrate is thinned. As it will be seen in the next section, substrate thinning, from 400 µm to 200 µm is important to improve the solar cell efficiency. Different solutions have been tested to thin the GaP substrate from chemical etching to mechanical polishing. The best results have been obtained using mechanical polishing.

After the mechanical polishing, a SiN layer is deposited by plasma enhanced chemical vapor deposition (PECVD) at 300°C and a second photolithography step is done. Then SiN layer is etched by a reactive ion etching (RIE) process using SF_6 gas. This dry etching step is then followed by the chemical etching of GaP-based material to create 3 mm x 2.5 mm mesas to ensure an electrical insulation between the front side

and the back side of the solar cell. The chemical solution HCL, H_2O_2 and, H_2O with a 40:2:1 ratio) used could partially remove the photoresist during the chemical etching. Therefore a hard SiN dielectric mask is used to protect the contact zone and the active area.

After the dry etching, the SiN layer and remaining photoresist are removed. The sample is then dipped 30s in a 5% HF chemical solution, dried and a Ni/Au/Ge based contact is deposed using an electron gun on the back side of the sample.

Finally a last annealing step is performed at 540°C 3 min to alloy both contact at the same time.

5.2 Study of the GaAsPN top junction

After the GaP doping and ohmic contact, with low specific resistance, developments, we have grown and study GaP (n) / GaAsPN (i) / GaP (p) p-i-n solar cells, on n-doped GaP substrates. We have choose to work on n-type substrate as first calculation on the tunnel junction polarity have shown that Si (p++) / GaP(n++) is more favorable for tunneling than the opposite interface. Also it's known that solar cells grown on p-type Si substrate have stronger degradation of its efficiency with time than solar cells grown on n-type Si. My main objectives were centered on the top cell efficiency improvement. Therefore, I have studied the effect of the following parameters: the annealing time, absorber doping, MBE growth rate and growth temperature, the substrate and the window layer thickness using optical and electrical measurements.

5.2.1 Annealing impact on GaAsPN solar cells

As seen in part 4.3.1.b the annealing process has a strong effect on the GaAsPN optical properties (Blue-shift, reduction of the PL linewidth). Though it would help to optimize the GaAsPN alloy using simple PL test structure, no clear correlation between PL and I-V properties has been established for the moment. In order to correlate the optical and electrical properties of the GaAsPN alloy, we have study the evolution upon annealing of solar cells parameters having absorber layers grown in the same conditions as section 4.3.1.b.

For the study of the annealing influence on GaAsPN solar cells, two quasi lattice matched samples have been grown at 450 °C and 480°C with the same V/III BEP ratio equal to 10 and a growth rate of 0.5 ML/s. Those parameters have been taken as they were seen has the best compromise between the necessity of high N incorporation and high growth rate. Figure 5-7 displays the solar cells structure.

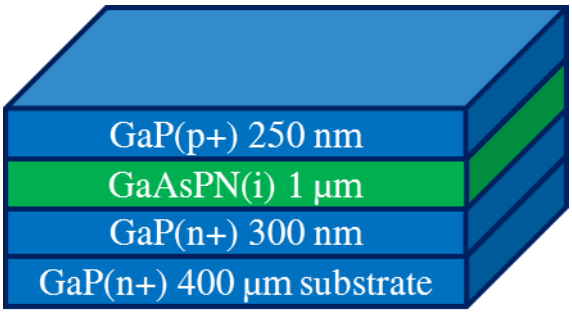

Figure 5-7: Solar cell structure.

A 1 µm thick absorber has been chosen following the solar cell efficiency modelling presented earlier. In the first-stage development, a 200 nm thick p-GaP window layer has been used in order to ensure a good electric contact and avoid any dopant diffusion from the contact to the GaAsPN absorber. Each sample has been cut in four smaller pieces and then annealed using our RTA system. For this study an annealing temperature of 800°C has been chosen according to the previous study on the GaAsPN (part 4.3.1.b). Table 5 gives the electrical parameters for the solar cell with an absorber grown at 450 and 480°C before and after annealing at 800°C for 1, 5 and 10 min. After each annealing, an increase of the open-circuit voltage (V_{oc}), short circuit current (J_{sc}) and fill factor (FF) is clearly seen, and it leads to a significant improvement of solar cells overall yields (Table 5). This underlines the importance of the annealing step to reduce the detrimental defects density in the absorber layer. However, it is clear for the sample grown at 450°C that the electric current saturates and stays at a low level (around 1 mA/cm²), which is coherent with the PL measurements presented earlier in Figure 4-8.

T_{growth} (°C)	$t_{annealing}$ (min)	J_{sc} (mA/cm²)	V_{oc} (mV)	FF (%)	η (%)
450	0	0.175	647	37	0.04
	1	0.27	541	33	0.05
	5	0.715	915	52.8	0.34
	10	0.805	890	60	0.43
480	0	1.21	0.865	47	0.49
	1	1.69	1.06	52	0.94
	5	1.28	1.05	39	0.52
	10	1.36	1.08	46	0.68

Table 5: solar cells I-V parameters.

For the sample grown at 480°C a decrease of the efficiency is observed for annealing time over 1 min. This was really surprising considering the evolution of its PL parameter. As explained in the following this efficiency decrease has been attributed to the annealing effects on the substrate.

5.2.2 Substrate effect

As explained in chapter 1, it has been shown that GaP substrates contain detrimental impurities for the PV properties (especially for the electric current delivered by the cell). Indeed, isoelectronic nearest-neighbor Zn-O pair, known to act as recombination centers, limit the efficiency of the GaP solar cells.[158,190] Also it has been shown that even epitaxial layers grown in a solid source MBE chamber can contain O impurities if the temperature of the phosphorus cracker is higher than 800°C.[195] Those detrimental impurities can be detected using PL measurements as explain by Montgomery *et al*. due to their characteristic PL peak emitting at 1.82 eV at 4K.[158] In order to evaluate the annealing step influence on the n-doped GaP substrate, I have performed room temperature PL on fresh and annealed (800°C 5 min) wafers. Figure 5-8 displays the annealed (black line) and non-annealed (red line) GaP substrate photoluminescence spectra. From this figure it is clear that the annealing step has an effect on the GaP substrate. According to the correlation made by Montgomery *et al.* between the presence of a 1.8 eV PL peak observed on GaP substrate at 4K and low spectral response in GaP solar cells, we have assumed that the annealing step degrades the substrate quality.[158]

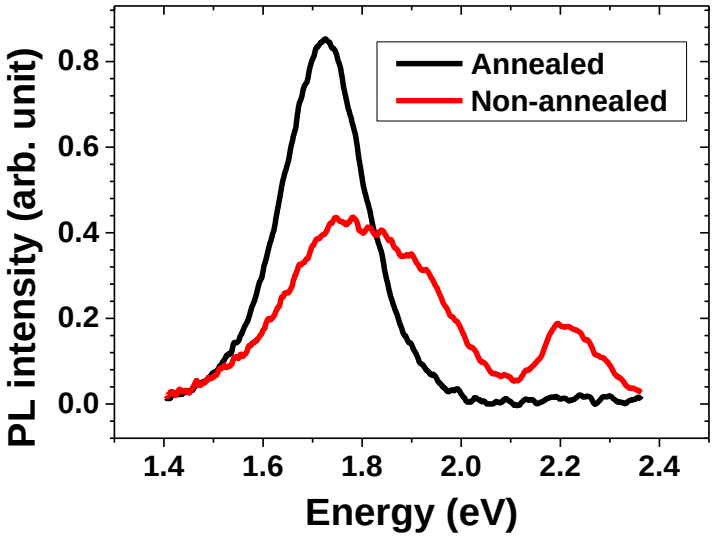

Figure 5-8: Annealed (black line) and non-annealed (red line) GaP substrate photoluminescence spectra.

Thus we have performed studies on the substrate thickness impact on the solar cell efficiency. For this study, the substrate of the sample grown at 480°C, with a V/III BEP ratio around 10, annealed at 800°C during 5 min and having the structure presented in Figure 5-9, has been mechanically polished from 400 µm to 200 µm. Then the solar cells efficiencies have been compared using I-V measurements under AM1.5G illumination and without illumination. This experiment highlights the negative substrate effect on solar cells electrical performance.

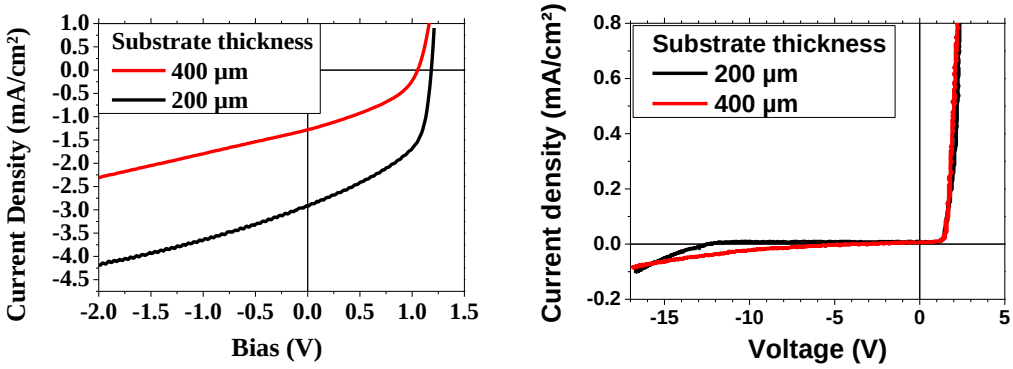

Figure 5-9: I-V measurements under AM1.5G illumination (left) and without illumination (right) performed on solar cells grown and processed in the same condition except from the substrate thickness 400 µm (red line) and 200 µm (black line).

Table 6 gives the electrical parameters for both solar cells with and without substrate thinning. The solar cell having a thinned substrate presents an increase of the open-

circuit voltage (V_{oc}), short circuit current (J_{sc}) and fill factor (FF), leading to a significant improvement of solar cells overall yields. Note that this issue should only be considered in the single cell architecture, as the GaP substrate is not used anymore in the targeted tandem solar cell architecture.

Substrate thickness (µm)	*J_{sc} (mA/cm²)*	*V_{oc} (mV)*	*FF (%)*	*η (%)*
400	1.28	1.05	39	0.52
200	2.8	1.18	49	1.6

Table 6: solar cells I-V parameters.

From the I-V measurements performed without illumination (Figure 5-9 right), the efficiency improvement seems to be due to an increase of the shunt resistance in the thinned solar cell. This effect is still not explained but could be due to O related deep center introduced by the annealing process at the GaP surfaces that would act as isolectronics traps.[191]

5.2.3 Doping impact.

This study has been made with two samples using structure 1 (presented in Figure 5-10**)** and with the following growth parameters (480°C, V/III BEP ratio equal to 10). The only difference resides in the absorber doping being not intentionally doped or n-doped.

Figure 5-10 presents the J-V measurements made on these solar cells under an AM1.5G illumination. The solar cell with the n-doped absorber has a lower efficiency (η=0.6%) compared to the one with an absorber not intentionally doped (η=1.04%) due to a decrease of all of its PV parameters (Voc → -0.15V, Jsc → -0.2 mA/cm², FF→-13)

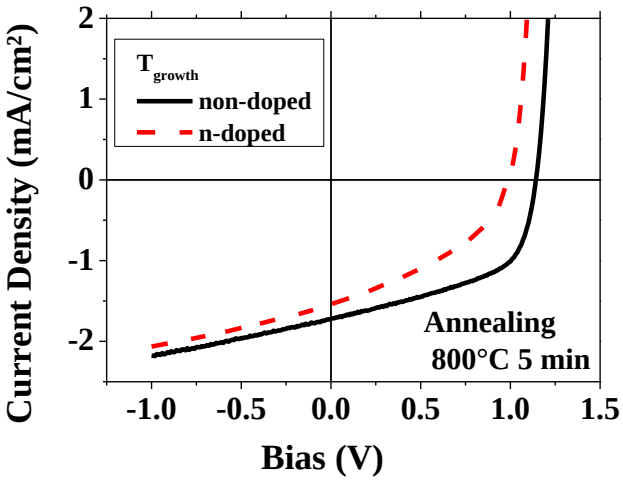

Figure 5-10: LIV measurements under AM1.5G made on solar cells having different absorber doping: n-doped (red dash) and not intentionally doped (black line).

These results are not in accordance with PL measurements made on these solar cells especially when looking at the abnormally high Jsc (1.54 mA/cm²) of the n-doped sample compared to its high PL quenching ratio (3400), as it can be seen in Table 7.

Doping	E_{long} (meV)	T_{short} (K)	E_{short} (meV)	$I_{10K/300K}$
Not intentional	44	180	20	400
n=1e17	44	180	20	3200

Table 7: PL properties of GaAsPN solar cells grown on GaP substrate with different absorber doping and annealed at 800°C during 5 min.

From the IQE measurements presented in Figure 5-11, this can be explained by the better collection of this cell in the blue region. Indeed the n-doped sample (purple curve) shows an increase of the collection for photon with energy above 3 eV, while the non-doped sample (red curve) behaves like the p-p-n structure (blue curve). This collection increase can be explained by a modification of the space charge zone (SCZ) position in the solar cells when the absorber is n doped. This result seems to indicate that the absorber is intrinsically p doped, with a doping density high enough to influence strongly the position of the SCZ. The very low quantum efficiency of the p-doped remain unexplained, but we think it can be due to an increase of the carrier density compare to the unintentionally doped sample that reduce the minority carrier diffusion length and thus carrier collection. This comforts us in our choice to use a p-i-n structure.

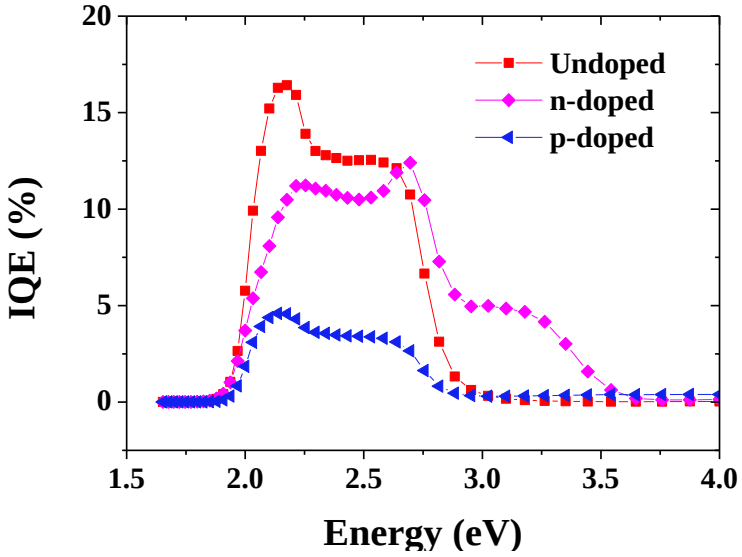

Figure 5-11: IQE measurements performed on a non-intentionally (red), a n-doped (purple) and a p-doped (blue) absorbers solar cells.

On the PL side, the higher intensity quenching with temperature in the n doped samples might be due to an increase in NR recombination at the sample surface due to the GaP high surface recombination rate. The carrier collections of the p-i-n cell being very weak in the blue-region we have investigated the effect of the window layer and absorber thickness.

5.2.4 GaAsPN absorber thickness influence

In order to improve the carrier collection in the blue region, I have proposed to grow a solar cells with a p-GaP window layer, that has been reduced from 250 nm to 30 nm as compared to structure 1 (Figure 5-7). In order to evaluate the influence of the window layer thickness on the carrier collection in the blue region, IQE measurements has been performed on this sample. No major effect due to the window layer thickness reduction has been evidenced on the carrier collection in the blue region. As no degradation of series resistance has been observed on this sample due to the window layer thickness reduction, I have decided to: reduce the absorber thickness from 1 µm to 300 nm to see if the blue collection in the cell was limited by the GaAsPN minority carrier diffusion length; while maintaining the 30 nm window layer in p-GaP. The sample has been

grown in the same growth conditions as the previous study (T_{growth} = 480°C ; V/III BEP ratio = 10 ; growth rate = 0.5 ML/s).

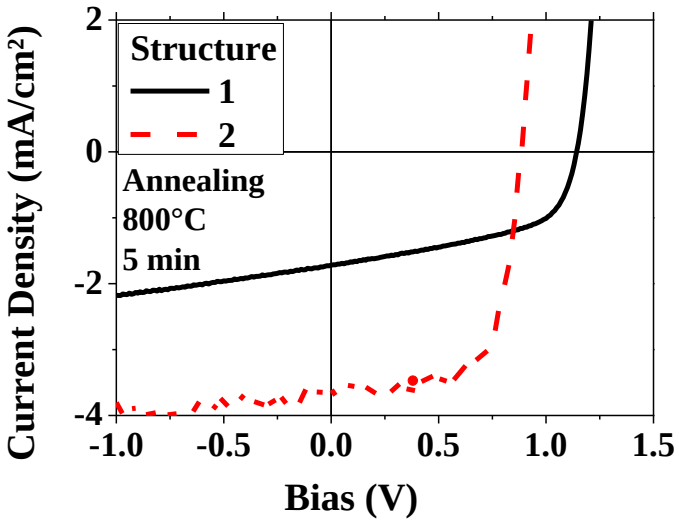

Figure 5-12: LIV measurements under AM1.5G made on solar cells having different structure: 2 (red dash) and 1 (black line).

The new structure (n°2) I-V displayed in Figure 5-12 shows a strong increase of the fill factor (FF) and the short current density (J_{sc}) from 49 to 71 % and from 2.8 to 3.77 mA/cm² respectively compared to structure 1 (Figure 5-7) with substrate thinned to 200 µm. One can observe the open-circuit voltage (V_{oc}) decrease from 1.18 to 0.886 V, this could be due to the higher energy scale of the compositional fluctuation of this sample (E_{long} = 48 meV). The J_{sc} increase origin is more difficult to explain due to the use of two different structures and to the difference in the absorber PL quenching. From the IQE measurements presented in Figure 5-13 one can see that the J_{sc} increase is mainly due to a strong increase of the carrier collection in the blue region. This seems to indicate that in structure 2 the absorber is thinner than the minority carrier diffusion length which is not the case in structure one. This effect would be enhanced by the PL quenching decrease from 400 to 100 between structure 1 and 2 respectively. The overall efficiency has been greatly enhanced from 1.6% to 2.25% using this new structure. On Figure 5-13, the IQE of the actual state of art GaAsPN / GaP solar cell developed at NREL, has been plotted for comparison. Considering that the best results obtain by the NREL has been obtained using a 600 nm thick GaAsPN absorber, the efficiency reach with structure 2 is really promising as dilute nitride absorber thickness is only 300 nm.

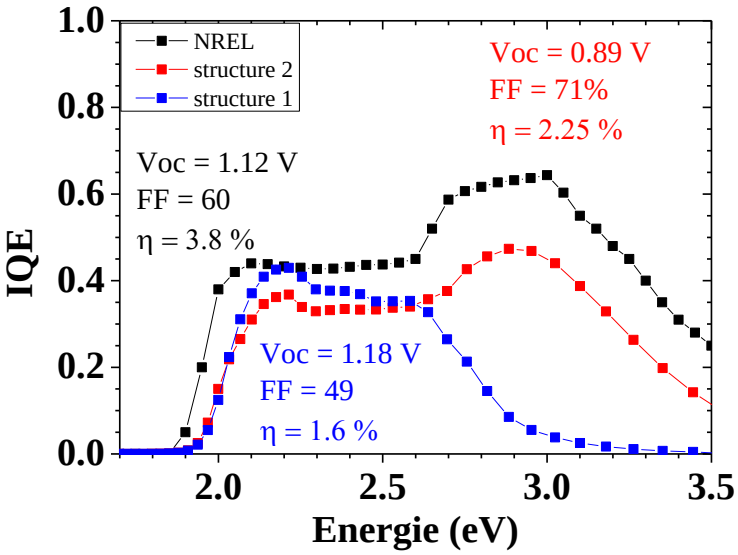

Figure 5-13: IQE measurements performed on GaAsPN solar cells developed at FOTON (red square structure 2 and blue square structure 1) compared to the best published GaAsPN single junction solar cells developed at NREL (black square).

5.3 Correlation between PL and I-V properties

The results of the bandgap-voltage offset ($W_{oc} = E_g/q - V_{oc}$) and short circuit current measured on solar cells correlate well to the energy scale of the compositional disorder at long range and to the PL intensity quenching measured on these solar cells respectively (see Chapter 4). Same kind of correlations has been attempted in the GaInAsN(Sb) system.[312]

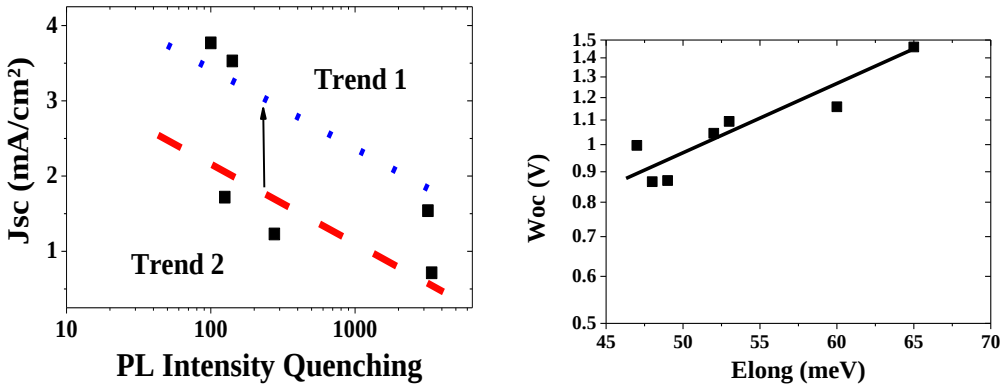

Figure 5-14: (a) Short-circuit current density plotted as a function of the PL intensity quenching measured on different solar cells (b) Bandgap-voltage offset plotted as a function of the energy scale of compositional fluctuation at long range measured on these solar cells.

In Figure 5-14 (a) short current density of several solar cells are plotted as a function of the PL intensity quenching measured on these solar cells. On this figure, two main trends (blue dot → trend 1 and red dash → trend 2) can be observed. This two trends can be explain by the fact that solar cells following the trend 1(blue dot) collect light in the blue region, increasing their J_{sc}. This is not the case in solar cells following the trend 2 (red dash line). Also from these measurements it is clear that the lower the PL quenching is the higher J_{sc} will be. This validates the interest of our approach to optimize Ga(As)PN-based alloys.

In Figure 5-14 (b) bandgap-voltage offset of different solar cells is plotted as a function of energy scale compositional disorder at long range measured on these solar cells. W_{oc} gives important information on material quality. Indeed when W_{oc} = 0.4 V, solar cells approach their theoretical maximum open circuit voltage. In this case, only one trend is observed. This indicates that W_{oc} and E_{long} parameters are less dependent from the solar cell structure than the PL quenching and the short current density. Moreover from these measurements it is clear that the lower the E_{long} is, the lower W_{oc} will be and thus the higher V_{oc} will be. This strengthen our approach to optimize Ga(As)PN-based alloys. According to the slope of Figure 5-14 (b), W_{oc} equal 0.4V when E_{long} equal roughly 25 meV. This can be explained as when E_{long} = 25 meV carrier has enough thermal energy at 300K to escape from the localization potential.

From these clear correlations, it becomes obvious that processes which limit PL performance are also the ones hindering optimum device performance. Those graphs can also be used to optimize devices using simple Ga(As)PN bulk test structures and measure temperature dependent PL properties under always identical conditions.

5.4 Summary

In this chapter I have first presented the preliminary studies made in order to make solar cells. Modelling has shown that a 1 µm thick GaAsPN layer should be optimal for the solar cell efficiency. Using modelling, two different tunnel junctions have been investigated and found suitable for the 1.7 eV / 1.1 eV targeted tandem cell structure Theoretical current densities as large as 4.4 10^5 mA/cm² in the GaP(n+)/Si(p+) TJ case and 5.5.10^2 mA/cm² for the Si(n+)/Si(p+) one has been calculated, suitable for the tandem cell application. High GaP doping level (1^{e19}) for both type of doping (n and p),

necessary for the solar cell realization, has been achieved. Low specific contact resistance (10^{-5} Ω.cm) has been demonstrated on both GaP (p) and GaP(n) using CTLM.

Then I have presented results on the solar cells growth and structure optimization. Using an annealing step (800°C), substrate (from 400 µm to 200 µm) and window layer thinning (from 200 nm to 30 µm), an improvement of the solar cell efficiency has been demonstrated. A GaAsPN /GaP single junction has been fabricated with 2.25% efficiency with a 300 nm-thick absorber. Considering the low thickness of the GaAsPN layer in this sample those results are very encouraging. Nevertheless IQE measurements on thicker sample have shown that the minority carrier diffusion length of the GaAsPN alloy still needs to be improved.

Clear correlations, between I-V and PL properties have been demonstrated. This shows that processes which limit PL performance are also the ones hindering optimum device performance. This information give a powerful tool to optimize devices using simple bulk Ga(As)PN test structures and measuring PL properties under temperature-dependent conditions. This gives the hope of improving the GaAsPN minority carrier diffusion length that has been shown to limit our device efficiency.

CONCLUSIONS AND PERSPECTIVES

This thesis focuses on the optimization of heterogeneous growth of III-N-V solar cells on GaP (001) substrate and III-V materials on Si (001). The main purpose is to build high efficiency solar cells on the low-cost Si substrate for CPV applications.

In the first part, we have worked on the optimization of the GaP/Si interface. This study reveals an important influence of the Ga exposure, III-V ratio and growth temperature on the reduction of MT. We have developed an optimized GaP/Si thin films growth recipe by achieving flat surface and very low MT density.

We have also demonstrated an early annihilation of APDs, using AlGaP interlayers. However, APDs and APBs are still present in the structure, which should be improved by further growth developments.

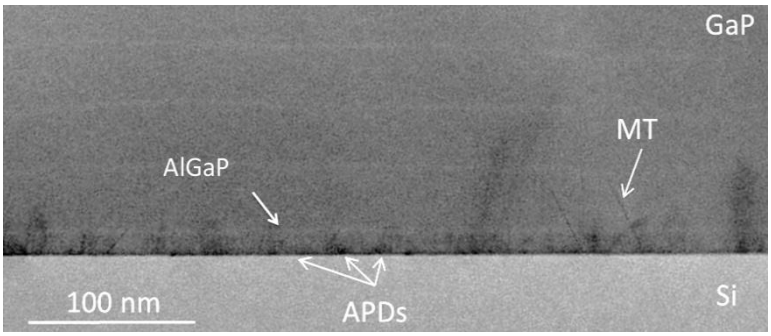

Sample TEM micrograph showing the APD annihilation on the first AlGaP marker.

In the second part we have first, studied the nitrogen incorporation in the GaPN-based alloys as a function of different key parameters of the growth. The influence of growth conditions on N incorporation has been clarified. Especially, the N content evolution with V/III BEP ratio for different growth temperatures clearly demonstrates prominent dependence of the former on the latter. We thus demonstrate that there is a competition between N and P at the growth front, implying that N incorporation coefficient depends on GaPN growth conditions. Moreover, we have shown that the growth rate controls the N concentration when other growth parameters are constant, as already shown in the GaInAsN(Sb) system.

Then we have developed a specific modelling of the photoluminescence properties and demonstrated that the quantitative determination of the E_{long}, E_{short} and $I_{10k/I300K}$ can be used to qualify the material overall quality. We then present results from temperature dependent PL measurements to optimize the GaPN-based growth and the annealing process. In order to grow high-quality high N-incorporation dilute nitride materials, it is found that the growth temperature should stay in the [300-500°C] range, with a V/III BEP ratio between 8 and 12, like in the growth of the GaInAsN compounds, to minimize the PL quenching and the energy scale of the compositional fluctuation at long and short range. An annealing step at 800°C during 1-10 min is found to improve the dilute nitride material quality as it strongly reduces the PL linewidth.

After the work performed on GaPN, I have worked on the bulk GaAsPN dilute nitride material. We have shown a good control of the As incorporation in GaP, which allows to grow quasi lattice matched GaAsPN layers on GaP(001) substrate. A comparison between a GaPN and a lattice matched GaAsPN sample grown in similar growth conditions shows an improvement of the optical properties attributed to the lattice mismatch decrease as no strong difference in their N incorporation has been evidenced, and also to the addition of As, which reinforces the direct bandgap character. A 1 µm thick GaAsPN absorber quasi lattice-matched with a GaP substrate has been grown. This sample presents no relaxation and a strong absorption around the desire 1.8 eV suitable for tandem applications on Si.

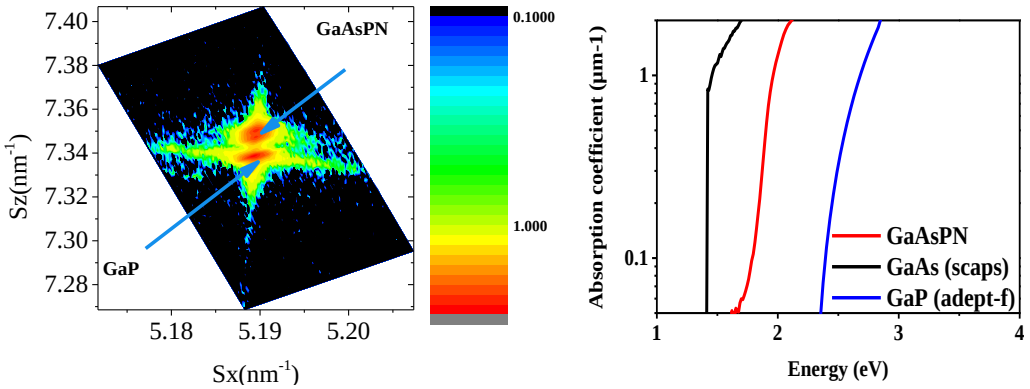

RSM (left) performed on the 224) GaP reflection,of a 1 µm thick GaAsPN layer grown quasi lattice matched with the substrate and absorption coefficient of a GaAsPN layer (red line), GaAs extracted from the software SCAPS (black line) and GaP (blue line) extracted from the software ADEPT-F

A study performed on 300 nm thick strained GaAsPN samples has shown that increasing the growth rate and decreasing the growth temperature decreases E_{long} and E_{short}, because it decreases the density of localized N-states caused by compositional fluctuations. Finally, a comparison between the GaInAsN and GaAsPN compounds has been drawn, in particular on the growth parameters influence. This comparison indicates clear similarities between both material systems, which pave the way to the growth of high quality GaAsPN alloys, continuing following the approach which has allowed the successful development of the GaInAsN-based 1 eV junction..

The third part of this thesis has been focused on the growth of GaPN based solar cells on GaP (001) substrate. I have first presented the preliminary studies made in order to fabricate solar cells. A modelling study has shown that a 1 µm thick GaAsPN layer should be optimal for the solar cell efficiency. Using modelling, two different tunnel junctions have also been investigated and found suitable for the 1.7 eV / 1.1 eV targeted tandem cell structure. Theoretical current densities as large as 4.4 10^5 mA/cm² in the GaP(n+)/Si(p+) TJ case and 5.5.10^2 mA/cm² for the Si(n+)/Si(p+) one has been calculated, suitable for the tandem cell application. High GaP doping level (1^{e19}) for both type of doping (n and p), necessary for the solar cell realization, has been achieved. Low specific contact resistance (10^{-5} Ω.cm) has been demonstrated on both GaP (p) and GaP(n) using CTLM.

Then I have presented results on the solar cells growth and structure optimization. Using an annealing step (800°C), substrate (from 400 µm to 200 µm) and window layer thinning (from 200 nm to 30 µm), an improvement of the solar cell efficiency has been demonstrated. A GaAsPN /GaP single junction has been fabricated with 2.25% efficiency with a 300 nm-thick absorber. Considering the low thickness of the GaAsPN layer in this sample those results are very encouraging. Nevertheless IQE measurements on 1 µm thick sample have shown that the minority carrier diffusion length of the GaAsPN alloy still needs to be improved.

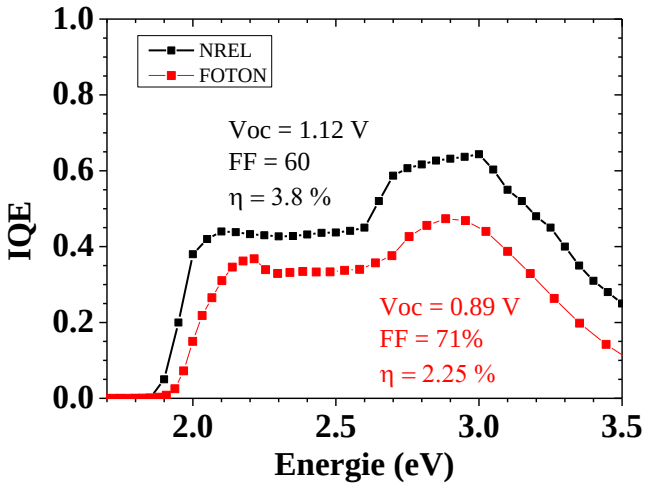

IQE measurements performed on our best GaAsPN solar cells (red square) compared to the best published GaAsPN cells (black square).[154]

Clear correlations, between I-V and PL properties have been demonstrated. This shows that processes which limit PL performance are also the ones hindering optimum device performance. This information gives a powerful tool to optimize devices using simple bulk Ga(As)PN test structures and measuring PL properties under temperature-dependent conditions. This gives the hope of improving the GaAsPN minority carrier diffusion length that has been shown to limit our device efficiency.

Suggestions for future works

In a general objective of growing a tandem cell architecture, the charge carriers should tunnel through the interface. Therefore, the growth of the GaP/Si should further be optimized in order to reduce the APD density at the interface. This could be done by working on the prenuclation layer using Al following the approach of Lin *et al.*[252] Also the use of bi-stepped Si on oriented substrate should help to reduce the APD density.[125] In order to connect the Si cell with GaAsPN top cell test on the modeled tunnel junction should be lead using either Si homotunnel junction or GaP(n)/Si(p) heterojunction.[304,313]

In this work, the control of the growth condition has been pointed as being of major importance to improve the electrical properties of GaPN-based materials. It has been found that by increasing the growth rate, compositional fluctuation in the dilute nitride decrease. Nevertheless due the constant sticking coefficient of N, confirmed in this

study, the increase of the growth rate decreases the N content in the layer.[297] Thus strategies to increase the N content must be found. Growth studies on plasma parameters effect on N incorporation could be interesting to increase the N content in GaPN based material while keeping a high growth rate. In order to understand the nature of defects in GaPN-based materials, deep level transient spectroscopies (DLTS) studies has been launched during this thesis on GaAsPN solar cells in collaboration with the group of M.Henini from the University of Nottingham.

Another way to improve GaPN-based alloys electrical and bandgap properties could be to study the growth effect of other atoms in the GaPN alloy. Studies on Sb incorporation could be very interesting as the use of antimony has been proven to improve the minority carrier diffusion length in dilute nitride material such as GaInAsNSb. Also a study of the growth influence of In, Al, B, or Bi on GaPN-based material could be interesting, as those atoms have all different effect on N incorporation and GaPN bandgap.

As this thesis focuses on the growth of high quality dilute nitride material, the impact of PV structure hasn't been fully studied. The use of window layer such as AlGaP or GaInP could improve the carrier collection on the front surface. Also no passivation layers have been used in the presented structure. However preliminary studies, have been launched in collaboration with the team of A. Etcheberry at Institut Lavoisier de Versailles (ILV) for the use of poly-phosphazene thin layer to passivate the GaP front surface.[314] Finally to fully optimize the top junction one should use a broadband anti-reflective coating such as MgF_2/ZnS that could reduce the reflective losses estimated to be around 20 % in our structure.[315,316]

RESUME

Cette thèse se concentre sur l'optimisation de la croissance hétérogène de couches minces de phosphure de gallium épitaxiées sur substrat de silicium (100) et de cellules solaires III-N-V sur des substrats de GaP (001). Le but de ce projet est l'élaboration des cellules solaires haute efficacité sur substrat de silicium à faible coût pour les applications de cellule solaire à concentration CPV.

Les principales motivations pour le développement de cellules solaires à haut rendement et à faible coût sont de réduire l'utilisation d'énergies non-renouvelables comme les combustibles fossiles, qui a été incriminé comme étant l'une des causes du réchauffement climatique ; et de fournir une alternative compétitive pour la production de masse de l'électricité pour les centrales nucléaires. À cet égard, les efforts de recherche sont axés vers d'importantes réductions de cout, pour atteindre la parité réseau dans le monde entier sans aucune forme de subventions.

D'un point de vue sociétal, l'industrie photovoltaïque a le potentiel de créer plus de 2.000.000 emplois à travers le monde. Aussi, étant une énergie décentralisée, le photovoltaïque (PV) pourrait faciliter l'accès à l'énergie dans les zones rurales, permettant ainsi l'amélioration de la santé, l'éducation et fournir des opportunités économiques dans les pays émergents.

Du point de vue économique, il est prévu que le PV sera compétitif dans le monde entier avant 2020. La décennie à venir est considérée comme décisive en termes de quels pays ou régions du monde vont dominer le secteur industriel futur du PV. Par conséquent, l'effort de recherche dans ce secteur est important compte tenu de sa croissance rapide et des possibilités économiques qu'elle peut apporter. Une façon possible d'atteindre la parité réseau est l'élaboration de cellules solaires hautes efficacités sur substrat à faible coût pour des applications type centrale à concentration.

De nos jours les cellules solaire atteignant les meilleurs rendements (supérieur à 44%) sont appelé multijonction (MJSC). Dans cette configuration, plusieurs cellules

sont connectées en série à travers une ou plusieurs jonctions tunnel, ainsi la cellule ayant le plus faible courant limite le courant électrique à travers la MJSC. Le courant d'une cellule étant intrinsèquement liée à son énergie de bande interdite, celle-ci doit être ajustée avec soin pour maximiser le courant délivré.

Les MJSC étant fabriquées sur des substrats couteux comme l'arséniure de gallium GaAs et le germanium Ge. L'utilisation du silicium comme substrat alternatif pour la fabrication de cellules solaire multijonction (MJSC) permettrait de réduire considérablement le coût de l'énergie photovoltaïque. En effet le Si est au moins 10 fois moins cher que les matériaux des substrats de MJSC classiques. En outre, les substrats de Si sont également disponibles en plus grande tailles de wafer (300 mm de diamètre en 2009 et 450 mm aujourd'hui) que les diamètres typique de 100 à 150 mm des substrats de Ge ou GaAs. Sachant que les coûts de traitement des substrats et d'épitaxie ne changent pas de manière significative avec la taille des wafers, cela permettrait également de diminuer le coût de fabrication de cellules solaires. Un autre des avantages du silicium est la maturité de son industrie, permettant la montée en cadence rapide, avec des volumes et un débit élevé. Avec des rendements de conversion solaire attendus autour de 30 à 40%, les MJSC sur Si sont très prometteuses et pourraient permettre d'accélérer la transition énergétique, avec un investissement en capital réduit comparé à ce qu'on pourrait attendre d'une technologie nécessitant la fabrication d'une nouvelle industrie. Il est clair que le cas de la technologie III-V / Si est très différent de toutes les autres technologies PV, déjà matures ou en cours d'élaboration grâce à la forte capacité de pénétration du marché de l'industrie du Si.

Dans la poursuite de cet objectif, les chercheurs du NREL ont proposé en 2002 de travailler sur les nitrures dilués de type Ga(As)PN. Ce matériau peut être fabriqué en accord de maille avec Si et avoir une forte absorption autour de 1,7 à 1.8 eV requis pour la fabrication de cellules tandems sur silicium. En utilisant cette approche, ils ont démontré une cellule solaire tandem avec un rendement de 5,2%. Cette valeur bien loin des 40% attendus a été attribuée à: de mauvaises performances au niveau de la jonction tunnel mais aussi à une faible longueur de diffusion des porteurs minoritaires dans le matériau à base de nitrures dilués. Les faibles performances au niveau de la jonction tunnel peuvent s'expliquer par la difficulté de faire croître des semiconducteurs III-V fortement dopés sur du Si, due à de nombreuses incompatibilités au niveau des

matériaux (Polarité, structure cristalline, paramètre de maille, coefficient d'expansion thermique) créant de nombreux défauts (paroi d'antiphases, micromacles).

Néanmoins des expériences menées sur des substrats de GaP ont montré que les performances de la cellule tandem étaient aussi limitées par les propriétés électriques du GaAsPN. La faible longueur de diffusion des porteurs minoritaires dans le matériau à base de nitrures dilués peut s'expliquer par la difficulté par la présence de défauts dans ce matériau (Ga interstitiel, lacune de Ga, P_{As} antisite, agrégat d'azote, fluctuation de composition). Cela peut s'expliquer par la métastabilité des nitrures dilués et le fait que dans l'étude menée par le NREL, la croissance a été réalisée par épitaxie en phase vapeur (MOCVD). En effet récemment plusieurs équipes ont montré qu'en utilisant l'épitaxie par jets moléculaires (MBE) et une stratégie de croissance adaptée à la fabrication de matériaux métastables, on pouvait obtenir des nitrures dilués ayant une longueur de diffusion des porteurs minoritaires supérieure à 1 µm, permettant la réalisation de cellules solaires haute performance.

Dans la première partie, nous avons travaillé sur l'optimisation de l'interface GaP/Si. Cette étude révèle une influence importante des paramètres de croissance sur la réduction de MT. Nous avons développé une recette de croissance pour la fabrication de film mince de GaP / Si ayant une surface plane et une densité de micro-macles très faible.

Des résultats préliminaires montrent que l'utilisation de film mince d'AlGaP permet de diminuer fortement la densité de paroi d'antiphase émergente.

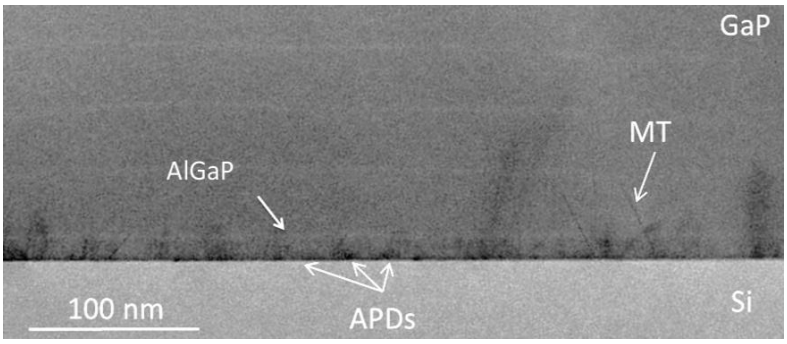

TEM micrographe montrant l'annihilation des APDs au premier marqueur d'AlGaP.

Dans la deuxième partie, nous avons d'abord étudié l'incorporation d'azote dans GaP, en fonction de différents paramètres clés de la croissance. L'influence des conditions de croissance sur l'incorporation d'azote a été clarifiée. L'évolution de la

composition en azote en fonction du rapport V / III pour différentes températures de croissance, démontre clairement la dépendance importante de la première sur la seconde. Nous démontrons ainsi qu'il existe une compétition entre l'azote et le phosphore lors de la croissance. Ceci implique que le coefficient d'incorporation de l'azote dépend des conditions de croissance. En outre, nous avons montré que la vitesse de croissance contrôle l'incorporation d'azote dans GaP lorsque les autres paramètres de croissance sont constants. Ce comportement a été aussi mis en évidence dans le système GaInAsN (Sb).

Ensuite, nous avons développé un modèle de photoluminescence pour les nitrures dilués et utilisé ce modèle pour optimiser la croissance du GaPN. D'après ces études, comme pour celles menées sur le système GaInAsN, la meilleure approche pour la croissance des nitrures dilués est de les faire croitre à basse température [300-500°C] (pour assurer une incorporation d'azote élevée), avec un rapport V / III entre 8 et 12 (pour minimiser la densité de défauts non radiatifs et la séparation de phase). Comme dans le cas de GaInAsN, une seconde étape de recuit à 800 ° C pendant 1 à 10 min permet d'améliorer les propriétés optiques des nitrures dilués.

Après l'optimisation de la croissance de GaPN, nous avons travaillé sur l'incorporation d'arsenic dans GaPN. Nous avons montré que l'incorporation d'As dans GaPN peut être contrôlée en faisant varier le flux d'As. Cela permet de faire croitre des couches de GaAsPN en quasi-accord de maille avec GaP (100). Une comparaison entre deux échantillons un de GaPN et un de GaAsPN, crut dans des conditions similaires (températures, rapport V/III) montre une amélioration des propriétés optiques dues à l'incorporation d'As. Cette amélioration a été attribuée à la diminution des contraintes, favorisant la diminution de la formation de défauts points, tels que le gallium interstitiel. Une fois le quasi accord de maille atteint, un absorbeur de GaAsPN d'1 µm sur un substrat de GaP a été fabriqué. Cet échantillon présente un désaccord de maille de 0.02%, est contraint et montre une forte absorption autour de 1.8 eV, adaptée pour la réalisation de cellule tandem sur Si.

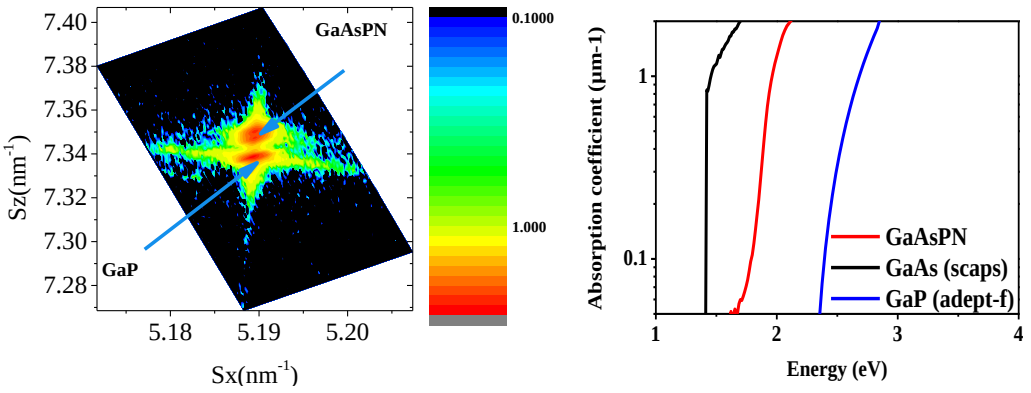

Cartographie de l'espace réciproque (gauche) faite sur la réflexion (224) du GaP d'un échantillon de GaAsPN d' 1 µm en quasi accord de maille avec un substrat de GaP (100) et les coefficients d'absorption du GaAsPN (ligne rouge), de GaAs extraite du programme SCAPS (ligne noire) et de GaP (line bleue) extraite du programme ADEPT-F

Une étude effectuée sur des échantillons contraints de GaAsPN d'épaisseur 300 nm a montré que l'augmentation de la vitesse de croissance et la diminution de la température de croissance diminue E_{long} et E_{short}. Ces effets ont été attribués à la diminution de la densité d'états localisés causée par des fluctuations de composition.

Enfin une discussion sur les effets des paramètres de croissance sur les propriétés optiques de GaInAsN(Sb) et GaAsPN indiquent des similarités au niveau de la croissance entre ces deux systèmes de matériaux. Ces informations donnent l'espoir de pouvoir fabriquer du GaAsPN ayant une longueur de diffusions des porteurs minoritaires supérieure à 1µm en utilisant l'approche développée avec succès pour le matériau GaInAsN(Sb).

La troisième partie de cette thèse a été axée sur la croissance de cellules solaires simple jonction à base de GaAsPN sur substrat de GaP (001). Les études préliminaires de modélisation sur la fabrication des cellules solaires menées avec le logiciel SILVACO montrent qu'une épaisseur de GaAsPN d' 1 µm permet d'optimiser l'efficacité des cellules solaires. D'autre part des niveaux de dopages élevés (1e19), (nécessaires à la réalisation de cellules solaires) dans GaP ont été atteints pour les deux types de dopages (n et p). Aussi des faibles résistances spécifiques de contacts (10^{-5} Ω.cm) ont été obtenues à la fois sur GaP (p) et GaP (n).

Ensuite, des résultats sur la croissance des cellules solaires et l'optimisation de la structure sont présentés. Une amélioration de l'efficacité des cellules solaires a été démontré, en utilisant une étape de recuit (800 ° C), un amincissement du substrat (de

400 µm à 200 µm) et de la couche de fenêtre (de 200 nm à 30 nm). Une cellule solaire simple jonction GaAsPN/GaP avec un rendement de 2.25% a été démontrée. Considérant la faible épaisseur de la couche de GaAsPN dans cet échantillon, ces résultats sont très encourageants. Néanmoins les mesures d'IQE sur des échantillons plus épais ont montré que les longueurs de diffusions des porteurs minoritaires dans l'alliage de GaAsPN limitent encore les performances des cellules solaires.

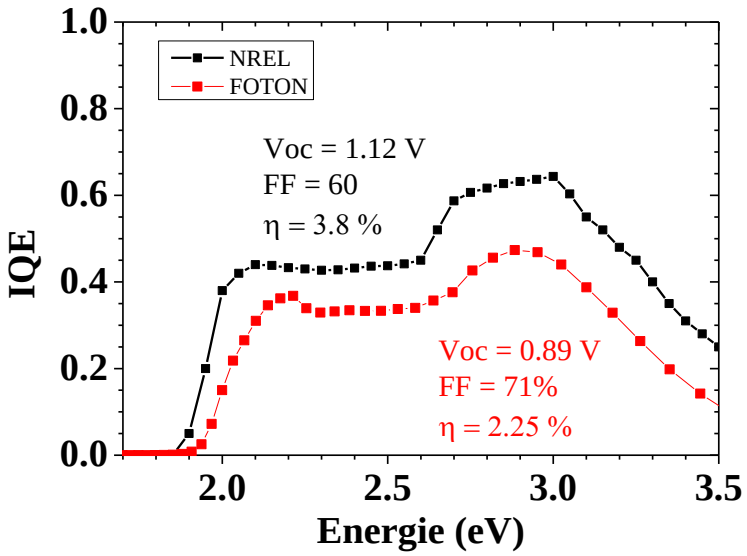

Mesure d'IQE faite sur notre meilleure cellule solaire GaAsPN (carrés rouges) comparé à la meilleure cellule solaire GaAsPN publiée (carrés noirs).[154]

Enfin des corrélations claires, entre les propriétés optiques et électriques ont été démontrées donnant un outil puissant pour optimiser la croissance de GaAsPN en utilisant des structures simples grâce à des mesures optiques comme la photoluminescence.

REFERENCES

[1] C.W. Team, (http://www.ipcc.ch/pdf/assessment-report/ar4/syr/ar4_syr.pdf).
[2] D. MacKay and D.J.C. Mackay, *Sustainable Energy: Without the Hot Air* (UIT withouthotair.com., Cambridge; [Online], 2009).
[3] http://www.rethinking2050.eu/fileadmin/documents/ReThinking2050_full_version_final.pdf EREC report (7/19/2013)
[4] http://www.iea.org/publications/freepublications/publication/pv_roadmap_foldout.pdf IEA report (7/23/2013)
[5] A. Luque and S. Hegedus, *Handbook of Photovoltaic Science and Engineering* (Wiley, Chichester, West Sussex, U.K., 2011).
[6] M. Yamaguchi, Energy Procedia **15**, 265 (2012).
[7] P.R. i Cabarrocas, in *Phys. Technol. Amorph.-Cryst. Heterostruct. Silicon Sol. Cells*, edited by W.G.J.H.M. van Sark, L. Korte, and F. Roca (Springer Berlin Heidelberg, 2012), pp. 131–160.
[8] M. Liu, M.B. Johnston, and H.J. Snaith, Nature **501**, 395 (2013).
[9] T.K. Todorov, J. Tang, S. Bag, O. Gunawan, T. Gokmen, Y. Zhu, and D.B. Mitzi, Adv. Energy Mater. **3**, 34 (2013).
[10] A. Duchatelet, T. Sidali, N. Loones, G. Savidand, E. Chassaing, and D. Lincot, Sol. Energy Mater. Sol. Cells **119**, 241 (2013).
[11] W. Shockley and H.J. Queisser, J. Appl. Phys. **32**, 510 (1961).
[12] T. Tiedje, E. Yablonovitch, G.D. Cody, and B.G. Brooks, Electron Devices IEEE Trans. On **31**, 711 (1984).
[13]http://pveducation.org/pvcdrom. (10/24/2014)
[14] P. Würfel, Phys. E Low-Dimens. Syst. Nanostructures **14**, 18 (2002).
[15] U. Gangopadhyay, S. Jana, and S. Das, Conf. Pap. Sci. **2013**, e764132 (2013).
[16] M.A. Green, K. Emery, Y. Hishikawa, W. Warta, and E.D. Dunlop, Prog. Photovolt. Res. Appl. **23**, 1 (2015).
[17] A. Luque and A. Martí, Phys. Rev. Lett. **78**, 5014 (1997).
[18] R.T. Ross and A.J. Nozik, J. Appl. Phys. **53**, 3813 (1982).
[19] M.A. Green, Prog. Photovolt. Res. Appl. **9**, 123 (2001).
[18]http://www.nrel.gov/ncpv/images/efficiency_chart.jpg. (10/24/2014)
[21] A. Martí and G.L. Araújo, Sol. Energy Mater. Sol. Cells **43**, 203 (1996).
[22] I. García, I. Rey-Stolle, and C. Algora, J. Phys. Appl. Phys. **45**, 045101 (2012).
[23] A. Aho, A. Tukiainen, V.-M. Korpijärvi, V. Polojärvi, J. Salmi, and M. Guina, in (2012), pp. 49–52.
[24] J.F. Geisz, D.J. Friedman, J.S. Ward, A. Duda, W.J. Olavarria, T.E. Moriarty, J.T. Kiehl, M.J. Romero, A.G. Norman, and K.M. Jones, Appl. Phys. Lett. **93**, 123505 (2008).
[25] R.R. King, D.C. Law, K.M. Edmondson, C.M. Fetzer, G.S. Kinsey, H. Yoon, R.A. Sherif, and N.H. Karam, Appl. Phys. Lett. **90**, 183516 (2007).
[26] M.S. Leite, R.L. Woo, W.D. Hong, D.C. Law, and H.A. Atwater, Appl. Phys. Lett. **98**, 093502 (2011).

[27] D.B. Jackrel, S.R. Bank, H.B. Yuen, M.A. Wistey, J.S. Harris, A.J. Ptak, S.W. Johnston, D.J. Friedman, and S.R. Kurtz, J. Appl. Phys. **101**, 114916 (2007).
[28] J.F. Geisz and D.J. Friedman, Semicond. Sci. Technol. **17**, 769 (2002).
[29] W. Shan, W. Walukiewicz, K.M. Yu, J. Wu, J.W. Ager, E.E. Haller, H.P. Xin, and C.W. Tu, Appl. Phys. Lett. **76**, 3251 (2000).
[30] H.P. Xin, C.W. Tu, Y. Zhang, and A. Mascarenhas, Appl. Phys. Lett. **76**, 1267 (2000).
[31] J.C.C. Fan, B.-Y. Tsaur, and B.J. Palm, in *16th Photovolt. Spec. Conf.* (1982), pp. 692–701.
[32] J.M. Olsen, S.R. Kurtz, and A.E. Kibbler, in *Conf. Rec. Twent. IEEE Photovolt. Spec. Conf. 1988* (1988), pp. 777–780 vol.1.
[33] J.M. Olson, S.R. Kurtz, A.E. Kibbler, and P. Faine, Appl. Phys. Lett. **56**, 623 (1990).
[34] S.R. Kurtz, P. Faine, and J.M. Olson, J. Appl. Phys. **68**, 1890 (1990).
[35] K.A. Bertness, S.R. Kurtz, D.J. Friedman, A.E. Kibbler, C. Kramer, and J.M. Olson, Appl. Phys. Lett. **65**, 989 (1994).
[36] D.J. Friedman, S.R. Kurtz, K.A. Bertness, A.E. Kibbler, C. Kramer, J.M. Olson, D.L. King, B.R. Hansen, and J.K. Snyder, Prog. Photovolt. Res. Appl. **3**, 47 (1995).
[37] S.R. Kurtz, K.A. Bertness, D.J. Friedman, A.E. Kibbler, C. Kramer, and J.M. Olson, in *IEEE Photovolt. Spec. Conf. - 1994 1994 IEEE First World Conf. Photovolt. Energy Convers. 1994 Conf. Rec. Twenty Fourth* (1994), pp. 2108–2111 vol.2.
[38] P.K. Chiang, D.D. Kurt, B.T. Cavicchi, K.A. Bertness, S.R. Kurtz, and J.M. Olson, in *IEEE Photovolt. Spec. Conf. - 1994 1994 IEEE First World Conf. Photovolt. Energy Convers. 1994 Conf. Rec. Twenty Fourth* (1994), pp. 2120–2123 vol.2.
[38](http://www.nrel.gov/news/press/2013/2226.html).
[40] S. Kurtz, D. Myers, W.E. McMahon, J. Geisz, and M. Steiner, Prog. Photovolt. Res. Appl. **16**, 537 (2008).
[41] C. Pelosi, G. Attolini, C. Bocchi, P. Franzosi, C. Frigeri, M. Berti, A.V. Drigo, and F. Romanato, J. Electron. Mater. **24**, 1723 (1995).
[42] Y. Li, G. Salviati, M.M.G. Bongers, L. Lazzarini, L. Nasi, and L.J. Giling, J. Cryst. Growth **163**, 195 (1996).
[43] J.C. Chen, M.L. Ristow, J.I. Cubbage, and J.G. Werthen, J. Electron. Mater. **21**, 347 (1992).
[44] J.M. Olson and W.E. McMahon, *Structure of Ge (100) Surfaces for High-Efficiency Photovoltaic Applications* (National Renewable Energy Laboratory, 1998).
[45] S. Bruckner, O. Supplie, E. Barrigon, P. Kleinschmidt, A. Dobrich, I. Rey-Stolle, C. Algora, H. Doscher, and T. Hannappel, in *2011 37th IEEE Photovolt. Spec. Conf. PVSC* (2011), pp. 002538–002542.
[46] S. Brückner, O. Supplie, E. Barrigón, J. Luczak, P. Kleinschmidt, I. Rey-Stolle, H. Döscher, and T. Hannappel, Appl. Phys. Lett. **101**, 121602 (2012).
[47] M.T. Currie, S.B. Samavedam, T.A. Langdo, C.W. Leitz, and E.A. Fitzgerald, Appl. Phys. Lett. **72**, 1718 (1998).
[48] S.M. Ting and E.A. Fitzgerald, J. Appl. Phys. **87**, 2618 (2000).
[49] R.R. King, D.C. Law, K.M. Edmondson, C.M. Fetzer, G.S. Kinsey, H. Yoon, D.D. Krut, J.H. Ermer, R.A. Sherif, and N.H. Karam, Adv. Optoelectron. **2007**, e29523 (2007).
[50] S.R. Kurtz, D. Myers, and J.M. Olson, in *Conf. Rec. IEEE Photovolt. Spec. Conf.* (IEEE INC, 1997), pp. 875–878.
[51] W. Guter, J. Schöne, S.P. Philipps, M. Steiner, G. Siefer, A. Wekkeli, E. Welser, E. Oliva, A.W. Bett, and F. Dimroth, Appl. Phys. Lett. **94**, 223504 (2009).
[52] S.P. Ahrenkiel, M.W. Wanlass, J.J. Carapella, L.M. Gedvilas, B.M. Keyes, R.K. Ahrenkiel, and H.R. Moutinho, J. Electron. Mater. **33**, 185 (2004).

[53] T. Takamoto, H. Washio, and H. Juso, in *Photovolt. Spec. Conf. PVSC 2014 IEEE 40th* (2014), pp. 0001–0005.
[54] M. Stan, D. Aiken, B. Cho, A. Cornfeld, V. Ley, P. Patel, P. Sharps, and T. Varghese, J. Cryst. Growth **312**, 1370 (2010).
[55] M. Reiche, Phys. Status Solidi A **203**, 747 (2006).
[56] U. Gösele and Q.-Y. Tong, Annu. Rev. Mater. Sci. **28**, 215 (1998).
[57] H. Moriceau, F. Rieutord, F. Fournel, Y.L. Tiec, L.D. Cioccio, C. Morales, A.M. Charvet, and C. Deguet, Adv. Nat. Sci. Nanosci. Nanotechnol. **1**, 043004 (2010).
[58] K. Derendorf, S. Essig, E. Oliva, V. Klinger, T. Roesener, S.P. Philipps, J. Benick, M. Hermle, M. Schachtner, G. Siefer, W. Jager, and F. Dimroth, IEEE J. Photovolt. **3**, 1423 (2013).
[59] D. Bhusari, D. Law, R. Woo, J. Boisvert, S. Mesropian, D. Larrabee, W. Hong, and N. Karam, in *2011 37th IEEE Photovolt. Spec. Conf. PVSC* (2011), pp. 001937–001940.
[60] D.C. Law, R.R. King, H. Yoon, M.J. Archer, A. Boca, C.M. Fetzer, S. Mesropian, T. Isshiki, M. Haddad, K.M. Edmondson, D. Bhusari, J. Yen, R.A. Sherif, H.A. Atwater, and N.H. Karam, Sol. Energy Mater. Sol. Cells **94**, 1314 (2010).
[61] K. Tanabe, D.J. Aiken, M.W. Wanlass, A.F. i Morral, and H.A. Atwater, in *Conf. Rec. 2006 IEEE 4th World Conf. Photovolt. Energy Convers.* (2006), pp. 768–771.
[62] M. Kondow, K. Uomi, K. Hosomi, and T. Mozume, Jpn. J. Appl. Phys. **33**, L1056 (1994).
[63] M. Kondow, T. Kitatani, S. Nakatsuka, M.C. Larson, K. Nakahara, Y. Yazawa, M. Okai, and K. Uomi, IEEE J. Sel. Top. Quantum Electron. **3**, 719 (1997).
[64] M. Kondow, K. Uomi, T. Kitatani, S. Watahiki, and Y. Yazawa, J. Cryst. Growth **164**, 175 (1996).
[65] S.-H. Wei and A. Zunger, Phys. Rev. Lett. **76**, 664 (1996).
[66] N. Shtinkov, P. Desjardins, and R.A. Masut, Phys. Rev. B **67**, 081202 (2003).
[67] P.R.C. Kent and A. Zunger, Phys. Rev. B **64**, 115208 (2001).
[68] W. Shan, W. Walukiewicz, J.W. Ager, E.E. Haller, J.F. Geisz, D.J. Friedman, J.M. Olson, and S.R. Kurtz, Phys. Rev. Lett. **82**, 1221 (1999).
[69] J.S. Harris, R. Kudrawiec, H.B. Yuen, S.R. Bank, H.P. Bae, M.A. Wistey, D. Jackrel, E.R. Pickett, T. Sarmiento, L.L. Goddard, V. Lordi, and T. Gugov, Phys. Status Solidi B **244**, 2707 (2007).
[70] W.M. Chen, I.A. Buyanova, C.W. Tu, and H. Yonezu, Phys. B Condens. Matter **376–377**, 545 (2006).
[71] R.J. Kaplar, S.A. Ringel, S.R. Kurtz, J.F. Klem, and A.A. Allerman, Appl. Phys. Lett. **80**, 4777 (2002).
[72] A. Aho, A. Tukiainen, V. Polojärvi, J. Salmi, and M. Guina, 86201I (2013).
[73] A.J. Ptak, S.W. Johnston, S. Kurtz, D.J. Friedman, and W.K. Metzger, J. Cryst. Growth **251**, 392 (2003).
[74] A. Erol, *Dilute III-V Nitride Semiconductors and Material Systems: Physics and Technology* (Springer, 2008).
[75] I.A. Buyanova and W.M. Chen, *Physics and Applications of Dilute Nitrides* (Taylor & Francis, New York, 2004).
[76] M. Henini, *Dilute Nitride Semiconductors* (Elsevier, Amsterdam; London, 2005).
[77] J.S. Harris Jr., J. Cryst. Growth **278**, 3 (2005).
[78] J. Neugebauer and C.G. Van de Walle, Phys. Rev. B **51**, 10568 (1995).
[79] E. Tournié, N. Grandjean, A. Trampert, J. Massies, and K.H. Ploog, J. Cryst. Growth **150**, 460 (1995).

[80] J.C. Harmand, G. Ungaro, L. Largeau, and G.L. Roux, Appl. Phys. Lett. **77**, 2482 (2000).
[81] S.G. Spruytte, M.C. Larson, W. Wampler, C.W. Coldren, H.E. Petersen, and J.S. Harris, J. Cryst. Growth **227–228**, 506 (2001).
[82] R.R. LaPierre, B.J. Robinson, and D.A. Thompson, J. Appl. Phys. **79**, 3021 (1996).
[83] F. Ishikawa, E. Luna, A. Trampert, and K.H. Ploog, Appl. Phys. Lett. **89**, 181910 (2006).
[84] H.P. Xin and C.W. Tu, Appl. Phys. Lett. **72**, 2442 (1998).
[85] S.B. Zhang and S.-H. Wei, Phys. Rev. Lett. **86**, 1789 (2001).
[86] P. Krispin, V. Gambin, J.S. Harris, and K.H. Ploog, J. Appl. Phys. **93**, 6095 (2003).
[87] N. Thinh, I. Buyanova, P. Hai, W. Chen, H. Xin, and C. Tu, Phys. Rev. B **63**, (2001).
[88] A.J. Ptak, S. Kurtz, M.H. Weber, and K.G. Lynn, J. Vac. Sci. Technol. B **22**, 1584 (2004).
[89] A. Janotti, S.-H. Wei, S.B. Zhang, S. Kurtz, and C.G. Van de Walle, Phys. Rev. B **67**, 161201 (2003).
[90] W. Li, M. Pessa, T. Ahlgren, and J. Decker, Appl. Phys. Lett. **79**, 1094 (2001).
[91] X.Z. Chen, D.H. Zhang, Y.J. Jin, J.H. Li, J.H. Teng, and N. Yakovlev, J. Cryst. Growth **362**, 197 (2013).
[92] W. Li, J. Turpeinen, P. Melanen, P. Savolainen, P. Uusimaa, and M. Pessa, Appl. Phys. Lett. **78**, 91 (2001).
[93] S.R. Bank, H.B. Yuen, H. Bae, M.A. Wistey, and J.S. Harris, Appl. Phys. Lett. **88**, 221115 (2006).
[94] S.L. Tan, C.J. Hunter, S. Zhang, L.J.J. Tan, Y.L. Goh, J.S. Ng, I.P. Marko, S.J. Sweeney, A.R. Adams, J. Allam, and J.P.R. David, J. Electron. Mater. **41**, 3393 (2012).
[95] K. Volz, D. Lackner, I. Németh, B. Kunert, W. Stolz, C. Baur, F. Dimroth, and A.W. Bett, J. Cryst. Growth **310**, 2222 (2008).
[96] S.Y. Xie, S.F. Yoon, and S.Z. Wang, J. Appl. Phys. **97**, 073702 (2005).
[97] H. Carrère, A. Arnoult, A. Ricard, X. Marie, T. Amand, and E. Bedel-Pereira, Solid-State Electron. **47**, 419 (2003).
[98] T.-C. Ma, Y.-T. Lin, and H.-H. Lin, J. Cryst. Growth **318**, 363 (2011).
[99] K. Klosek, M. Sobanska, G. Tchutchulashvili, Z.R. Zytkiewicz, H. Teisseyre, and L. Klopotowski, Thin Solid Films **534**, 107 (2013).
[100] M.M. Oye, T.J. Mattord, G.A. Hallock, S.R. Bank, M.A. Wistey, J.M. Reifsnider, A.J. Ptak, H.B. Yuen, J.S. Harris, and A.L. Holmes, Appl. Phys. Lett. **91**, 191903 (2007).
[101] H.B. Yuen, M.A. Wistey, S.R. Bank, H. Bae, and J.S. Harris, J. Vac. Sci. Technol. B Microelectron. Nanometer Struct. **23**, 1328 (2005).
[102] M.A. Wistey, S.R. Bank, H.B. Yuen, H. Bae, and J.S. Harris Jr., J. Cryst. Growth **278**, 229 (2005).
[103] D. Derkacs, R. Jones-Albertus, F. Suarez, and O. Fidaner, J. Photonics Energy **2**, 021805 (2012).
[104] H. Döscher, O. Supplie, M.M. May, P. Sippel, C. Heine, A.G. Muñoz, R. Eichberger, H.-J. Lewerenz, and T. Hannappel, Chemphyschem Eur. J. Chem. Phys. Phys. Chem. **13**, 2899 (2012).
[105] T.G. Deutsch, J.L. Head, and J.A. Turner, J. Electrochem. Soc. **155**, B903 (2008).
[106] N.S. Fatemi, H.E. Pollard, H.Q. Hou, and P.R. Sharps, in *Photovolt. Spec. Conf. 2000 Conf. Rec. Twenty-Eighth IEEE* (IEEE, 2000), pp. 1083–1086.
[107] C.-W. Cheng, K.-T. Shiu, N. Li, S.-J. Han, L. Shi, and D.K. Sadana, Nat. Commun. **4**, 1577 (2013).
[108] H. Taguchi, T. Soga, and T. Jimbo, Sol. Energy Mater. Sol. Cells **85**, 85 (2005).

[109] J.C.C. Fan, C.O. Bozler, R.P. Gale, R.W. McClelland, R.L. Chapman, G.W. Turner, and H.J. Zeiger, in *Electron Devices Meet. 1980 Int.* (1980), pp. 534–537.
[110] M.J. Archer, D.C. Law, S. Mesropian, M. Haddad, C.M. Fetzer, A.C. Ackerman, C. Ladous, R.R. King, and H.A. Atwater, Appl. Phys. Lett. **92**, 103503 (2008).
[111] O. Skibitzki, A. Paszuk, F. Hatami, P. Zaumseil, Y. Yamamoto, M.A. Schubert, A. Trampert, B. Tillack, W.T. Masselink, T. Hannappel, and T. Schroeder, J. Appl. Phys. **115**, 103501 (2014).
[112] M.L. Lee, E.A. Fitzgerald, M.T. Bulsara, M.T. Currie, and A. Lochtefeld, J. Appl. Phys. **97**, 011101 (2005).
[113] E.A. Fitzgerald, Mater. Sci. Rep. **7**, 87 (1991).
[114] S.G. Thomas, S. Bharatan, R.E. Jones, R. Thoma, T. Zirkle, N.V. Edwards, R. Liu, X.D. Wang, Q. Xie, C. Rosenblad, J. Ramm, G. Isella, and H.V. Känel, J. Electron. Mater. **32**, 976 (2003).
[115] C.L. Andre, D.M. Wilt, A.J. Pitera, M.L. Lee, E.A. Fitzgerald, and S.A. Ringel, J. Appl. Phys. **98**, 014502 (2005).
[116] M.R. Lueck, C.L. Andre, A.J. Pitera, M.L. Lee, E.A. Fitzgerald, and S.A. Ringel, IEEE Electron Device Lett. **27**, 142 (2006).
[117] E.A. Fitzgerald, P. Sharma, M. Bulsara, T. Milakovich, S. Ringel, A. Pitera, J. Hennessy, and A. Malonis, in *Meet. Abstr*. (The Electrochemical Society, 2012), pp. 3236–3236.
[118] A.J. Pitera, J. Hennessy, A.C. Malonis, E.A. Fitzgerald, and S.A. Ringel, in *2011 37th IEEE Photovolt. Spec. Conf. PVSC* (2011), pp. 003703–003706.
[119] J.F. Geisz, J.M. Olson, D.J. Friedman, K.M. Jones, R.C. Reedy, and M.J. Romero, in (IEEE, 2005), pp. 695– 698.
[120] K. Yamane, T. Kobayashi, Y. Furukawa, H. Okada, H. Yonezu, and A. Wakahara, J. Cryst. Growth **311**, 794 (2009).
[121] T.J. Grassman, M.R. Brenner, S. Rajagopalan, R. Unocic, R. Dehoff, M. Mills, H. Fraser, and S.A. Ringel, Appl. Phys. Lett. **94**, 232106 (2009).
[122] A.C. Lin, M.M. Fejer, and J.S. Harris, J. Cryst. Growth **363**, 258 (2013).
[123] B. Kunert, I. Németh, S. Reinhard, K. Volz, and W. Stolz, Thin Solid Films **517**, 140 (2008).
[124] H. Jussila, S. Nagarajan, P. Mattila, J. Riikonen, T. Huhtio, M. Sopanen, and H. Lipsanen, Phys. Status Solidi C **9**, 1607 (2012).
[125] T. Quinci, J. Kuyyalil, T.N. Thanh, Y.P. Wang, S. Almosni, A. Létoublon, T. Rohel, K. Tavernier, N. Chevalier, O. Dehaese, N. Boudet, J.F. Bérar, S. Loualiche, J. Even, N. Bertru, A.L. Corre, O. Durand, and C. Cornet, J. Cryst. Growth **380**, 157 (2013).
[126] A.M. Carlin, T.J. Grassman, M.R. Brenner, J. Grandal, C. Ratcliff, L. Yang, M. Mills, P. Sharma, E.A. Fitzgerald, and S.A. Ringel, in (2012), pp. 000918 –000921.
[127] T.J. Grassman, M.R. Brenner, A.M. Carlin, S. Rajagopalan, R. Unocic, R. Dehoff, M. Mills, H. Fraser, and S.A. Ringel, in (IEEE, 2009), pp. 002016–002021.
[128] W. Guo, A. Bondi, C. Cornet, A. Létoublon, O. Durand, T. Rohel, S. Boyer-Richard, N. Bertru, S. Loualiche, J. Even, and A. Le Corre, Appl. Surf. Sci. **258**, 2808 (2012).
[129] W. Guo, T. Nguyen Thanh, G. Elias, A. Letoublon, C. Cornet, A. Ponchet, A. Bondi, T. Rohel, N. Bertru, C. Robert, O. Durand, J.S. Micha, and A. Le Corre, in (2011), pp. 1 –4.
[130] T. Nguyen Thanh, C. Robert, W. Guo, A. Létoublon, C. Cornet, G. Elias, A. Ponchet, T. Rohel, N. Bertru, A. Balocchi, O. Durand, J.S. Micha, M. Perrin, S. Loualiche, X. Marie, and A. Le Corre, J. Appl. Phys. **112**, 053521 (2012).
[131] H. Yonezu, Y. Furukawa, and A. Wakahara, J. Cryst. Growth **310**, 4757 (2008).

[132] H. Yonezu, Semicond. Sci. Technol. **17**, 762 (2002).
[133] H. Döscher, T. Hannappel, B. Kunert, A. Beyer, K. Volz, and W. Stolz, Appl. Phys. Lett. **93**, 172110 (2008).
[134] A. Beyer, J. Ohlmann, S. Liebich, H. Heim, G. Witte, W. Stolz, and K. Volz, J. Appl. Phys. **111**, 083534 (2012).
[135] K. Volz, A. Beyer, W. Witte, J. Ohlmann, I. Németh, B. Kunert, and W. Stolz, J. Cryst. Growth **315**, 37 (2011).
[136] H. Döscher, B. Borkenhagen, G. Lilienkamp, W. Daum, and T. Hannappel, Surf. Sci. **605**, L38 (2011).
[137] E. Tea, J. Vidal, L. Pedesseau, C. Cornet, J.-M. Jancu, J. Even, S. Laribi, J.-F. Guillemoles, and O. Durand, J. Appl. Phys. **115**, 063502 (2014).
[138] S. Liebich, M. Zimprich, A. Beyer, C. Lange, D.J. Franzbach, S. Chatterjee, N. Hossain, S.J. Sweeney, K. Volz, B. Kunert, and W. Stolz, Appl. Phys. Lett. **99**, 071109 (2011).
[139] K. Yamane, K. Noguchi, S. Tanaka, Y. Furukawa, H. Okada, H. Yonezu, and A. Wakahara, Appl. Phys. Express **3**, 074201 (2010).
[140] C. Ratcliff, T.J. Grassman, J.A. Carlin, D.J. Chmielewski, and S.A. Ringel, in (2014), pp. 898118–898118–8.
[141] H. Kawanami, K. Baskar, I. Sakata, and T. Sekigawa, MRS Online Proc. Libr. **485**, null (1997).
[142] R.M. Sieg, S.A. Ringel, S.M. Ting, E.A. Fitzgerald, and R.N. Sacks, J. Electron. Mater. **27**, 900 (1998).
[143] Q. Xu, J.W.P. Hsu, S.M. Ting, E.A. Fitzgerald, R.M. Sieg, and S.A. Ringel, J. Electron. Mater. **27**, 1010 (1998).
[144] Y. Furukawa, H. Yonezu, A. Wakahara, S. Ishiji, S.Y. Moon, and Y. Morisaki, J. Cryst. Growth **300**, 172 (2007).
[145] V. Narayanan, S. Mahajan, K.J. Bachmann, V. Woods, and N. Dietz, Philos. Mag. A **82**, 685 (2002).
[146] Y. Takagi, H. Yonezu, K. Samonji, T. Tsuji, and N. Ohshima, J. Cryst. Growth **187**, 42 (1998).
[147] E.A. Fitzgerald, J.M. Kuo, Y.H. Xie, and P.J. Silverman, Appl. Phys. Lett. **64**, 733 (1994).
[148] N.J. Curson, S.R. Schofield, M.Y. Simmons, L. Oberbeck, J.L. O'Brien, and R.G. Clark, Phys. Rev. B **69**, 195303 (2004).
[149] S.M. Sze and K.K. Ng, *Physics of Semiconductor Devices* (John Wiley and Sons, 2007).
[52]*http://hyperphysics.phy-astr.gsu.edu/hbase/solids/zener.html (14/10/2014)*
[151] D. Jung, C.A. Parker, J. Ramdani, and S.M. Bedair, J. Appl. Phys. **74**, 2090 (1993).
[152] T.G. Deutsch, C.A. Koval, and J.A. Turner, J Phys Chem B **110**, 25297 (2006).
[153] D.A. Kudryashov, A.S. Gudovskikh, E.V. Nikitina, and A.Y. Egorov, Semiconductors **48**, 381 (2014).
[154] J.F. Geisz, D.J. Friedman, and S. Kurtz, in (IEEE, 2002), pp. 864– 867.
[155] A.S. Epstein, W.O. Groves, and J. Dowdy, Solid-State Electron. **14**, 757 (1971).
[156] X. Lu, S. Huang, M.B. Diaz, N. Kotulak, R. Hao, R. Opila, and A. Barnett, Photovolt. IEEE J. Of **2**, 214 (2012).
[157] X. Lu, R. Hao, M. Diaz, R.L. Opila, and A. Barnett, Electron Devices Soc. IEEE J. Of **1**, 111 (2013).
[158] K. Montgomery, C. Allen, I. Wildeson, J.-H. Jeon, A. Ramdas, and J. Woodall, J. Electron. Mater. **40**, 1457 (2011).

[159] J.M. Olson, A. Kibbler, and S. Kurtz, in *19th IEEE Photovolt. Spec. Conf.* (1987), pp. 285–288.
[160] J.W. Matthews and A.E. Blakeslee, J. Cryst. Growth **27**, 118 (1974).
[161] R. People and J.C. Bean, Appl. Phys. Lett. **47**, 322 (1985).
[162] R. People and J.C. Bean, Appl. Phys. Lett. **49**, 229 (1986).
[163] A. Fischer, H. Kühne, M. Eichler, F. Holländer, and H. Richter, Phys. Rev. B **54**, 8761 (1996).
[164] H. Jussila, S. Nagarajan, S. Sintonen, S. Suihkonen, A. Lankinen, T. Huhtio, C. Paulmann, H. Lipsanen, T.O. Tuomi, and M. Sopanen, Thin Solid Films (2013).
[165] S. Almosni, C. Robert, T. Nguyen Thanh, C. Cornet, A. Létoublon, T. Quinci, C. Levallois, M. Perrin, J. Kuyyalil, L. Pedesseau, A. Balocchi, P. Barate, J. Even, J.M. Jancu, N. Bertru, X. Marie, O. Durand, and A. Le Corre, J. Appl. Phys. **113**, 123509 (2013).
[166] B.W. Dodson and J.Y. Tsao, Appl. Phys. Lett. **51**, 1325 (1987).
[167] B.W. Dodson and P.A. Taylor, Appl. Phys. Lett. **49**, 642 (1986).
[168] J.F. Geisz, M.A. Steiner, I. García, S.R. Kurtz, and D.J. Friedman, Appl. Phys. Lett. **103**, 041118 (2013).
[169] S. Lu, L. Ji, W. He, P. Dai, H. Yang, M. Arimochi, H. Yoshida, S. Uchida, and M. Ikeda, Nanoscale Res. Lett. **6**, 1 (2011).
[170] I. Ho and G.B. Stringfellow, J. Cryst. Growth **178**, 1 (1997).
[171] Y. Furukawa, H. Yonezu, A. Wakahara, Y. Yoshizumi, Y. Morita, and A. Sato, Appl. Phys. Lett. **88**, 142109 (2006).
[172] S. Hatakenaka, Y. Nakanishi, A. Wakahara, Y. Furukawa, and H. Okada, J. Cryst. Growth **310**, 5147 (2008).
[173] Z. Liu, H. Kawanami, and I. Sakata, Appl. Phys. Lett. **96**, 032106 (2010).
[174] O. Rumyantsev, P. Brunkov, E. Pirogov, and A. Egorov, Semiconductors **44**, 893 (2010).
[175] J. Wu, K.M. Yu, and W. Walukiewicz, Optoelectron. IEE Proc. - **151**, 460 (2004).
[176] T. Liu, S. Chandril, A.J. Ptak, D. Korakakis, and T.H. Myers, J. Cryst. Growth **304**, 402 (2007).
[177] Y. Furukawa, H. Yonezu, K. Ojima, K. Samonji, Y. Fujimoto, K. Momose, and K. Aiki, Jpn. J. Appl. Phys. **41**, 528 (2002).
[178] H. Jussila, S. Sintonen, M. Sopanen, H. Lipsanen, and T.O. Tuomi, (2013).
[179] A. Utsumi, H. Yonezu, Y. Furukawa, K. Momose, and K. Kuroki, Phys. Status Solidi C **0**, 2741 (2003).
[180] O. Rubel, S. Baranovskii, K. Hantke, B. Kunert, W. Rühle, P. Thomas, K. Volz, and W. Stolz, Phys. Rev. B **73**, (2006).
[181] B. Kunert, D. Trusheim, V. Voßebürger, K. Volz, and W. Stolz, Phys. Status Solidi A **205**, 114 (2008).
[182] M. Izadifard, I. Buyanova, J. Bergman, W. Chen, A. Utsumi, Y. Furukawa, A. Wakahara, and H. Yonezu, Semicond. Sci. Technol. **20**, 353 (2005).
[183] S. Sanorpim, F. Nakajima, N. Nakadan, T. Kimura, R. Katayama, and K. Onabe, J. Cryst. Growth **298**, 150 (2007).
[184] C. Robert, M. Perrin, C. Cornet, J. Even, and J.M. Jancu, Appl. Phys. Lett. **100**, 111901 (2012).
[185] W. Shan, W. Walukiewicz, K.M. Yu, J.W. Ager III, E.E. Haller, J.F. Geisz, D.J. Friedman, J.M. Olson, S.R. Kurtz, H.P. Xin, and C.W. Tu, Phys. Status Solidi B **223**, 75 (2001).
[186] W. Shan, W. Walukiewicz, K.M. Yu, J.W. Ager, E.E. Haller, J.F. Geisz, D.J. Friedman, J.M. Olson, S.R. Kurtz, and C. Nauka, Phys. Rev. B **62**, 4211 (2000).

[187] W. Walukiewicz, W. Shan, J. Wu, K.M. Yu, and J.W. Ager III, in *Dilute Nitride Semicond.*, edited by M. Henini (Elsevier, Amsterdam, 2005), pp. 325–359.
[188] I.A. Buyanova, M. Izadifard, A. Kasic, H. Arwin, W.M. Chen, H.P. Xin, Y.G. Hong, and C.W. Tu, Phys. Rev. B **70**, 085209 (2004).
[189] I.A. Buyanova, M. Izadifard, W.M. Chen, H.P. Xin, and C.W. Tu, Optoelectron. IEE Proc. - **151**, 389 (2004).
[190] M. Gershenzon and R.M. Mikulyak, Appl. Phys. Lett. **8**, 245 (1966).
[191] P.J. Dean, J. Lumin. **1–2**, 398 (1970).
[192] A.S. Epstein and W.O. Groves, Adv. Energy Convers. **5**, 161 (1965).
[193] C.R. Allen, J.-H. Jeon, and J.M. Woodall, Sol. Energy Mater. Sol. Cells **94**, 865 (2010).
[194] C.R. Allen, J.M. Woodall, and J.-H. Jeon, Sol. Energy Mater. Sol. Cells **95**, 2655 (2011).
[195] G.W. Wicks, M.W. Koch, J.A. Varriano, F.G. Johnson, C.R. Wie, H.M. Kim, and P. Colombo, Appl. Phys. Lett. **59**, 342 (1991).
[196] O.V. Sulima, P.E. Sims, J.A. Cox, M.G. Mauk, R.L. Mueller, J. Reedy, R.C., A.M. Khammadov, P.D. Paulson, and G.A. Landis, in *Photovolt. Energy Convers. 2003 Proc. 3rd World Conf. On* (2003), pp. 737 –740 Vol.1.
[196] http://www.doitpoms.ac.uk/tlplib/semiconductors/ (02/02/2015)
[198] I. Németh, B. Kunert, W. Stolz, and K. Volz, J. Cryst. Growth **310**, 1595 (2008).
[199] J.M. Hartmann, V. Benevent, J.F. Damlencourt, and T. Billon, Thin Solid Films **520**, 3185 (2012).
[200] O.L. Alerhand, A.N. Berker, J.D. Joannopoulos, D. Vanderbilt, R.J. Hamers, and J.E. Demuth, Phys. Rev. Lett. **64**, 2406 (1990).
[201] A.J. Hoeven, J.M. Lenssinck, D. Dijkkamp, E.J. van Loenen, and J. Dieleman, Phys. Rev. Lett. **63**, 1830 (1989).
[202] B.S. Swartzentruber, Y.-W. Mo, R. Kariotis, M.G. Lagally, and M.B. Webb, Phys. Rev. Lett. **65**, 1913 (1990).
[203] G.W. Wicks, M.W. Koch, J.A. Varriano, F.G. Johnson, C.R. Wie, H.M. Kim, and P. Colombo, Appl. Phys. Lett. **59**, 342 (1991).
[204] T.P. Chin, J.C.P. Chang, J.M. Woodall, W.L. Chen, G.I. Haddad, C. Parks, and A.K. Ramdas, J. Vac. Sci. Technol. B **13**, 750 (1995).
[205] J. Kuyyalil, T. Nguyen Thanh, T. Quinci, S. Almosni, A. Létoublon, T. Rohel, N. Bertru, A. Le Corre, O. Durand, and C. Cornet, J. Cryst. Growth **377**, 17 (2013).
[206] M. Izadifard, I. Buyanova, J. Bergman, W. Chen, A. Utsumi, Y. Furukawa, A. Wakahara, and H. Yonezu, Semicond. Sci. Technol. **20**, 353 (2005).
[207] X.Z. Chen, D.H. Zhang, Y.J. Jin, J.H. Li, J.H. Teng, and N. Yakovlev, J. Cryst. Growth **362**, 197 (2013).
[208] H. Jussila, K.M. Yu, J. Kujala, F. Tuomisto, S. Nagarajan, J. Lemettinen, T. Huhtio, T.O. Tuomi, H. Lipsanen, and M. Sopanen, J. Phys. Appl. Phys. **47**, 075106 (2014).
[209] Y.-T. Lin, T.-C. Ma, H.-H. Lin, J.-D. Wu, and Y.-S. Huang, Appl. Phys. Lett. **96**, 011903 (2010).
[210] M. Baranowski, R. Kudrawiec, M. Syperek, J. Misiewicz, T. Sarmiento, and J.S. Harris, Nanoscale Res. Lett. **9**, 81 (2014).
[211] L. Grenouillet, C. Bru-Chevallier, G. Guillot, P. Gilet, P. Ballet, P. Duvaut, G. Rolland, and A. Million, J. Appl. Phys. **91**, 5902 (2002).
[212] I.A. Buyanova, G. Pozina, P.N. Hai, N.Q. Thinh, J.P. Bergman, W.M. Chen, H.P. Xin, and C.W. Tu, Appl. Phys. Lett. **77**, 2325 (2000).

[213] H.D. Sun, A.H. Clark, H.Y. Liu, M. Hopkinson, S. Calvez, M.D. Dawson, Y.N. Qiu, and J.M. Rorison, Appl. Phys. Lett. **85**, 4013 (2004).
[214] S.R. Bank, H.B. Yuen, H. Bae, M.A. Wistey, A. Moto, and J.S. Harris, Appl. Phys. Lett. **88**, 241923 (2006).
[215] S.R. Bank, M.A. Wistey, H.B. Yuen, V. Lordi, V.F. Gambin, and J.S. Harris, J. Vac. Sci. Technol. B Microelectron. Nanometer Struct. **23**, 1320 (2005).
[216] N. Miyashita, N. Ahsan, and Y. Okada, Sol. Energy Mater. Sol. Cells **111**, 127 (2013).
[217] H.B. Yuen, S.R. Bank, H. Bae, M.A. Wistey, and J.S. Harris, J. Appl. Phys. **99**, 093504 (2006).
[218] M.H. Tsutagawa and S. Michael, in *2009 34th IEEE Photovolt. Spec. Conf. PVSC* (2009), pp. 001954–001957.
[219] P.F. Fewster, *X-Ray Scattering from Semiconductors* (Imperial College Press, 2000).
[220] B.E. Warren, *X-Ray Diffraction* (Courier Dover Publications, 1969).
[221] S. Adachi, P. Capper, and S. Kasap, *Properties of Semiconductor Alloys: Group-IV, III-V and II-VI Semiconductors* (John Wiley and Sons, 2009).
[222] null Botha and null Leitch, Phys. Rev. B Condens. Matter **50**, 18147 (1994).
[223] Y. FURUKAWA, H. YONEZU, A. UTSUMI, and K. MOMOSE, (2013).
[224] Y.-L. Gao, Y.-J. Lu, J.-S. Zheng, Z.-G. Cai, H.-Y. Sang, and X.-R. Zeng, Eur. Phys. J. B **28**, 145 (2002).
[225] J.H. Klootwijk and C.E. Timmering, in (IEEE, 2004), pp. 247– 252.
[226] G.K. Reeves, Solid-State Electron. **23**, 487 (1980).
[227] G.K. Reeves and H.B. Harrison, IEEE Electron Device Lett. **3**, 111 (1982).
[228] H.C. Montgomery, J. Appl. Phys. **39**, 2002 (1968).
[229] E.H. Hall, Am. J. Math. **2**, 287 (1879).
[229]*http://gorgia.no-ip.com/phd/html/thesis/phd_html/node5.html#SECTION00530000000000000000*. (02/02/2015)
[231] G.H. Glover, IEEE Trans. Electron Devices **19**, 138 (1972).
[232] S.S. Hegedus and W.N. Shafarman, Prog. Photovolt. Res. Appl. **12**, 155 (2004).
[233] B.M. Kayes, H. Nie, R. Twist, S.G. Spruytte, F. Reinhardt, I. Kizilyalli, and G.S. Higashi, in *2011 37th IEEE Photovolt. Spec. Conf. PVSC* (2011), pp. 000004–000008.
[234] P.A. Lynn, *Electricity from Sunlight: An Introduction to Photovoltaics* (Wiley, Chichester, 2010).
[235] O. Skibitzki, F. Hatami, Y. Yamamoto, P. Zaumseil, A. Trampert, M.A. Schubert, B. Tillack, W.T. Masselink, and T. Schroeder, J. Appl. Phys. **111**, 073515 (2012).
[236] S. Mader and A.E. Blakeslee, Appl. Phys. Lett. **25**, 365 (1974).
[237] D. Hull and D.J. Bacon, *Introduction to Dislocations* (Butterworth-Heinemann, 2001).
[217]*Perfect and Partial Dislocations* (http://www.tf.uni-kiel.de/matwis/amat/def_en/kap_5/backbone/r5_4_2.html).
[239] P. Zaumseil and T. Schroeder, J. Appl. Phys. **104**, 023532 (2008).
[240] J. Cheng, L. Largeau, G. Patriarche, P. Regreny, G. Hollinger, and G. Saint-Girons, Appl. Phys. Lett. **94**, 231902 (2009).
[241] A. Létoublon, W. Guo, C. Cornet, A. Boulle, M. Véron, A. Bondi, O. Durand, T. Rohel, O. Dehaese, N. Chevalier, N. Bertru, and A. Le Corre, J. Cryst. Growth **323**, 409 (2011).
[242] W. Guo, A. Bondi, C. Cornet, A. Létoublon, O. Durand, T. Rohel, S. Boyer-Richard, N. Bertru, S. Loualiche, J. Even, and A. Le Corre, Appl. Surf. Sci. **258**, 2808 (2012).

[243] V. Narayanan, S. Mahajan, K.J. Bachmann, V. Woods, and N. Dietz, Acta Mater. **50**, 1275 (2002).
[244] I. Németh, B. Kunert, W. Stolz, and K. Volz, J. Cryst. Growth **310**, 4763 (2008).
[245] O. Rubel and S.D. Baranovskii, Int. J. Mol. Sci. **10**, 5104 (2009).
[246] S.N.G. Chu, S. Nakahara, S.J. Pearton, T. Boone, and S.M. Vernon, J. Appl. Phys. **64**, 2981 (1988).
[247] D.B. Holt, C. Hardingham, L. Lazzarini, L. Nasi, C. Zanotti-Fregonara, G. Salviati, and M. Mazzer, Mater. Sci. Eng. B **42**, 204 (1996).
[248] T.S. Kuan and C.-A. Chang, J. Appl. Phys. **54**, 4408 (1983).
[249] S.F. Fang, K. Adomi, S. Iyer, H. Morkoç, H. Zabel, C. Choi, and N. Otsuka, J. Appl. Phys. **68**, R31 (1990).
[250] I. Németh, B. Kunert, W. Stolz, and K. Volz, J. Cryst. Growth **310**, 4763 (2008).
[251] T.N. Thanh, Silicon Photonics Based on Monolithic Integration of III. V Nanostructures on Silicon, INSA Rennes (FOTON), 2014.
[246] ALL-EPITAXIAL ORIENTATION-PATTERNED III-V SEMICONDUCTORS FOR NONLINEAR OPTICS A.C. Lin thesis.
[253] G. Brocks, P.J. Kelly, and R. Car, Phys. Rev. Lett. **70**, 2786 (1993).
[254] B. Bourguignon, K.L. Carleton, and S.R. Leone, Surf. Sci. **204**, 455 (1988).
[255] J.L. Murray and A.J. McAlister, Bull. Alloy Phase Diagr. **5**, 74 (1984).
[256] P.H. Keck and J. Broder, Phys. Rev. **90**, 521 (1953).
[257] P.M. Petroff, A.C. Gossard, and W. Wiegmann, Appl. Phys. Lett. **45**, 620 (1984).
[258] C. Robert, Study of III-V Nanostructures on GaP for Lasing Emission on Si, Rennes, INSA, 2013.
[259] C. Cornet, T. Nguyen Thanh, T. Quinci, S. Almosni, T. Rohel, J. Kuyyalil, A. Rambaud, A. Létoublon, N. Bertru, O. Durand, and A. Le Corre, Appl. Phys. Lett. **101**, 251906 (2012).
[260] M.-A. Pinault and E. Tournié, Appl. Phys. Lett. **79**, 3404 (2001).
[261] O. Durand, A. Letoublon, D.J. Rogers, and F. Hosseini Teherani, Thin Solid Films **519**, 6369 (2011).
[262] G.B. Stringfellow, *Organometallic Vapor-Phase Epitaxy: Theory and Practice* (Academic Press, 1999).
[263] A. Zoroddu, F. Bernardini, P. Ruggerone, and V. Fiorentini, Phys. Rev. B **64**, 045208 (2001).
[264] P. Kratzer, E. Penev, and M. Scheffler, Appl. Phys. A **75**, 79 (2002).
[265] V. Virkkala, V. Havu, F. Tuomisto, and M.J. Puska, Phys. Rev. B **88**, 035204 (2013).
[266] W.G. Bi and C.W. Tu, Appl. Phys. Lett. **69**, 3710 (1996).
[267] I.A. Buyanova, M. Izadifard, W.M. Chen, H.P. Xin, and C.W. Tu, Phys. Rev. B **69**, 201303 (2004).
[268] O. Rubel, S. Baranovskii, K. Hantke, B. Kunert, W. Rühle, P. Thomas, K. Volz, and W. Stolz, Phys. Rev. B **73**, (2006).
[269] K. Jandieri, M.K. Shakfa, S. Liebich, M. Zimprich, B. Kunert, C. Karcher, A. Chernikov, K. Volz, W. Stolz, M. Koch, S. Chatterjee, W. Heimbrodt, F. Gebhard, and S.D. Baranovskii, Phys. Rev. B **86**, 125318 (2012).
[270] C. Karcher, K. Jandieri, B. Kunert, R. Fritz, K. Volz, W. Stolz, F. Gebhard, S.D. Baranovskii, and W. Heimbrodt, J. Lumin. **133**, 125 (2013).
[271] S.R. Bank, M.A. Wistey, H.B. Yuen, V. Lordi, V.F. Gambin, and J.S. Harris, J. Vac. Sci. Technol. B Microelectron. Nanometer Struct. **23**, 1320 (2005).

[272] K. Alberi, B. Fluegel, S. Crooker, D. Beaton, A. Ptak, and A. Mascarenhas, in *Bull. Am. Phys. Soc.* (American Physical Society, 2013).
[273] M. Oueslati, M. Zouaghi, M.E. Pistol, L. Samuelson, H.G. Grimmeiss, and M. Balkanski, Phys. Rev. B **32**, 8220 (1985).
[274] K.I. Lin and J.S. Hwang, Appl. Phys. Lett. **89**, 192116 (2006).
[275] R. Kudrawiec, M. Latkowska, M. Baranowski, J. Misiewicz, L.H. Li, and J.C. Harmand, Phys. Rev. B **88**, 125201 (2013).
[276] S. Mazzucato, R.J. Potter, A. Erol, N. Balkan, P.R. Chalker, T.B. Joyce, T.J. Bullough, X. Marie, H. Carrère, E. Bedel, G. Lacoste, A. Arnoult, and C. Fontaine, Phys. E Low-Dimens. Syst. Nanostructures **17**, 242 (2003).
[277] P.R.C. Kent and A. Zunger, Phys. Rev. B **64**, 115208 (2001).
[278] C. Karcher, K. Jandieri, B. Kunert, R. Fritz, M. Zimprich, K. Volz, W. Stolz, F. Gebhard, S.D. Baranovskii, and W. Heimbrodt, Phys. Rev. B **82**, 245309 (2010).
[279] I. Bosa, D. McPeake, and S. Fahy, Phys. Rev. B **78**, 245206 (2008).
[280] X.J. Wang, Y. Puttisong, C.W. Tu, A.J. Ptak, V.K. Kalevich, A.Y. Egorov, L. Geelhaar, H. Riechert, W.M. Chen, and I.A. Buyanova, Appl. Phys. Lett. **95**, 241904 (2009).
[281] F. Ishikawa, S. Fuyuno, K. Higashi, M. Kondow, M. Machida, H. Oji, J.-Y. Son, A. Trampert, K. Umeno, Y. Furukawa, and A. Wakahara, Appl. Phys. Lett. **98**, 121915 (2011).
[282] J. Slotte, K. Saarinen, E.-M. Pavelescu, T. Hakkarainen, and M. Pessa, Appl. Phys. Lett. **89**, 061903 (2006).
[283] T. Ahlgren, E. Vainonen-Ahlgren, J. Likonen, W. Li, and M. Pessa, Appl. Phys. Lett. **80**, 2314 (2002).
[284] J.W. Matthews and A.E. Blakeslee, J. Cryst. Growth **27**, 118 (1974).
[285] Y. Takagi, Y. Furukawa, A. Wakahara, and H. Kan, J. Appl. Phys. **107**, 063506 (2010).
[286] O. Skibitzki, F. Hatami, Y. Yamamoto, P. Zaumseil, A. Trampert, M.A. Schubert, B. Tillack, W.T. Masselink, and T. Schroeder, J. Appl. Phys. **111**, 073515 (2012).
[287] V.-M. Korpijärvi, A. Aho, P. Laukkanen, A. Tukiainen, A. Laakso, M. Tuominen, and M. Guina, J. Appl. Phys. **112**, 023504 (2012).
[288] Y.-J. Kuang, S.-W. Chen, H. Li, S.K. Sinha, and C.W. Tu, J. Vac. Sci. Technol. B Microelectron. Nanometer Struct. **30**, 02B121 (2012).
[289] S. Liebich, M. Zimprich, A. Beyer, C. Lange, D.J. Franzbach, S. Chatterjee, N. Hossain, S.J. Sweeney, K. Volz, B. Kunert, and W. Stolz, Appl. Phys. Lett. **99**, 071109 (2011).
[290] C. Robert, A. Bondi, T.N. Thanh, J. Even, C. Cornet, O. Durand, J.P. Burin, J.M. Jancu, W. Guo, A. Létoublon, H. Folliot, S. Boyer-Richard, M. Perrin, N. Chevalier, O. Dehaese, K. Tavernier, S. Loualiche, and A. Le Corre, Appl. Phys. Lett. **98**, 251110 (2011).
[291] W. Guo, A. Bondi, C. Cornet, A. Létoublon, O. Durand, T. Rohel, S. Boyer-Richard, N. Bertru, S. Loualiche, J. Even, and A. Le Corre, Appl. Surf. Sci. **258**, 2808 (2012).
[292] C. Cornet, T. Nguyen Thanh, T. Quinci, S. Almosni, T. Rohel, J. Kuyyalil, A. Rambaud, A. Létoublon, N. Bertru, O. Durand, and A. Le Corre, Appl. Phys. Lett. **101**, 251906 (2012).
[293] R. Kudrawiec, T. Sarmiento, P. Poloczek, J. Misiewicz, and J.S. Harris, J. Appl. Phys. **107**, 043523 (2010).
[294] Y. Furukawa, H. Yonezu, K. Ojima, K. Samonji, Y. Fujimoto, K. Momose, and K. Aiki, Jpn. J. Appl. Phys. **41**, 528 (2002).
[295] K. Jandieri, M.K. Shakfa, S. Liebich, M. Zimprich, B. Kunert, C. Karcher, A. Chernikov, K. Volz, W. Stolz, M. Koch, S. Chatterjee, W. Heimbrodt, F. Gebhard, and S.D. Baranovskii, Phys. Rev. B **86**, 125318 (2012).

[296] J.S. Harris, R. Kudrawiec, H.B. Yuen, S.R. Bank, H.P. Bae, M.A. Wistey, D. Jackrel, E.R. Pickett, T. Sarmiento, L.L. Goddard, V. Lordi, and T. Gugov, Phys. Status Solidi B **244**, 2707 (2007).
[297] J. Kuyyalil, T. Nguyen Thanh, T. Quinci, S. Almosni, A. Létoublon, T. Rohel, N. Bertru, A. Le Corre, O. Durand, and C. Cornet, J. Cryst. Growth **377**, 17 (2013).
[298] A. Aho, A. Tukiainen, V. Polojärvi, J. Salmi, and M. Guina, 86201I (2013).
[299] H.B. Yuen, S.R. Bank, H. Bae, M.A. Wistey, and J.S. Harris, Appl. Phys. Lett. **88**, 221913 (2006).
[300] H. Jussila, K.M. Yu, J. Kujala, F. Tuomisto, S. Nagarajan, J. Lemettinen, T. Huhtio, T.O. Tuomi, H. Lipsanen, and M. Sopanen, J. Phys. Appl. Phys. **47**, 075106 (2014).
[301] D. Dagnelund, I.A. Buyanova, X.J. Wang, W.M. Chen, A. Utsumi, Y. Furukawa, A. Wakahara, and H. Yonezu, J. Appl. Phys. **103**, 063519 (2008).
[302] A. Aho, V. Polojärvi, V.-M. Korpijärvi, J. Salmi, A. Tukiainen, P. Laukkanen, and M. Guina, Sol. Energy Mater. Sol. Cells **124**, 150 (2014).
[303] A. Aho, A. Tukiainen, V. Polojärvi, and M. Guina, Nanoscale Res. Lett. **9**, 1 (2014).
[304] A. Rolland, L. Pedesseau, J. Even, S. Almosni, C. Robert, C. Cornet, J.M. Jancu, J. Benhlal, O. Durand, A.L. Corre, P. Rale, L. Lombez, J.-F. Guillemoles, E. Tea, and S. Laribi, Opt. Quantum Electron. 1 (n.d.).
[305] S. Fahy and E.P. O'Reilly, Appl. Phys. Lett. **83**, 3731 (2003).
[306] J. Sjakste, N. Vast, and V. Tyuterev, Phys. Rev. Lett. **99**, (2007).
[307] C. Gmachl, S.V. Frolov, H.M. Ng, S.-N.G. Chu, and A.Y. Cho, Electron. Lett. **37**, 378 (2001).
[308] L. Esaki, Phys. Rev. **109**, 603 (1958).
[309] L. Peternai, J. Jakabovič, and M. Michalka, in *9th Int. Workshop APCOM* (2003), pp. 157–160.
[310] L. Baojun, L. Enke, and Z. Fujia, Solid-State Electron. **41**, 917 (1997).
[311] F. Zhang, D. Zhang, B. Li, E. Liu, F. Liu, and R. Gan, Mater. Sci. Eng. B **48**, 198 (1997).
[312] K. Volz, D. Lackner, I. Németh, B. Kunert, W. Stolz, C. Baur, F. Dimroth, and A.W. Bett, J. Cryst. Growth **310**, 2222 (2008).
[313] J. Yang, J. Goguen, and R. Kleiman, IEEE Electron Device Lett. **33**, 1732 (2012).
[314] A.-M. Gonçalves, N. Mézailles, C. Mathieu, P. Le Floch, and A. Etcheberry, Chem. Mater. **22**, 3114 (2010).
[315] S.L. Diedenhofen, G. Grzela, E. Haverkamp, G. Bauhuis, J. Schermer, and J.G. Rivas, Sol. Energy Mater. Sol. Cells **101**, 308 (2012).
[316] R.Y. Zhang, B. Shao, J.R. Dong, K. Huang, Y.M. Zhao, S.Z. Yu, and H. Yang, Opt. Mater. Express **2**, 173 (2012).

PERSONAL BIBLIOGRAPHY

PUBLICATIONS

S. Almosni, C. Robert, T. Nguyen Thanh, C. Cornet, A. Létoublon, T. Quinci, C. Levallois, M. Perrin, J. Kuyyalil, L. Pedesseau, A. Balocchi, P. Barate, J. Even, J.M. Jancu, N. Bertru, X. Marie, O. Durand, and A. Le Corre, Journal of Applied Physics 113, 123509 (2013).

C. Cornet, T. Nguyen Thanh, T. Quinci, **S. Almosni**, T. Rohel, J. Kuyyalil, A. Rambaud, A. Létoublon, N. Bertru, O. Durand and A. Le Corre, "*Preferential incorporation of substitutional nitrogen near the atomic step edges in diluted nitride alloys*", Appl. Phys. Lett. 101, 251906 (2012). *I. f.: 3.8*

J. Kuyyalil, T. Nguyen Thanh, T. Quinci, **S. Almosni**, A. Létoublon, T. Rohel, N. Bertru, A. Le Corre, O. Durand, and C. Cornet, Journal of Crystal Growth 377, 17 (2013).

T. Quinci, J. Kuyyalil, T.N. Thanh, Y.P. Wang, **S. Almosni**, A. Létoublon, T. Rohel, K. Tavernier, N. Chevalier, O. Dehaese, N. Boudet, J.F. Bérar, S. Loualiche, J. Even, N. Bertru, A.L. Corre, O. Durand, and C. Cornet, Journal of Crystal Growth 380, 157 (2013).

T. Nguyen Thanh, C. Robert, A. Létoublon, C. Cornet, T. Quinci, E. Giudicelli, **S. Almosni**, N. Boudet, A. Ponchet, J. Kuyyalil, M. Danila, O.Durand., N.Bertru, A. Le Corre, "Synchrotron X-ray diffraction analysis for quantitative defect evaluation in GaP/Si nanolayers", Thin Solid Films (2012), doi: 10.1016/j.tsf.2012.11.116. *I. f.: 1.9*

J. Even, L. Pedesseau, E. Tea, **S. Almosni**, A. Rolland, C. Robert, dric, J.-M. Jancu, C. Cornet, C. Katan, J.-F. Guillemoles, ois, and O. Durand, International Journal of Photoenergy 2014, e649408 (2014).

A. Rolland, L. Pedesseau, J. Even, **S. Almosni**, C. Robert, C. Cornet, J.M. Jancu, J. Benhlal, O. Durand, A.L. Corre, P. Rale, L. Lombez, J.-F. Guillemoles, E. Tea, and S. Laribi, Opt Quant Electron 1 (2014). DOI 10.1007/s11082-014-9909-z

O. Durand, **S. Almosni**, C. Robert, T.T. Nguyen, Y. Wang, C. Cornet, A. Létoublon, C. Levallois, L. Pedesseau, J. Even, J.-M. Jancu, N. Bertru, A. Le Corre, A. Bondi, P. Râle, L. Lombez, J.-F. Guillemoles, E. Tea, S. Laribi, J. Stodolna, A. Ponchet, and N. Boudet, 'Monolithic Integration of Diluted-Nitride III–V-N Compounds on Silicon Substrates: Toward the III–V/Si Concentrated Photovoltaics' Energy Harvesting and Systems. ISSN (Online) 2329-8766, ISSN (Print) 2329-8774, DOI: 10.1515/ehs-2014-0008, November 2014.

J.-P. Gauthier, C. Robert, **S. Almosni**, Y. Léger, M. Perrin, J. Even, A. Balocchi, H. Carrere, X. Marie, C. Cornet, and O. Durand. "Effect of the nitrogen incorporation and fast carrier dynamics in (In,Ga)AsN/GaP self-assembled quantum dots", Applied Physics Letters (in press) (2014).

T. Nguyen Thanh, J. Stodolna, Y. Ping Wang, A. Létoublon, **S. Almosni**, T. Rohel, A. Ponchet, N. Boudet, J.F. Bérar, A. Le Corre, N. Bertru, C. Cornet, and O. Durand. "Origin of microtwin generation at the GaP/Si heterointerface", Journal of Applied Physics (submitted) (2014).

Proceedings

O. Durand, C. Robert, T. Nguyen Thanh, **S. Almosni**, T. Quinci, J. Kuyyalil, C. Cornet, A. Létoublon, C. Levallois, J.-M. Jancu, J. Even, L. Pédesseau, M. Perrin, N. Bertru, A. Sakri, N. Boudet, A. Ponchet, P. Rale, L. Lombez, J.-F. Guillemoles, X. Marie, A. Balocchi, P. Turban, S. Tricot, M. Modreanu, S. Loualiche, and A. Le Corre, 863126 (2013).

J.-P. Gauthier, C. Robert, **S. Almosni**, C. Cornet, Y. Leger, M. Perrin, A. Letoublon, C. Levallois, C. Paranthoen, J.-P. Burin, J. Even, T. Rohel, K. Tavernier, J. Lepouliquen, H. Carrere, A. Balocchi, X. Marie, and O. Durand, in 26th International Conference on Indium Phosphide and Related Materials (IPRM) (2014), pp. 1–2.

Invited Talk

O. Durand, **S. Almosni**, Y. Ping Wang, C. Cornet, A. Létoublon, C. Levallois, A. Rolland, J. Even, N. Bertru, A. Le Corre, P. Râle, L. Lombez, J.-F. Guillemoles, A. Ponchet. "Monolithic integration of GaAsPN dilute-nitride compounds on silicon substrates: toward the III-V/Si tandem solar cell", Invited talk at the « SPIE Photonics West conference », San Fransisco, USA, 7-12 February 2015.

O.Durand, Y. Ping Wang, **S. Almosni**, M. Bahri, J. Stodolna, A. Létoublon, N. Bertru, A. Le Corre, A. Ponchet, G. Patriarche, L. Largeau, C. Magen, J.-P. Gauthier, C. Robert, C. Levallois, J. Even, A. Rolland, C. Cornet, P. Rale, L. Lombez, J.-F. Guillemoles. "Thorough structural and optical analyses of GaP -based heterostructures monolithically grown on silicon substrates for photonics on Si applications: towards the laser on silicon and high efficiency photovoltaics on silicon", Invited talk at the "International workshop on advanced optical and X-ray characterization techniques of multifunctional materials for information and communication technologies, health and renewable energy applications, Bucharest, Romania, 10-12 September 2014.

C. Cornet, C. Robert, T. Nguyen Thanh, Y. Ping Wang, **S. Almosni**, M. Perrin, A. Létoublon, J. Even, P. Turban, A. Balocchi, X. Marie, N. Bertru, O. Durand, A. Le Corre "Intégration optique par croissance directe de nanostructures III-V sur silicium", Invited talk at 14èmes Journées Nano, Micro et Optoélectronique (JNMO), Evian, France, 21-23 May 2013.

O.Durand, C. Robert, T. Nguyen Thanh, **S. Almosni**, T. Quinci, J. Kuyyalil, C. Cornet, A. Létoublon, C. Levallois, J.-M. Jancu, J. Even, L. Pédesseau, M. Perrin, N.Bertru, A. Sakri, N. Boudet, A. Ponchet, P. Rale, L. Lombez, J.-F. Guillemoles, X. Marie, A. Balocchi, P. Turban, S. Tricot, M. Modreanu, S. Loualiche, A. Le Corre,
"Structural and optical properties of (In,Ga)As/GaP quantum dots and (GaAsPN/GaPN) diluted-nitride nanolayers coherently grown onto GaP and Si substrates for photonics and photovoltaics applications"
Invited talk at "Photonics west 2013" San Francisco, USA, February 2-4 (2013).

C. Cornet, C. Robert, **S. Almosni**, T. Nguyen Thanh, T. Quinci, Y. Ping Wang, A. Létoublon, M. Perrin, J. Even, N. Bertru, A. Balocchi, P. Barate, X. Marie, O. Durand and A. Le Corre,
"GaAsPN compounds for Si photonics",
Invited talk at International Workshop "Silicon & Photonics", Rennes, France, June 11-12, (2013).

O. Durand, **S. Almosni**, C. Robert, T. Nguyen Thanh, C. Cornet, A. Létoublon, C. Levallois, L. Pedesseau, J. Even, J.-M. Jancu, N. Bertru, A. Le Corre, F. Mandorlo, M. Lemiti, P. Rale, L Lombez, J.-F. Guillemoles, E. Tea, S. Laribi, J. Stodolna, A. Ponchet, P. Bellavoine, P. Laferriere and N. Boudet
"Monolithic growth of III-V-N diluted nitride devices on Si substrate for solar cells"
Invited talk at JNPV 2012, Chantilly, France (2012).

Communications with internationnal audience

S. Almosni, C. Robert, C. Cornet, T. Nguyen Thanh, Y. Ping Wang, P. Rale, L. Lombez, J.-F. Guillemoles,

A. Létoublon, C. Levallois, N. Bertru, A. Le Corre and O. Durand. "Development of GaAsPN alloy for its integration in III-V/Si tandem solar cell", Poster at the "Workshop on above 25% efficiency solar cells via low cost approaches", Palaiseau, France, 10 July 2014.

O. Durand, **S. Almosni**, P. Râle, J. Rodière, Y. PingWang, A. Létoublon, H. Folliot, A. Le Corre, C. Cornet, A. Ponchet, L. Lombez, J.-F. Guillemoles. "Advanced concepts of III-V-based Solar Cells heterostructures: towards III-V/Si CPV on Si substrates and hot-carrier solar cells on InP substrates", Talk at the "European Materials Research Society 2014 Spring Meeting" E-MRS 2014, Lille, France, 26-30 May 2014.

S. Almosni, P. Râle, C. Cornet, C. Levallois, L. Lombez, K. Tavernier, T. Rohel, N. Bertru, J.-F. Guillemoles and O. Durand. "Annealing effect on electrical properties of GaAsPN solar cells", Poster at "29th European PV Solar Energy Conference and Exhibition" Amsterdam, The Netherlands, 22-26 September 2014.

S. Almosni, P. Râle, C. Cornet, C. Levallois, L. Lombez, K. Tavernier, T. Rohel, N. Bertru, J.-F. Guillemoles and O. Durand. "Impact of annealing on the performances of GaAsPN-based solar cells", Poster at "Compound semiconductor week" Montpellier, France, 11-15 May 2014.

J.-P. Gauthier, C. Robert, **S. Almosni**, C. Cornet, Y. Léger, M. Perrin, J.-P. Burin, A. Létoublon, J. Even, H. Carrère, A. Balocchi, X. Marie, and O.Durand. "Electrical injection in GaP-based laser waveguides and active areas", Poster at "Compound semiconductor week" Montpellier, France, 11-15 May 2014.

O. Durand, **S. Almosni**, C. Robert, T. Nguyen Thanh, Y. Ping Wang, C. Cornet, A.Létoublon, C. Levallois, L. Pedesseau, J. Even, J.-M. Jancu, N. Bertru, A. Le Corre, A. Bondi, P. Râle, L. Lombez, J.-F. Guillemoles, E. Tea, S. Laribi, J. Stodolna, A. Ponchet and N. Boudet "Monolithic integration of diluted-nitride III-V-N compounds on silicon substrates: toward the III-V/Si Concentrated Photovoltaics", Talk at "International Symposium on Inorganic and Environmental Materials" Rennes, France, 27-30 October 2013.

A. Rolland, L. Pedesseau, J. Even, **S. Almosni**, C. Robert, C. Cornet, J.M. Jancu, J. Benhlal, O. Durand, A. Le Corre, P. Râle, L. Lombez, J.-F. Guillemoles, E. Tea, S. Laribi. "Design of a lattice-matched III-V-N/Si photovoltaic tandem cell monolithically integrated on silicon substrate" Talk at "NUmerical Simulation of Optolectronic Devices (NUSOD)" Vancouver, Canada, 19-22 August (2013).

S. Almosni, C. Cornet, T. Quinci, T. Nguyen Thanh, J. Kuyyalil, C. Paranthoen, P. Rale, L. Lombez, J.-F. Guillemoles, J. Stodolna, A. Ponchet, C. Robert, Y. Ping Wang, A. Létoublon, N. Boudet, C. Levallois, N. Bertru, O. Durand and A. Le Corre "UHVCVD-MBE growth cluster for III-N-V/Si solar cells", Talk at "Compound semiconductors week, ISCS, 2013" Kobe, Japan 19-23 May 2013.

S. Almosni, C. Cornet, T. Quinci, T. Nguyen Thanh, J. Kuyyalil, P. Rale, L. Lombez, J.-F. Guillemoles, J. Stodolna, A. Ponchet, C. Robert, Y. Ping Wang, A. Létoublon, N. Boudet, C. Levallois, N. Bertru, O. Durand and A. Le Corre, "UHVCVD-MBE growth for tandem solar cells", Poster at the "Photovoltaic technical conference – thin film & advanced silicon solutions 2013" Aix-en-Provence, France, May 22-23 (2013).

P. Râle, **S. Almosni**, C. Cornet, L. Lombez, S. Laribi, O. Durand and J.F. Guillemoles "Toward a III-V/Si tandem solar cell: characterization and modeling" Poster at the "European Materials Research Society meeting E-MRS 2013" Strasbourg, Mai 26th-June 1st (2013).

P. Râle, L. Lombez, **S. Almosni**, C. Cornet, O. Durand and J.-F. Guillemoles "Investigation of GaAsPN material towards III-V/Si solar cells"Poster at EUPVSEC 2013, Paris, France, 30 september-04 October 2013.

C. Cornet, T. Nguyen Thanh, T. Quinci, **S. Almosni**, J. Kuyyalil, A. Létoublon, N. Bertru, O. Durand and A. Le Corre " Enhanced incorporation of nitrogen on atomic step edges adsorption sites in diluted nitrides alloys" Poster at Euro-MBE 2013, Levi, Finland 10-13 March 2013.

T. Nguyen Thanh, C. Robert, A. Létoublon, C. Cornet, T. Quinci, E. Giudicelli, **S. Almosni**, N. Boudet, A. Ponchet, J. Kuyyalil, M. Danila, O. Durand., N.Bertru and A.Le Corre."Synchrotron X-ray diffraction

complementary peak analysis for quantitative defect evaluation in GaP/Si nanolayers" Talk at EMRS 2012, Strasbourg, France (2012).

S. Almosni, C. Robert, T. Quinci, T. Nguyen Thanh, C. Cornet, C. Levallois, A. Létoublon, J. Even, J.M. Jancu, N. Bertru, O. Durand and A. Le Corre "Evaluation of InGaP(N) and Ga(As)P(N) materials lattice-matched to Si for multi-junction solar cells" Poster at international MBE conference 2012, Nara, Japan (2012).

C. Robert, T. Nguyen Thanh, **S. Almosni**, T. Quinci, M. Perrin, C. Cornet, J. Even, J.M. Jancu, A. Létoublon, C. Levallois, O. Durand and A. Le Corre "Dilute nitride GaNAsP for photonic applications on silicon" Poster ISTN2012 : International Symposium on nitrides, Saint Malo, France, June 3th-6th 2012

S. Almosni, C. Robert, T. Nguyen Thanh, C. Cornet, A. Létoublon, C. Levallois, T. Quinci, J. Even, J.M. Jancu, O. Durand and A. Le Corre. "InGaPN and GaAsPN layers for tandem solar cells on silicon". Poster at EMRS 2012, Strasbourg, France, (2012).

S. Almosni, C. Robert, C. Cornet, C. Levallois, T. Quinci, A. Létoublon, J. Even, J.M. Jancu, O. Durand and A. Le Corre. "Potentiality of GaAsPN and InGaPN for photovoltaic applications". Poster at PVTC 2012, Thin films and advanced silicon solutions, Aix-en-provence, France, (2012).

Communications with National audience

O. Durand, **S. Almosni**, Y.Ping Wang, C. Cornet, A. Létoublon, C. Levallois, L. Pedesseau, A. Rolland, J. Even, N. Bertru, A. Le Corre, A. Ponchet, P. Rale, L. Lombez, J.-F. Guillemoles. "Epitaxie cohérente de composés GaP et GaAsPN à azote dilué sur substrats de Si pour l'élaboration de cellules PV tandem III-V/Si", Talk at "Matériaux 2014" Montpellier, France, 24-28 November 2014.

A. Létoublon, T. Nguyen Thanh, Y.Ping Wang, **S. Almosni**, C. Cornet, N. Bertru, N. Boudet, J. Stodolna, A. Ponchet, E. Tea, J. Even, S. Laribi, A. Le Corre and O. Durand. "Analyse quantitative de la perfection cristalline de nanocouches épitaxiales GaP/Si", Talk at "Xème colloque rayons X et matière" Nantes, France, 12-15 November 2013.
P. Râle, L. Lombez, **S. Almosni**, C. Cornet, O. Durand, J.-F. Guillemoles, "Etude optoélectronique du GaAsPN dans l'optique de cellules solaires III-V/Si" Poster presentation at "Journées nationales du Photovoltaïque JNPV 2013" Dourdan, France, 3-6 December 2013.

S. Almosni, C. Robert, C. Cornet, T. Nguyen Thanh, Y.Ping Wang, P. Rale, L. Lombez, J.-F. Guillemoles, A. Létoublon, C. Levallois, N. Bertru, O. Durand and A. Le Corre. "Optimisation des propriétés structurale de l'interface GaP/Si et des propriétés électroniques de cellules solaires GaAsPN/GaP pour la fabrication de cellule tandem", Poster presentation at "Journées nationales du Photovoltaïque JNPV 2013" Dourdan, France, 3-6 December 2013.

P. Rale, E. Tea, **S. Almosni**, C. Cornet, L. Lombez, S. Laribi, L. Pedesseau, J.-M. Jancu, J. Even, O. Durand, and J.F. Guillemoles. "Toward a III-V/Si tandem solar cell: characterization and modeling", poster at JNPV 2012, Chantilly, France (2012).

S. Almosni, P. Râle, C. Robert, T. Nguyen Thanh, C. Cornet, C. Levallois, A. Létoublon, J. Even, J.M. Jancu, N. Bertru, J.F. Guillemole, O. Durand and A. Le Corre. "Evaluation of InGaPN and GaAsPN materials lattice-matched to Si for multi-junction solar cells", poster at JNPV 2012, Chantilly, France (2012).

Selected seminars

C. Cornet, O. Durand, A. Létoublon, C. Robert, T. Nguyen Thanh, **S. Almosni**, T. Quinci, Y. Ping Wang, J. Kuyyalil, L. Pédesseau, M. Perrin, C. Levallois, S. Boyer-Richard, J.-P. Burin, Y. Léger, H. Folliot, J. Even, J.-M. Jancu, S. Loualiche, N. Bertru and A. Le Corre. "Emetteurs/absorbeurs optiques sur silicium: intégration pseudomorphique de semi-conducteurs III-V" Invited seminar (talk) at IPR, Rennes, France, december 2012.

AVIS DU JURY SUR LA REPRODUCTION DE LA THESE SOUTENUE

Titre de la thèse:
Growth, structural and electrooptical properties of GaP/Si and GaAsPN/GaP single junctions for lattice-matched tandem solar cells on silicon

Nom Prénom de l'auteur : ALMOSNI SAMY

Membres du jury :
- Monsieur DURAND Olivier
- Monsieur LEVALLOIS Christophe
- Monsieur CORNET Charles
- Monsieur LINCOT Daniel
- Monsieur ETCHEBERRY Arnaud
- Monsieur HANNAPPEL Thomas
- Monsieur LEMITI Mustapha

Président du jury : M. Lemiti

Date de la soutenance : 23 Février 2015

Reproduction de la these soutenue

Thèse pouvant être reproduite en l'état
~~Thèse pouvant être reproduite après corrections suggérées~~

Fait à Rennes, le 23 Février 2015

Signature du président de jury

Le Directeur,

M'hamed DRISSI

Résumé

Cette thèse se concentre sur la fabrication de cellule solaire III-N-V sur substrat de GaP (001) et sur la croissance de couche de GaP sur Si (001). Le but est de réaliser des cellules solaires hautes efficacité sur un substrat à faible coût afin de les intégrer dans des centrales solaire photovoltaïque sous concentration. Les principaux résultats obtenus montrent :

- L'importance de l'utilisation d'AlGaP en tant que couche de prénucléation pour annihiler les parois d'antiphase à l'interface GaP/Si (néfaste pour les propriétés optoélectroniques des dispositifs)
- De nombreuses similitude entre la croissance de GaAsN et de GaPN ce qui permet d'élaborer une stratégie afin d'optimiser les propriétés optoélectroniques du GaAsPN
- De fortes corrélations entre les propriétés optique et éléctriques dans les nitrures dilués
- La réalisation préliminaire d'une cellule solaire monojonction sur GaP ayant un rendement encourageant de 2.25% considérant la faible épaisseur de l'absorbeur dans cette cellule (300 nm)

Abstract

This thesis focuses on optimizing the heterogeneous growth of III-N-V solar cells on GaP (001) and GaP nanolayers on Si (001). The goal is to build high efficiency solar cells on low-cost substrate for the realization of concentrated photovoltaic powerplant. The main results shows:

- AlGaP as prenucleation layer increase the annihilations of anti-phase boundaries at the GaP/Si interface (harmful for the electronic properties of the devices).
- Similarities between the growth of GaAsN and GaPN giving strategies to improve the GaAsPN electrical properties
- Clear correlations between the optical and electrical properties of dilute nitride solar cells, giving interesting tools to optimize the growth of those materials using optical measurements.
- The realization of a GaAsPN solar cell on GaP with a yield of 2.25%. This results is encouraging given the thin GaAsPN absorber used in this cell

N° d'ordre : D15 - 02 / 15ISAR 02

Institut National des Sciences Appliquées de Rennes
20, Avenue des Buttes de Coësmes • CS 70839 • F-35708 Rennes Cedex 7
Tel : 02 23 23 82 00 - Fax : 02 23 23 83 96